SYNTHESIS AND APPLICATIONS OF ONE- AND TWO-DIMENSIONAL POLYMER–CARBON NANOMATERIAL COMPOSITES

by

Wanji Seo

B.S., The Ohio State University, 2007

Submitted to the Graduate Faculty of the

Dietrich School of Arts and Sciences in partial fulfillment

of the requirements for the degree of

Doctor of Philosophy

University of Pittsburgh

2016

UNIVERSITY OF PITTSBURGH

DIETRICH SCHOOL OF ARTS AND SCIENCES

This dissertation was presented

by

Wanji Seo

It was defended on

Aug 15th, 2016

and approved by

Prof., Tara Y. Meyer, Associate Professor, Department of Chemistry

Prof., W. Seth Horne, Associate Professor, Department of Chemistry

Prof., Lei Li, Assistant Professor, Department of Chemical and Petroleum Engineering

Thesis Director/Dissertation Advisor: Prof., Alexander Star, Professor, Department of Chemistry

SYNTHESIS AND APPLICATIONS OF ONE- AND TWO-DIMENSIONAL POLYMER–CARBON NANOMATERIAL COMPOSITES

Wanji Seo, PhD

University of Pittsburgh, 2016

SYNTHESIS AND APPLICATIONS OF ONE- AND TWO-DIMENSIONAL POLYMER–CARBON NANOMATERIAL COMPOSITES

Wanji Seo, PhD

University of Pittsburgh, 2016

This dissertation describes the synthesis of polymer and carbon nanomaterial composites and their applications in drug delivery, chemical sensing, and catalytic oxidative patterning. The first part studies polyethylene glycol functionalized oxidized single-walled carbon nanotubes (PL-PEG/ox-SWCNT) as a drug nanocarrier to prolong the circulation of two mitochondria targeting radiomitigators TPP-IOA and XJB-5-131. In *in vivo* tests with mice exposed to a single total body irradiation of 9.25 Gy, the PL-PEG/ox-SWCNT nanocarrier prolongs the circulation of TPP-IOA without developing apparent toxicity and exhibits radiation mitigating effects, slightly better than that of free TPP-IOA. The i*n vivo* drug effect of the XJB-5-131 conjugate is inconclusive. The stability of Doxorubicin-loaded PL-PEG/ox-SWCNT is investigated under oxidative bursts that occur in neutrophils and macrophages. Myeloperoxidase-catalyzed and peroxynitrite-mediated oxidations of the drug conjugate are studied *ex vivo*, and the *in vitro* tests in B16 melanoma cells and tumor-activated myeloid cells are conducted. Both *ex vivo* and *in vitro* results indicate that the nanocarrier protects Doxorubicin from the oxidative degradation.

The second part of the dissertation discusses the synthesis and applications of two-dimensional polymers. A novel crystalline polybenzobisimidazole-based two-dimensional supramolecular polymer (2DSP-PBBI) is synthesized by condensation/precipitation polymerization under solvothermal conditions. The surface morphology of 2DSP-PBBI is

analyzed with electron and atomic force microscopy, revealing planar surfaces formed by hydrogen bonding. An iron(III)-coordinated porphyrin-based covalent organic framework (Fe-DhaTph-COF) is synthesized for the fabrication of oxidatively patterned graphite in the presence of H_2O_2 and/or NaOCl. The vertical channel created by patterning is ~3 nm in depth, and liquid-exfoliation of the patterned graphite provides few-layer porous graphene. Although the shape and size of the pores are not uniform, this study demonstrates that metallated COFs can be utilized as surface catalysts and master templates for patterning.

TABLE OF CONTENTS

LIST OF TABLES

LIST OF FIGURES

Chapter 1

Chapter 2

Chapter 3

Chapter 4

Chapter 5

PREFACE

Thank you Dr. Star!

Prefer what is positive and multiple, difference over uniformity, flows over unities, mobile arrangements over systems. Believe that what is productive is not sedentary but nomadic.

— Michel Foucault

1.0 INTRODUCTION

Carbon nanomaterials (CNMs) such as carbon nanotubes and graphene have demonstrated a wide range of applications in nanotechnology over the last two decades. CNMs are used independently or in combination with other materials to create a variety of novel properties that a single carbon material cannot provide. Therefore, studies of CNMs often cross many disciplines and will continue to have a broad impact on many fields in the future.

An overwhelming number of studies of carbon nanotubes (CNTs) have been published over the past couple of decades, and much of fundamental and applied graphene research has already surpassed the number of CNT publications. Each of these materials offers its own merit and exhibits distinct properties arising from the unique geometry and size, resulting in outstanding optical, thermal, mechanical, and chemical properties.[1] To investigate and identify extraordinary novel properties of CNMs, all available characterization techniques and even unorthodox methods should be implemented. Despite the tremendous efforts, interpretation of acquired data is occasionally highly challenging especially for new hybrid materials possessing multiple different characteristics and novel properties.

To understand diverse subjects covered in this dissertation, the fundamental chemistry and properties of one-dimensional CNTs and two-dimensional graphene will be discussed in Chapter 1. Despite the interesting properties exhibited in the pure form of carbon allotropes, their poor solubility often necessitates chemical modification of carbon atoms prior to utilization

in real world applications such as complex devices, reinforced composites, and organic/inorganic hybrid materials. Therefore, the chemical functionalization of CNMs, which has been developed on the basis of organic chemistry, is an important step that should be considered in the design of new materials as well as in the realization of scalable applications. On the basis of tunable chemical characteristics, CNMs are readily modified and integrated into the components of materials, and ultimately their performance as functional materials is evaluated in various contexts.

This dissertation introduces the synthesis and characterization of two different types of polymer–carbon nanomaterial composites: (1) polymer–carbon nanotubes and (2) polymer–graphene composites. Then the demonstration of these composites as functional materials will be described in the context of drug delivery (Chapter 2 and 3), chemical sensing (Chapter 4), and oxidative patterning (Chapter 4 and 5). Despite the focus on completely different applications, each subject has significantly contributed to the study of CNMs. To better understand the research projects discussed in Chapter 2–5, the backgrounds of CNMs and polymer nanocomposites will be overviewed in Chapter 1. Particular polymers are chosen to achieve compatibility with CNMs for specific applications, and therefore polymers are an integral part of this dissertation. However, Chapter 1 is centered on the types of CNMs and their basic properties that have been studied mostly over the last decade. Relevant information on each polymer employed in the research projects will be discussed in depth in later chapters.

1.1 CARBON NANOMATERIALS

CNMs are commonly based on carbon allotropes, composed of sp^3-, sp^2-, and sp-hybridized carbon atoms.[2] Since the discovery of Buckminsterfullerene in 1985, new carbon allotropes have been developed besides naturally existing graphite and diamond.[2] Generally, carbon allotropes are stable and can serve as versatile building blocks in the synthesis of numerous materials. Synthetic carbon allotropes play significant roles in materials chemistry and nanotechnology. Several synthesis and growth methods such as arc discharge (>1700 °C), laser ablation, and chemical vapor deposition (>800 °C), which are mostly performed at high temperatures, successfully afforded commercial CNMs with competitive prices.[3] The physical parameters of CNMs such as size, diameter, and the number density of defects slightly vary from one supplier to another. However, the mass production of batch-by-batch structurally homogeneous materials is not easy to control, and the post-synthetic purification process of monodisperse CNMs precludes the low-end fabrication. Advances in modern organic synthetic chemistry offer novel bottom-up routes[4] for the synthesis of structurally well-defined carbon allotropes. Although the total synthesis of carbon allotropes is not common, the approach to incorporating different hybridizations into a single material offers limitless resources for designing a variety of structures and novel properties of CNMs on demand.[5]

Among carbon allotropes that have been developed to date, fullerenes, CNTs, and graphene/graphite have been most extensively studied with respect to both theory and applications. Both carbon nanotubes and graphene are composed of sp^2-hybridized carbon atoms in a honeycomb lattice.[1] The conjugated network of π–electrons confined in low dimensions imparts unique electronic properties and redox activity.[6] The excellent mechanical strength (e.g., elastic modulus of CNTs, ~1000 GPa) has already resulted in a rapid growth of commercial

structural materials and reinforced composites.[6] CNTs are essentially rolled up graphene sheets (Figure 1.1), but their unique shapes have imparted them different properties and enabled various applications.

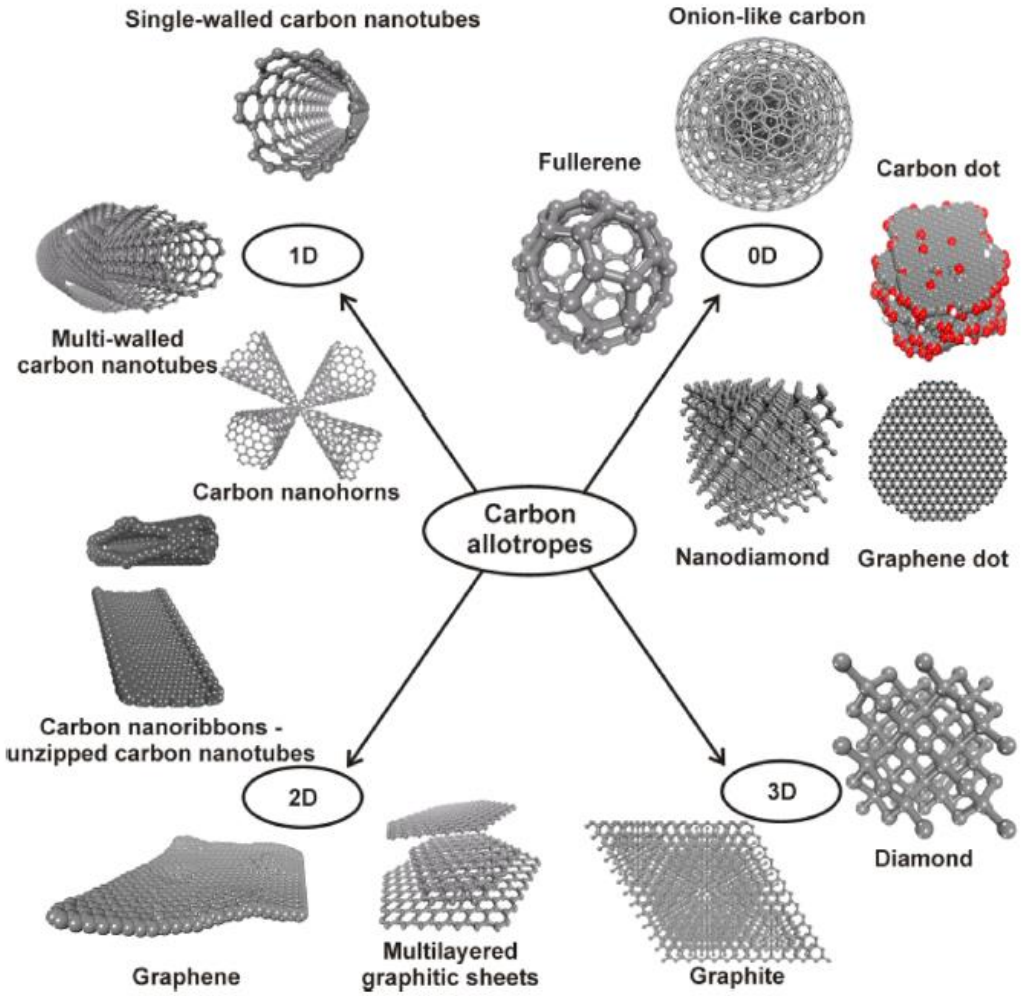

Figure 1.1 Carbon allotropes based on dimensionality.[6]

1.1.1 One-dimensional carbon nanotubes

Important parameters to determine the properties of CNTs are the number of walls (e.g., single-walled (SWCNT), double-walled (DWCNT), and multi-walled (MWCNT)), length, diameter, and chiral angle.[7-8] As Chapter 2 and 3 deal with SWCNT-based drug nanocarriers, this dissertation focuses only on SWCNTs.

As the size of SWCNTs and even the degree of impurities vary with manufacturing processes,[3,9] an appropriate commercial brand should be chosen before chemical treatments. Most as-prepared SWCNTs are sold as bundles with ca. 1–1000 μm in length and ca. 1–2 nm in diameter.[10] They are poorly dispersible in most organic solvents as well as water.[11] *N*,*N*-Dimethylformamide (DMF) and *N*-methylpyrrolidone (NMP) are solvents most frequently used in fabrication processes although 1,2-dichlorobenzene has shown the best dispersibility with CNTs.[12] To suspend CNTs in solutions, cutting as-prepared CNTs by sonication, an oxidation reaction occurring at the ends of CNTs, or surface modifications are required.[13] When graphene sheets are rolled up, they form different chiral indices (n,m) and angles (θ) (Figure 1.2a).[7-8,10] These major characteristics of CNTs impart varying degrees of strains which influence their stability and reactivity in different conditions.[8] Generally, cylindrical CNTs exhibit better chemical reactivity than graphene.[14] The chiral indices (n,m) in the chiral vector ($C_h = n\mathbf{a}_1 + m\mathbf{a}_2$) indicate the electronic properties of CNTs: metallic nanotubes are $n - m = 3k$ with k being an integer, semimetallic for $n = m$, and semiconducting for $n - m \neq 3k$.[10] Most as-synthesized SWCNTs contain different chiral species unless they are separated in post-synthetic steps.[15] Different chirality determines the energy band gap of semiconducting CNTs.[15] Although most bundled semiconducting CNT samples have a band gap of ~1 eV, each chiral species has a distinct energy band gap ranging 0.5–3 eV.[16] Therefore, bundles of CNTs may behave

differently depending on the relative amount of different chiral species contained in a sample (Figure 1.2b), and a sample consisting of an isolated single chiral species is ideal for achieving homogenous properties.[10,17]

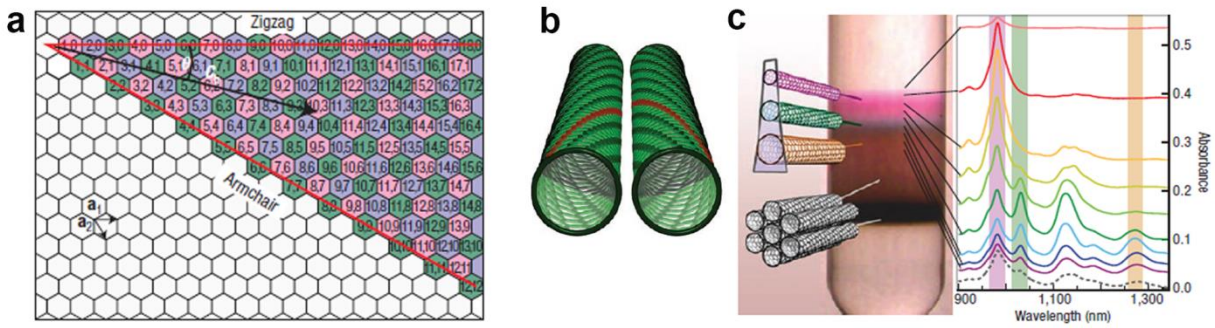

Figure 1.2 Physical properties of single-walled carbon nanotubes. (a) Chiral vector of nanotubes ($C_h = n\mathbf{a_1} + m\mathbf{a_2}$) where a_1 and a_2 are unit vectors with the chiral angle (θ). (b) SWCNTs with identical chiral vectors but different chiral handedness. (c) Sorting SWNTs with different diameters by density gradient ultracentrifugation (DGU) and corresponding optical absorbance spectra for the different fractions.[10]

1.1.2 Two-dimensional graphene

Graphene is a single-layer material isolated from three-dimensional graphite, and has a hexagonal honeycomb lattice with a sp^2-hybridized C–C bond length of 1.42 Å and an interlayer spacing of 3.35 Å.[1] The properties of a single layer graphene are very different from those of bulk graphite. Graphene layers strongly form AB stacks supported by van der Waals forces.[18] The most remarkable characteristic of graphene is π–electrons delocalized on the atomically thin plane where sp^2 carbon atoms provide two orbitals π and π* to form the valence and conduction

bands.[19] The orthogonal π and π* orbitals touching at the hexagonal lattice points (Dirac points) do not overlap with each other, rendering graphene zero band gap semimetallic.[19-20] The massless electrons with high carrier mobility, which is dramatically different from epitaxially grown conventional 2D semiconducting layers, have garnered much attention primarily as an alternative to silicon electronics.[20] However, the zero band gap property limits the direct applications of graphene, especially in standard logic circuits and devices such as transistors due to high current leakage and energy dissipation.[21] In addition to the excellent electron conductivity and ambipolarity in the field effect configuration, graphene possesses outstanding mechanical, thermal, and optical properties.[21-22] For example, the optical transparency of graphene is particularly advantageous for conductive electrodes in touch screens and flexible electronics.[22]

Few-layer graphene can be isolated by both top-down and bottom-up approaches. Generally, top-down approaches have been found more efficient, such as liquid-phase exfoliation of graphite, mechanical exfoliation (e.g., pull-off by cellophane tape and cleavage with a razor), reduction of graphite oxide (GO), and unzipping of CNTs.[23-26] Preparation of free-standing, atomically thin layered graphene without generating additional defects is crucial. Random defects generated in the course of mechanical and chemical treatment reduce the homogeneity of samples, and may degrade device performance.[20,27] The exfoliated graphene should be transferred to a different substrate without creating wrinkles and folds, which can be highly challenging. Some bottom-up methods can remove the cumbersome step of transfer by directly growing graphene from organic precursors on a substrate using chemical vapor deposition.[28-30] Common substrates are SiC, Si, SiO_2, and metal substrates (e.g., Cu, Ni, Au).[20,31] The direct

growth is convenient in that a separate graphene transfer step is not necessary and single-layer graphene on a dielectric substrate can be directly incorporated into device fabrication.[30]

Once single- or few-layer of graphene is isolated, the energy band gap should be tuned for electronic devices. To open the energy band gap of graphene, precise manipulation of defects, edges, and strain is required to provide high quality 2D crystal lattice. These graphene-like materials bearing semiconducting properties include reduced graphene oxide (rGO) prepared from graphene oxide (GO), holey graphene, and graphene nanoribbons.[6,22-23,32] Fabrication methods for obtaining the controlled nanostructures of these graphene-based materials will be continuously investigated to develop excellent semiconducting materials.

1.1.3 Characterization methods

Microscopy and spectroscopy are implemented to characterize CNMs and CNM composites.[20,33] Transmission electron microscopy (TEM) and scanning electron microscopy (SEM) are imaging techniques most commonly employed in nanoscience. TEM provides information on size, shape, and aggregation/dispersion using high-energy electron beam (up to 300 keV) and is especially useful for identifying structural integrity and changes after surface modification.[34] Atomic force microscopy (AFM) employs a cantilever to measure the force (attraction/repulsion) between the sample surface and the probe on the order of nanometers. The most powerful feature of AFM is to resolve the height profile of a sample–substrate. Theoretically the vertical (or depth) resolution can be achieved up to 0.1 nm, allowing estimation of the thickness of single-layer graphene.[21]

Optical spectroscopy is a noninvasive tool for analyzing structure-dependent optical transitions of CNMs. Major techniques routinely used in CNM characterization are UV-Vis-Near Infrared (UV-Vis-NIR), infrared (IR), Raman, and photoluminescence (PL).[8,33-34] UV-Vis-NIR spectroscopy has been frequently used to characterize the distinct electronic transition (i.e., energy gap) of metallic and semiconducting carbon nanotubes (Figure 1.3a) corresponding to the energy density states.[15] In addition, the dispersion condition (e.g., bundled vs. separate nanotubes) and the electronic perturbation caused by the conversion from sp^2 to sp^3 hybridization upon covalent functionalization are translated into the absorption profile (Figure 1.3b).[35]

Raman spectroscopy has provided insights into the properties of sp^2 carbon allotropes including CNTs and graphite/graphene (Figure 1.3c).[36-37] The major peaks characteristic of the graphitic lattice are shown in Figure 1.3c. G (1584 cm^{-1}) and G′ (2700 cm^{-1}) bands are attributed to the intrinsic pristine sp^2 graphitic structure.[21] If a sample consists of pure sp^2 carbon atoms, a sharp G peak is observed.[38] The G′ peak is most useful for probing the thickness of graphite flakes (i.e., the number of layers) based on the peak shape and intensity.[38] D (1350 cm^{-1}) and D′ (1617 cm^{-1}) bands are associated with the density of defects where symmetry is broken due to the formation of vacancy and the altered hybridization of carbon bonds.[37] The ratio of I_D/I_G estimated by measuring the height or the area under the curve can provide a convenient metric of sp^3-defects to pristine sp^2 graphitic carbons, and the bandwidth of D′ band indicates the degree of vacancy-defect.[36-37] The 2D peak (2680 cm^{-1}) provides information on the number and the relative orientation of graphene layers by showing significant changes in shape and intensity (Figure 1.3d).[36]

FTIR and X-ray photoelectron spectroscopy (XPS) are used to identify organic functional groups incorporated into the graphitic lattice.[34] Bulk samples can be analyzed with FTIR, but

some functional groups show weak signals for accurate characterization.[33] Thus XPS, which quantifies the binding energy of photoelectrons ejected from the sample, is utilized to probe defects and covalently functionalized samples.[33] XPS measures the atomic content and identifies the chemical environment of an atom of interest when samples are irradiated with X-rays, but the surface sensitivity is limited to the small inelastic mean free path (<10 nm) of the ejected photoelectrons.[34] Although it can be crucial to the analysis of some elemental information and bond types, the deconvolution data process of XPS spectra can be sometimes ambiguous and subjective.[34]

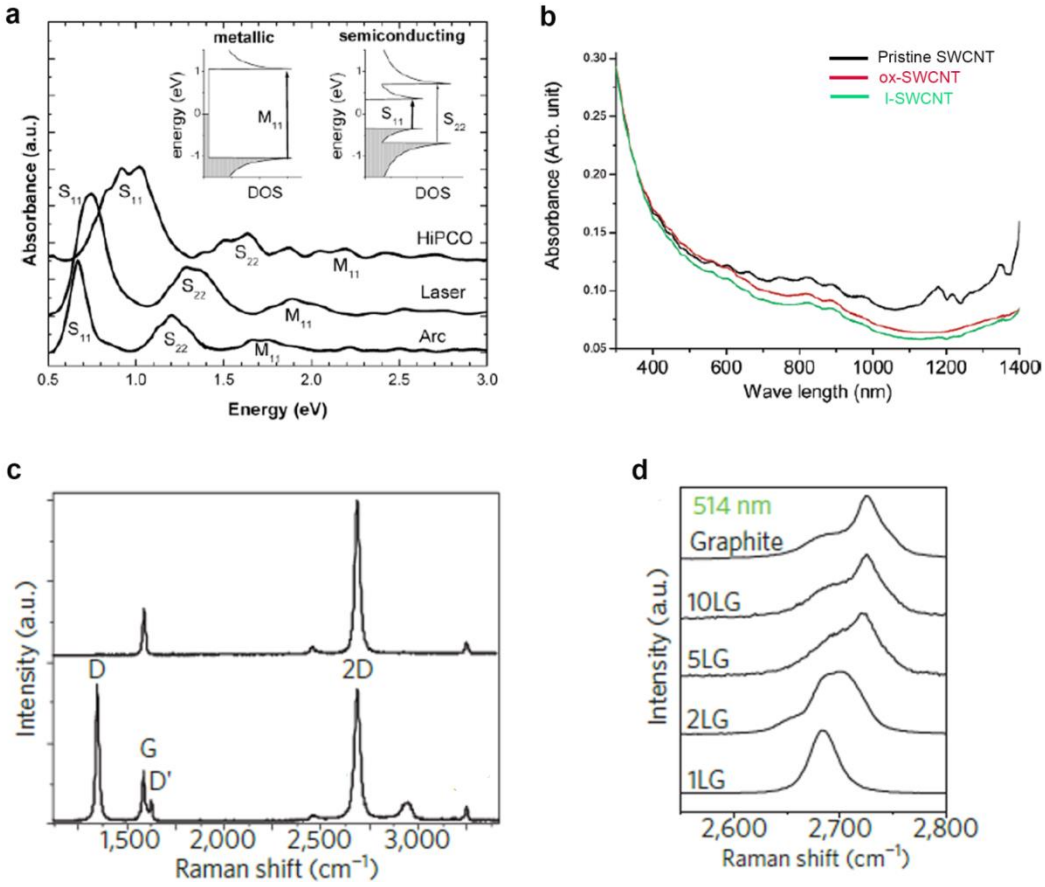

Figure 1.3 UV-Vis-NIR and Raman spectroscopy. (a) UV-Vis-NIR absorption spectra corresponding to the energy band gaps of different types of SWCNTs.[8] (b) UV-Vis-NIR absorption spectra for pristine SWCNT (black), oxidized ox-SWCNT (red), and iodinated I-SWCNT (green).[39] (c) Raman spectra of pristine (top) and defected (bottom) graphene.[36] (d) Different shapes and shift of the 2D peak dependent on the number of graphene layers.[36]

1.2 POLYMER–CARBON NANOMATERIAL COMPOSITES

Polymer–carbon nanomaterial composites refer to systems made of a polymer matrix and CNM particles, which can be found in a broad range of materials such as biomaterials and surface catalysts as well as structural reinforcement. Polymers and CNMs are ideal for producing lightweight materials, and a variety of new composites can be designed with the diverse types of polymers available on the market.[40] To integrate the unique characteristics of each component into a composite, the surface properties, polarity, and dispersibility in solvents of each component should be examined to ensure good compatibility and long-term stability.[41] To prepare CNM-based polymer composites, chemical modification (i.e., covalent and noncovalent functionalization) of CNMs is often required to optimize the compatibility before blending with polymers.[42] Therefore, the types of chemical treatment are discussed first, and then examples of polymer–CNM composites are selected to introduce the subjects covered in this dissertation.

1.2.1 Covalent and noncovalent chemistry of carbon nanomaterials

Generally, noncovalent functionalization, also often described as physical adsorption onto the graphitic surface, offers relatively convenient routes to modify the surface properties of CNMs without undergoing rigorous chemical alteration of the original material.[43] On the other hand, covalent functionalization of conjugated π-systems requires aggressive reaction conditions to break the inert sp^2 C–C bond in the graphitic lattice.[13] Nevertheless, the oxidation process is the most important covalent functionalization method, which introduces oxygen-containing functionalities (e.g., carboxylic, hydroxyl, and epoxy groups) into both the edge and the basal

plane of CNMs.[13,44] These new functional groups impart hydrophilicity to inherently hydrophobic CNMs and also alter the original solubility.[13] Oxidation of CNTs with strong oxidants (e.g., H_2O_2/H_2SO_4 or HNO_3/H_2SO_4) provides a means to shorten the length, and more oxidized samples tend to have a greater number of defects than pristine CNTs.[45] Oxidation of graphene provides a chemical route for exfoliation as well as newly incorporates oxygen-containing groups, which facilitates delamination between graphene layers.[46] Both oxidized CNTs and GO can be kinetically suspendable even in water for ca. 100 days due to hydrogen bonding,[47] but aggregates slowly form and precipitate out over an extended period of time. The extent of dispersibility range can be further controlled by the oxidation method and the degree of oxidation.[48] Thus oxidized CNTs and GO are common precursors for multiple synthetic steps by covalent functionalization.[49] Figure 1.4 shows covalent chemistry schemes utilized in CNTs and graphene.[50-51]

Two different methods for functionalization with polymers have been developed: (1) Grafting-To approaches involve coupling between functional groups (e.g., carboxylic and hydroxyl groups) on CNMs and the end-group of polymer chains, resulting in the formation of covalently linked polymer–nanocomposites.[41,52] Occasionally, linkers (or spacers) such as amide and ester derivatives are connected to CNMs, followed by coupling reaction with a polymer.[49, 52] (2) Grafting-From approaches require a polymerization initiator reacting on the CNM surface where *in situ* polymerization occurs on the activated functional groups of CNMs. Atom transfer radical polymerization (ATRP), reversible addition-fragmentation chain transfer (RAFT), ring opening polymerization (ROP), and many other methods were developed.[41,52] Grafting-From methods provide higher grafting density than Grafting-To methods because the polymer growth is impeded by steric hindrance.[41]

Another type of covalent functionalization is chemical doping which facilitates the substitution of heteroatoms (e.g., nitrogen and boron) with graphitic carbon atoms without altering the original sp^2 hybridization of carbons.[50] The doping process is based on catalysis and disproportionation, in which CNMs are subject to an atomic-nitrogen flow and nitrogen atoms are doped by N_2 dissociation in microwave plasma.[53] Doping is employed mainly to control the Fermi level and the properties of CNM-based electronics.[20, 53]

Noncovalent functionalization is achieved by intermolecular interactions between the polymer and the CNM, such as π–π stacking, CH–π, van der Waals, electrostatic, and nonspecific hydrophobic interactions.[43] Oxidized CNMs such as ox-SWCNT and GO can have significant contributions from hydrogen and ionic bonding interactions in addition to π–π stacking.[50] Noncovalent functionalization may form weak interfaces because of the dynamic nature of noncovalent bonding, and thus the stability of composites can be dependent on the polymer–solvent interaction in solution.[43] However, when cooperative intermolecular bonding occurs between polymers and CNMs that have a large number of aromatic rings fused together on the surface, the bond strength can significantly increase, allowing the formation of sufficiently robust polymer–CNM composites.[43] The extended π–conjugation and planarity of graphene impart stronger π–π interactions with small aromatic molecules (e.g., pyrene, quinoline, and porphyrin) than rGO and GO.[43,54] Even rGO reduced from GO with sp^3 defects exhibits much higher binding affinity with sulfonated aluminum phthalocyanine than GO and SWCNTs.[54-55] Therefore, the planar nanostructure can result in enhanced dispersibility, biocompatibility, binding capacity, and sensing properties.[43] The one-dimensionality of CNTs does not impart the binding affinity arising from π–π stacking as strong as two-dimensional graphene.[55] However, CNTs have shown effective, strong binding with linear polymers that can

wrap around the CNT sidewall and remain undisrupted in solution.[13] The binding strength dependent on hydrophilicity/hydrophobicity can be further tuned by the functional groups of CNTs and polymers.[56]

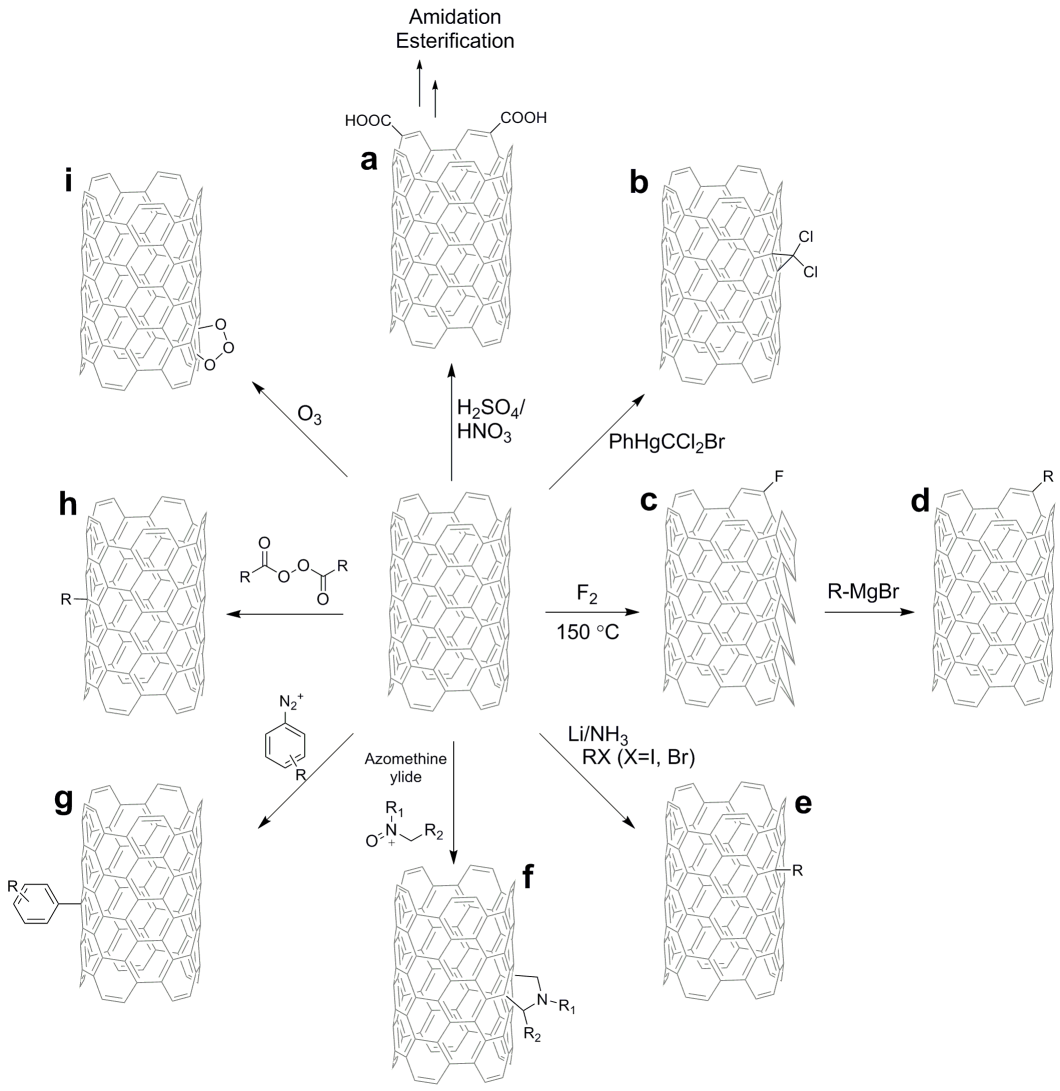

Figure 1.4 Covalent functionalization of SWCNTs. (a) Oxidation, (b) carbine addition, (c) fluorination, (d) followed by alkylation, (e) Birch reduction, (f) 1,3-dipolar cycloaddition, (g) diazonium coupling, (h) radical addition, and (i) ozonolysis.[49]

1.2.2 Applications of polymer–carbon nanomaterial composites

Polymer–carbon nanomaterial composites composed of CNTs and graphene have demonstrated excellent properties particularly in mechanical, electrical, and thermal applications.[41,57] Both CNTs and graphene find numerous applications as composite reinforcers,[40,52] conducting materials for electrical devices,[58-59] biomedical devices,[60] etc. The production of CNT-based composites is generally more costly than graphene due to the use of metal catalysts in the CNT synthesis.[20] Nonetheless, needle-like 1D CNT composites would be more effective for particular applications such as intracellular drug delivery.[61] Flat 2D polymer−graphene composites featuring large surface coverage would make excellent surface catalysts and gas separation membranes.[46] Here we focus on polymer–CNM composites used in three different areas, whose relevant research topics will be investigated in later chapters.

1.2.2.1 Polymer reinforcement

Polymer reinforcement finds useful applications in structural materials because low density and high aspect ratios provide extraordinary mechanical properties.[40] Reinforced materials are manufactured for lightweight with CNT loadings of 0.1–20 wt % while increasing the tensile modulus and strength to bear strong deformations.[40] Composites are prepared by blending the low fraction of CNM-fillers with a polymer matrix[44] or by *in situ* polymerization which provides better interaction during the growth stage.[41] Before blending with a polymer matrix, CNM fillers are chemically treated to ensure good dispersion.[40] Even moderate agglomeration of CNTs impacts the diameter and length distributions of the filler, decreasing the surface aspect ratio and stress transfer.[40] Further investigations of tunable mechanical properties are undergoing to optimize the interface between polymers and CNMs.

Polymers such as epoxy resin, polyvinyl alcohol, polyurethane, etc., have been used as matrices.[41] These polymer composites prepared with CNTs are already commercialized in sporting goods and automotive industry.[62] Electrically conductive CNT fillers in plastics and unconventional devices such as strain sensors utilizing the flexibility of stretchable reinforced polymer nanocomposites are good examples of future applications.[63]

1.2.2.2 Drug delivery

Biocompatibility, biodegradability, low immunogenicity, and antibacterial property are important parameters considered in biomedical applications of CNMs.[20] Thus modification of the inherent hydrophobic surface of CNMs by incorporating auxiliary components is unavoidable.[64] In drug delivery, polymers and low molecular weight surfactants were used as nonfouling surface coatings by noncovalent physisorption.[65] Polymers are resistant towards biochemical interactions compared to low-molecular weight surfactants such as sodium cholate.[66] The large surface contact with the drug carrier also provides stability in biological fluids during circulation.[67-68] Natural biopolymers (e.g., polysaccharides and proteins) and synthetic polymers (e.g., hydrophilic polymers and highly charged amphiphilic polymers) have been employed to surface-coat pristine and pre-functionalized CNMs bearing carboxylic and amine groups.[69-73]

Among synthetic polymers, polyethylene glycol (PEG) is most frequently utilized in biomedical applications.[74] Numerous examples of drug carriers utilizing PEG derivatives were studied in CNM-based drug delivery systems.[74-75] Other synthetic polymers including polyethyleneimine (PEI), poly-L-lysine (PLL), poly(vinyl alcohol) (PVA), and poly(*N*-isopropylacrylamide) (PNIPAM) exhibit significantly reduced cellular toxicity.[76]

In addition to biocompatibility, polymer topology (e.g., linear, branched, star, and dendrimer) can be an important parameter to be considered with respect to drug loading and circulation.[77] Linear chains of PEG and PEG derivatives can efficiently wrap around CNTs and also be grafted on GO.[64,78] Two-dimensional polymers could provide more effective surface coverages with graphene.[69] However, most 2D polymers have not been much explored as nonfouling surface coating in biomedical applications due to poor solubility in water.[79]

1.2.2.3 Chemical sensing

Polymer–CNM composites have garnered a great deal of interest in the design of electrochemical sensors and have shown promise for use in flexible devices.[20,59,80] The sensor response relies on charge/electron transfer upon chemical interactions of the analyte and the sensing moiety.[81] Large surface areas, high adsorption sites in thin composite films, and the excellent surface contact between conjugated polymers and graphene allow for high sensitivity in the detection of analytes and enhanced current signals in conductance compared to bulk materials.[82] Especially, many 2DPs are composed of aromatic ring-based conjugated macromolecules that impart planarity and rigidity, and thus the 2DP–graphene composite can be an excellent heterostructure self-assembled by cooperative π–π stacking.[80] The high surface-to-volume ratio and the charge mobility of graphene (or reduced graphene oxide) provide an excellent semiconducting channel for field-effect transistor (FET) sensors.[83] Despite the successful synthesis of 2DP–graphene composites, their applications to electronic devices have been rarely studied.[84]

Various polymers have been utilized in electronic sensing devices.[46] Both intrinsically conducting (e.g., polyacetylene, polythiophene, and polyaniline)[85] and nonconducting polymers (e.g., polystyrene, poly(vinylalcohol), poly(methyl methacrylate), and polyurethane)[86] were employed to achieve particular goals and synergistic effects. As good conductivity can be

achieved with low CNM loading (<10 wt %),[57] the use of conducting polymers is not critical. However, to be applicable in electronic sensing devices, polymer–CNM composites should be semiconducting. CNTs were found to provide sufficient sensitivity for detecting gas analytes (NO_2 and NH_3) without employing a sensing material,[87] but polyethyleneimine-coated SWCNTs showed enhanced selectivity and sensitivity to the same analytes.[88] To achieve high selectivity in analyte detection, the sensing moiety, which is designed primarily based on molecular recognition of the analyte, can be incorporated into devices by chemically modifying either polymers or CNMs.[89]

1.3 OXIDATION OF CARBON NANOMATERIALS

The oxidative reaction pathways of CNMs have been studied in the context of biological and nonbiological settings, in which oxidation results in simple chemical transformation to aggressive defect generation.[45,90-91] Oxidation in biological settings involves endogenous species such as enzymes and reactive oxidation species (ROS) *in situ* generated in many complex metabolic pathways.[92] The biological oxidation of CNMs began to be studied only a few years ago in relation to nanotoxicology mainly focusing on environmental health and safety.[93] The oxidative metabolism investigated in earlier studies was inflammatory responses by the innate immune system.[94] Despite the recent efforts to elucidate the toxicity of CNMs, only a few studies have investigated polymer–CNM composites in the context of oxidation.[95] Thus more studies for predicting the long-term safety of chemically diverse CNMs should be pursued in the future, as these issues will have a direct impact on their palpable applications to biomedical technology.[93]

Oxidation of CNMs in nonbiological settings is not restricted to any particular conditions. Previous studies introduced the degradation of GO using well-established oxidation methods such as Fenton chemistry.[91,96] Surface modification, especially oxidation of CNMs has been indispensable as a prefabrication treatment method,[13,50] and thus exploration of new oxidation routes will provide convenient means for flexible fabrication and manufacturing processes. The easiest way to come up with a new nonbiological method would be mimicking biosystems.[97-98] Here, iron-catalyzed oxidation pathways in nonbiological systems will be briefly discussed as ferric and ferrous ions are involved in many catalytic oxidation systems as well as Fenton chemistry.

1.3.1 Oxidation in biological systems

A variety of oxidative metabolisms occur in biological systems such as mutation, inflammation, aging carcinogenesis, and degenerative diseases.[92] Biological oxidations often occur in the presence of enzymes such as cytochrome P-450, peroxidases, chloroperoxidases, and catalases, well-known iron-containing heme enzymes.[99] Along with these catalysts, generally highly reactive and short-lived reactive oxygen species (ROS) participate in catalytic oxidation. ROS causing oxidative stress and damage to organs in living systems can include both radicals (e.g., superoxide, hydroxyl, nitric oxide, peroxyl, and alkoxyl) and nonradical species (e.g., singlet oxygen, hydrogen peroxide (H_2O_2), hypochlorous acid, aldehyde, and ozone). Among these compounds hypochlorous acid (HOCl) and hydrogen peroxide (H_2O_2) are produced in relatively high concentrations in living cells. The vast sources of the ROS and relevant oxidative mechanisms cannot be summarized in this chapter. This section focuses on (1) peroxidase-catalyzed and (2) peroxynitrite-mediated oxidative schemes. Chapter 3 focuses on the central role of catalytic and noncatalytic pathways to the oxidative degradation of the drug carrier composed of a polymer–CNM composite that activates the innate immune system, neutrophils and macrophages, respectively. Therefore, the discussion of oxidative degradation in biological settings is limited to the peroxidase catalytic cycle and peroxynitrite.

1.3.1.1 Enzyme-catalyzed oxidation

The classic peroxidase oxidative cycle is illustrated in Figure 1.5, which is the basis of redox reactions of most peroxidases such as myeloperoxidase (MPO), lactoperoxidase (LPO), and horse radish peroxidase (HRP).[100] MPO released from neutrophils by the immune response is an

enzyme containing two heme iron centers.[101] Respiratory burst comprising NADPH oxidase and O_2 produces H_2O_2, one of a reactive oxygen species (ROS).[101] The H_2O_2 concentration in stimulated neutrophils and monocytes is about 1.5 nmol/10^4 cells per hour.[102] Once H_2O_2 is generated, MPO (native enzyme, Fe^{III}) is converted into MPO-I ($Fe^{IV}=O^{+\bullet}$) in a two-electron process, yielding hydroxyl radical (•OH) and a subsequent conversion into MPO-II ($Fe^{IV}=O$) proceeds in a one-electron reducing process.[100] The original state of MPO is restored through another one electron reduction in which a reducing substrate (RH) reacts with MPO-II an order of magnitude slower than with MPO-I.[100] Important by-products generated from the oxidation cycle are reactive radical species hydroxyl radical (•OH) and alkyl radical (R•).[103]

A major difference between MPO and HRP is the generation of a strong oxidant HOCl in the MPO-catalyzed oxidative cycle. Once MPO-I is formed in Step I, it oxidizes chloride (Cl^-), abundant in physiological fluids (about 0.14 mM), and produces a strong oxidant HOCl.[100] Hypochlorous acid in equilibrium with hypochlorite ($^-$OCl/HOCl) at physiological conditions is one of the most important antimicrobial agent that can effectively kill bacteria, germs, and any harmful species.[100]

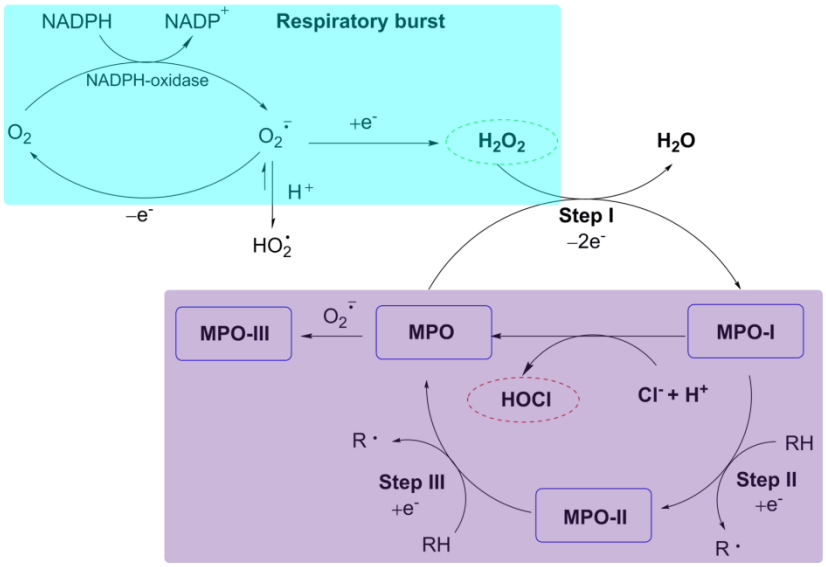

Figure 1.5 Scheme of classic peroxidase cycle activated by H_2O_2. (a) Generation of H_2O_2 in respiratory burst. NADPH oxidase and O_2 present in phagosomal and vascular endothelial membranes initiate the formation of H_2O_2.[103] (b) Conversion of MPO that undergoes a two-electron oxidation (Step I) and subsequent one-electron reductions (Step II and III). MPO is the resting state; MPO-I produces HOCl capable of oxidation of CNTs. HRP has the same catalytic pathway except the generation of HOCl/$^{-}$OCl.[103]

1.3.1.2 Peroxynitrite-mediated oxidation

Peroxynitrite (pk_a=6.8) is spontaneously produced from the diffusion-controlled reaction of highly reactive radical species nitric oxide (•NO) and superoxide radical anion ($O_2^{-\bullet}$).[104] A large amount of peroxynitrite can form in the phagosomal compartments of macrophages over a 60–120 min period.[105] The generation of nitric oxide (•NO) is catalyzed by a group of nitric oxide synthases (NOS)s.[106] In macrophages, the peroxynitrite formation requires immunostimulation

with cytokines that induce iNOS expression.[107] Upon the phagocytic process initiated by pathogens, the plasma membrane NADPH oxidase is activated to produce $O_2^{-\bullet}$.[106-107] Superoxide radical anion is ubiquitous in normal cellular metabolism, and the rate of superoxide generation increases several-fold during cellular redox homeostasis and inflammation.[108] The reaction of •NO with $O_2^{-\bullet}$ occurs biologically even in the presence of superoxide dismutase (SOD).[92]

As is the case with H_2O_2 and HOCl, peroxynitrite can be an endogenous toxicant and a cytotoxic effector against pathogens, serving as either an oxidant or a nucleophile.[106] The great stability of peroxynitrite ($ONOO^-$) in alkaline conditions enables it to diffuse through cells to reach a target.[106] Peroxynitrous acid (ONOOH) is a strong oxidant that can attack biological molecules by very complex mechanisms.[109] In the excited state of trans-peroxynitrous acid, hydroxyl radical (•OH) and nitrogen dioxide ($\bullet NO_2$) radical are generated.[109] Another important oxidative mechanism is a heterolytic cleavage to form hydroxide and nitronium (NO_2^+) catalyzed by transition metal ions especially contained in metalloenzymes or reaction of peroxynitrite with SOD.[106]

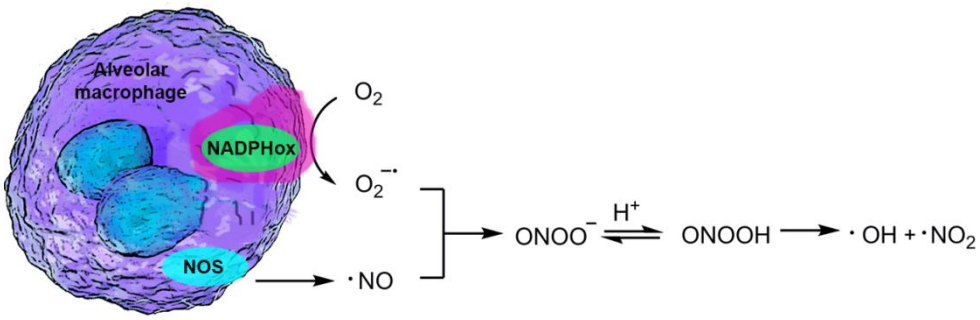

Figure 1.6 Scheme of peroxynitrite formation. Generation of both superoxide and nitric oxide in alveolar macrophages upon stimulation by pathogens.[109]

1.3.1.3 Oxidative biodegradation of carbon nanomaterials

Currently, two different oxidative pathways have been investigated concerning the CNT degradation: (1) enzyme (MPO, LPO, and HRP)-catalyzed and (2) peroxynitrite-mediated oxidations.[107,110-113] Since our research group demonstrated the horseradish peroxidase (HRP)-catalyzed degradation of CNTs in the seminal work,[113] the degradation of SWCNTs,[114] MWNTs,[115] and GO[116-117] have been investigated further. In addition, the role of peroxidases and their varying degrees of oxidation of pristine and functionalized CNMs were investigated with myeloperoxidase (MPO)[110,118] and eosinophil peroxidase.[111] The CNM biodegradation was also corroborated by evidence of the mitigating effect of an antioxidant glutathione in the MPO oxidative system.[118]

Our research group and others conjectured that hypochlorite/hypochlorous acid and the reactive intermediates formed in the course of MPO cycle were capable of degrading carbon nanotubes.[110,116,119] MPO-catalyzed degradation occurs both intra- and extra-cellularly (neutrophil extracellular trap).[95] Three major steps are involved in the CNT degradation by the MPO catalytic cycle: (1) formation of a HOCl (Step I), (2) oxidation of Ar–H (Step II and III), and (3) the resulting formation of free radical species.[118] EPO oxidation has the same catalytic cycle except for the formation of hypobromous acid (HOBr) instead of HOCl.[111] The role of reactive free radical species has not been fully explained. It is highly likely that aromatic as well as hydroxyl radicals generated during the peroxidase cycle may induce a variety of radical transformations with sp^2 carbon atoms. Either H_2O_2 or HOCl alone can be a strong oxidant, and thus oxidation of CNTs was investigated *ex vivo*. However, these oxidants alone did not degrade SWCNTs as effectively as the MPO system. Although it seems reasonable that the coexistence of H_2O_2 and HOCl can create a very powerful oxidation condition, the mechanistic details of

how the reactive radical species and HOCl formed in the MPO cycle have not been elucidated. When the oxidative cleavage of sp^2 C–C bonds proceeds extensively in the basal plane, vacancy defects are formed, generating large holes and by-products (e.g., CO, CO_2, and oxidized carbonaceous products).[90] Graphene oxide (GO) treated with HRP and H_2O_2 was degraded whereas reduced graphene oxide (rGO) was intact under the same oxidative condition.[117] Computational docking studies showed that HRP was preferentially bound to the basal plane rather than the edge. When GO was treated with MPO, aggregated GO failed to degrade.[117] However, highly dispersed samples were completely metabolized.[116]

Noncovalently functionalized CNTs coated with pulmonary phospholipid surfactants (e.g., phosphatidyl choline and phosphatidyl serine)[120] and polyethylene glycols (PEG)[95, 121] were also investigated. Anionic phosphatidyl serine showed a 1.8 times higher uptake of ox-SWCNT by neutrophils than phosphatidyl choline.[120] PEGylated ox-SWCNTs were exposed to activated neutrophils *ex vivo* and in vitro.[95,121] Both covalent and noncovalent functionalization methods were employed for MPO-catalyzed degradation.[95] The *in vitro* study revealed that covalently functionalized samples degraded faster, and that the low molecular weight PEG (e.g., 2 kDa vs. 10 kDa) was more efficient in the oxidative degradation.[95] The small PEG features low grafting density, allowing for better exposure of SWCNTs to MPO and facile degradation without the MPO–PEG interaction.[95] Despite the faster degradation rates observed in the *ex vivo* study, the molecular weight and the type of functionalization of PEG did not influence the degradation kinetics as much as they appeared in the *in vitro* study.[95] In addition, this study also suggests that other enzymes released from neutrophils *ex vivo*, such as neutrophil elastase and antibacterial serine proteases, could participate in PEG stripping besides MPO. Therefore,

different *ex vivo* experimental methods, i.e., the addition of isolated MPO vs. activated neutrophils, can impact the degradation kinetics.[95]

Under the same oxidative condition, the degree of nanotube degradation was found to be dependent upon the different functional groups of the nanotube.[90] It was also reported that oxidized nanotubes (ox-CNTs) were more susceptible to oxidative biodegradation than pristine samples (nonfunctionalized nanotubes).[90,110,115,122] Because functionalization introduces new defect sites on the sidewalls, such as chemically reactive bonds and heteroatoms on the graphitic lattice, a large number of covalently functionalized CNTs become susceptible to oxidation.[123] The peroxidase-catalyzed systems indicated that the type of surface functionalization was critical in influencing the fate of degradation, and that the strong electrostatic interaction between positively charged residues of MPO and an anionic species (e.g., carboxylate of ox-SWCNT) promoted the enzymatic degradation based on a docking study.[110]

The peroxynitrite-mediated degradation of ox-SWCNTs *in vitro* was investigated in activated macrophages known to produce peroxynitrite.[107] Although NADPH oxidase and iNOS synthases are involved in the peroxynitrite generation,[104,106] these enzymes do not directly interact with CNTs, different from the specific binding interaction between CNTs and the reactive intermediates of peroxidases (MPO and EPO).[107] Thus peroxynitrite-mediated oxidation appears less dependent on the surface charge of initial CNTs (i.e., the number of carboxylate groups).[107]

1.3.2 Catalytic oxidation of nonbiological systems

One of the important strategies for nonbiological catalytic oxidation is to mimic biological processes and implement green chemistry.[124] For example, redox enzymes for catalytic oxidation in biological systems are often translated into synthetic models consisting of transition metals as catalysts and clean oxidants such as O_2 and H_2O_2.[124] Catalytic oxidation that can proceed at room temperature and ambient pressure instead of high temperatures are ideal for the environment and economy. However, only a few nonbiological catalytic oxidations have been studied with respect to CNMs.[91,96,125-126] They are employed mainly to modify the original zero energy band gap of graphene, rather than aiming at degrading CNMs.[126] Fenton-like reactions based on the original Fenton chemistry have been known to be very efficient in the formation of oxidative defects,[91] but further applications have not been actively pursued. Slight changes in reaction condition using UV light-promoted or Cu(I)/Cu(II)[127] instead of Fe(II)/Fe(III) have been most frequently employed. In Chapter 4, the Fenton-like reactions using a Cu(II) coordinated supramolecular polymer catalyst will be discussed. In the same vein, metalloporphyrin complexes have been widely used as catalysts in various organic reactions with oxidants (e.g., PhIO, NaOCl, $KHSO_5$, and H_2O_2).[98] However, the use of a synthetic metalloporphyrin complex in the fabrication of CNMs has not been reported other than in the case of the patterned graphite described in Chapter 5 of this dissertation.

1.3.2.1 Fenton-like oxidation

The Fenton-like mechanism is based on an electron transfer between hydrogen peroxide and a metal catalyst (e.g., Fe^{2+}, Cu^{+}).[128] The classic Fenton reaction is catalyzed by ferrous ions (Fe^{2+})

in acidic conditions and the regeneration of Fe^{2+} is catalyzed by the ferric ions (Fe^{3+}) upon reaction with hydrogen peroxide, eq (1).[128] While the catalytic cycle propagates between Fe^{2+} and Fe^{3+}, hydroxyl (•OH) and hydroperoxyl (HO_2•) radicals form as by-products. Generally, the reactivity, i.e., oxidizing power, of the former is much higher than the latter.[128] Fenton-like reaction (2) is much slower than (1), but the presence of HO_2• can speed up the conversion of Fe^{3+} into Fe^{2+} (3).[128] This conversion is also observed in the presence of organic radials (•R) generated by hydroxyl radical (•OH) eq (4) and (5) but at a much faster rate.[128] The reaction rate of aromatic organic compounds and the formation of phenolic species was found to be very efficient.[128]

(Fenton reaction) $Fe^{2+} + H_2O_2 + H^+ \rightarrow Fe^{3+} + H_2O + \bullet OH$ (1)

($k_2 = 63\ M^{-1}\ s^{-1}$)

(Fenton-like reaction) $Fe^{3+} + H_2O_2 \rightarrow Fe^{2+} + HO_2\bullet + H^+$ (2)

($k = \sim 3 \times 10^{-3}\ s^{-1}$)

$Fe^{3+} + HO_2\bullet \rightarrow Fe^{2+} + O_2 + H^+$ (3)

($k_2 = 2 \times 10^3\ M^{-1}\ s^{-1}$)

(Organic radical formation) $RH + \bullet OH \rightarrow R\bullet + H_2O$ (4)

($k_2 = 10^7$–$10^9\ M^{-1}\ s^{-1}$)

$Fe^{3+} + R\bullet \rightarrow Fe^{2+} + R^+$ (5)

($k_2 = 10^7$–$10^8\ M^{-1}\ s^{-1}$)

$ArH + \bullet OH \rightarrow ArHOH\bullet$

$ArHOH\bullet + O_2 \rightarrow ArOH + HO_2\bullet$ (6)

($k_2 = 10^8$–$10^9\ M^{-1}\ s^{-1}$)

To enhance the catalytic activity in different environments, this basic oxidative model has been modified into various conditions and is referred to as Fenton-like reactions. In addition to Fe(II), copper(II)[127] and cobalt(II) can be used as catalysts in the decompositions of polycylic aromatic hydrocarbons and small aromatic compounds such as benzene, toluene, ethylbenzene, and xylenes.[129] Fenton chemistry is effective under acidic conditions (pH 2–4) whereas cobalt and copper catalysts can be useful in the wide range of pH 3–9. [129] In addition, different organic ligands influence the catalytic activity by forming a metal–ligand–radical complex in the presence of H_2O_2, which may prevent the aggregation of metal ions in solution and accelerate the interaction with H_2O_2.[129]

1.3.2.2 Synthetic iron porphyrin catalysts

Porphyrin derivatives are probably the most versatile ligands, capable of forming well-defined complexes with various transition metal ions, notably iron(III), Mn(III), Co(II), and Ru(II).[130] The tetrapyrrole ligand structure of porphyrin allows for modification with substituents that can be linked to pyrrolic β sites or the methines.[97] Compared to heme-containing enzymes, synthetic metalloporphyrin catalysts can be more robust when exposed to a large amount of oxidants.[131] Many early examples of metalloporphyrin catalysts were reported in the epoxidation of alkenes and hydroxylation of alkanes.[131] Although electron-rich aromatic substrates have not been employed for iron porphyrin-catalyzed oxidation, oxidative degradation of lignin and organic pollutants have also been reported.[132] Lignin dimers composed of benzylic and phenyl carbons were subjected to oxidative cleavage which was sensitive to porphyrin substituents and oxidants (oxygen donors).[133] When immobilized on graphene supports, hemin and iron porphyrin

derivatives with H_2O_2 showed high catalytic activity in the oxidation of a small aromatic molecule pyrogallol.[134]

1.3.2.3 Nonbiological catalytic oxidation of carbon nanomaterials

Photo-Fenton reactions have been used in the oxidative degradation of MWCNTs[135] and GO.[96] The mechanism of the photo-Fenton reaction of GO was elucidated by mass spectrometer analysis and density functional theory (DFT) calculations.[96] The oxidation mechanism of GO seems similar to that of CNTs in that the oxidant H_2O_2 is dissociated by UV irradiation into •OH, a very powerful oxidant, and generates hydroxide, quinone, and carboxylic groups.[136] Ultimately, the functional groups with low oxidation states will be converted to higher oxidation states such as carboxylic acid, followed by decarboxylation and return to the C–H bond formation. Zhang and coworkers prepared graphene quantum dots (GQDs) with an average size of 40 nm (width) × 1.2 nm (thickness) using a photo-Fenton oxidation of GO sheets (about 1μm).[91] They found that the photo-Fenton reaction of GO was initiated at carbon atoms connected with oxygen containing groups, and that GQDs were functionalized with carboxylic groups along the edges.[91]

The use of metal nanoparticles (NPs) as catalysts is another type of catalytic thermal oxidation, in which metal NPs are deposited on graphene sheets and annealed at elevated temperatures. Bulk preparation of holey graphene was demonstrated with an AgNP catalyst on graphene that was exposed to controlled air oxidation at 250–400 °C, and the high annealing temperature yielded a high oxygen content in the graphene sample.[125] Similarly, AuNPs were deposited on rGO and catalyzed the oxidation of rGO by •OH as well as the generation of •OH by UV photolysis.[126] The catalytic role of AuNP was attributed to changes in localized oxidation potentials at the AuNP surface effectively assisting the reaction of •OH with rGO.[126]

2.0 SYNTHESIS OF POLYMER–CARBON NANOTUBE COMPOSITES FOR DRUG DELIVERY

2.1 CHAPTER PREFACE

This research was conducted in collaboration with the Professor Valerian Kagan group, Departments of Environmental and Occupational Health, and the Professor Peter Wipf group, Department of Chemistry at the University of Pittsburgh. These groups provided mitochondria targeting drugs, TPP-IOA and XJB-5-131, respectively. W. Seo synthesized and characterized the drug nanoconjugates; Michael W. Epperly administered *in vivo* experiments; Alexandr A. Kapralov, Vladmir A. Tyurin, and Yulia Y. Tyurina performed *in vitro* experiments and analyzed biological data; E. Skoda synthesized XJB-5-131. W. Seo thanks Seth C. Burkert for performing X-ray photoelectron spectroscopy (XPS). As biological studies were conducted in other groups, only the key results of drug conjugates are highlighted in this dissertation.

2.2 INTRODUCTION

Chapter 2 and Chapter 3 investigate drug nanocarriers composed of phospholipid-polyethylene glycol (PL-PEG) functionalized ox-SWCNTs in the context of drug circulation. In Chapter 2, the PL-PEG/ox-SWCNT nanocarrier is employed to improve the *in vivo* circulation time of two mitochondria targeting drugs TPP-IOA and XJB-5-131, and the role of polymer nanocomposite as a drug carrier is examined. These drugs aim to serve as radiomitigators/radioprotectors in biomedicine and biodefense applications. Chapter 2 focuses on the synthesis and characterization of drug conjugates and their *in vivo* pharmacokinetic properties upon exposure to ionizing radiation. Chapter 3 centers on the oxidative degradation and clearance of the drug carrier specifically triggered by the innate immune system.

A similar drug carrier prepared from PL-PEG and SWCNT was reported by Hongjie Dai and coworkers, demonstrating excellent *in vivo* drug delivery properties.[137] They studied PL-PEG models with some slight variations in chemical structure for coating SWCNT-based carriers. Based on the noncovalently functionalized short pristine SWCNTs with PL-PEG studied earlier, we prepared drug conjugates by noncovalently attaching drug molecules, TPP-IOA and XJB-5-131 onto the PL-PEG/SWCNT surface (Figure 2.1). The therapeutic effects of the TPP-IOA and XJB-5-131 as mitochondria targeting free drugs were previously investigated.[138-140] Both TPP-IOA and XJB-5-131 are employed as radiation mitigators. TPP-IOA is a highly aqueous soluble whereas XJB-5-131 exhibits poor solubility in water. The pharmacokinetic properties of the drug conjugates are investigated *in vivo*.

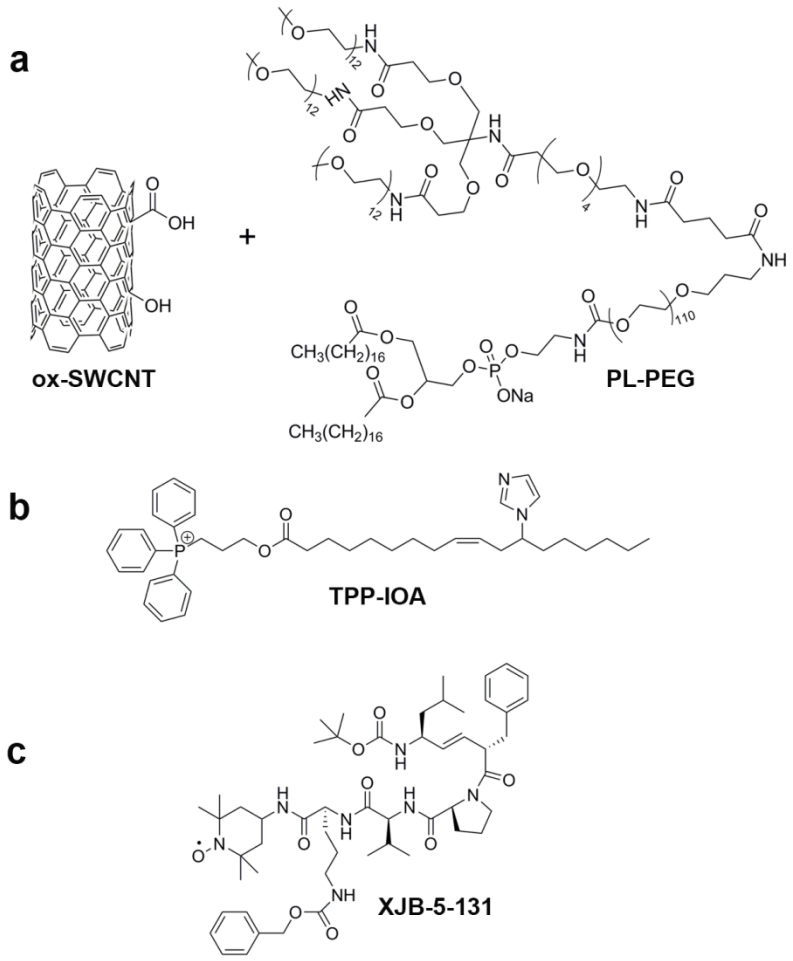

Figure 2.1 Representation of a nanocarrier and drugs. (a) ox-SWCNT and PL-PEG. (b) TPP-IOA, and (c) XJB-5-131.

2.2.1 Drug nanocarriers and carbon nanotubes

Many different types of drug delivery systems, including the first generation nontargeted and targeted (or smart) delivery, have been developed to improve the therapeutic effects of conventional drug administrations.[141] Generally, drug carriers are employed to improve pharmacological properties of existing drugs (e.g., solubility and circulation), and are designed primarily to protect drug molecules from the external environment.[142] Some carriers are built upon sophisticated molecular systems made of multiple components and functions, resulting in localized release of therapeutic agents near target cells and tissues with minimal side effects.[143-144]

CNT-based molecular vehicles have been utilized in drug and gene delivery, imaging, and photothermal therapy.[74,94] Many examples of these devices have also been developed into a carrier capable of multiple functionalities such as theranostics, a combination of therapeutic and imaging contrast agents. The shape of drug carriers plays a role in permeation of the drug carrier.[145] Compared to spherical nanoparticles such as liposomes and micelles, CNTs featuring 1D needle shapes and high aspect ratios (>200:1 of length to width for HiPco SWCNT) are reportedly advantageous for intracellular drug delivery by endocytosis, allowing facile translocation of drug carriers into the cytoplasm through cell membranes.[146-147]

HiPco SWCNTs prepared by high-pressure carbon monoxide disproportionation[148] are employed in drug delivery due to their small diameters (0.8–1.2 nm). For biological applications, most commercial HiPco CNTs are cut short by chemical and mechanical treatments (<300 nm in length).[149] It is widely accepted that short CNTs are relatively safe whereas pristine CNTs as long as 10 μm have been shown to cause pulmonary inflammation and mesothelioma in mice.[150] Semiconducting nanotubes have intrinsic fluorescence in the NIR region ($\lambda_{emission}$ =

1100–1400 nm, $\lambda_{excitation}$ = 750–900 nm), which eliminates the need for using toxic fluorophores in biological studies.[151] CNTs are capable of passive self-accumulation near the tumor site without the aid of the ligand–receptor interaction programmed in targeted drug delivery.[145, 152] This phenomenon, referred to as the enhanced permeation and retention (EPR) effect, can also be observed in other nanoparticle-based drug carriers that are easily trapped onto the irregular, abnormal surface of cancer cells and tissues.[153]

Examples of SWCNT-based drug conjugates functionalized by different auxiliary components are illustrated in Figure 2.2.[69] Incorporation of surfactants or hydrophilic polymers to impart biocompatibility is a common procedure.[74] Occasionally, functional modules such as fluorescence tags for cellular imaging and ligand–target recognition (e.g., antigen–antibody) are also incorporated into CNT carriers.[60,69] Drug molecules can be attached to CNTs covalently as prodrugs or can be noncovalently bound to the CNT surface through intermolecular interactions (Figure 4a–c).[154] Generally, covalently linked drug molecules can be resistant to random adsorption by various biomolecules in serum unless the linker is cleaved by metabolic processes. However, covalent attachment of drug molecules may result in low drug payloads because CNTs have insufficient anchoring sites for drug conjugation, localized only at the ends and some defects on the sidewall.[151,155-156] To increase the loading capacity, drug molecules are linked to PEG instead of CNTs.

Drug molecules can also be noncovalently loaded onto SWCNTs.[154] Hydrophobic drugs bearing aromatic moieties such as Doxorubicin are good substrates because the sidewall of SWCNTs drives π–π stacking.[154,157] In addition, the carboxylate of ox–SWCNTs form electrostatic interactions with positively charged groups (e.g., RNH_3^+) under physiological conditions.[157] Despite the functionalization of CNTs with hydrophilic or amphiphilic coatings,

the inherent poor aqueous solubility of drugs significantly influences the stability and the pharmacokinetics of drug conjugates as observed in the *in vivo* pharmacokinetics study of paclitaxel.[155] It was suggested that the high hydrophobicity of paclitaxel would compromise the biological inertness of a PEG-functionalized SWCNTs, significantly reducing blood circulation times.[155]

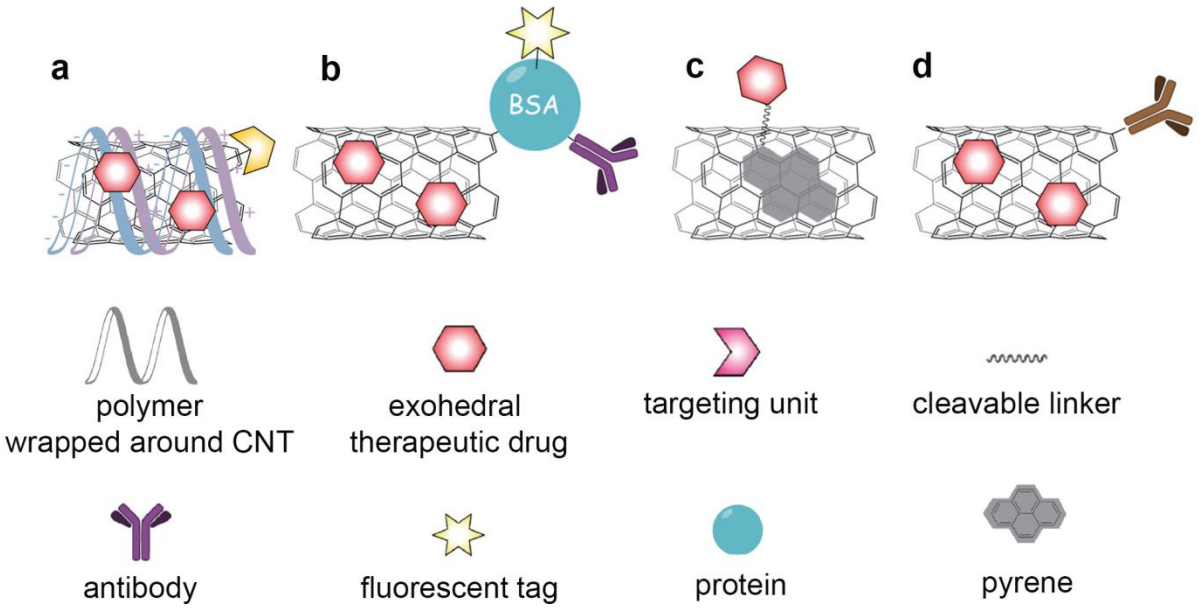

Figure 2.2 SWCNT-based drug conjugates.[69]

2.2.2 Functionalization with phospholipid-polyethylene glycol

Polyethylene glycol (PEG) derivatives have been extensively used in biomedical applications mainly due to excellent biocompatibility although PEG is not biodegradable.[60,68,158] The molecular weight (MW) range of PEG used for drug delivery is usually between 1 and 40 kDa.[159] As many studies reported the rapid uptake of NPs by the reticuloendothelial system (RES) and the resulting short blood circulation times, PEGylation became an important strategy to improve drug circulation. It was believed that PEG suppressed the formation of protein corona (i.e., stealth effect) and prevented the nonspecific cellular uptake of nanocarriers as well as drugs.[160] However, Mailänder and Wurm have recently found that PEG has specific binding affinity with clusterin in blood plasma, which reduces the macrophage uptake.[158] This result was further corroborated by the high phagocytic uptake of PEGylated NPs incubated in water without plasma.[158]

Bottini and coworkers reported that coagulation proteins, immunoglobulins, apolipoproteins, and proteins of the complement system were most strongly bound to a noncovalently functionalized PL-PEG (MW=2 kDa)–SWCNT composite among 240 proteins screened in the study.[160] They also found that the protein recruitment was independent of the isoelectric point, molecular weight, and total hydrophobicity of proteins.[160] Phospholipid (PL) moieties are strongly adhered to the sidewall of SWCNTs while the PEG chains extends and help dispersion into water.[161] Interestingly, neither PL nor PEG has any functional groups that can drive selective binding with proteins.[158] Based on the *in vivo* results, the topology of PEG (e.g., mushroom vs. brush forms illustrated in Figure 2.3) was found to be more important in protein selectivity than the surface charge (e.g., amine vs. methyl groups).[160] With the lack of the biochemical mechanistic understanding of PEG–protein adsorption, some of the findings

reported in the past have been often debated.[159] It is generally believed that large PEG chains prevent protein corona.[158,160] The dependence of nonspecific cellular uptake upon the PL-PEG size was confirmed with PL-PEG (MW= 5 kDa), but PL-PEG (MW= 2 kDa) did not show improved drug circulation.[159] With the same molecular weight of 5 kDa, *in vivo*[161-162] and *in vitro*[163] stealth effects were very inconsistent. The surface coverage (or packing density) of PL-PEG on the SWCNT would affect the interaction with proteins. Phospholipids can randomly adsorb to the CNT during functionalization, which may expose the bare CNT surface to plasma. Similarly, branched PL-PEG/SWCNTs that were developed to improve the blood circulation of the carrier showed PL-PEG's size- and packing density-dependent circulation results.[67] While exploration of new parameters in the study of the PEG–protein interaction continues, a few changes in the structure of CNTs as well as PEG and biological environments may impart completely different properties and stability to drug conjugates.

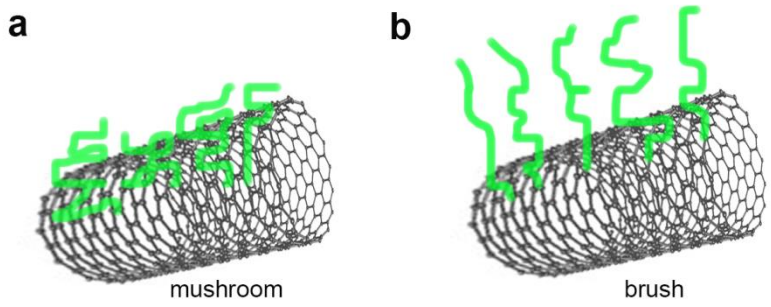

Figure 2.3 Topology of Polyethylene glycol. (a) Mushroom and (b) brush hydrodynamic conformations of polyethylene glycol. Brush conformations can develop steric interactions with protein in plasma, attenuating the formation of protein corona.

2.2.3 Mitochondria targeting drugs

Protective medical countermeasures need to be developed to prevent ionizing radiation injury potentially caused by accidental exposure during radiation therapy and terrorism.[140] Ionizing radiation triggers generation of reactive oxygen species (ROS) and radicals arising from radiolysis of water, inducing mitochondria-mediated cell apoptosis.[164] To date, no effective medical radiation countermeasures against acute and delayed radiation injuries are currently available.[165] Based on the new finding that cytochrome c in mitochondria oxidizes cardiolipin as the result of radiation-induced apoptosis, 3-hydroxypropyl-triphenylphosphonium-conjugated imidazole-substituted oleic acid (TPP-IOA) was developed.[140] The lipophilic triphenylphosphonium moiety promotes the drug molecules to efficiently traverse the highly negative mitochondrial lipid membrane, serving as an excellent selective targeting agent to treat ROS-induced mitochondrial damage.[166] TPP-IOA demonstrated the suppression of cell death induced by irradiation and protected C57BL6 mice against total body irradiation.[140]

XJB-5-131 possesses a nitroxide group functionalized into the S segment of a natural product gramicidin, a peptide-mimetic mitochondrial targeting radiomitigators.[167] XJB-5-131 delivers 4-amino-TEMPO, a stable nitroxide radical-based antioxidant scavenging electrons and ROS.[168] The sterically hindered free radical can serve as either an electron-accepting or electron-donating group, depending on the redox potential of the environment.[169] This drug was found effective in preventing superoxide production in cells and cardoilipin (CL) oxidation in mitochondria and also in protecting cells against a range of pro-apoptotic triggers such as actinomycin D and radiation.[167]

2.3 EXPERIMENTAL

2.3.1 Synthesis of drug carrier (PL-PEG/ox-SWCNT)

Raw HiPco (NanoIntegris®) SWCNTs (25 mg) were oxidized in 50 mL of an acid mixture (H_2SO_4 /HNO_3, 3/1, v/v) in an ultrasonic bath set at 25 ˚C over 3 h 20 min. After thorough washing with distilled water several times, the ox-SWCNTs were dried under vacuum over 24 h, which yielded 18 mg. A phospholipid–polyethylene glycol (PL-PEG) was prepared by amide coupling of DSPE-050PA (115 mg) and TMS$(PEG)_{12}$ (71 mg) in anhydrous CH_2Cl_2 (3.0 mL). After 12 h, *N*,*N*-dicyclohexylcarbodiimide (DCC) (20 mg, 97 mmol) and 4-dimethylaminopyridine (DMAP) (10 mg, 82 mmol) were added to ensure reactivation of the hydrolyzed *N*-hydroxysuccinimide (NHS) group of TMS$(PEG)_{12}$ for amide coupling. After 24 h of stirring at room temperature, the reaction solvent (CH_2Cl_2) was dried on a rotary vacuum evaporator. The reaction mixture was washed with nanopure water (61 mL) and was collected by vacuum filtration. Excess DMAP was further removed by dialysis. MALDI: m/z ~7.4 kDa.

2.3.2 Preparation of the TPP-IOA conjugate (TPP-IOA-SWCNT)

After sonication of ox-SWCNTs (4.00 mg) in phosphate buffer (pH 8.2, 7 mL) for 30 min, TPP-IOA (8.71 mg, 0.01 mmol) was added to the nanotube suspension. Immediately, a PL-PEG(17.2 mg) solution in phosphate buffer (pH 8.2, 20 mL) was added to the mixture. The mixture of TPP-IOA/PL-PEG/ox-SWCNT was sonicated for 30 min and allowed to stir for 24 h. TPP-IOA was added before PL-PEG addition because binding of the long alkyl chain of TPP-IOA to the

SWCNT sidewall may be interfered with the phospholipid moiety of the PL-PEG. The drug conjugate was collected by vacuum filtration and washed further with phosphate buffer (pH 8.2) by centrifugation (11,000 rpm, 30 min × 5) using a 100 kDa centrifuge filter. The final wash solution was analyzed with ^{1}H NMR spectra to ensure that no trace of TPP-IOA remained in the solution. The drug conjugate was dried under high vacuum over 12 h.

2.3.3 Preparation of the XJB-5-131 conjugate (XJB-SWCNT)

PL-PEG/ox-SWCNT (1.00 mg) was dissolved and sonicated in PBS solution (5.0 mL, pH 8.20, 0.1 M) for 5 min. An aliquot of XJB-5-131 solution in ethanol (500.0 µL, equivalent to 2.24 mg of XJB-5-131) was injected dropwise to the solution of PL-PEG/ox-SWCNT. The reaction solution was pale gray, and a fine white powder of XJB-5-131 was dispersed in the solution. After 30 min of sonication to break the drug aggregates, the reaction was stirred at room temperature over 24 h under N_2. The reaction solution was filtered using a 100 kDa MWCO Amico centrifugal filter (11,000 rpm, 20 min). The solid drug conjugate (XJB-SWCNT) was purified further through four wash cycles with phosphate buffer (pH 8.20, 0.05 M). In each wash cycle, the collected drug conjugate in the centrifugal filter was sonicated again for about 2 min in the same phosphate buffer and filtered by centrifugation. After drying under high vacuum over 15 h, the sample was sonicated in 1.5 mL of PBS solution (0.01 M, pH 7.4). The approximate concentration of XJB-SWCNT was 0.7 mg/mL.

An alternate protocol was employed to optimize the maximum drug loading using zeta potential titration that provides an approximate threshold value for the maximum solubility of the XJB-SWCNT conjugate. The titration experiment was performed with a PL-PEG/ox-SWCNT

solution in water (0.09 mg/mL). Then an aliquot of XJB-5-131 in ethanol (5.0 mg/mL, 5.2 mM) was added to the PL-PEG/ox-SWNT solution and sonicated for 10 min. The serial titration continued until the zeta potential value did not change. The total amount of XJB-5-131 present in the solution was 0.25 mg and the concentration of the drug conjugate was estimated 0.08 mg/mL, in which a loading capacity of 90% was achieved in contrast with 50% observed in the previous method.

2.3.4 *In vivo* experiments of the TPP-IOA conjugate (TPP-IOA-SWCNT)

All procedures were approved and performed according to the protocols established by the Institutional Animal Care and Use Committee (IACUC) of the University of Pittsburgh. C57BL/6NTac female mice were exposed to total body irradiation (TBI) to a dose of 9.25 Gy (n = 10). Intraperitoneal injection with TPP-IOA (5 mg/kg body weight) and TPP-IOA-SWCNT (2.5 mg of TPP-IOA/kg body weight) was performed on the mice 24 h after TBI.[165]

2.3.5 *In vivo* experiments of the XJB-5-131 conjugate (XJB-SWCNT)

C57BL/6NHsd female mice were irradiated with 9.25 or 9.5 Gy TBI using a J. L. Shepherd Mark 1 Model 68 cesium irradiator at a dose rate of 80 cGy/min. As soon as the mice developed the hematopoietic syndrome, they were sacrificed for analysis. Mouse embryonic cells were cultured in Dulbecco's Modified Eagle's Medium (DMEM) supplemented with 15% fetal bovine serum, 25 mM HEPES, 50 mg/L of uridine, 110 mg/L of pyruvate, 2 mM of glutamine, 1 × nonessential amino acids, 0.05 mM of 2-mercaptoethanol, 0.5 × 106 U/L of mouse leukemia

inhibitory factor, 100 U/L of penicillin, and 100 μg/L of streptomycin in humidified atmosphere of 5% CO_2 and 95% air at 37 °C.[170]

2.4 RESULTS AND DISCUSSION

2.4.1 Characterization of PL-PEG/ox-SWCNT

The degree of oxidation of pristine HiPCo SWCNTs was analyzed by Raman Spectroscopy (Figure 2.4) based on the Raman signature peaks of graphitic structures.[171] The I_D/I_G value of the oxidized SWCNTs (0.35) was substantially larger than that of the pristine SWCNTs (0.08). The increased I_D/I_G indicates the presence of defects newly formed on the sidewalls and the ends of SWNTs.[172] After the acid treatment, the D band became wider and was blue-shifted (Table 2.1).

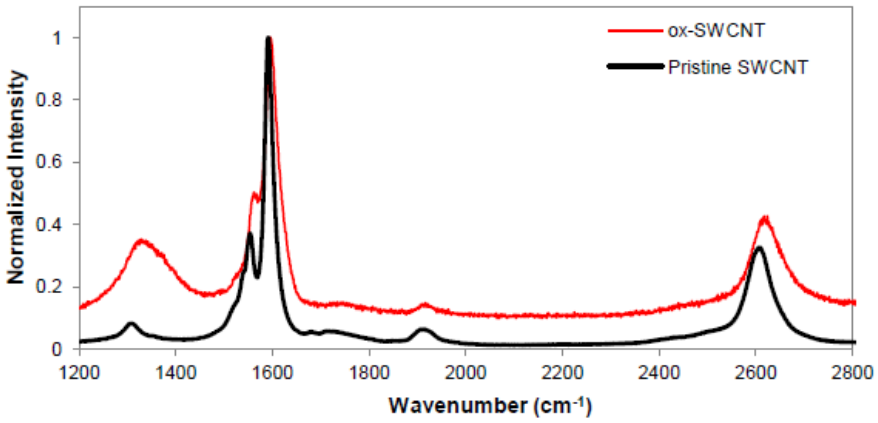

Figure 2.4 Raman spectroscopy of pristine HiPco SWCNT and ox-SWCNT.

Table 2.1 Raman characteristic peaks and the ratio of D to G.

Nanotube	D band (cm^{-1})	G band (cm^{-1})	I_D/I_G
Pristine SWCNT	1309	1591	0.08
ox-SWCNT	1327	1596	0.35

In addition, FTIR (Figure 2.11 and Table 2.2 in the section 2.6) and XPS data (Figure 2.12 in the section 2.6) indicate the oxidation of pristine SWCNTs. Carboxylic acid (1728 and 3433–2684 cm^{-1}) and phenolic (3587 cm^{-1}) groups are present in IR absorption spectrum. XPS analysis reveals a large amount of carboxylic and ketone groups. TEM micrographs show each stage of preparing the PL-PEG/ox-SWCNT composite (Figure 2.5a–c). Pristine CNTs are long and aggregated. After oxidation, the CNTs became short and less bundled with an average length of 162 nm. PEGylation did not significantly change the high aspect ratios, but the diameter increased due to multiple PL-PEG chains covering the ox-SWCNT surface.

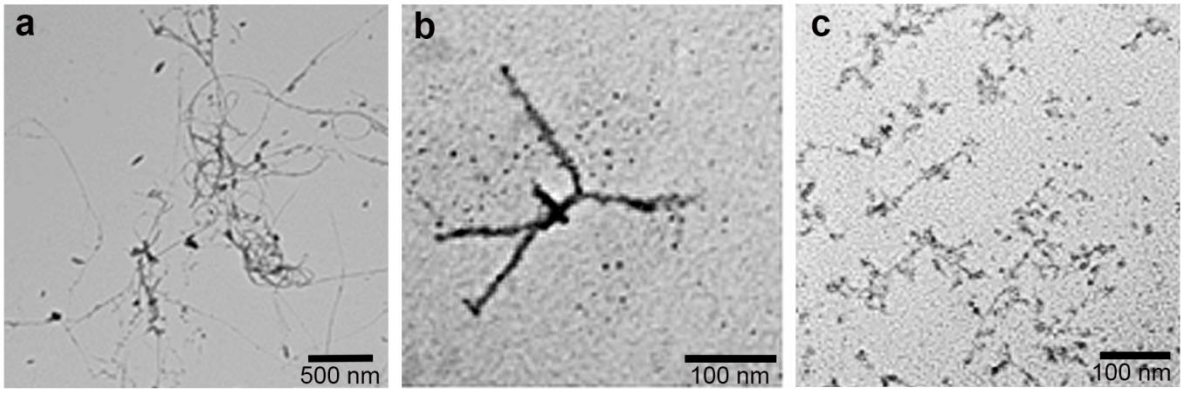

Figure 2.5 TEM micrographs of (a) Pristine SWCNT, (b) ox-SWCNT, and (c) PL-PEG/ox-SWCNT.

2.4.2 Characterization of the TPP-IOA conjugate

TEM analysis indicates that the TPP-IOA conjugate (TPP-IOA-SWCNT) did not substantially aggregate (Figure 2.6a). To quantify the drug loading and predict the dispersibility of the drug conjugate, we implemented zeta potential (ζ) titration which determines the maximum drug

loading (Figure 2.6b). Binding of TPP-IOA to PL-PEG/ox-SWCNT becomes saturated between 0.8 and 1.6 wt equiv, suggesting that the maximum drug loading is about 160%. Because free TPP-IOA is highly water-soluble (ζ= +55.7 mV), the TPP-IOA conjugate remained well-dispersed in solution throughout the titration experiment and even after a week of storage at room temperature.

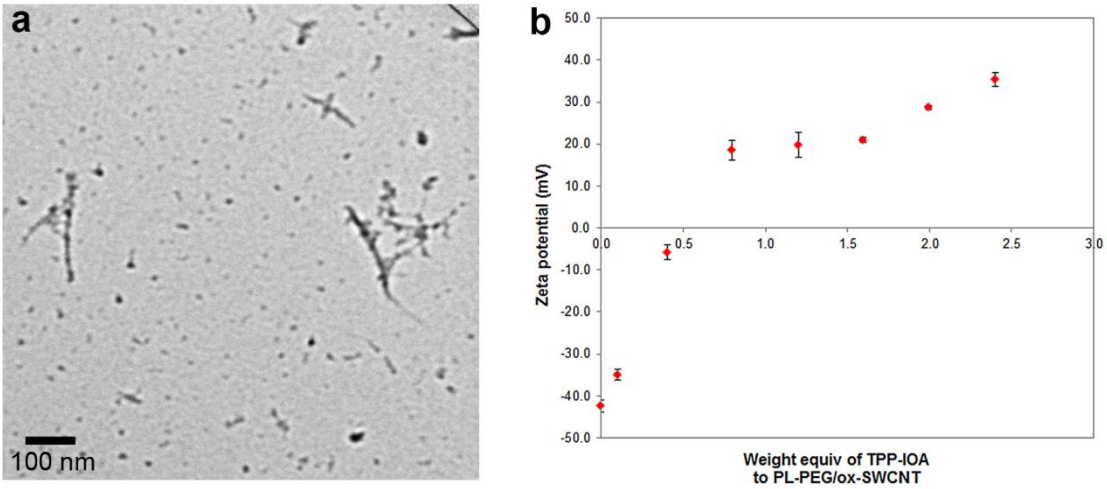

Figure 2.6 (a) TEM micrograph and (b) zeta potential measurement of TPP-IOA-SWCNT at pH 7.0. Data are means ± SD of five replicate measurements.

2.4.3 Characterization of the XJB-5-131 conjugate

A TEM image (Figure 2.7a) did not show significant degrees of bundled SWCNTs despite the presence of highly hydrophobic XJB-5-131 which is only soluble in polar organic solvents such as dimethyl sulfoxide (DMSO) and ethanol. Zeta potential titration data indicate that the binding of XJB-5-131 with ox-SWCNTs was saturated between 0.1 and 0.6 wt equiv (ζ= −20.0 mV) while still being dispersible in water (Figure 2.7b). Further addition of XJB-5-131 up to 0.9 wt

equiv did not reduce the zeta potential dramatically. In order to maximize the drug loading, we chose 0.9 equiv of XJB-5-131 to PL-PEG/ox-SWCNT (i.e., 90% drug loading). The loading capacity at a lower PL-PEG/ox-SWCNT concentration (0.09 mg/mL) significantly improved compared to higher concentrations of the carrier (0.2 mg/mL and 0.7 mg/mL). The prepared drug conjugate in water appeared stable for about 24 h without significant change in zeta potential (within ±1.0 mV). However, slow precipitation of XJB-5-131 from the solution was increasingly noticeable over time due to the intrinsically poor solubility of XJB-5-131. After about 1 week, the drug conjugate solution had to be resonicated for 30 min to disperse the nanoconjugate.

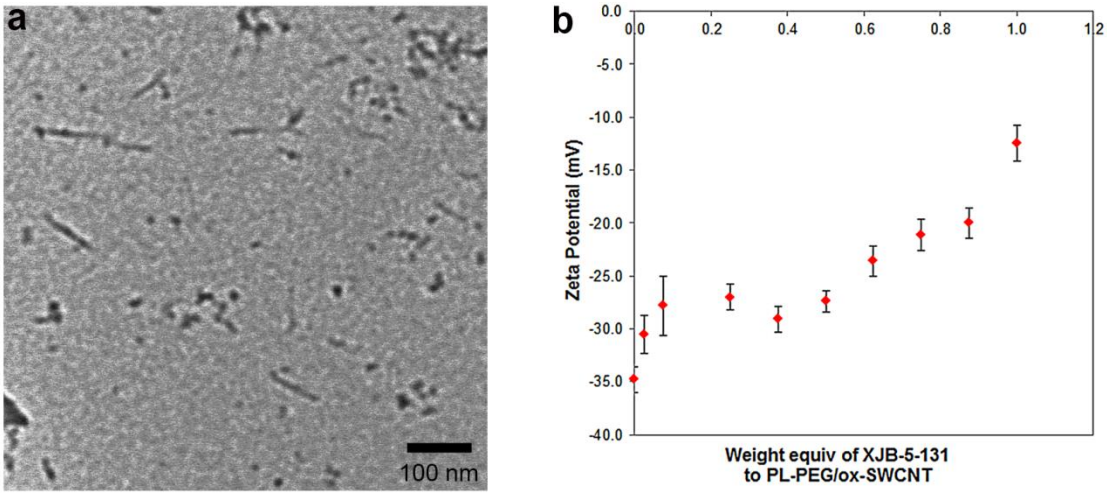

Figure 2.7 (a) TEM micrograph(average length: 82 ± 44 nm) and (b) zeta potential titration of XJB-SWCNT under pH 7.5. Data are means ± SD of five replicate measurements.

2.4.4 *In vivo* results of the TPP-IOA conjugate

The TPP-IOA conjugate (TPP-IOA-SWCNT) was shown more effective as a radiomitigator than free TPP-IOA. The therapeutic effect of TPP-IOA-SWCNT began to show after 12 h and the mouse survival rate was markedly higher than untreated mice (Figure 2.8a). However, the mitigating effect of TPP-IOA-SWCNT was very similar to that of free TPP-IOA up to 16 d and slowly differed by ~15% after 20 d. The drug conjugate showed consistently higher rates throughout the given time period whereas a lower survival rate of free TPP-IOA was observed in the early stages of the experiment, which may be due to the high potency of free TPP-IOA. The TPP-IOA-SWCNT conjugate clearly demonstrated a prolonged life span of TPP-IOA especially over 1 h and maintained about a 35% margin over 24 h (Figure 2.8b).

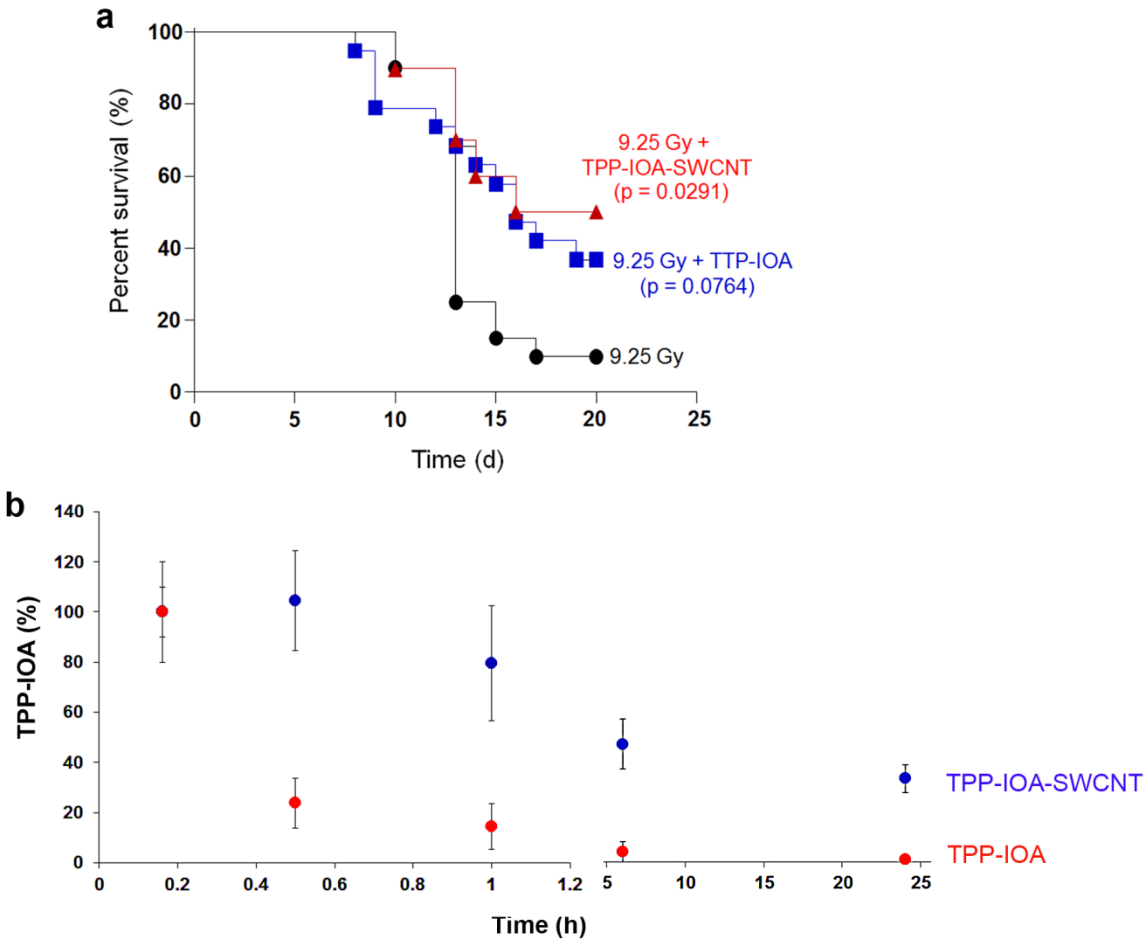

Figure 2.8 *In vivo* results of TPP-IOA-SWCNT. (a) Radiomitigative effect by TPP-IOA-SWCNT. (b) Free TPP-IOA and TPP-IOA-SWCNT remaining in plasma over 24 h after intravenous injection into of C56BL mice. The drug concentration was analyzed by LC-MS. Data are means ± S.E., n=5.[165]

2.4.5 *In vivo* results of the XJB-5-131 conjugate

The drug efficacy of XJB-5-131 after exposure of 9.5 Gy is shown in Figure 2.9a. In an earlier *in vivo* study of free XJB-5-131, the drug concentration administered to a mouse was 1 mg/kg.[139] A high dose of XJB-SWCNT was intravenously injected into mice (XJB-5-131, 0.35 mg/mL; PL-PEG/ox-SWCNT, 0.7 mg/ml). The dose administered was very toxic and no mouse survived in 5 min after the injection probably due to intrinsically hydrophobic drug aggregation (Figure 2.9b). The toxicity of the drug conjugate was not reduced even when the drug dosage was diluted to × 1/3. The concentration of PL-PEG/ox-SWCNT was much lowered to 0.09 mg/mL and the amount of XJB-5-131 loaded onto the carrier was about 180 times lower than the first failed experiment. Interestingly, with the lower carrier concentration, a higher drug loading capacity (0.9:1) was achieved, and a control group treated with XJB-SWCNT survived over 40 d (Figure 2.9c). However, all mice treated with a single dose of 9.25 Gy TBI without XJB-SWCNT survived after 40 d whereas 80% of those treated a 9.25 Gy TBI and XJB-SWCNT survived, showing no therapeutic effect. In contrast, the mouse survival rate with exposure to a 9.5 Gy TBI showed above 80% for 20 d, higher than that of untreated mice. However, the survival rate dramatically dropped after 20 d, far lower than control mice exposed to the same TBI without drug treatment. In Figure 2.9d, the same dose of XJB-5-131 was mixed with a nonionic solubilizer Cremophor ELP (XJB-Cremophor), and the data was compared to XJB-SWCNT. Although XJB-SWCNT outperformed the XJB-Cremophor, the mouse survival rates of both administration routes were lower than untreated mice with a 9.5 Gy TBI throughout the experiment. Because of the unexpected failure and inconsistent data repeatedly observed, no further study was continued.

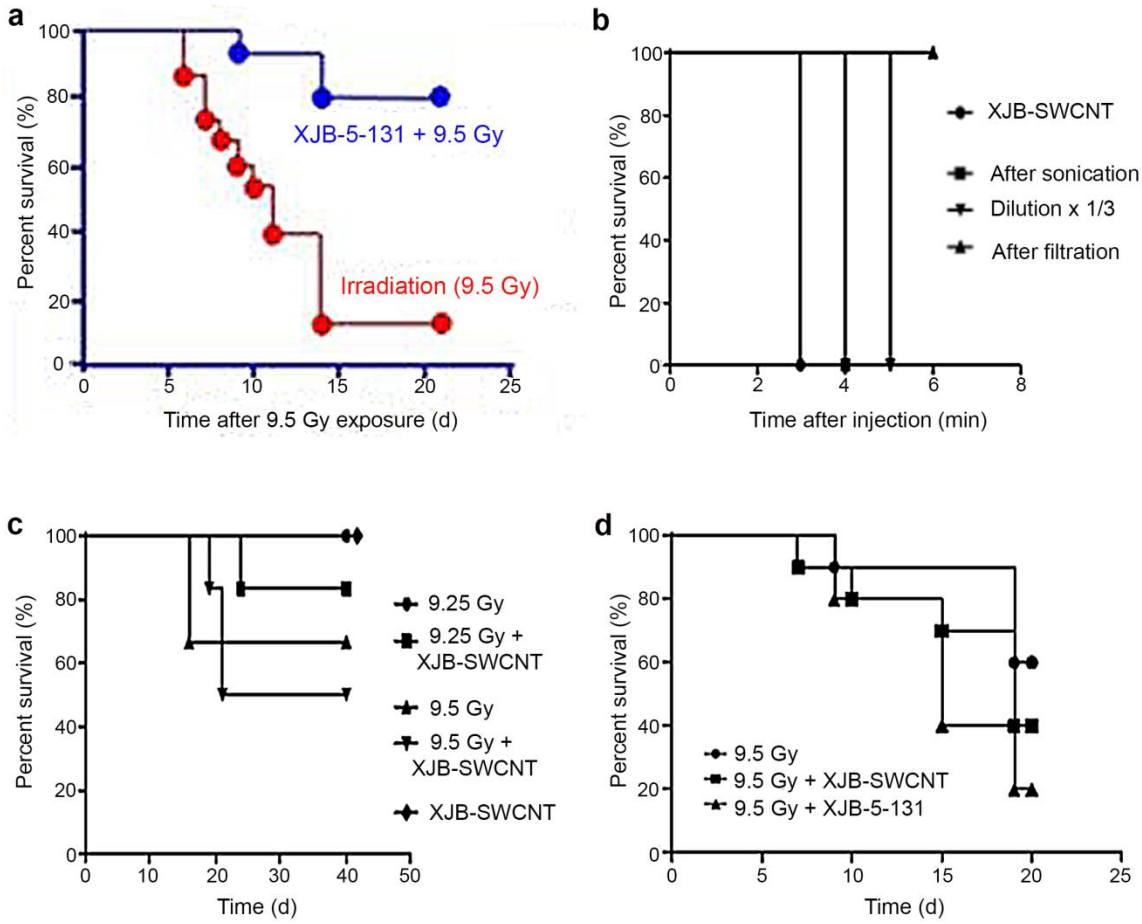

Figure 2.9 *In vivo* results of XJB-SWCNT. (a) Protection effect of free XJB-5-131. Intraperitoneal injection with XJB-5-131 (10 mg/kg of body weight) was performed on mice and irradiated to 9.5 Gy 10 min later. (b)Toxicity of XJB-SWCNT after intravenous injection (PL-PEG/ox-SWCNT: 0.7 mg/ml and XJB-5-131: 0.35 mg/ml). (c) Effect of XJB-SWCNT on the mouse survival rate after TBI 9.25 and 9.5 Gy, respectively. The concentration of XJB-5-131 was 0.18 mg/ml. (d) Effect of XJB-SWCNT and XJB-Cremophor on the mouse survival rate after a TBI of 9.5 Gy. Mice were intravenously injected with 200 μL of XJB-SWCNT (0.018 mg) 20 h after the TBI irradiation. 10 mg/kg XJB-5-131 (0.2 mg in 100 uL) dissolved in Cremophor EL/ethanol (10% Cremophor EL, 10% ethanol, and 80% water).[170]

2.5 CONCLUSION

The PL-PEG/ox-SWCNT composite was employed to improve the circulation time of mitochondria targeting drugs TPP-IOA and XJB-5-131. The *in vivo* study of the TPP-IOA-SWCNT conjugate revealed that the drug efficacy for 8–20 d after exposure to a TBI of 9.25 Gy was marginally better than free TPP-IOA without an apparent sign of toxicity. The i*n vivo* experiments of the XJB-SWCNT conjugate did not show reasonable ground to employ a nanocarrier. An interesting finding is that the drug loading capacity actually improved with a low concentration of the nanocarrier. This result suggests that the high density of PEG chain does not provide the high number of anchoring site for drugs, which seems counterintuitive. PL-PEG successfully imparted biocompatibility to XJB-5-131, but failed to demonstrate the nanocomposite as a reliable drug carrier.

2.6 SUPPORTING INFORMATION

2.6.1 Materials and instrumental

HiPco SWCNT was purchased from NanoIntegris®. Lyophilized human myeloperoxidase (MPO) was received from Athens Research and Technology, INC. (Athens, GA, USA). N-(aminopropylpolyethyleneglycol)carbamyl-disteaoyl phosphatidylethanolamine (DSPE-050PA) was purchased from NOF Corporation. (Methyl-PEG_{12})$_3$-PEG-NHS Ester (TMS$(PEG)_{12}$) was obtained from Thermo Scientific. N_3-(2-hydroxy-2-nitroso-1-propylhydrazino)-1-propanamine (Papa NONOate) was purchased from Cayman Chemical Company (Ann Arbor, MI). All other chemicals were purchased from Sigma Aldrich, and were used without further purification. All samples were prepared by dispersing dry solid in either nanopure water or phosphate buffer (pH 7.4).

Nanopure water was collected from Thermo Scientific BarnsteadTM NanopureTM. Branson 5510 was used for ultrasonication. Thermo Scientific Savant SPD 1010 SpeedVac was employed to dry aqueous samples (pressure: 5.6 Torr, temperature: 45 ˚C). The size distribution and the morphology were analyzed with Transmission Electron Microscope (FEI-Morgani, 80 keV). Renishaw inVia Raman microscope was utilized to collect Raman spectra (laser $\lambda_{excitation}$: 633 nm). Dried CNTs were drop-cast on a microscope slide. Spectra were collected with a 10 second exposure time and averaged across 5 scans per location. The collected spectra were normalized to 1 with respect to the maximum intensity. MALDI mass spectra were recorded on a Voyager-DE PRO Instrument. Zeta potential was measured using a Brookhaven ZetaPals at 25 ˚C under specified conditions of pH. NMR spectra were acquired on a Bruker Avance III 400MHz NMR. Fourier Transform spectroscopy (FTIR) was performed employing an IR-

Prestige spectrophotometer (Shimadzu Scientific) outfitted with an EasiDiff accessory (Pike Technologies). X-ray photoelectron S2 spectroscopy (XPS) was obtained via a Thermo Scientific ESCALAB 250xi photoelectron spectrometer using monochromated Al K Alpha X-rays as the source.

2.6.2 Characterization of PL-PEG and ox-SWCNT

2.6.2.1 Matrix-assisted laser desorption ionization (MALDI)

A matrix solution was prepared with α-Cyano-4-hydroxycinnamic acid (10.0 mg) in a mixture of 0.2 % trifluoroacetic acid (TFA) in H_2O/CH_3CN (2 mL). A PL-PEG was dispersed in water (1 mg/mL) and then mixed with the prepared 0.2% TFA solution/CH_3CN (1:1, v/v).

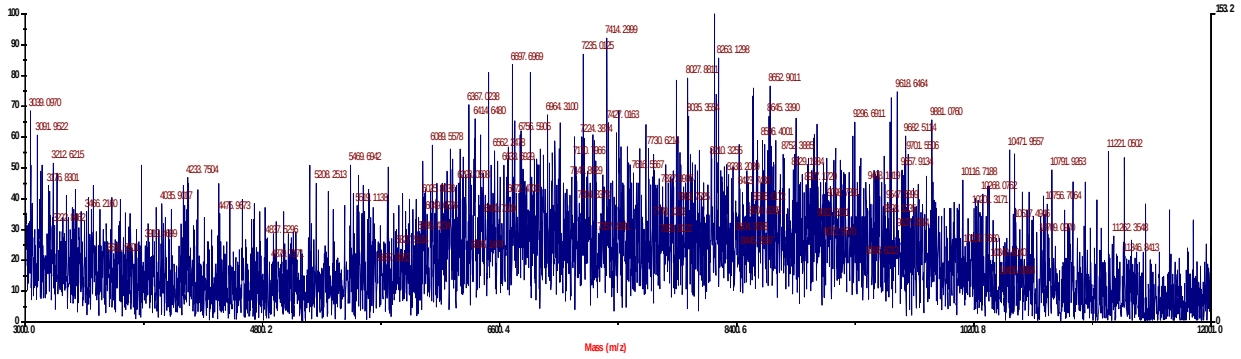

Figure 2.10 MALDI mass spectrum of PL-PEG. The average molecular weight was estimated around 7.4– 8.2 kDa.

2.6.2.2 Fourier transform infrared spectroscopy

A dried ox-SWCNT sample was homogeneously mixed with KBr. Using KBr as the background and taking 32 scans per sample, a spectrum was obtained over the range of 800 to 4000 cm^{-1} with a resolution of 4 cm^{-1}.

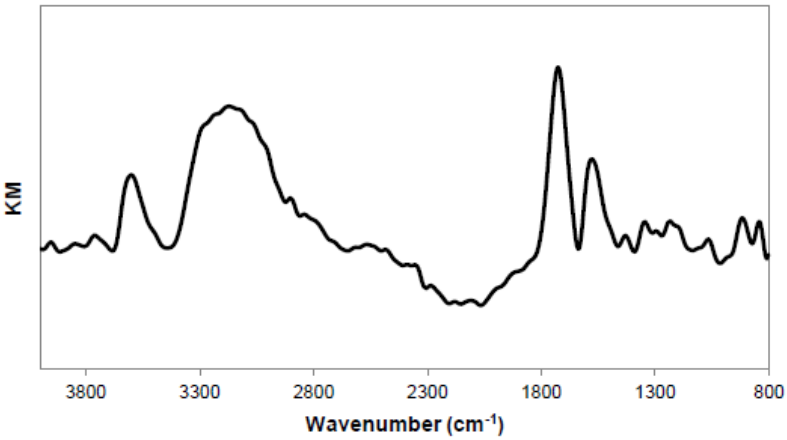

Figure 2.11 IR absorption spectrum of ox-SWCNT.

Table 2.2 Identification of functional groups by FTIR analysis.

Peak (cm^{-1})	Functional group
3587	Ar–**OH**
2684–3433	(C=O)–**OH**
1728	(**C=O**)–OH
1567	–**C=C**–
1334	–**S=O**–

2.6.2.3 X-ray photoelectron spectroscopy

The spot size of the sample was 400 μm (microns) prepared on an aluminum plate. Charge compensation was provided by a low energy electron source and Ar^+ ions. Survey scans were collected using a pass energy of 150 eV, and high resolution scans were collected using a pass energy of 50 eV. The average percentage indicates a mean obtained by analyzing three different sample spots.

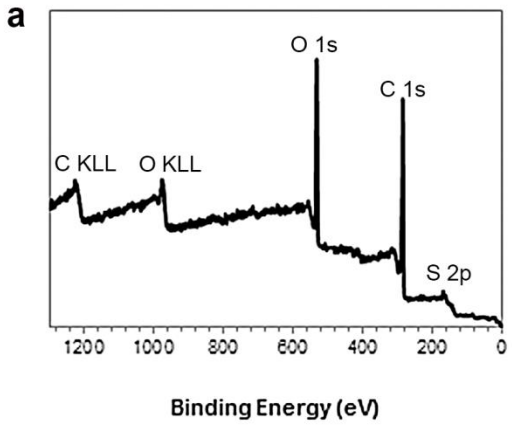

Element	Binding Energy (eV)	Relative Abundance (%)
C 1s	285.12	70.37
O 1s	532.47	25.22
S 2p	168.11	3.26

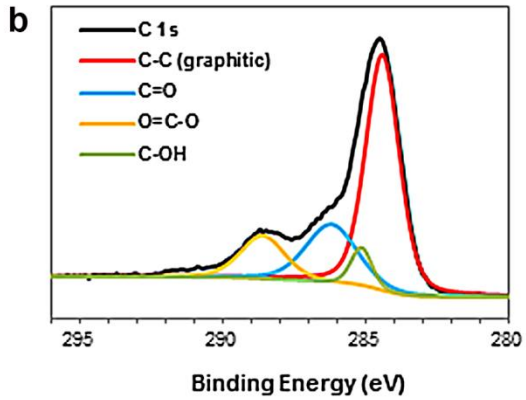

Surface functional group	Binding Energy (eV)	Relative Abundance (%)
C–C (graphitic)	284.40	58.50
C=O	286.19	21.64
O=C–O	288.59	14.04
C–OH	285.14	5.85

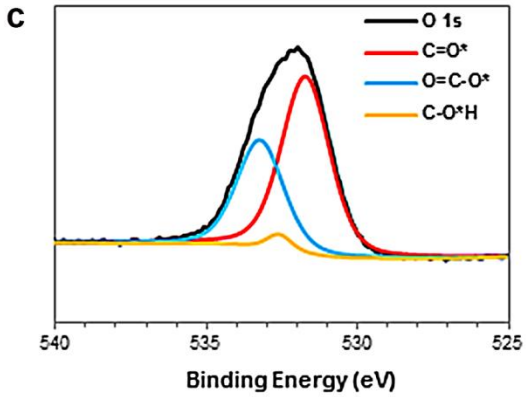

Surface functional group	Binding Energy (eV)	Relative Abundance (%)
O–C=O*	531.78	61.73
O=C–O*	533.23	35.80
C–O*H	532.64	2.47

Figure 2.12 X-ray photoelectron spectroscopy of ox-SWCNT. (a) Survey scan of the sample, (b) deconvolution of high resolution spectra of C 1s and corresponding functional groups, and (c) deconvolution of high resolution spectra of O 1s and corresponding functional groups.

3.0 OXIDATIVE BIODEGRADATION STUDIES OF DOXORUBICIN-SINGLE WALLED NANOTUBE DRUG CONJUGATE

3.1 CHAPTER PREFACE

Collaborative efforts were made to investigate the stability of a drug nanoconjugate in the context of the innate immune response. A communication based on this work was published in *Nanoscale* (DOI: 10.1039/C5NR00251F)[173] and all figures were reproduced by permission of The Royal Society of Chemistry. The Professor Michael Shurin group, Department of Pathology at the University of Pittsburgh Medical Center, and the Professor Valerian Kagan group, Department of Environmental and Occupational Health at the University of Pittsburgh conducted the biological studies. W. Seo prepared a Doxorubicin nanoconjugate and performed *ex vivo* experiments for the degradation of the drug nanoconjugate; Gallina V. Shurin conducted *in vitro* experiments and analyzed data. W. Seo thanks Prof. Valerian E. Kagan and Prof. Michael R. Shurin for their help in the course of manuscript preparation, and also acknowledges Alexandr A. Kapralov for sharing the *ex vivo* experimental details of peroxynitrite-mediated degradation.

3.2 INTRODUCTION

Chapter 3 focuses on the oxidative degradation of a drug nanoconjugate by the components of innate immune system and addresses issues implicated in drug circulation. The susceptibility of the drug and the nanoconjugate to enzymatic reactions occurring in inflammatory cells can shorten the circulation time and alter drug efficacy.[174-175] This issue can be especially problematic if a drug nanocarrier degrades upon immune response. As described in Chapter 1, CNTs and PEGylated CNTs are able to undergo oxidative degradation.[95,121] Thus drug carriers consisting of those materials may need strategies to protect drug conjugates from oxidation and facilitate controlled drug release.

For a proof-of-concept study, a Doxorubicin conjugate (DOX-SWCNT) is prepared for a model system by noncovalent functionalization of an anticancer agent Doxorubicin (DOX) with the PL-PEG/ox-SWCNT composite that was described in Chapter 2 (Figure 3.1). Several DOX conjugates with slight modifications in the functional group and topology of PEG were developed. *In vivo* studies of pharmacokinetics demonstrated that the use of PL-PEG/SWCNT composites resulted in the prolonged circulation of DOX.[137] Thus DOX-SWCNT conjugates provide a good starting point for investigating the role of the immune system within the context of drug circulation. Furthermore, knowledge of the degradation and stability of DOX under various conditions will help us analyze results accurately.

Our study aims at investigating the lifespan of the drug and the degradation behavior of DOX-SWCNT upon exposure to oxidative conditions mimicking oxidative burst of phagocytes. For oxidative conditions, we chose (1) myeloperoxidase and hydrogen peroxide in the presence of chloride ($MPO/H_2O_2/Cl^-$) and (2) peroxynitrite ($ONOO^-$), which neutrophils and macrophages spontaneously release to intra- and extracellular domains during the host-immune

response, particularly phagocytosis.[103-104] The degradation kinetics of DOX-SWCNT is compared with that of free DOX, thereby demonstrating a significant role of the drug carrier in the oxidative burst. Despite the presence of PL-PEG coated on the ox-SWCNT surface, which is known to mitigate opsonization (or phagocytosis) of NPs,[160,176] the DOX nanoconjugate is also subject to oxidative degradation. Further evidence is provided by a binding study of MPO–DOX conjugate. In order to establish parameters involved in the binding interaction, we have focused on the surface charge effect and utilized the zeta potential measurement of the individual components of DOX-SWCNT. Lastly, the *in vitro* cytostatic and cytotoxic effects of free DOX and the DOX nanoconjugate on melanoma and lung carcinoma cell lines are investigated in the presence of tumor-activated myeloid regulatory cells that create unique myeloperoxidase- and peroxynitrite-induced oxidative conditions. Both *ex vivo* and *in vitro* studies demonstrate that the PL-PEG/ox-SWCNT drug carrier protects DOX against oxidative biodegradation. Also, important insight has been gained in developing strategies for the design of drug nanoconjugates in relation to the immune defense system.

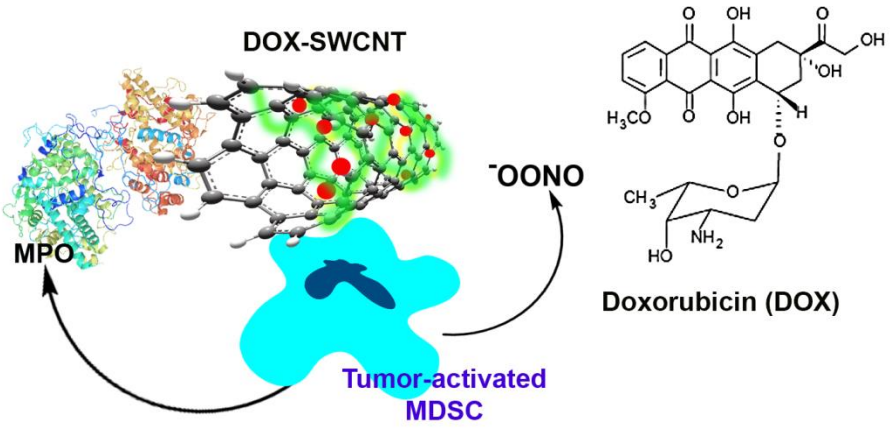

Figure 3.1 Doxorubicin is noncovalently bound to the PL-PEG/ox-SWCNT composite (DOX-SWCNT) and major oxidation routes activated by the immune system.[173]

3.2.1 Safety and toxicity of drug nanocarriers

Recent advances in nanotechnology have provided a great opportunity for precise engineering in the current state-of-the-art nanomedicine such as drug delivery, *in vivo* diagnostics, and tissue engineering.[177] Nanoparticles (NPs) have proven to be versatile building blocks for hybrid biomaterials. Controllable synthesis of NPs[178] and realization of finely tunable functionalities have greatly enhanced the performance of medical therapeutics with specific functions.[178-179]

Liposomes, polymers, micelles, proteins, and CNMs have been developed as common therapeutic carriers and cargos,[177] and their biocompatibility/biodegradability has been investigated in many biological studies. However, commercialization of these drug carriers has been extremely slow compared to the amount of research accumulated over the past few decades.[141] Accurate assessment of toxicity involved in NP-based drug delivery systems can be highly difficult. For example, toxicity can arise from either intended cytotoxic therapeutic agents or intrinsic properties of nanocarriers.[69] The use of degradable drug carriers is imperative in clinical applications,[180] but their degradation may reduce drug efficacy and cause side effects—regardless of whether the degradation is programmed or naturally occurs.[181] Further challenges lie in elucidating the complex degradation pathways of nanocarriers, frequently arising from heterogeneous compositions and propreties.[67,182] Despite recent findings in biodegradable CNTs under certain oxidative conditions, short oxidized CNTs do not guarantee absolute long-term safety in drug delivery. The research of potential toxic effects associated with complex biological processes should be further explored.

3.2.2 Innate immune responses to nanocarriers and pharmacokinetic implications

NPs with small sizes and high surface area to volume ratios provide excellent platforms for high reactivity in living organisms.[145] Utilization of nanocarriers allows for better carrier-target interactions (e.g., enhanced permeation and retention (EPR) effect) and efficient cellular/tissue uptakes.[153] However, the intrinsically high surface energy of NPs may cause major problems in pharmacokinetics: (1) low solubility arising from the formation of aggregates, (2) nonspecific binding with plasma proteins and deterioration by other chemical species that exist in the blood and lymphatics,[152] (3) premature drug loss due to size-dependent phagocytosis by innate immune cells during circulation,[183] and (4) fast clearance through reticuloendothelial systems (RES) such as liver and spleen.[152] Despite the enhanced permeability and retention (EPR) effect of NPs, generally the rate of drug permeation through cell membranes was found extremely low.[184] To improve clinical efficacy, especially circulation, optimization of the thermodynamic properties (e.g., surface free energy) in physiological conditions and investigation of relevant parameters (e.g., size, shape, and surface charge) in relation to clearance routes through different organs are crucial in the early stage of developing new drug delivery systems (Figure 3.2).[152,175] All these properties interplay with each other, generate fundamentally complex problems, and eventually converge into the issue of biocompatibility and biodegradation regulated by the FDA.[180]

Behind the success of targeted drug delivery, the issue of designing NPs resistant toward the innate immune system has been only marginally addressed. Because the human body reacts to drug conjugates nonspecifically, immune responses vary with the reactivity and toxicity of individual drugs and nanocarriers.[185] As a consequence, fewer drug molecules may reach the target than administered doses, thereby dramatically altering the original pharmacokinetics properties of drugs.[145,175] In addition, harmful self-immune responses such as inflammation or

even infectious diseases could be induced.[186] White blood cells (leukocytes), an essential component in innate immunity, and various tissues contain neutrophils (polymorphonuclear phagocytes) and monocytes/macrophages (typically Kupffer cells or macrophages of the liver).[174,176] Upon cellular ingestion of invading organisms, specific opsonin proteins present in serum, particularly C3, C4, and C5, and immunoglobulins, are recognized in the phagocytosis.[176] Neutrophils are ready to activate the immune response in the circulating blood, whereas macrophages can fight against toxins and infectious agents only in tissues.[187] In order to initiate phagocytosis in tissues, neutrophils in the blood migrate to the tissue and are attracted to an inflammatory area by chemotaxis—a chemical signaling process.[186] Because neutrophils are most abundant among white blood cells and can be very effective for killing pathogens within a short time period (about 3–4 d),[101] evaluation of the stability of drug conjugates toward neutrophils is critical. In contrast to neutrophils, the immune response activated by macrophages persists over weeks of chronic inflammation.[107] Although the oxidizing power of peroxynitrite is weaker than the MPO-catalyzed oxidative cycle, the long-term immune response and inflammation can sufficiently influence cellular and tissue environments as well as drug conjugates.

With growing interests in the nonspecific clearance of therapeutic NPs promoted by self-immune responses, a few recent studies have demonstrated that chemical modification of the NP surface may alter their properties and prevent a shortened life span of drug delivery systems and premature drug release.[188] For example, a synthetic molecular ligand incorporated onto the surface of a nanocarrier interferes with molecular recognition and signaling processes at the initial stage of phagocytosis.[188] Addition of a polymer that can alter C3 cascade complement system reduces nonspecific binding between nanocarriers and hepatic macrophages.[189] These

strategies of chemical modification allow nanocarriers to overcome intrinsic immune responses and prolong the circulation time of NPs.[176,190]

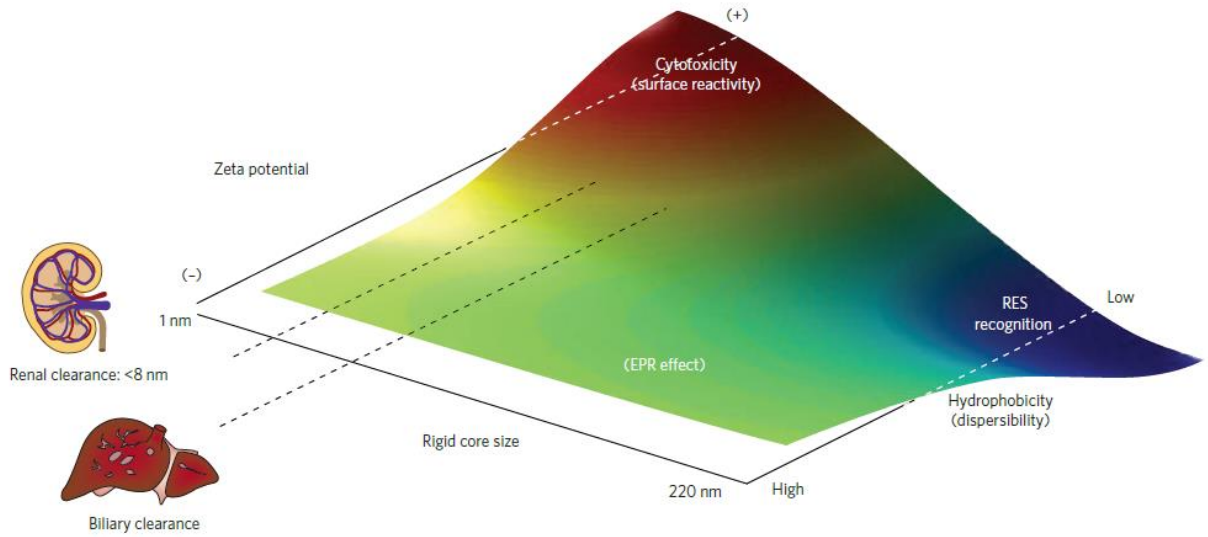

Figure 3.2 *In vivo* biocompatibility, clearance, and cytotoxicity of nanoparticles (NPs) are determined by size, zeta potential (surface charge), and dispersibility (hydrophobicity). Color representation: red (likely toxicity), blue (likely safety), and blue–green–yellow (intermediate levels of safety). Cationic and small particles with high surface reactivity are more likely to be toxic (red zone) than the larger relatively hydrophobic particles, which are rapidly and safely (blue hue) removed by the reticuloendothelial system (RES).[152]

3.2.3 Doxorubicin conjugates with PL-PEG/ox-SWCNT composites

Doxorubicin is an anthracycline anticancer drug utilized in many drug delivery systems for cancer treatment.[69,71,157] Presumably, the drug actions of anthracyclines in cancer cells are associated with DNA intercalation, such as inhibition of biochemical processes and DNA damage by generation of free radical species, etc.[191] However, inherent pharmacokinetic and

metabolic changes resulting in drug resistance and toxicity, notably cardiotoxicity, are well-documented in many occasions.[191-192] Various properties of free Doxorubicin have been extensively studied in addition to the pharmacokinetics and side effects,[193-194] such as photolytic and enzymatic degradations[192-193] and stability in infusion fluids.[195] Among many examples, the one-electron promoted redox cycle of quinone/semiquinone formation has been considered important due to the generation of a strong oxidant hydroxyl radical and oxidative damage in cells.[191]

Such paradigms as target/nontarget delivery and controlled release have been employed to improve the clinical efficacy of free DOX. Liposome carrier-based commercial products such as Doxil® and Myocet® have shown therapeutic indices far better than free DOX.[196] A great number of CNM-based DOX conjugates have been developed.[60,69] The pharmacokinetics (i.e., biodistribution and clearance) and toxicity of noncovalently functionalized DOX-SWCNT conjugates and PL-PEG/ox-SWCNT carriers were studied previously.[137,197] The surface density of PL-PEG coated on a SWCNT carrier was found about 10% of the total area of SWCNT.[154] Generally, the DOX loading capacity of 1–4 mg can be achieved with 1 mg of SWCNT-based carriers.[137] The binding energy of DOX to HiPco SWCNTs commonly used in drug delivery was estimated to be approximately 14 kcal/mol in water.[154] Drug release was found pH-dependent; at pH 5.5, about 40% of DOX was released from the carrier over 1 day.[154] DOX-SWCNT conjugates were demonstrated to be safe *in vivo* without apparent toxicity over 3–4 months when drug loading of 2.5 mg/mL (the wt of DOX per SWCNT carrier) was achieved.[197-198] The intravenously administered DOX-SWCNT accumulated largely in the liver and the spleen after 6 h in mice.[198] While increasing the half-life time of DOX, the drug uptake by tumors was doubled with DOX-SWCNT and was far better than Doxil.[137] The improved

therapeutic efficacy was attributed mainly to the longer circulation half-life time.[137] When only the PL-PEG/SWCNT carrier was tested, the nanocomposite began *in vivo* clearance from the liver through biliary excretion without significant adverse effects.[197]

3.3 EXPERIMENTAL

3.3.1 Preparation of the Doxorubicin conjugate (DOX-SWCNT)

PL-PEG/ox-SWCNT was prepared using the same method as described in Chapter 3. Doxorubicin (4.8 mg) was dissolved in 10 mL of phosphate buffer (0.1 M, pH 8.2). The DOX solution was sonicated for 30 min and was stirred overnight. After thorough washing with the same buffer solution through centrifugation, the amount of DOX wash-off was calculated from a UV-Vis calibration curve. The calculation showed that about 2.3 mg of DOX was bound to 3.0 mg of PL-PEG/ox-SWCNT, which corresponds to a 77% of drug loading. This estimation differs by 23% from the UV-Vis titration (Figure 3.10).

3.3.2 *Ex vivo* oxidation of the Doxorubicin conjugate

3.3.2.1 Myeloperoxide-catalyzed degradation

Each DOX-SWCNT sample was prepared by dispersing 0.03 mg of DOX-SWCNT in 720 μL of phosphate buffer (pH 7.4, 0.1 M). The concentration of free DOX was 0.02 mg/mL. Stock solutions of DTPA and NaCl were added to the DOX-SWCNT solution, and their final concentrations were adjusted to 0.38 mM and 0.14 M respectively. The concentration of DOX-SWCNT was 0.04 mg/mL. For the experiment of $+MPO/+H_2O_2/+Cl^-$, 4.4 μg of MPO was added every 24 h, and the H_2O_2 stock solution (18.75 mM) was added every 4 h (total volume of 30 μL per day). For $-MPO/-H_2O_2/+Cl^-$, the same amount of the pH 7.4 buffer solution was added. The samples were stored in a standard cell culture incubator at 37 ˚C. For UV-Vis-NIR

analysis, samples were cooled at ambient temperature for about 10 min. Each spectrum was collected with 700 μL of a sample solution in a quartz sample holder (path length: 1 cm), and further absorbance was recorded after each new addition of H_2O_2. A 0.02 mg/mL PL-PEG/ox-SWCNT solution was prepared in the same buffer condition. Then the same procedure was used to monitor the degradation of the nanocarrier. TEM analysis of degraded PL-PEG/ox-SWCNT samples were prepared by diluting the original 1:20 or 1:50 times with ethanol, and 3 μL of the diluted solution was placed on a lacey carbon copper grid and then permitted to dry in ambient conditions over 24 h.

3.3.2.2 Peroxynitrite-mediated degradation

Each DOX-SWCNT sample had a concentration of 0.03 mg of DOX-SWCNT in 808 μL of phosphate buffer (pH 7.4, 0.1 M), and 0.02 mg/mL of free DOX was prepared in the same buffer. Stock solutions of all other reagents were prepared every day. Then 7.5 μL of a xanthine oxidase (XO) solution (×50 diluted from the original enzyme) containing 0.15–0.3 mU of XO, was added once per day, followed by additions of 7.5 μL of xanthine solution (7.0 mM) and 7.5 μL of a PAPA NONOate solution (3.5 mM) every 2 h (total 6 times per day). Due to the dilution effect, the concentrations of both xanthine and PAPA NONOate solutions were raised after 6 additions, maintaining the same amount of each reagent relative to the total volume of the DOX-SWCNT solution. After incubation over a given time period, all the samples were filtered using Amicon centrifuge filters (size: 1,000 Da). The filtrate and the concentrate were separately collected by ultracentrifugation (14,000 × g, 10 min), and the concentrate was further diluted in phosphate buffer (0.1M, pH 7.4) for proper analysis. Then fluorescence emission spectroscopy ($\lambda_{excitation}$=488 nm, $\lambda_{emission}$=592 nm) was utilized to measure the concentration of DOX-SWCNT within a linear calibration range at room temperature. Due to some loss of DOX-SWCNT after

the ultracentrifugal filtration, a separate test determining the average recovery rate of DOX-SWCNT was performed to estimate the concentration accurately. The average recovery rate of five replicated samples was 62 ± 4 (%) from the original amount.

3.3.3 Zeta potential of MPO and DOX-SWCNT

The laser of the zeta potential analyzer was set at 532 nm. The zeta potential of unbound pure MPO was measured separately, which gave a negative potential (−9.0 ± 1.7 mV). A rapid color change to a very bright yellow upon the laser irradiation suggests the photosensitive heme of MPO.[199] After each titration, a sample containing DOX-SWCNT and MPO solutions was placed under ambient temperature and pressure over 1 h until their binding reached equilibrium, and then zeta potential was recorded. For the titration sample, solutions of DOX-SWCNT (0.3 mg/mL) and MPO were prepared in a mixture of nanopure water and 0.05 M, pH 7.4 phosphate buffer (17:1, v/v).

3.3.4 *In vitro* oxidation of the Doxorubicin conjugate

Pathogen-free C57BL/6 mice (7–8 week old) obtained from Jackson Labs (Bar Harbor, ME, USA) were individually housed and acclimated for 2 weeks. Animals were supplied with water and food *ad libitum* and housed under controlled light, temperature, and humidity conditions. All animal studies were conducted under a protocol approved by the Institutional Animal Care and Use Committee. Data were analyzed using one-way ANOVA and Student unpaired t-test

with Welch's correction for unequal variances. All experiments were either done in triplicates or repeated at least twice, and the results were presented as means ± SEM (standard error of the mean). P values of < 0.05 were considered to be statistically significant.

B16 melanoma cells were obtained from American Type Culture Collection (ATCC, Manassas, VA, USA) and maintained in RPMI 1640 medium that was supplemented with 2 mM L-glutamine, 100 U/ml penicillin, 100 μg/ml streptomycin, 10 mM HEPES, 10% heat-inactivated FBS, 0.1 mM nonessential amino acids, and 1 mM sodium pyruvate (Invitrogen Life Technologies, Inc., Grand Island, NY, USA). Tumor conditioned medium was collected from sub-confluent cultures by centrifugation (300 g, 15 min). The cell-free supernatant was collected, aliquoted, and used to treat MDSC.

For MDSC generation, bone marrow cells from tibia were isolated, filtered through a 70 μm cell strainer, and red blood cells were lysed with lysing buffer (155 mM NH_4Cl in 10 mM Tris-HCl buffer pH 7.5, 25°C) for 3 min. After RBC lysis, cells were washed and used for MDSC sorting. CD11b+ Gr-1+ MDSC were isolated from the bone marrow cell suspensions by magnetic cell sorting using a mouse MDSC Isolation Kit (MACS, Miltenyi Biotec, Auburn, CA, USA) according to the manufacturer's instructions. Isolated MDSC were cultured in supplemented RPMI 1640 medium with 25% (v/v) B16 conditioned medium for 48 h to generate tumor-activated MDSC expressing high levels of MPO.

Cell proliferation assay 3LL cells were labeled with CellTracker™ Orange CMTMR (5-(and-6)-(((4-chloromethyl)benzoyl)amino) tetramethylrhodamine) (Molecular Probes) and co-incubated with free DOX and DOX-SWCNT in the presence of tumor-activated MDSC. Co-incubation of 3LL cells with SWCNT, MDSC or both served as controls. After 24 h of incubation, the number of labeled 3LL cells was determined by flow cytometry (FacsCalibur)

events calculated for 1 min. Increased number of cells (vs. control medium group) indicates an increase in cell proliferation, while the lower cell number reflects cytotoxic (cell death) and/or cytostatic (inhibition of cell proliferation) effects on tumor cells.

3.4 RESULTS AND DISCUSSION

3.4.1 Characterization of Doxorubicin and nanocarrier

DOX-SWCNT was synthesized following a published procedure.[137,197] DOX-SWCNT was prepared with the PL-PEG/ox-SWCNT composite that was described in Chapter 2 (Figure 3.3a and b). Although most of the drug conjugate particles maintain high aspect ratios, agglomerates are relatively abundant.

UV-Vis-NIR absorption spectra confirm the presence of each component of the drug conjugate (Figure 3.3c). The suppressed S_{11} optical transitions near 870–1100 nm are characteristic of oxidized HiPco SWCNTs,[200] in which the broad absorption band constitutes the residual peaks of numerous chiral species (n,m).[15] A slightly red-shifted DOX absorption maximum at 495 nm from the free DOX absorption (480 nm) is indicative of noncovalent adsorption of drug molecules on the ox-SWCNT surface,[201] which was further demonstrated by the quenched fluorescence emission of DOX by mainly π–π stacking[154] at 555 and 595 nm (Figure 3.3d). The drug loading capacity of DOX was measured by titrations using UV-Vis absorption spectroscopy (Figure. 3.10, Ch. 3.6) and zeta potential analysis under pH 7.0 (Figure 3.11, Ch. 3.6). The binding ratio of DOX to the nanocarrier (bound DOX/nanocarrier, w/w) was found to be approximately 1:1.

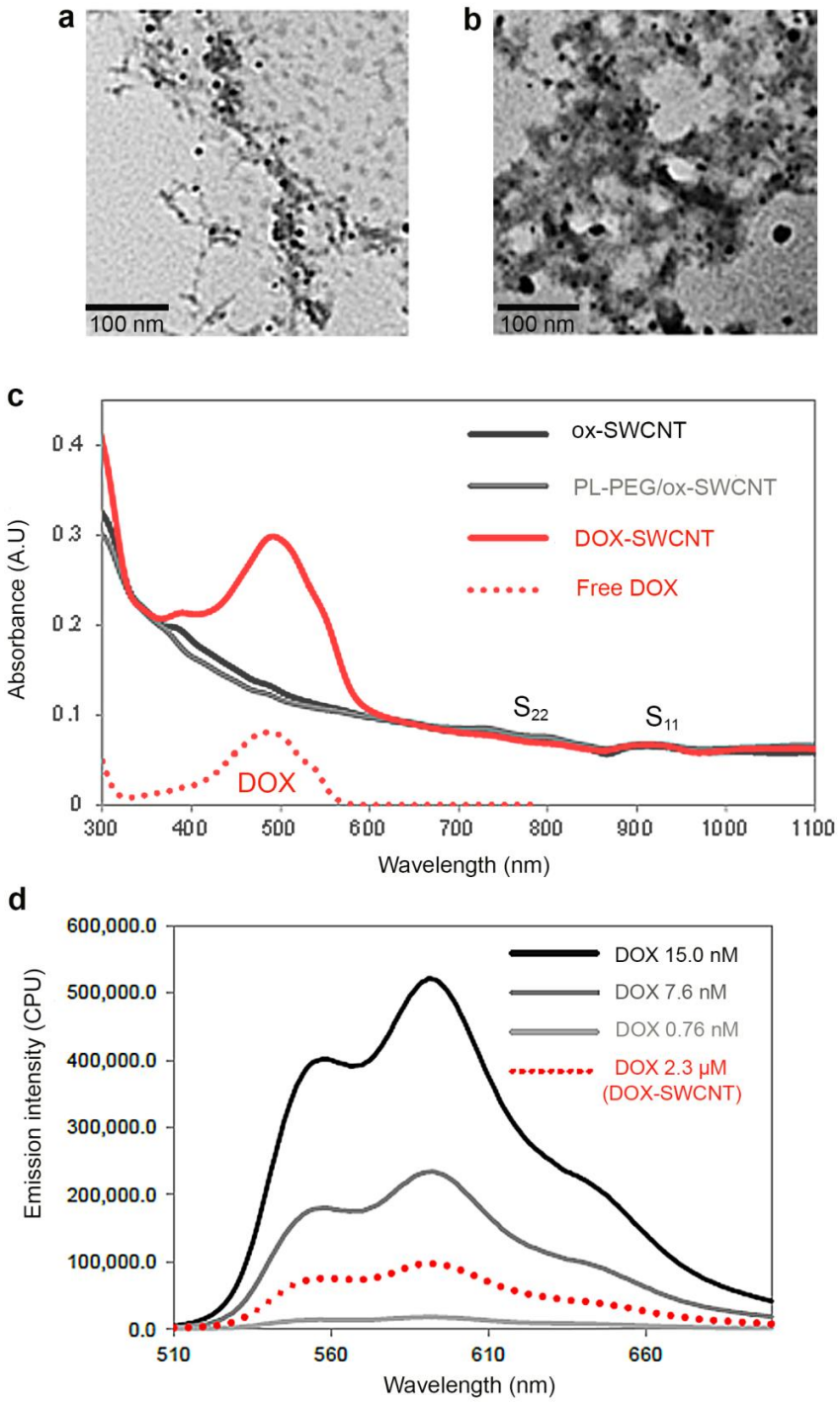

Figure 3.3 TEM micrographs of (a) PL-PEG/ox-SWCNT and (b) DOX-SWCNT. (c) UV-Vis-NIR absorption spectra for each functional nanomaterial. The spectra for SWCNT samples were normalized at 364 nm for comparison. (d) Fluorescence emission spectra of DOX-SWCNT in comparison to free DOX of varying concentrations.[173]

3.4.2 *Ex vivo* oxidative degradation of Doxorubicin and nanocarrier

3.4.2.1 Myeloperoxidase-catalyzed degradation

The degradation profiles of ox-SWCNT and DOX in phosphate buffer solution (0.1 M, pH 7.4) were investigated by monitoring spectral changes in UV-Vis-NIR absorption spectroscopy. Each sample contained NaCl (0.14 M) as a chloride source and diethylenetriamine pentaacetic acid (DTPA) as a chelating agent coordinating with residual transition metal catalyst ions present in the commercial HiPco CNTs. The peroxidase-catalyzed oxidation cycle was initiated by addition of an aliquot of H_2O_2, which produced hypochlorous acid/hypochlorite ($HOCl/OCl^-$) equilibrating at pH 7.4 and reactive intermediate species.[110,119] Hypochlorite (OCl^-) can further induce oxidation, and MPO-I and MPO-II, each of which drives one-electron oxidation,[202] promote the formation of reactive radical intermediates and electron transfer reactions.

The samples were incubated at 37 °C, and the resulting spectral changes were recorded periodically at room temperature. In the presence of $MPO/H_2O_2/Cl^-$, Figure. 3.4a and b show decreases in absorbance of DOX at 495 nm and the S_{11} region (900–1100 nm) of ox-SWCNT. The absorption profile of the residual peaks near 950 nm changed significantly. Likewise, the NIR absorbance of PL-PEG/ox-SWCNT (no drug) decreased (Figure 3.4c), indicating that the nanotube surface coated with the PL-PEG had also undergone oxidative degradation, as demonstrated by TEM (Figure 3.4d–i). This result is in good agreement with previous degradation studies of PEG-SWCNTs that were noncovalently functionalized with PEGs of various molecular weights (ca. 600–10 000 Da).[95,121]

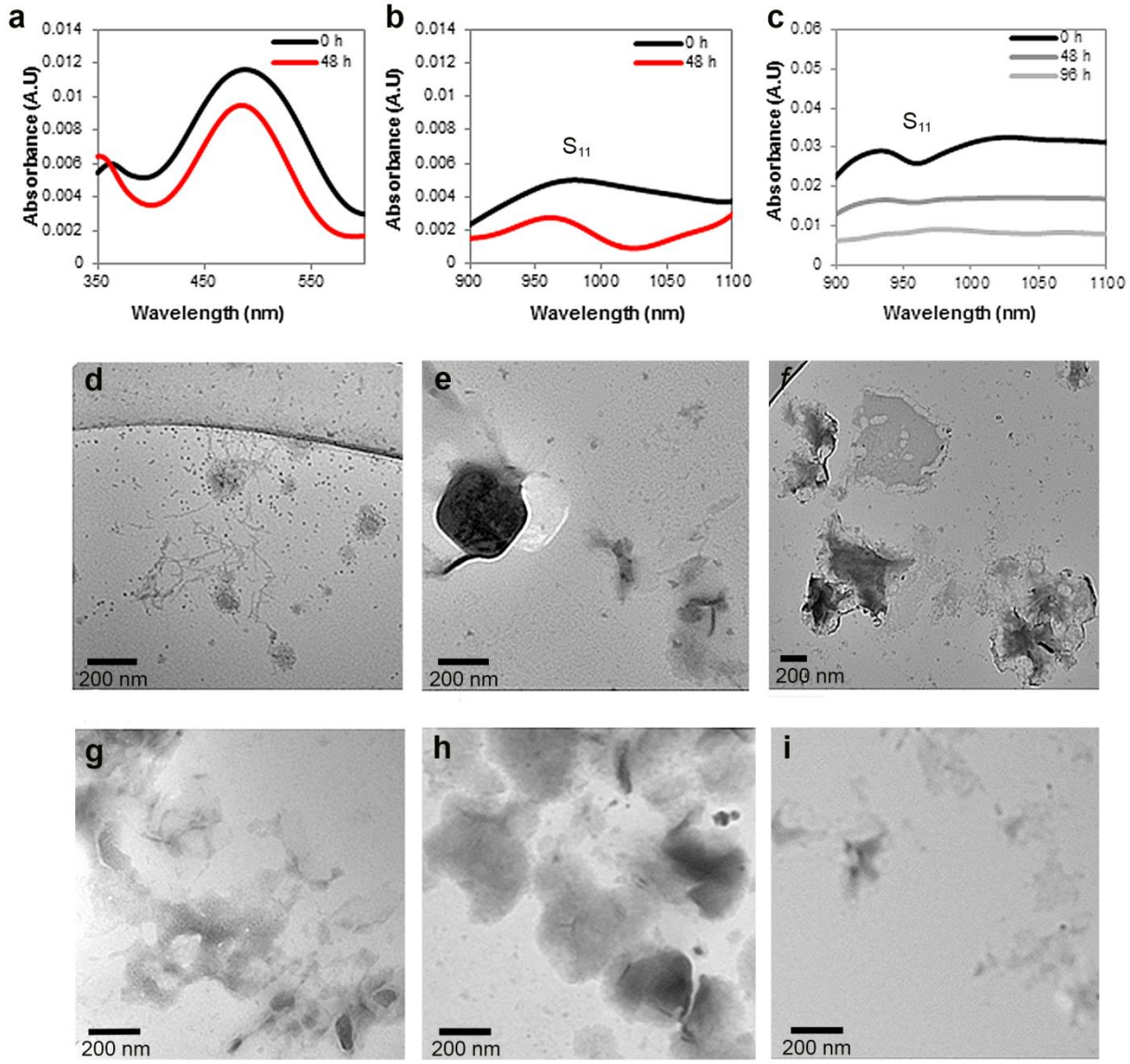

Figure 3.4 MPO-catalyzed oxidative degradation under pH 7.4 at 37 °C. (a) Change in DOX absorbance (495 nm) and (b) S_{11} band (900–1100 nm) before and after 48 h. (c) Degradation of PL-PEG/ox-SWCNT under the same condition. (d)–(i) TEM images of the degraded PL-PEG/ox-SWCNT over (d) 0 h, (e) and (f) 24 h, (g) 48 h, (h) 72 h, and (i) 96 h.[173]

The dramatically different NIR absorption profiles over the course of degradation (Figure 3.4b) suggest that the altered energy band gaps of the nanotubes possibly resulted from changes in the electronic structures and functional groups of the nanotube sidewall and ends. The oxidation of the drug carrier may disrupt the π–π stacking of DOX and initiate dissociations of the drug molecules from the CNT surface. This observation further raises the concern that the drug molecules could be released in an untimely manner during circulation. However, the relatively small change in the DOX absorption at 495 nm (Figure 3.4a) compared to free DOX (Figure 3.5a) indicates that most drug molecules still remained intact during the oxidation process. In the presence of MPO/H_2O_2/Cl^-, free DOX degraded about four times faster than DOX of the drug conjugate (Figure 3.5b), which suggests that the nanocarrier may serve as a scavenger for the strong oxidant ($^-$OCl) and reactive intermediate species generated from the MPO cycle. Because phenolic derivatives are especially good reducing substrates for conversion of MPO-I into MPO-II,[100] ox-SWCNT carrier containing hydroxyl groups can facilitate competing reactions with DOX. Interestingly, except for the free DOX under the MPO-catalyzed oxidation, the drug molecules in all other samples degraded relatively evenly, considering that the error bars slightly overlap with one another. These similar degradation patterns in the nonenzymatic oxidative conditions for both free DOX and DOX-SWCNT samples indicate that DOX is unstable to some extent and may undergo pH-dependent degradation in the pH 7.4 buffer at 37 °C.

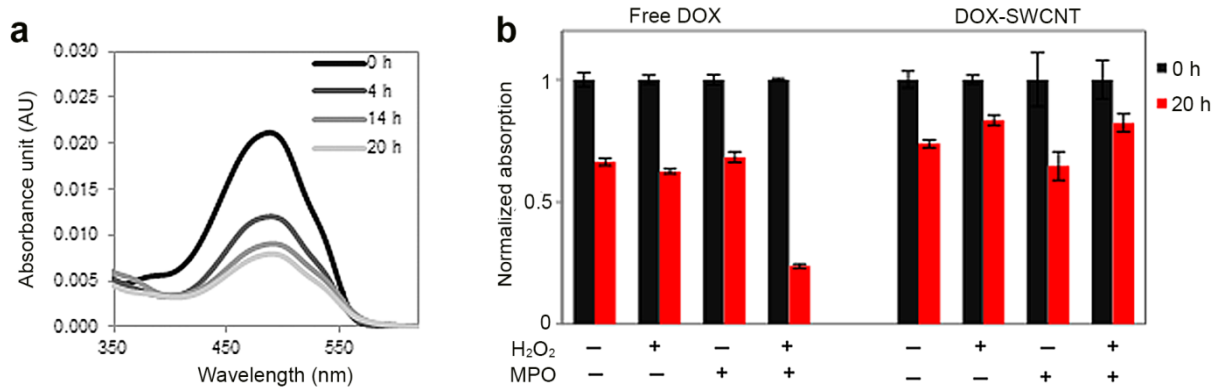

Figure 3.5 MPO-catalyzed oxidative Degradation of free DOX and DOX-SWCNT. (a) Decreasing absorbance of free DOX over 20 h. (b) Degradation of DOX (free DOX vs. DOX-SWCNT) under four different conditions of (±) MPO/(±) H_2O_2. The error bars indicate the means ± SD of three replicate measurements.[173]

We propose the major chemical transformations of DOX in Figure 3.6, where **1** is likely to undergo radical reactions due to the hydroquinone (B-ring) adjacent to the electrophilic quinone (C-ring) moieties. The one-electron oxidation generates **2** (semiquinone ($O^{\bullet-}$) of B-ring), and **3** can be formed through multiple steps by electron transfer and radical rearrangement on the carbons of A- and B-ring in the presence of excess H_2O or ^{-}OH.[203] We attributed this result to pH-dependent degradation resulting from keto–enol tautomerization upon deprotonation at C14 of **1**, followed by deacetylation and deglycosylation.[204] Our analyses with ^1H NMR and LC/MS confirmed the formation of **4** (Figure 3.12–3.14).

Other possible degradation products and competing reactions are listed in Figure 3.6. HOCl produced from MPO/H_2O_2/Cl^- can induce both oxidation and chlorination of DOX. The hydroxyl groups undergo conversion into carbonyl groups of **6**,[205] and the primary amine group are chlorinated selectively in **7**.[206] Simultaneously, compound **11** can be formed from phenolic

(ArOH) groups of ox-SWCNTs. If CNTs contain dangling bonds terminated with –C=C–,[123] compound **12** may provide another competing reaction with DOX. Compounds **8** and **9** were previously identified in MPO/H_2O_2/NO_2^-, in which nitrite, a strong oxidant (or cofactor), promotes reduction of the hydroquinone moiety of the B-ring.[207] However, this pathway seems to less likely occur in our MPO/H_2O_2/Cl^- system. Compound **3** is a known metabolite resulting from cleavage of the daunosamine by hydrolysis although the mechanism has not been well understood.[208] However, **3** was not found in the control experiment. In the case of *in vivo* experiments, we may see different degradation pathways. Compounds **3** and **5** can be formed under reductive cellular environments. Enzymes such as NADPH-cytochrome P450 reductase and flavoenzymes initiate conversion of the quinone of DOX to a semiquinone (1-electron reduction) or hydroquinone (2-electron reduction).[209] Compound **5** is formed by conversion of the ketone to an alcohol in ring A. Compound **3** is associated with various pathways, including electron transfer and quinone methide formation.[210] No matter how the reduction proceeds, DOX will eventually cleave the daunosamine, and a new bond is formed with nucleophiles, electrophiles, or radicals besides the hydroxyl group at C7 depending on the degradation pathway.

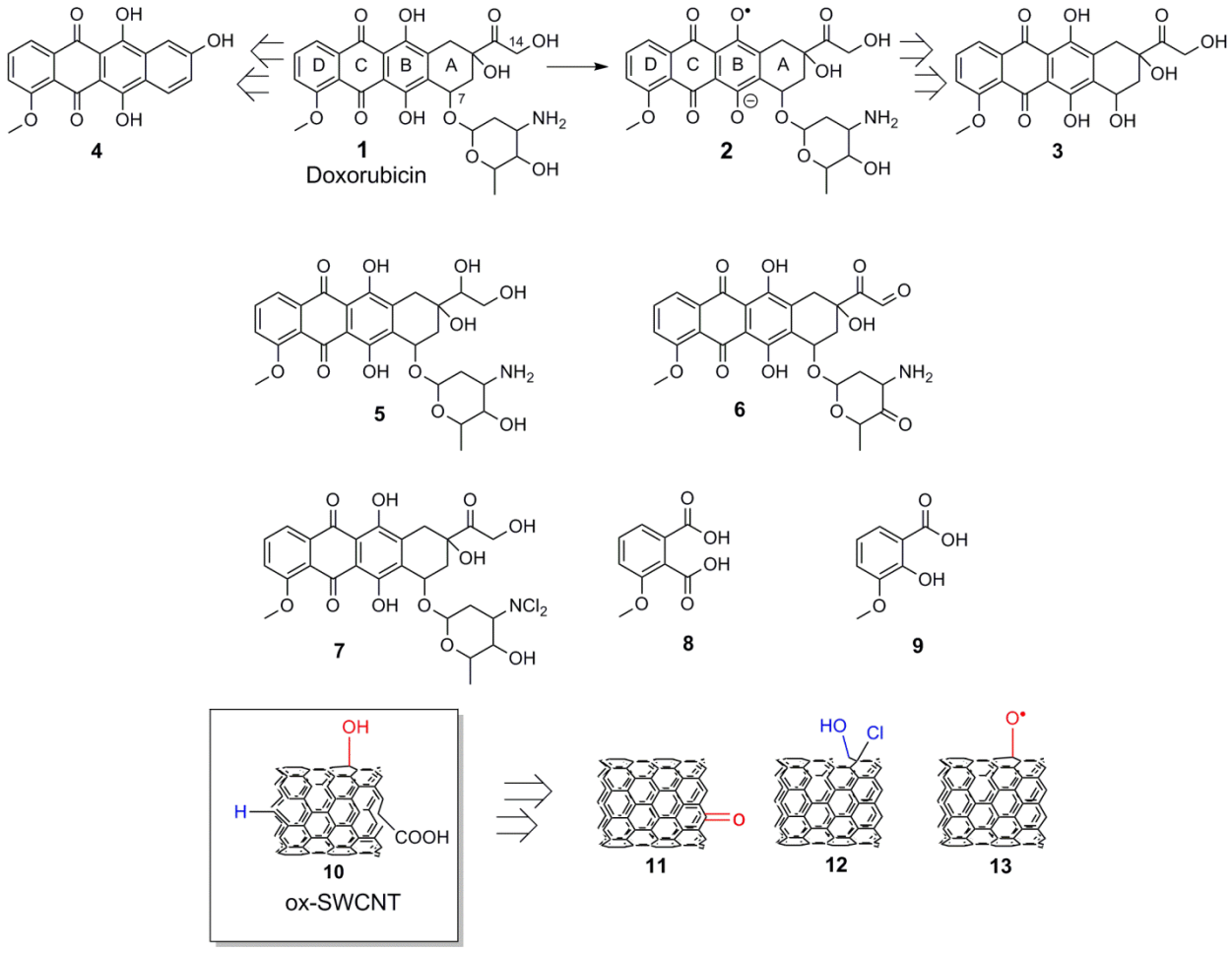

Figure 3.6 Degradation products of DOX possibly formed in the MPO-catalyzed oxidative and the control (nonoxidative) conditions. ox-SWCNT and possible products upon reaction with HOCl.[173]

3.4.2.2 Peroxynitrite-mediated degradation

In the analysis of peroxynitrite-mediated oxidation, we utilized fluorescence emission spectroscopy to investigate the stability of DOX-SWCNT because the absorption band of the by-product overlapped with that of free DOX (Figure 3.15). The drug conjugate was incubated in phosphate buffer (0.1 M, pH 7.4) at 37 °C. Peroxynitrite ($ONOO^-$) was generated *in situ* by the reaction of superoxide radicals ($O_2^{\bullet-}$) with nitric oxide (•NO) as shown in Figure 3.7a. Xanthine oxidase (XO) catalyzes the oxidation of xanthine and produces superoxide radicals; N_3-(2-hydroxy-2-nitroso-1-propylhydrazino)-1-propanamine (PAPA NONOate) serves as a nitric oxide donor. Peroxynitrite randomly diffuses through biological compartments and directly oxidizes SWCNTs. Similarly, HOCl produced during MPO catalytic cycle can permeate through the PEG-coated nanotubes, resulting in the stripping of PEG and biodegradation.[95]

As in the MPO-catalyzed oxidation, the drug conjugate (DOX-SWCNT) shows a smaller change of DOX emission intensity than that of free DOX (Figure 3.7b). It appears that the nanocarrier protects the drug molecules from the strong oxidant peroxynitrite ($ONOO^-$). The TEM images and the NIR band profiles of degrading ox-SWCNT/PL-PEG (Figure 3.7c–f and Figure 3.15) demonstrate that the nanocarrier was subject to structural transformation, where peroxynitrite ($ONOO^-$) can promote (1) direct nucleophilic reactions and (2) one- or two-electron transfer oxidations.[119]

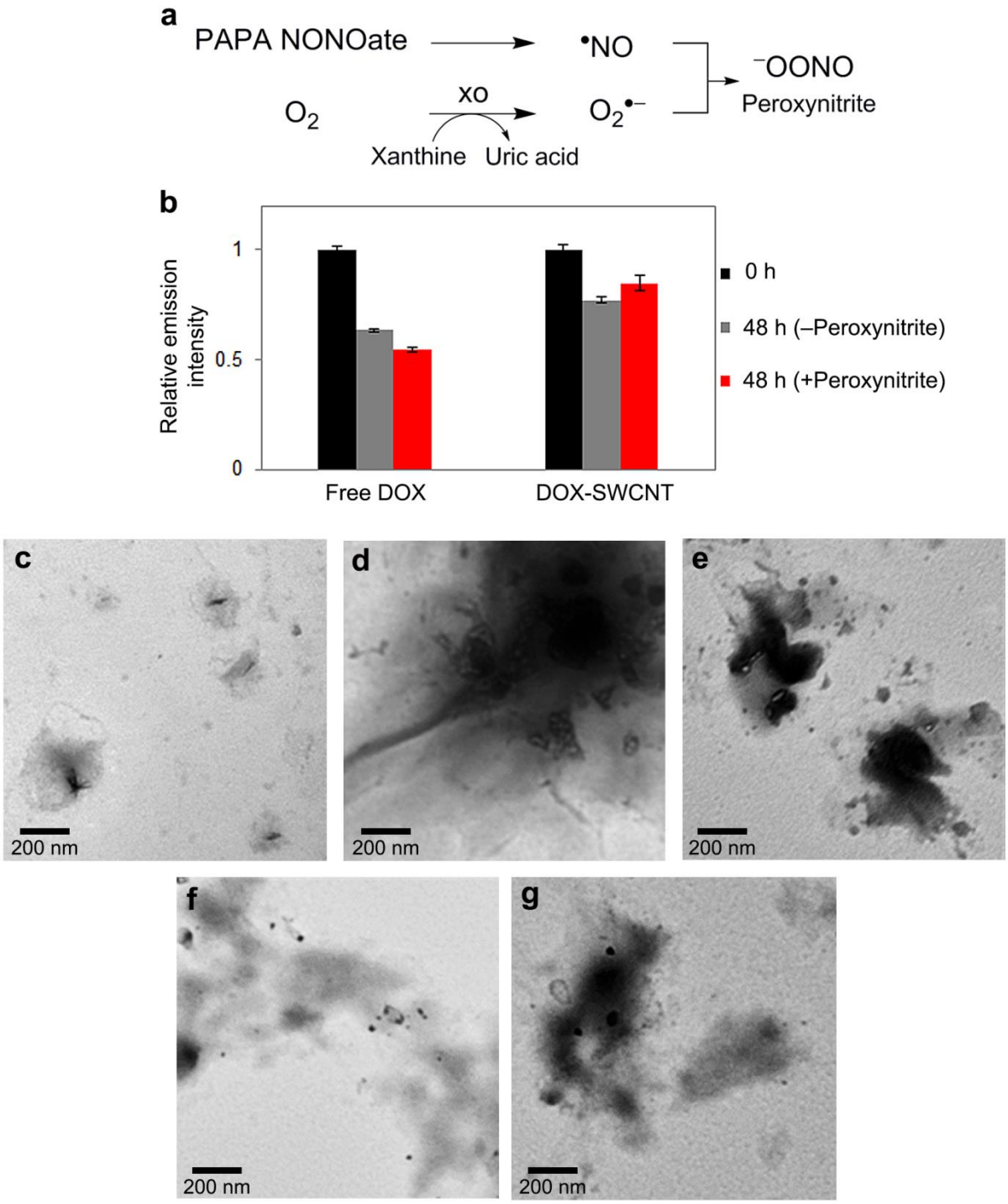

Figure 3.7 Peroxynitrite-mediated degradation. (a) Formation of peroxynitrite (b) peroxynitrite-mediated degradation of free DOX vs. DOX-SWCNT in phosphate buffer (0.1 M, pH 7.4) at 37 °C. The error bars indicate the means ± SD of three replicate measurements. (c)–(g)TEM images of peroxynitrite-mediated degradation in phosphate buffer (0.1M, pH 7.4) of PL-PEG/ox-SWCNT over (c) 0 h, (d) 24 h, (e) 48 h, (f) 72 h, and (g) 96 h.[173]

3.4.2.3 Binding interactions with myeloperoxidase

Peroxynitrite randomly diffuses through biological compartments and directly oxidizes SWCNTs. Similarly, HOCl produced during the MPO catalytic cycle can permeate through the PEG-coated nanotubes, resulting in the stripping of PEG and biodegradation.[95] However, MPO recognizes ox-SWCNT first, which is an electrostatically driven and selective process.[119] Once highly cationic MPO is positioned in close proximity to ox-SWCNT (mostly present as SWCNT-COO^- under pH 7.4), oxidation of the nanotubes occurs in the vicinity of the bound enzyme. Because the surface charge of DOX-SWCNT is different from that of ox-SWCNT due to the functionalization with PL-PEG and DOX, we further implemented zeta potential analysis to characterize the surface charge of each functionalization and find the effective concentration range of MPO that can bind with the drug conjugate (Fig. 3.8).

PL-PEG and DOX reduced the negative charge effect of ox-SWCNT in the synthesis of DOX-SWCNT, as indicated in the zeta potential change from −48.3 mV to −14.2 mV (Table 3.1), which could further delay the MPO-catalyzed oxidation. To analyze the threshold binding ratio of MPO to DOX-SWCNT, we performed zeta potential titration by gradually adding MPO to a DOX-SWCNT solution. It appears that the binding of MPO became saturated near 0.18 wt equiv. We chose 0.13 wt equiv (lower than the threshold value) for our degradation experiment, which probably resulted in the effective enzymatic oxidation with the drug conjugate. The fact that the addition of PL-PEG did not completely prevent the binding with MPO is interesting although, according to the literature,[176] some PEGs could reduce the nonspecific interaction with MPO under certain circumstances.

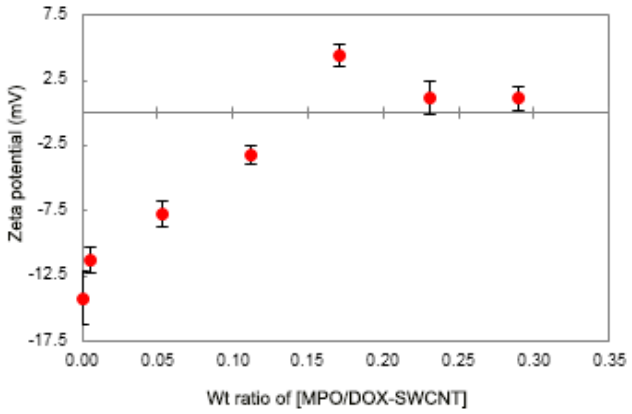

Figure 3.8 Zeta potential titration of the DOX-SWCNT with MPO at pH 7.4. Data are means ± SD of five replicate measurements. [173]

Table 3.1 Zeta potential changes upon sequential addition of each component at pH 7.4.

Sample	Zeta Potential (mV)
ox-SWCNT	-48.3 ± 1.6
PL-PEG/ox-SWCNT	-34.3 ± 1.1
DOX/PL-PEG/ox-SWCNT (DOX-SWCNT)	-14.2 ± 2.0
Free DOX	+9.2 ± 1.2

3.4.3 *In vitro* study of Doxorubicin nanoconjugate in myeloid cells

To investigate whether cellular MPO- and peroxynitrite-mediated pathways may exhibit differential biodegradation activity towards free DOX and nanotube-bound DOX, we cocultured fluorescent dye labeled B16 melanoma cells with each of the DOX samples in the presence of bone marrow-derived, tumor-activated, myeloid-derived suppressor cell (MDSC) known to express high levels of MPO and iNOS.[211] This method indicates that both MPO- and peroxynitrite-mediated oxidative biodegradation pathways are active in these cells. Importantly, both MPO and iNOS expression are essential for the immune-suppressive function of MDSC during growth of the tumor in the host.[212] After 24 h, DOX-induced apoptosis was assessed in B16 melanoma cells by Annexin V binding. Figure 3.9a demonstrates the results of a representative flow cytometry analysis, and Figure 3.9b shows the summary results from the triplicated experiments. As expected, free DOX in moderate pharmacological dose of 5 μM increased the level of tumor cell death up to two-fold ($p < 0.01$) whereas DOX-SWCNT was significantly more potent and caused an up to six-fold increase of apoptosis ($p < 0.01$). The concentrations of DOX released from the nanotubes in the cell medium remained constant (about 1 μM) over 24 h whereas free DOX concentrations were three times higher than DOX-SWCNT initially and then dropped by about 50% after 24 h (Figure 3.16). However, direct comparison of a cytotoxic effect of free DOX or nanotube-bound DOX is not appropriate in cell cultures due to the differences in concentrations and dynamics of DOX degradation. Important to note is the fact that the addition of MDSC significantly abolished the cytotoxic effect of free DOX, but not nanotube-bound DOX, suggesting that the nanotube-bound cytotoxic drug exhibits a stronger antitumor potential in the *in vitro* model of the tumor microenvironment than the free chemotherapeutic agent. As shown in Figure 3.9, the absence of the cytotoxic effects in all

additional control groups (PL-PEG/ox-SWCNT, MDSC alone, and MDSC + ox-SWCNT/PL-PEG) supports this conclusion.

The effects of free DOX and DOX-SWCNT on tumor cells in the presence of tumor-activated MDSC was confirmed using another tumor cell line –3LL Lewis lung carcinoma, where tumor cell proliferation was determined. As shown in Figure 3.18, both free DOX and DOX-SWCNT decreased the number of 3LL cells in cultures up to two-fold ($p < 0.01$). However, addition of MDSC abolished the cytostatic/cytotoxic effect of free DOX but not DOX-SWCNT, suggesting that nanotube-bound DOX exhibits a significantly stronger antitumor potential than free DOX in the presence of tumor-activated MDSC expressing high levels of MPO and iNOS.

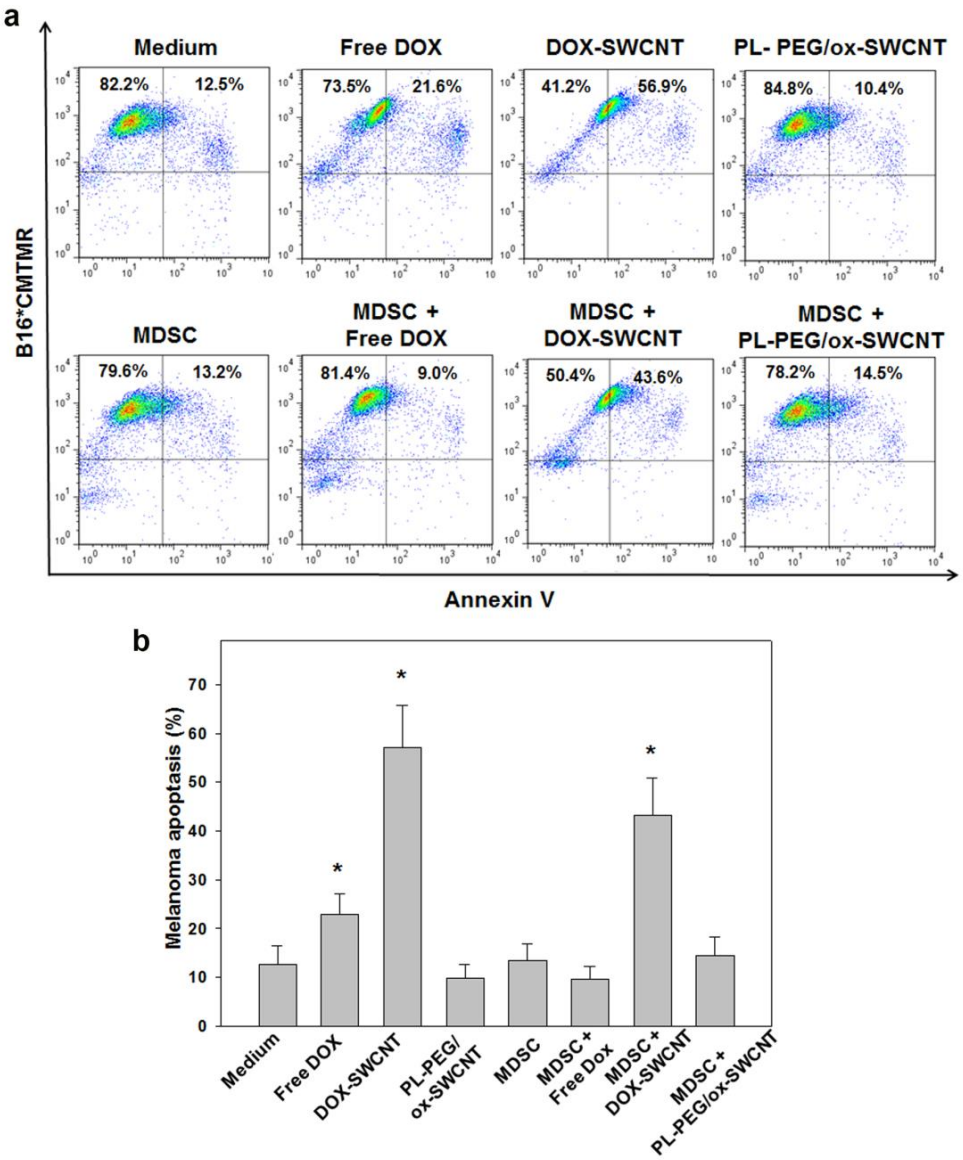

Figure 3.9 Cytotoxic effects of free DOX vs. DOX-SWCNT in B16 melanoma cells and bone marrow-derived, tumor-activated MDSC. DOX-SWCNT but not free DOX induces significant apoptosis of B16 melanoma cells even in the presence of MDSC. B16 melanoma cells and bone marrow-derived, tumor-activated MDSC were generated and cocultured in the presence of free DOX or DOX-SWCNT. PL-PEG/ox-SWCNT served as a control. The level of tumor cell apoptosis was determined 24 h later by Annexin V binding. All cell cultures were set in triplicates, and results are shown as representative flow cytometry dot plots in (a) and the mean ± SEM (standard error of the mean) (N = 3) in (b). *, $p < 0.01$ versus control (medium) group (one way ANOVA).[173]

3.5 CONCLUSION

We have demonstrated a degradable carbon nanotube-drug conjugate (DOX-SWCNT) by MPO-catalyzed and peroxynitrite-mediated oxidations. The degradation behavior of free DOX was analyzed in comparison to DOX-SWCNT under the same conditions, which allowed us to evaluate the effect of the nanotube carrier on the stability of DOX towards the oxidative reactions by enzymatic systems of innate immune cells—particularly neutrophils and macrophages. In both of the oxidative conditions, the drug molecules (DOX-SWCNT) degraded more slowly than free DOX. Our in vitro study also suggests that the chemotherapeutic agent delivered by the nanocarrier may be protected from the enzymatic inactivation associated with myeloid cells in the tumor microenvironment while exhibiting a constant DOX release rate. However, DOX demonstrated pH-dependent degradation in the nonoxidative conditions, and the nanotube carrier seems to be ineffective in slowing down this degradation process. Optimizing the balance between the degradation and resistance of the drug carrier and the payload towards the oxidants generated by inflammatory cells is critical to meet the needs for safety and prolonged circulation while orchestrating the stability and therapeutic effect of the drug. This strategy opens opportunities for exploring new parameters in biodegradation and developing controllable degradation properties by chemical modification of the surface of nanotubes.

3.6 SUPPORTING INFORMATION

3.6.1 Material and instrumental

All UV-Vis-NIR spectra were acquired using a Lambda 900 spectrophotometer (PerkinElmer). Fluorescent spectra were taken using a Horiba Jovin Yobin Fluoromax 3. A reverse-phase LC/MS (LC/MS-2020 Shimadzu) equipped with a Phenomenex C18 column and a photodiode array (PDA) detector was utilized. NMR spectra were acquired on a Bruker Avance III 400MHz NMR. Chemical shifts were reported in ppm (δ) relative to residual solvent peaks (DMSO-d_6 = 2.50 ppm for ^{1}H). Coupling constants (J) were reported in Hz. C18 column chromatography was performed on a C18-reversed phase silica gel purchased from Sigma-Aldrich.

3.6.2 Characterization of drug loading

3.6.2.1 UV-Vis titration

The maximum binding ratio of DOX to PL-PEG/ox-SWCNT was determined from the fitting curve. When the value of ΔA ($\Delta A = A_{\text{bound DOX}} - A_{\text{freeDOX}}$) reaches the maximum, the binding of DOX to the nanotube is saturated, in which the wt equiv value (x) of the maximum is 0.964. Therefore, a 1:1 weight ratio of DOX to PL-PEG/ox-SWCNT was obtained from the fitting equation below.

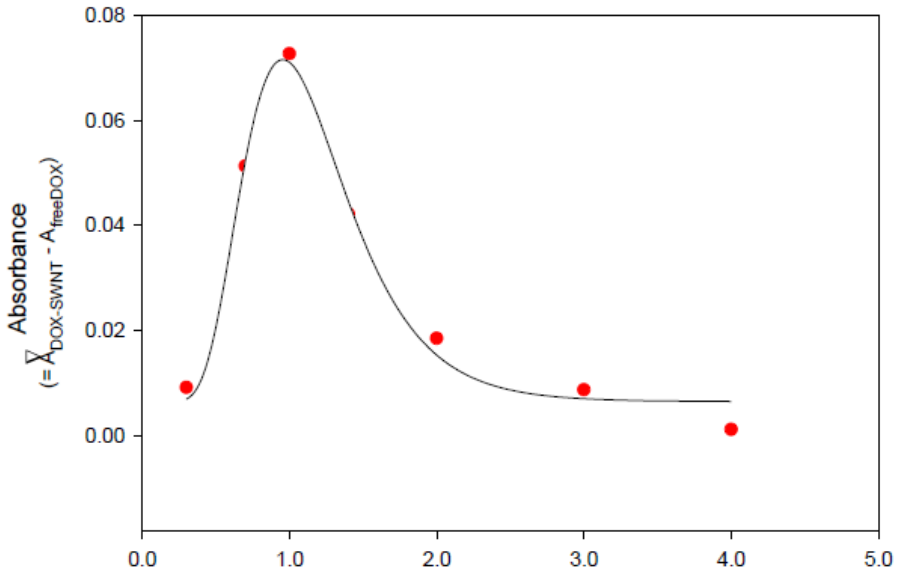

$$y = y_0 + ae^{\left[-0.5\left(\left(\frac{\ln\frac{x}{x_0}}{b}\right)^2\right)\right]} \quad (R^2 = 0.9870)$$

Fitting parameter	Coefficient	STD Error
a	0.0665	0.0049
b	0.3698	0.0382
x_o	1.0960	0.0386
y_o	0.0065	0.0026

Figure 3.10 UV-Vis titration of PL-PEG/ox-SWCNT with DOX. The fitting curve was found using SigmaPlot 11.0. Parameters were obtained from the fitting curve.[173]

3.6.2.2 Zeta potential titration

A solution of PL-PEG/ox-SWCNT in nanopure water (0.2 mg/mL) was prepared, and a 3 mL of the aliquot was transferred to a 20 mL scintillation vial. Then the varying amount of DOX solution in water (1.3 mg/mL) was added to the vial. After 30 min of sonication, the zeta potential of the solution mixture was measured with a dynamic light scattering detector. Using a graphical linear fitting curve near the saturation point at y-axis (0 mV), the corresponding wt equiv value was estimated. Approximately at 1.12 equiv, the zeta potential remains constant. Here, a 1.1:1 binding ratio of DOX to PL-PEG/ox-SWCNT was found. The graphical linear fit was obtained by OriginPro 8.5.

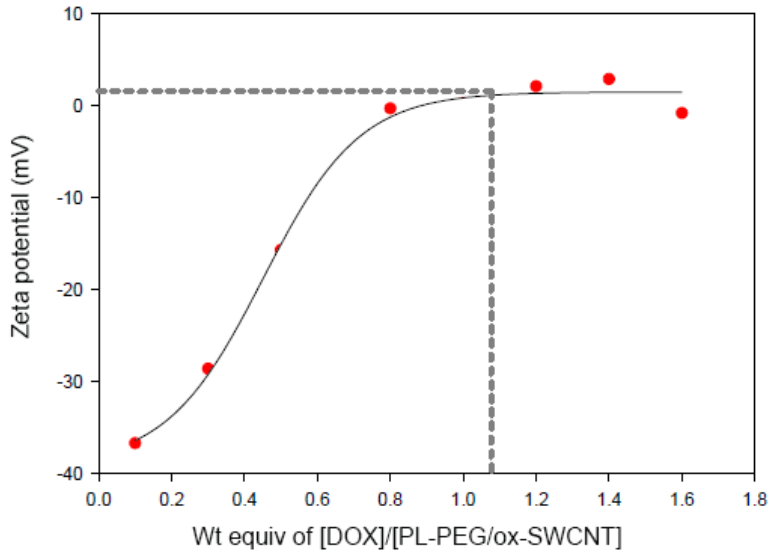

Figure 3.11 Zeta potential titration of PL-PEG/ox-SWCNT with DOX.[173]

3.6.3 Identification of degradation products

3.6.3.1 ^{1}H NMR analysis

In order to collect a large amount of sample for analysis, the weight and volume of each Doxorubicin solution was scaled up by 48 times while maintaining the same concentration used in the UV-Vis-NIR experiments. After incubation, the water in the samples was removed using SpeedVac over 6.5 h. The collected solid contained Doxorubicin degradation products and phosphate salt. Using methanol, *N*,*N*-dimethylformamide (DMF) and toluene, the collected samples were washed thoroughly and dried with a rotary evaporator and then a high vacuum pump over 24 h.

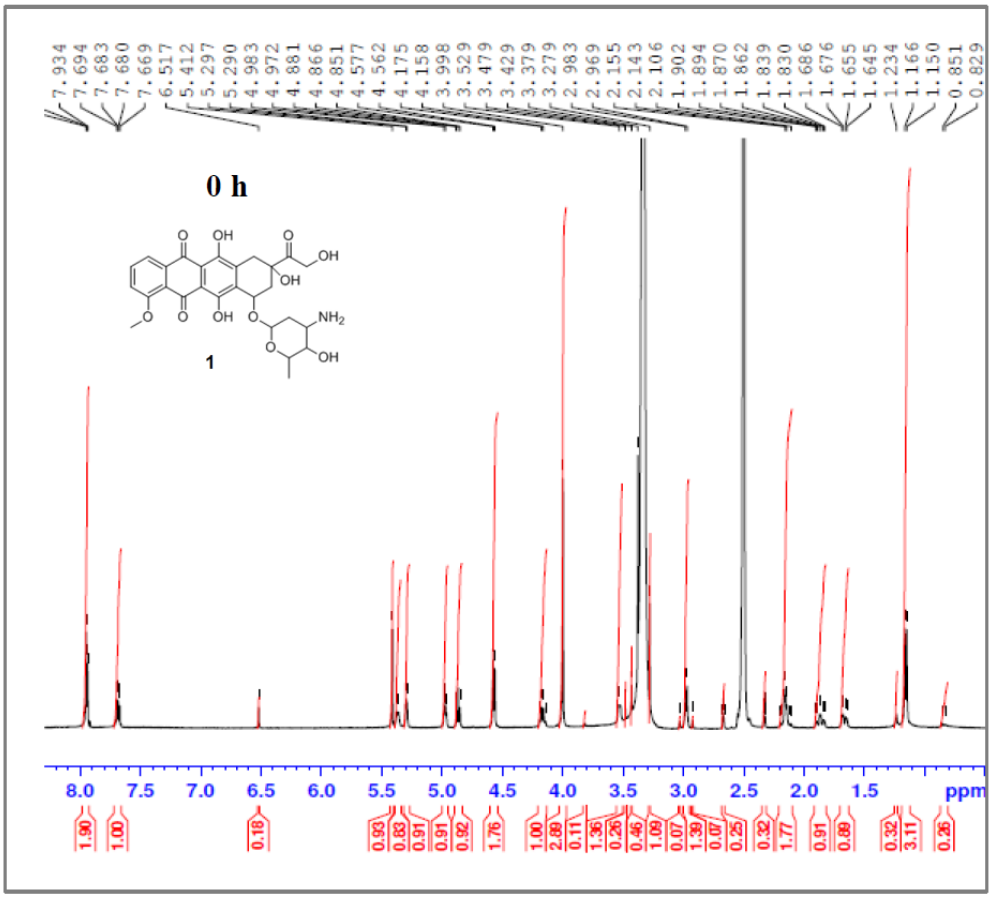

Figure 3.12 ^{1}H NMR spectrum of free DOX (dimethyl sulfoxide-d_6, 400 MHz) at 0 h.

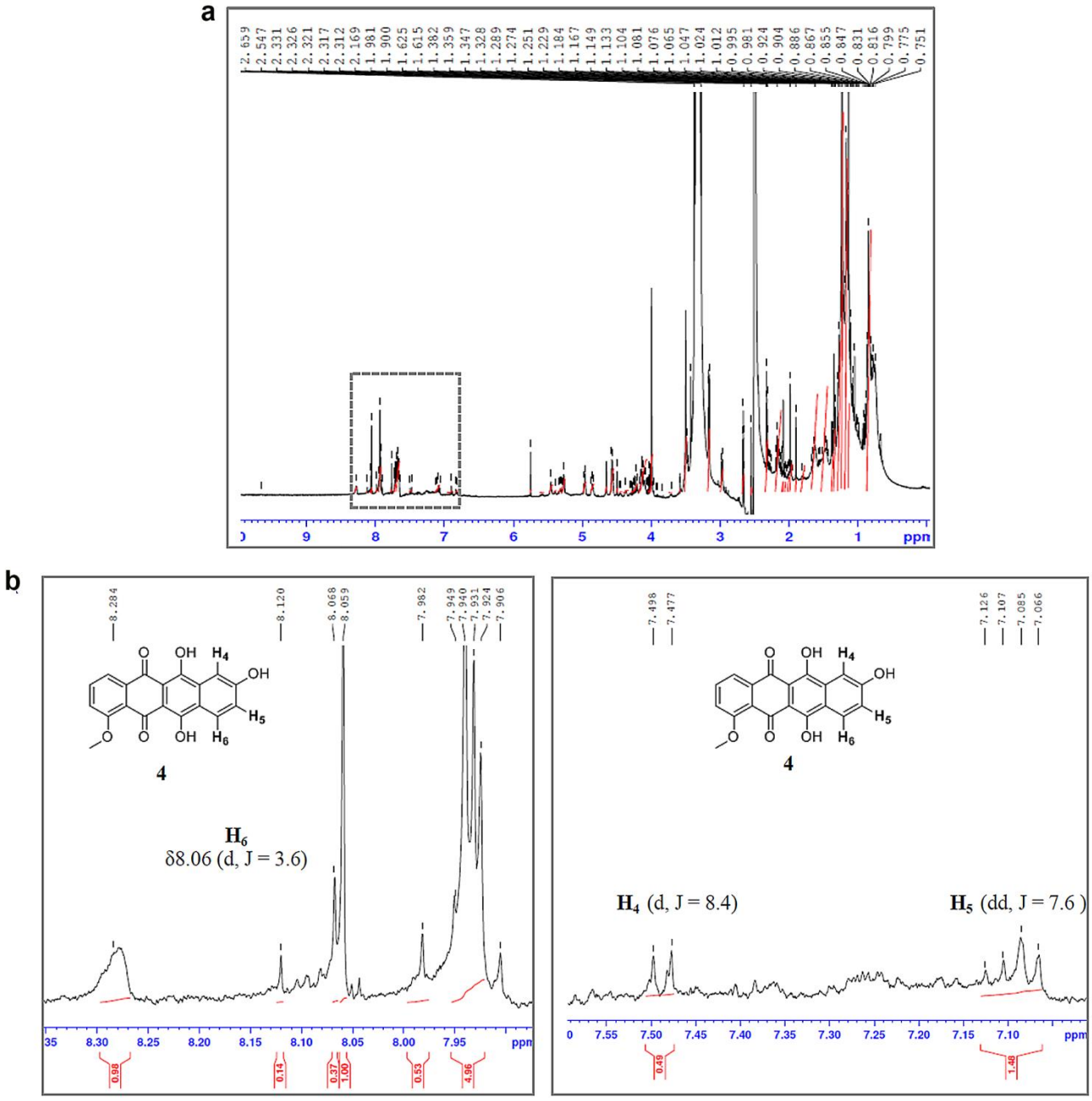

Figure 3.13 (a) ^{1}H NMR spectrum of free DOX (−MPO/−H_2O_2) without purification after 32 h and (b) the aromatic proton shift region (δ7.0–8.3) of the same spectrum. The protons of compound 4 were assigned based on a precedent analysis[213] and a predicted NMR data using Advanced Chemistry Development, INC. (ACS/Labs) Software V11.01 (©1994–2013 ACD/Labs)[173]

3.6.3.2 LC/MS

Electro spray ionization (ESI-MS) was used to measure the mass of the degradation products. The samples were scanned in both positive and negative modes. H_2O and CH_3CN were used as eluents.

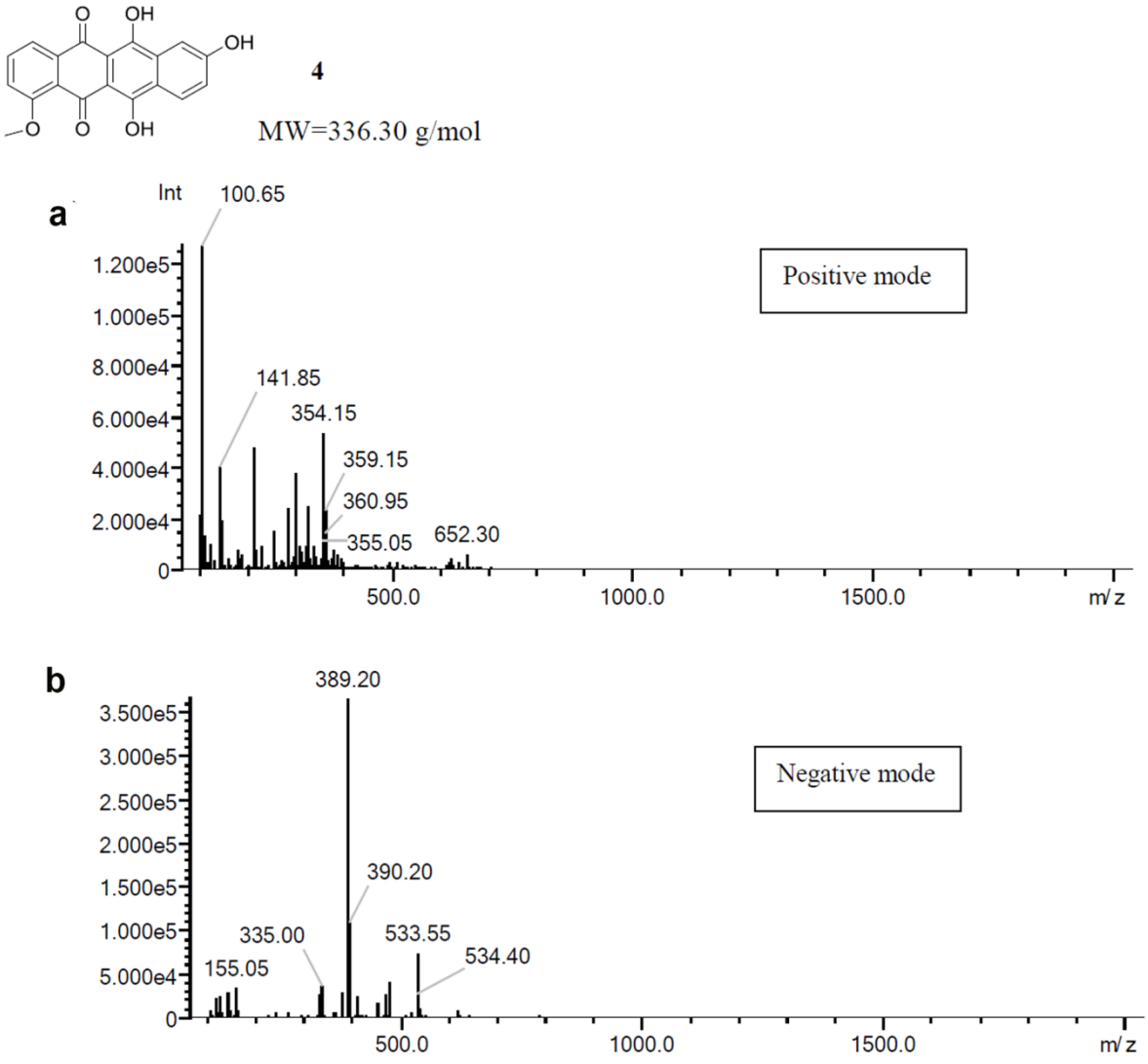

Figure 3.14 LC/MS chromatograms and mass spectra of the control sample after 32 h. To remove the phosphate salt, these samples were purified with C18 mini-column chromatography. (a) The peak 359.15 (m/z) is an adduct of [MW + Na]. (b) The peak of 335 (m/z) is indicative of a negative adduct [MW−H].[173]

3.6.4 Characterization of peroxynitrite-mediated oxidation

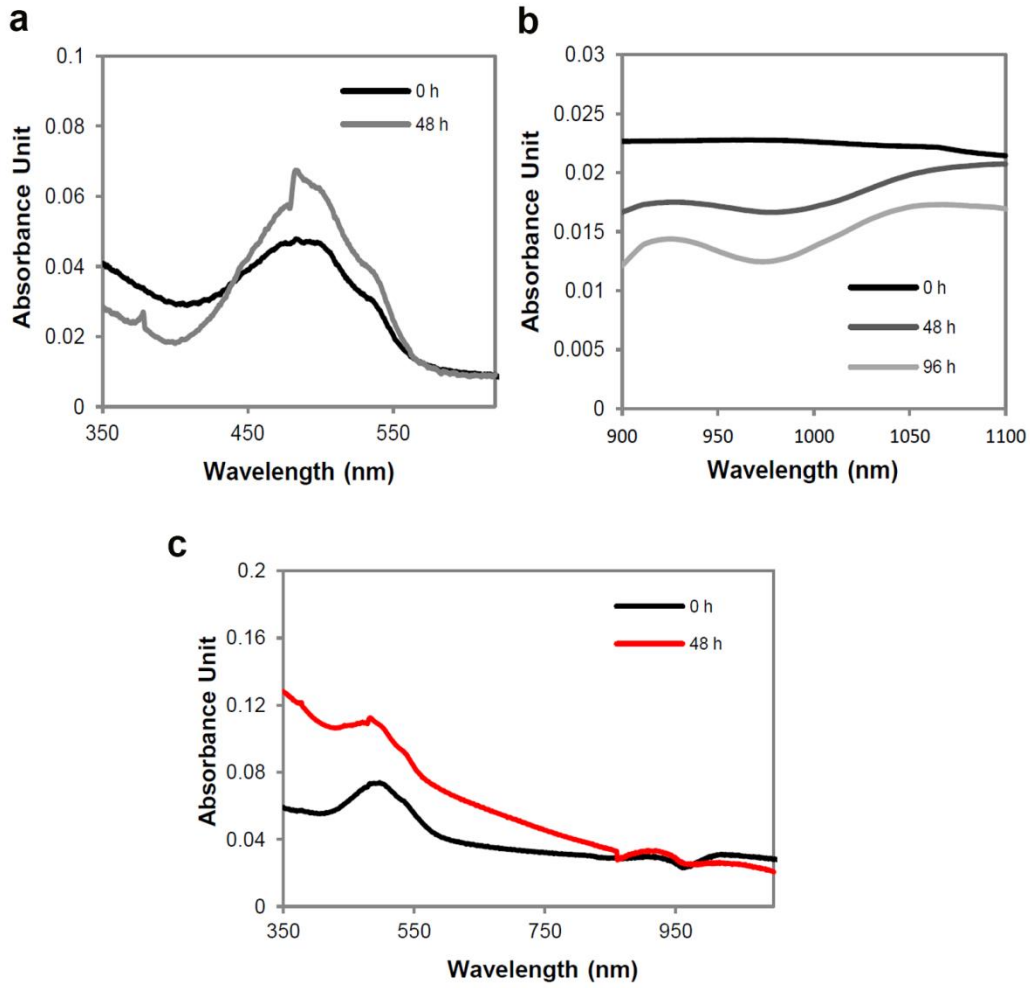

Figure 3.15 Peroxynitrite-mediated degradation of free DOX (UV-Vis-NIR). (a) Degradation of free DOX after 48 h (UV-Vis-NIR). Absorption increased at 480 nm probably due to the formation of a degradation product with the same absorption properties. (b) NIR absorption spectra of PL-PEG/ox-SWCNT and (c) UV-Vis-NIR absorption spectra of DOX-SWCNT. The spectra were normalized at 862 nm.[173]

3.6.5 Characterization of drug release

3.6.5.1 *Ex vivo* pH-dependent DOX released from SWCNT

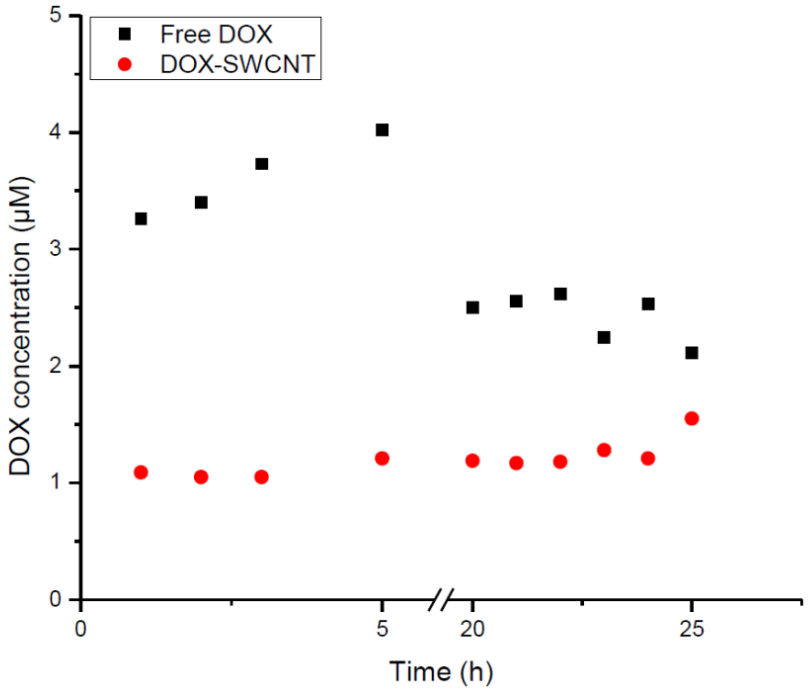

Figure 3.16 MDSC were incubated in the medium containing 5 μM solutions of free DOX and DOX-SWCNT (with 100% drug loading). After 25 h, each supernatant of the drug-incubated cell medium was collected by centrifugation (10,000 g, 15 min), and the concentration of free DOX was estimated by measuring fluorescence emission intensity at 590 nm ($\lambda_{excitation}$=488 nm) using standard calibration fit.[173]

3.6.5.2 DOX released in cell medium

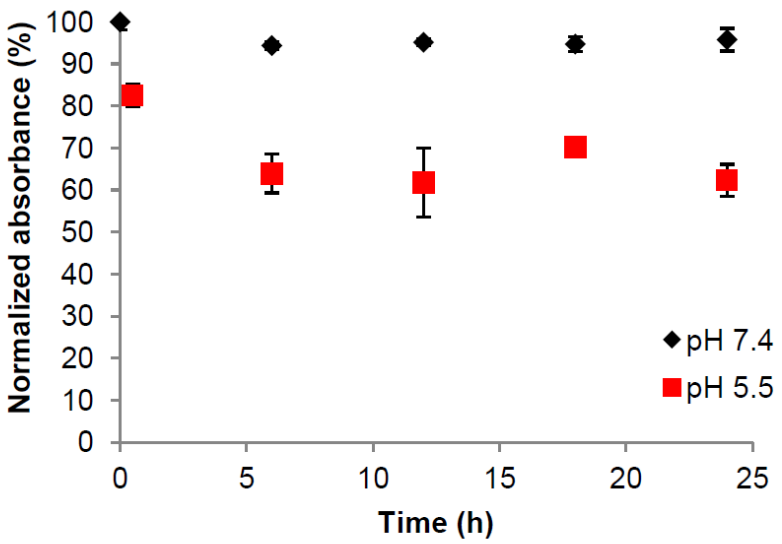

Figure 3.17 The same concentration of DOX-SWCNT (with 100% drug loading) used in the degradation experiment was prepared in phosphate buffer (0.1 M, pH 7.4) and acetate buffer (0.1 M, pH 5.5) over 24 h, respectively. The free DOX released from the nanotube carrier was collected by filtration through a 10kD Amicon centrifugal filter (11,000 rpm, 10 min), and the concentration of free DOX was measured using UV-Vis at 480 nm. The error bars indicate the means ± SD of three replicate measurements.173

3.6.6 MDSC abrogated cytotoxic/cytostatic effect of free DOX, but not DOX-SWCNT, on 3LL cells in vitro

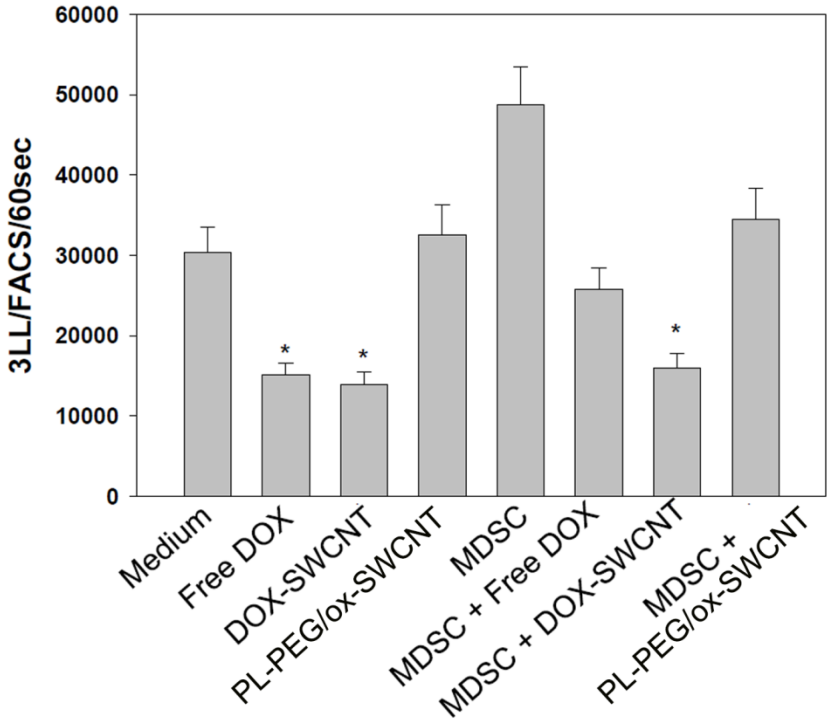

Figure 3.18 3LL lung carcinoma cells and bone marrow-derived tumor-activated MDSC were generated and cultured as described in M&M. Cells were co-cultured for 24 h in the presence of soluble free DOX or DOX-SWCNT alone or together. PL-PEG/ox-SWCNT and MDSC+ PL-PEG/ox-SWCNT served as controls. The number of tumor cells was determined by assessing flow cytometry events for 60 sec as described in M&M. All cell cultures were set in triplicates and results are shown as the mean SEM (N=2). *, $p<0.01$ versus control (medium) group (One way ANOVA).[173]

4.0 SYNTHESIS AND CHARACTERIZATION OF TWO-DIMENSIONAL SUPRAMOLECULAR POLYMERS

4.1 CHAPTER PREFACE

This study is described in a manuscript entitled *Polybenzobisimidazole-Derived Two-Dimensional Supramolecular Polymer*, which was submitted for publication. Additionally, a short application study of a surface catalyst for Fenton-like oxidation is described. W. Seo thanks Damodaran Krishnan Achary for ^{13}C CP MAS solid-state NMR analysis and Keith A. Werling and Professor Daniel S. Lambrecht Department of Chemistry at the University of Pittsburgh for computational modeling. W. Seo synthesized and characterized the supramolecular polymer. Philip M. Fournier performed SEM analysis; James A. Gaugler and Keith L. Carpenter assisted in preparation of monomers.

4.2 INTRODUCTION

Chapter 4 describes the design and synthesis of a novel two-dimensional polymer (2DP). Envisioning realization of a 2D semiconducting and chemical sensing material for field effect transistor (FET) devices, we designed a novel covalent organic framework COF-Salophen consisting of multiple salophen macrocycles (Figure 4.1). This covalent organic framework (COF) can be synthesized by condensation of aromatic monomers bearing aldehyde and amine functional groups,[214,215] which provides an imine linker connecting salophen units and pores of two different sizes. The salophen ligands can serve as a sensing moiety for the detection of Co(II) ions,[216] and the extended π–conjugated system imparts planarity and rigidity, thereby providing semiconducting properties to the polymer.[217] The high surface-to-volume ratio of 2D COFs allows for facile electron transfer due to the excellent surface contact with FET chips.[218] However, an initial effort for direct condensation of **1** and commercially available 1,2,4,5-benzenetetramine tetrahydrochloride, the precursor of **2**, in the presence of *N*,*N*-diisopropylethylamine failed to provide COF-Salophen. We also attempted to neutralize 1,2,4,5-benzenetetramine tetrahydrochloride before polymerization, but found that spontaneous air-oxidation of an unstable **2** provided **3** under atmospheric conditions. Despite the conversion into the diamine group of **3**, we have utilized it as a monomer for polycondensation with **1** to investigate whether the product forms a conjugated linear polymer that may possess electrical properties. Interestingly, we have found that a novel supramolecular polymer (SP-PBBI) by self-assembly of linear polybenzobisimidazole (PBBI) chains in a one-step reaction. SP-PBBI features a regular arrangement of rigid rod-like PBBI chains stabilized by intramolecular hydrogen bonding within a planar sheet. The size of SP-PBBI crystal growth can be tuned by employing a nonisothermal condition in the precipitation polymerization process.

Liquid-phase exfoliation of as-synthesized, bulk SP-PBBI that is insoluble in most organic solvents provides thin layers of the polymer 2DSP-PBBI (thickness of <20 nm). The surface morphology of the polymer is analyzed with liquid-exfoliated samples, based on which the supramolecular polymerization of PBBI building units is elucidated. Titration with cobalt chloride ($CoCl_2$) using UV-Vis spectroscopy confirms the presence of bidentate NO pendant ligands coordinating with Co(II) and Cu(II). The Cu(II)/2DSP-PBBI complex is further utilized for catalyzing oxidation of highly ordered pyrolytic graphite (HOPG) by a Fenton-like process. The resulting defect formation is analyzed with Raman spectroscopy data and AFM micrographs of the oxidized HOPG surface.

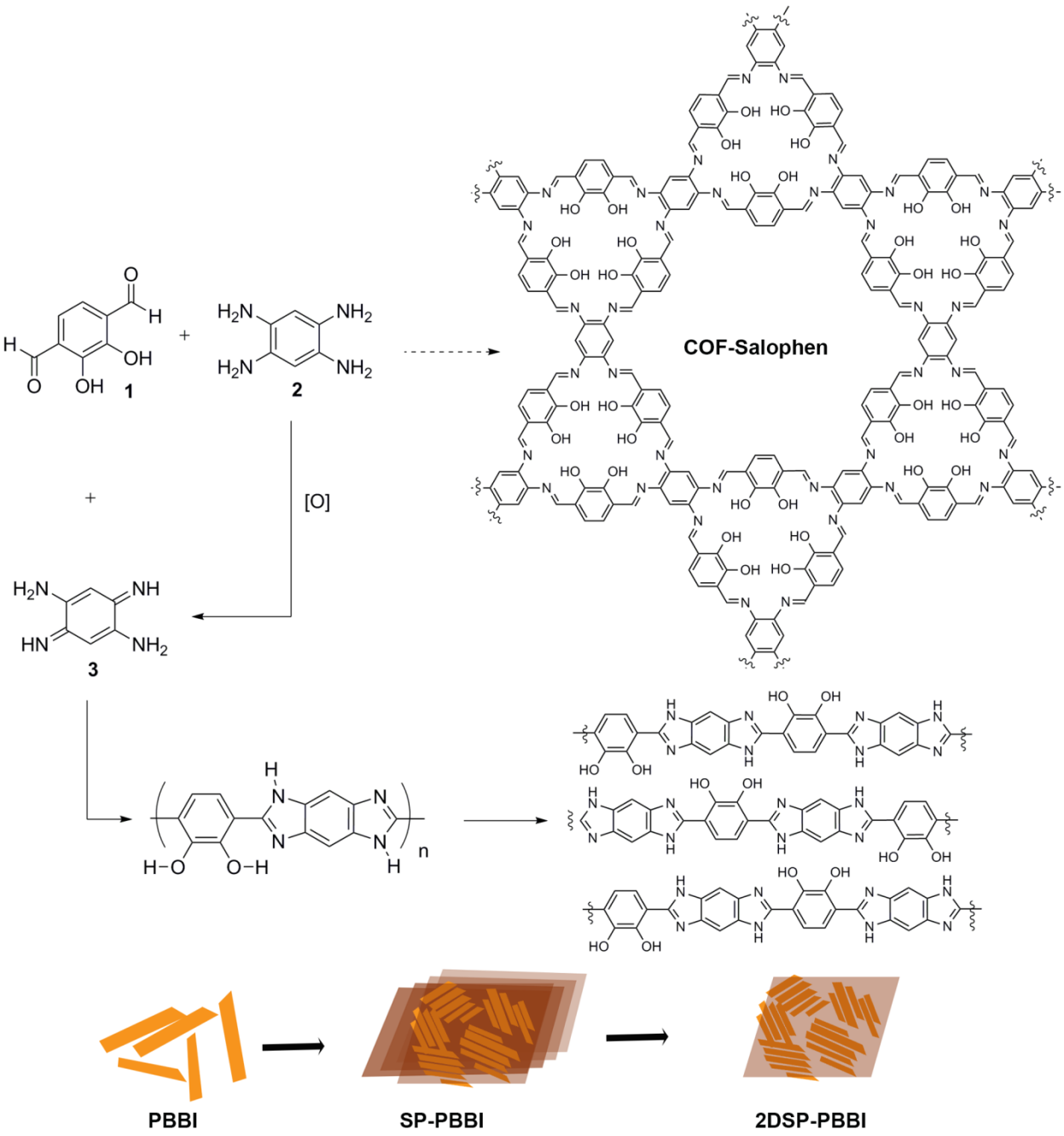

Figure 4.1 Scheme of COF-Salophen and 2DSP-PBBI. Attempted synthesis of COF-Salophen yields a supramolecular polymer of polybenzobisimidazole (SP-PBBI) consisting of multiple polycrystalline domains, and exfoliation of the bulk SP-PBBI affords a two-dimensional supramolecular polymer (2DSP-PBBI).

4.2.1 Two-dimensional polymers

The importance of two-dimensional graphene-like materials such as 2D polymers (2DPs), hexagonal boron nitride, organic/inorganic hybrids and hierarchically ordered various van der Waals heterostructures is rapidly recognized.[219-224] The development of 2D materials will allow for exploration of novel properties that can greatly enhance the performance of materials and nanodevices.[220] However, the synthesis of 2D materials, whether by top-down or bottom-up approaches, requires high precision at the atomic scale to achieve fine-tuned properties.[219,225] 2D materials processing has often encountered a great deal of difficulty translating benchtop research into scalable production.[226]

A large number of 2DPs have been studied as a new class of emerging materials for the last half a decade.[219,227,229] The current and future applications of 2DPs include FETs, supercapacitors,[228] photovoltaic cells,[215,229] surface catalysts,[230] and colorimetric sensing[231]. 2DPs can be constructed by connecting building units covalently (e.g., COFs) or noncovalently (e.g., SPs).[58,219,227,232] Supramolecular polymers are formed based on geometric preorganization generated by noncovalent intermolecular forces existing in the building unit, such as hydrogen bonding, π–π stacking, and metal–ligand complexation.[233-236] Supramolecular systems provide convenient synthetic routes to build complex macromolecular frameworks.[233] The intrinsically dynamic nature is suitable for recyclable, degradable, stimulus-responsive, sensing, and self-healing materials.[235] However, reversible noncovalent interactions in supramolecular systems could inadvertently be disrupted depending on the external environment and the entire polymer can disintegrate.[237] Metallosupramolecular polymers (MSP) complement properties most organic macromolecules lack intrinsically. A diverse range of metal ions offers great applications to optoelectronics, sensing, nanopatterning, and macromolecular catalysts.[235-236]

The properties of metal–polymer complexes can be tuned by employing different metal ions/ligands and altering the metal binding site (e.g., in the polymer backbone or in the pendant group).[236]

Although boronate-based COFs exhibited issues of hydrolysis at ambient conditions, COFs have been conceived as a stable alternative to SPs because all building units are secured by covalent bonds.[79] Most COFs have been successfully prepared as polycrystalline materials using a few different monomers.[238] Because as-synthesized COFs are obtained as bulk powders,[239] liquid-exfoliation is required in applications to thin films.[231] However, poor solubility impedes the solution-based fabrication of COFs, which is a major obstacle to real world applications.[231] The solubility issue also complicates characterization because most instrumental methods require macromolecule samples dispersed in solution. Thus unconventional techniques are utilized in determination of size, such as imaging analysis (e.g., AFM, SEM, and TEM) instead of gel permeation chromatography (GPC) and MALDI.[218,219] The optical properties of exfoliated 2DP samples may not be the same as bulk samples, and different numbers of 2DP layers may change electronic transition in optical absorption spectroscopy.[240]

4.2.2 Synthetic approaches for two-dimensional polymers

Due to difficulties synthesizing well-ordered polymers on a large lateral scale (up to the size of 1 m^2), only a few methods have been available for synthesizing 2DPs.[241] The most common approach is thermodynamically controlled polymerization under reversible reaction conditions.[227,239] The polymerization continues until insoluble polymers form precipitates. Slow polycondensation under solvothermal conditions, which proceeds at high temperature, typically

>100 °C, has been a standard procedure for COF synthesis.[239] The continuous bond formation–cleavage under equilibrium allows an error-correction mechanism while slowly driving the reaction to completion by removing water.[242-243] Yaghi and coworkers hypothesized that a sparingly soluble monomer in the reaction solvent could control the diffusion of the building blocks and facilitate crystallite formation in the course of the condensation while sustaining the reversible reaction promoted by H_2O in a completely sealed vessel at 120 °C.[244] Although the nucleation process of COF crystallites has not been fully understood, most COFs have been synthesized under similar solvothermal conditions for 3–7 d, mostly at 120 °C with a few exceptions.[241]

A similar synthetic approach is found in supramolecular polymerization. Many examples of SPs have characteristics similar to step growth polymerization which usually yields polymers with high polydispersity indices.[235] Two major growth mechanisms of supramolecular polymerization are (1) isodesmic and (2) cooperative growth (Figure 4.2a), analogous to kinetically and thermodynamically controlled reaction pathways (Figure 4.2b).[235,245] Isodesmic polymerization maintains the same reactive site at the end of polymer chain and the polymer grows as monomers add to the reactive site.[237] The polymerization of cooperative model initially proceeds isodesmically (nucleation, binding constant K_n), and then undergoes another isodesmic process with a different binding constant (elongation, binding constant K_e).[245] The cooperative effect arises from the binding constant K_e, higher than K_n.[237]

To control the shape, size, and stability of SPs, new strategies for controllable supramolecular polymerization have been introduced.[235] One of them is living supramolecular polymerization which lowers the energy barrier of the initiation step and promotes chain growth-like polymerization in the nucleation–elongation process.[235] Sugiyasu and Takeuchi et al.

demonstrated an intricate reversible reaction pathway that converts kinetically formed porphyrin-based aggregates into thermodynamically formed SP chains above the critical temperature, providing a narrow polydispersity index of 1.1.[245]

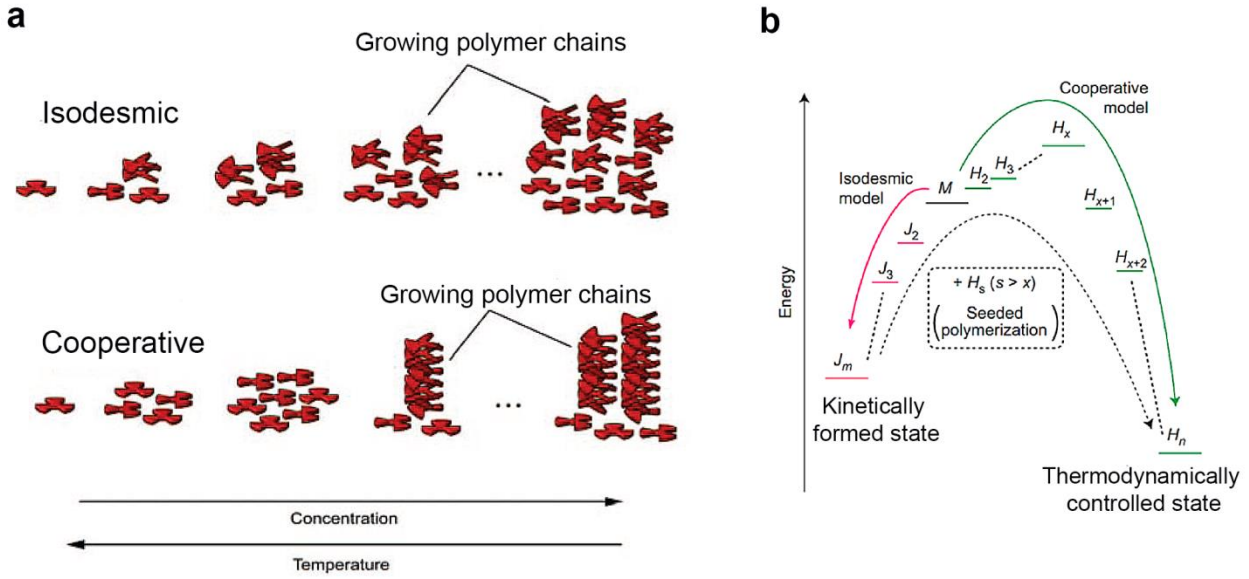

Figure 4.2 Mechanistic models of supramolecular polymerization. (a) Illustration of two growth mechanisms, isodesmic and cooperative supramolecular polymerizations. (b) Energy pathways determined in supramolecular polymerization of a porphyrin-based monomer.[235]

4.2.3 Polybenzimidazole-based polymers

Polybenzimidazoles (PBI) are aromatic heterocyclic high-performance polymers commercially used as heat-resistant materials.[246] PBI can be synthesized with condensation of an amine and a carbonyl group (e.g., carboxylic acid,[247] ester,[248] or aldehyde[249]). Polymerization occurs at high temperatures (100–350 °C) and a by-product such as H_2O or ROH is driven out of the system during the reaction.[246] The aromaticity and planar conformation of molecular chains impart

thermal stability, mechanical strength, and chemical resistance to the polymer.[250] The rigid rod structure of crystalline PBI decomposes only with strong acids.[250] Some PBI-based polymers bearing hydroxyl groups on the benzene ring can promote intramolecular hydrogen bonding of OH···N=C on the backbone, reinforcing the rigidity of PBI chain.[251] Most commercial PBIs were successfully fabricated into spun fibers, but other shapes such as ribbon- and needle-like crystals were observed when prepared with different reaction solvents.[250] Fiber XRD analysis of poly(pyridobisimidazole) (PIPD), a PBBI analogue with good mechanical strength (Figure 4.3), showed that PIPD could possess two possible crystal structures.[252-253] The triclinic structure was preferred based on the ab initio total energy and molecular dynamics calculations, featuring a sheet-like structure.[252] However, studies of PBI-based polymers have reported neither a two-dimensional morphology nor supramolecular polymerization of PBI.[253-255]

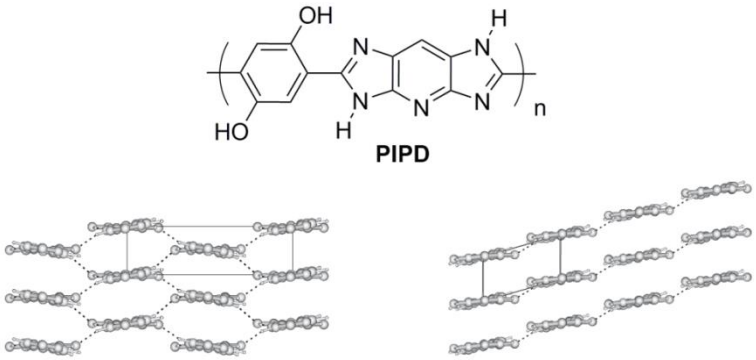

Figure 4.3 Monoclinic (left) and triclinic (right) structures of PIPD. Hydrogen bonds are indicated as dashed lines.[252]

4.3 EXPERIMENTAL

4.3.1 Synthesis of SP-PBBI and 2DSP-PBBI

Monomers **1** and **3** were synthesized as described in Ch. 4.6 Supporting Information. A solution of **1** (6.0 mg, 0.04 mmol) and **3** (3.3 mg, 0.02 mmol) in *N*,*N*-dimethylformamide (1 mL) was prepared in a 25 mL round bottom flask. The solution of the monomers was degassed by two freeze–pump–thaw cycles and was sealed with a septum and PTFE tape. After sonication for 5 min, the reaction mixture was kept at 95 °C (for 2 d) in an oil bath without stirring at 100 °C for 1 d. After raising the temperature to 145°C, the reaction was left undisturbed for 3 d. After total 6 d, the reaction flask was cooled to room temperature for 2 h, and the crude polymer was washed with dichloromethane (4 × 15 mL) and methanol (4 × 15 mL) over a Millipore filter and a 200 nm fluorophore filter membrane. After drying *in vacuo* for 48 h over 100 °C, 2DSP–PBBI was obtained as a dark brown solid (89 %). ^{13}C CP MAS solid-state NMR (15 kHz) δ ppm, 198.6, 150.0, 147.0, 138.2, 129.9, 121.3, 119.0, 116.5, 99.0. IR (KBr, ATR) 3327, 1641, 1440, 1394, 1302, 1152, 839 cm^{-1}.

Exfoliation was performed in a 100 mL round bottom flask containing dry SP-PBBI (2.0 mg) and anhydrous DMF (12 mL) with gentle stirring for 24 h at 60 °C.

4.3.2 Instrumentation

Fourier transform infrared spectroscopy (FTIR) was performed using an IR-Prestige spectrophotometer (Shimadzu Scientific) outfitted with an EasiDiff accessory (Pike

Technologies). Solid samples were ground with KBr to prepare a homogenous mixture. ^{13}C CP MAS spectroscopy was performed on a Bruker Avance spectrometer (500 MHz). Powder X-ray diffraction (PXRD) was recorded on a Bruker X8 Prospector Ultra equipped with a Bruker Smart Apex CCD diffractometer and a copper micro-focus X-ray source employing Cu Kα radiation at 40 kV, 40 mA. A ground sample was loaded in a capillary tube (D: 1 mm) for analysis. The size and the morphology of materials were analyzed with transmission electron microscope (FEI-Morgani, 80 keV). TEM samples were prepared by drop-casting 3.5 µL of a sample onto a lacey carbon films/400 mesh copper grid and dried under ambient conditions over 24 h. An Asylum MFP-3D atomic force microscope (AFM) was utilized with high resolution probes (Hi'Res-C14/Cr-Au) purchased from MikroMasch. AFM samples were prepared by deposition of 10 µL of an exfoliated solution onto freshly cleaved mica. The sample was spin coated and then allowed to dry under ambient conditions over 24 h. UV-Vis-NIR spectra were acquired using a Lambda 900 spectrophotometer (PerkinElmer). Scanning Electron Microscopy (SEM) was performed with FEI XL-30 (20 keV). The computational molecular structure optimizations were performed at the B3LYP/6-31g(d) level with Q-Chem software packages.[256-257] A fine integration grid and stricter self-consistent-field and integral thresholds were utilized.

4.3.3 Titration of metal–polybenzobisimidazole complexation

A supernatant containing relatively well-suspended polymer flakes was collected from the exfoliated solution of 2DSP-PBBI for the spectroscopy measurements. A 5.3 mM $CoCl_2$ solution was prepared in DMF, and 5 µL was delivered to an exfoliated polymer solution (600 µL) for each titration at ambient conditions. The optical change of 2DSP-PBBI solution was

measured using UV-Vis absorption spectroscopy immediately after each addition of $CoCl_2$. The exfoliated 2DSP-PBBI solution was also titrated with $CuSO_4$ using the same protocol. A Cu(II) solution (2.0 mM) was prepared with $CuSO_4 \cdot 5H_2O$ and DMF for serial addition of 30 μL to an exfoliated 2DSP-PBBI solution (625 μL). An estimated weight of the polymer in 625 μL was about 36 μg.

4.3.4 Fabrication of porous graphene by Fenton-like oxidation

HOPG flakes (0.5 mm × 0.5 mm) were mechanically cleaved with a razor. The surface was mechanically exfoliated with cellophane tape to smoothen the HOPG surface. Each flake was cleaned with CH_2Cl_2, acetone, DI water, and acetone sequentially. The flake was dried over a hot plate at 50 °C for 24 h. An exfoliated 2DSP–PBBI solution (625 uL) in DMF was gently mixed with Cu(II) (2 mM, 390 μL) at room temperature based on the titration experiment data. The cleaned HOPG flakes were placed on a glass slide and the aliquot of Cu(II)/2DSP–PBBI solution was drop-cast on the HOPG flake (20 μL). After 6 h, the solution was applied to the other side of HOPG flakes and the samples were allowed to dry for 12 h at 50 °C.

A polymer-deposited HOPG flake was placed in a 1 dram vial containing 0.2 mL of acetonitrile or a mixture of acetonitrile: pH 5.0 buffer (1:1, v/v). A 20 μL of H_2O_2 solution 30% (w/w) was added, followed by gentle shaking for 30 sec, and the capped vial was placed in a sand bath at 65 °C. The same amount of H_2O_2 solution was replenished at every 6 h (20 μL per addition). For UV-activated photo-Fenton reactions, a quartz cuvette (3.5 mm × 12.5 mm × 45 mm) was used to store the HOPG sample in the biphasic solution at room temperature and was

held ~20 cm from a UV lamp (Blak-Ray B100AP, 100-W long wave UV, which produces fluorescence with a ballasted bulb).

4.4 RESULTS AND DISCUSSION

4.4.1 Characterization of SP-PBBI

In an attempt to perform imine condensation under neutral conditions, 1,2,4,5-benzenetetramine tetrahydrochloride was treated under a basic condition in air prior to polymerization. However, rapid conversion of **2** to **3** led to polycondensation of 2,3-dihydroxybenzene-1,4-dicarbaldehyde **1** and 3,6-diimino-1,4-cyclohexadiene-1,4-diamine **3** in *N*,*N*-dimethylformamide (DMF) at 95–145 °C. An aprotic polar solvent DMF was employed to completely solubilize both **1** and **3**, thereby initiating precipitate polymerization in a homogenous solution. DMF may also have facilitated π–π stacking due to the enhanced solvophobic effect and self-assembled macromolecular structures.[258-259] Condensation of **1** and **3** allowed formation of two imine bonds and subsequent cyclization to a benzobisimidazole (PBBI) moiety. To confirm the formation of benzobisimidazole from the diamino diene **3**, a model compound **4** was prepared with salicylaldehyde and **3** under the same nonisothermal condition (Figure 4.10 and 4.12c–e). The reaction afforded a brown powder of as-synthesized SP-PBBI in 89% yield, exhibiting insolubility in water and most common organic solvents at room temperature. The sufficiently long reaction time (total 6 d) was crucial to high polymer conversions whereas reactions performed less than 3 d formed the precipitated product in much lower conversions.

The FTIR spectrum (Figure 4.4a) of SP-PBBI confirms the formation of an imine (C=N) stretching at 1641 cm^{-1} in the polymer sample while peaks characteristic to the monomers such as the aldehyde C–H stretching (2866 and 2769 cm^{-1}) of **1** and primary amine N–H stretching (3444 and 3417 cm^{-1}) of **3** are clearly absent (Figure 4.11b–c). The relatively high frequency of an imine stretching can be observed due to the highly rigid conformation arising from the cyclic

imine of benzobisimidazole and a strong intramolecular hydrogen bond occurring between the hydroxyl hydrogen and the imino nitrogen (OH···N=C)[260-262] although a different hydrogen bonding motif (HO···H–N) was proposed in addition to the former by x-ray crystal structure analysis of PIPD.[251,253] The distinct O–H stretching peak at 3321 cm^{-1} can be used as a marker for predicting the crystallinity of the polymer. Also, the shift in O–H stretching by about 40 cm^{-1} from the monomer **1** and a higher intensity suggest that a strong intramolecular hydrogen bond is present.[260] When a less crystalline polymer sample was analyzed, only a broad O–H stretching was observed in the region between 3100 and 3400 cm^{-1} (Figure 4.11d). The structure of the polymer was further confirmed by ^{13}C cross-polarization magic-angle spinning (CP MAS) solid-state nuclear magnetic resonance (NMR) spectrum (Figure 4.4b). The characteristic phenolic (C_1) and cyclic imino (C_2) carbons resonate at δ = 150.0 and 147.0 ppm respectively, and the resonance at δ = 129.2 ppm was attributed to C_3 connecting the benzobisimidazole moiety.[261-262] In the case of the less crystalline polymer sample, a weak resonance of downfield carbon was present at δ = 175.6 ppm, most likely a carbonyl carbon (C=O) resulting from the keto–enamine tautomerization (Figure 4.12a).

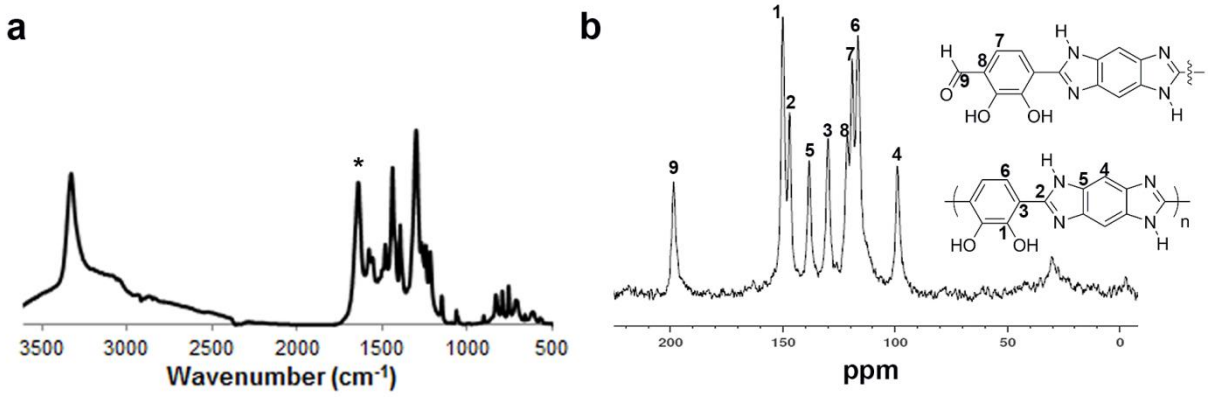

Figure 4.4 Characterization of SP-PBBI using (a) FTIR and (b) ^{13}C CP MAS solid state NMR.

To support the evidence of a periodic structure with well-defined crystalline parameters, powder X-ray diffraction (PXRD) was implemented. As shown in the experimental PXRD spectrum (Figure 4.5a), d spacing values corresponding to the well-defined peaks were found (16.67, 8.43, 6.33, 5.86, and 3.31 Å), based on which a two-dimensional unit cell model (*a* and *b* axes) was proposed (Figure 4.5b). To construct a periodic alignment of the PBBI chains, we referred to the structural analyses of PIPD that is very similar to PBBI except for the position of one hydroxyl group and the pyridine moiety.[251-253] Based on the bond lengths and unit cell (either monoclinic or triclinic) data of PIPD provided by two different groups, we indexed a = 16.67 Å and b = 6.63 Å for SP–PBBI parameters (Figure 4.5b). These lattice parameters are very different from those of the COF-Salophen estimated at the B3LYP/6-31g(d) level (Figure 4.5c). We reason that the interlayer spacing (*c* axis) is 3.31 Å (Figure 4.5d), which is within van der Waals contact distances arising from the π–π stacking of aromatic rings and comparable to previously synthesized arene-based polymers.[263] Due to limited structural information gleaned from the powder diffraction data, the analysis of angles between unit cell parameters was not proposed.[253] Thermogravimetric analysis (TGA) showed a weight loss of 10% around 330 °C and a slow decomposition of 20% up to approximately 400 °C (Figure 4.14).

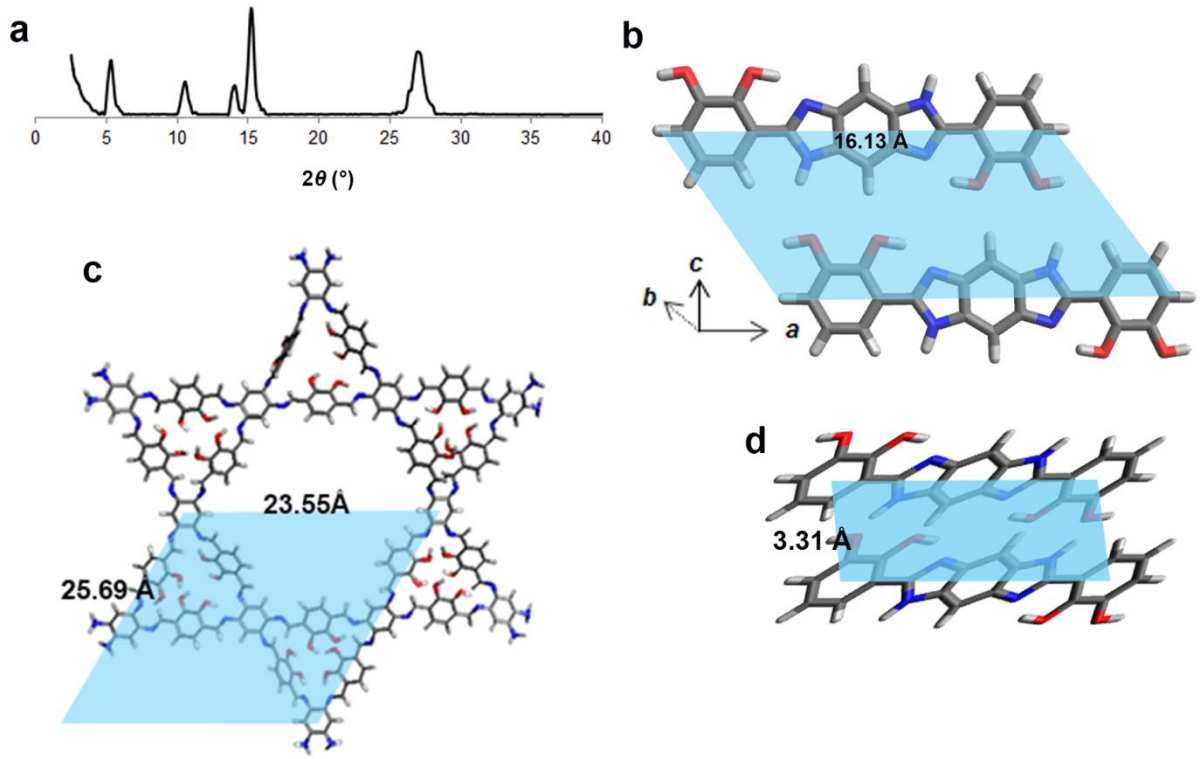

Figure 4.5 Characterization of SP-PBBI. (a) Experimental PXRD spectra. (b) Proposed two-dimensional structures (*ab* plane) and optimization of the unit cell parameters calculated by B3LYP/6-31g(d) level (*a* = 16.13 Å) for SP-PBBI, which is close to 16.67 Å of an experimental PXRD d spacing value. (c) Unit cell parameters (*a* = 23.55 Å, b = 25.69 Å) of COF-Salophen. (d) Stacking distance (*c* = 3.31 Å) between the layers of SP-PBBI obtained from PXRD.

4.4.2 Surface morphology of 2DSP-PBBI

The morphology and the size of 2DSP-PBBI were investigated using TEM and noncontact-mode AFM shown in Figure 4.6a–e. Both bulk SP-PBBI and exfoliated 2DSP-PBBI samples exhibit a planar morphology consisting of mostly stacked platelets (Figure 4.6a). We confirmed the supramolecular polymerization process with SP-PBBI samples that were sonicated or manually

ground from 5 to 30 min in MeOH. It appears that large planar sheets were disintegrated into small rods under the mechanical forces, probably due to weakened intermolecular bonds (Figure 4.15a). The planar configuration and rigidity arise from the individual PBBI chain capable of arranging in a quasi-aromatic six-membered chelate ring induced by intramolecular hydrogen bonding between the imino nitrogen and the *o*-hydroxyl group enolimine (OH···N=C).[251,254,264] Once linear PBBI backbones are formed and ready for self-preorganization, the secondary amine (NH), the imine (N=C), and 1,2-dihydroxyphenyl (OH) groups of PBBI provide intermolecular hydrogen bonding motifs for promoting self-assembly and the resulting formation of SP. Each 2DSP-PBBI layer consists of multiple crystallites aligned in various orientations, as indicated in the presence of moiré fringes shown in two different directions (Figure 4.6b).[265] A 100 nm-lateral resolution AFM image also confirms the polycrystalline grain boundaries (Figure 4.6e). 2DSP-PBBI also vertically grows into a 3D bulk (i.e., the formation of SP-PBBI), mainly driven by π–π stacking existing between the aromatic PBBI backbones. Thus most as-synthesized samples were multiple stacks strongly held by each 2DSP-PBBI layer and poorly soluble in any solvents at room temperature. However, we were successfully able to exfoliate bulk SP-PBBI in DMF at 60 °C. After 2 h-exfoliation, mostly small molecular weight and amorphous-like flakes were visible under TEM, but larger flakes were slowly delaminated into thin layers (<30 layers) within 4–6 d (Figure 4.6c and 4.15c). The height distribution of exfoliated layers analyzed by AFM ranges from 0.4 to 8.6 nm, equivalent to ca. 1–25 layers of the polymer in the sample (Figure 4.6d and e).

Large polymer sheets up to 0.1–10 μm in lateral dimension were observed under both TEM (Figure 4.6a and 4.15b) and AFM (Figure 4.16a). Given that cooperative supramolecular polymerization is based on the two-step mechanism of (1) nucleation and (2) elongation,[235] the

formation of the large SP-PBBI seems reasonable. The size of as-synthesized SP-PBBI was dependent on temperature control. We tested it by initiating the reaction at 95 °C and completing it at 145 °C. The SP-PBBI crystals grew in larger sheets if the temperature was gradually raised in multiple stages. Precipitation polymerization involves monomers that are initially soluble in the reaction solvent, and the locus of polymerization remains in a homogeneous solution until the growing macromolecular network reaches the critical molecular weight for precipitation.[266] We reason that slow diffusion of building blocks and formation of dynamic intermolecular bonds under the gradual increments of temperature (95–145 °C) would furnish slow nucleation and growth of structurally well-defined, large polymer crystallites (ca. >1 μm) over an extended period of time. Notably, the growth rate of polymer layer postulated from the morphology of 2DSP-PBBI suggests that cooperative interchain hydrogen bonding was more effective in the elongation of polymer sheet than the interlayer π–π stacking under the given reaction condition (i.e., $rate_{ab–axis} >> rate_{c–axis}$). To further verify the temperature effect, a different reaction batch was stored at a constant temperature of 145 °C throughout the entire polymerization. Interestingly, the isothermal condition resulted in the same PXRD pattern as that of the nonisothermally treated sample, but yielded much smaller and more monodisperse polymer flakes (Figure 4.7a). To see the effect of temperature and solvent in supramolecular polymerization, we attempted a higher temperature increment (T_1 = 95 °C, T_2 = 170 °C) in a mixture of dimethylsulfoxide/mesitylene (10:1) for 6 d. The reaction yielded a significantly different crystalline polymer PBBI-170 (see FTIR, ^{13}C CP MAS solid-state NMR, and PXRD in Figure 4.11e, 4.12b, and 4.13, respectively). PBBI-170 was hardly exfoliated in most organic solvents even after 7 d, and only small rod fragments were isolated, probably delaminated at the early stage of exfoliation (Figure 4.7b).

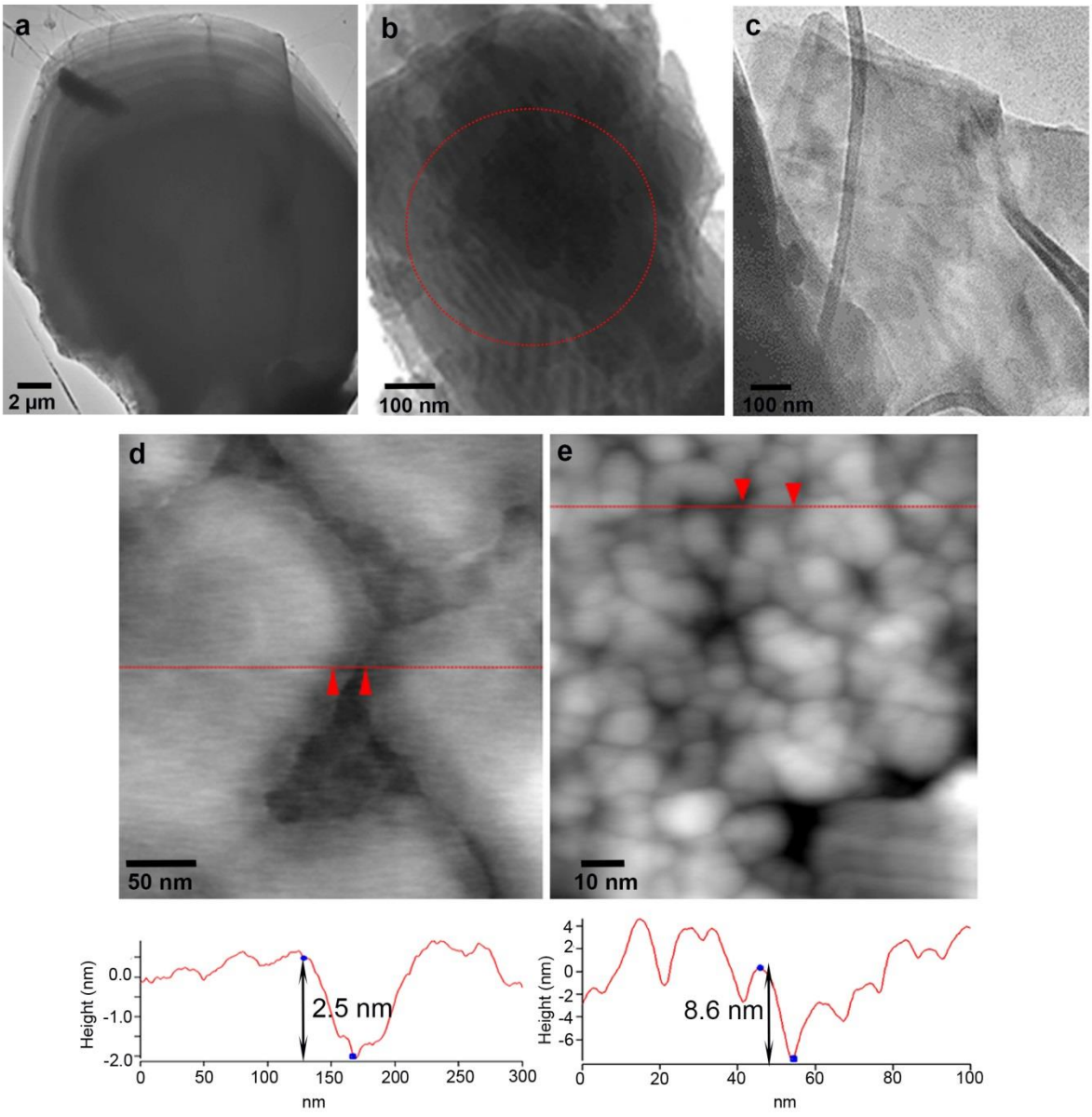

Figure 4.6 TEM (a–c) and AFM (d, e) micrographs of 2DSP-PBBI. (a) A large flake 2DSP-PBBI showing the stacked edges seen through multiple layers (1 d-exfoliation). (b) Moiré fringes marked in the red circle is indicative of high crystallinity. (c) 4 d-exfoliation. (d) A height of 2.5 nm of exfoliated 2DSP-PBBI on mica and its height profile (below). (e) Grain boundaries of a polycrystalline sample show the height profile of 6–12 nm (below) in a 100 nm lateral dimension.

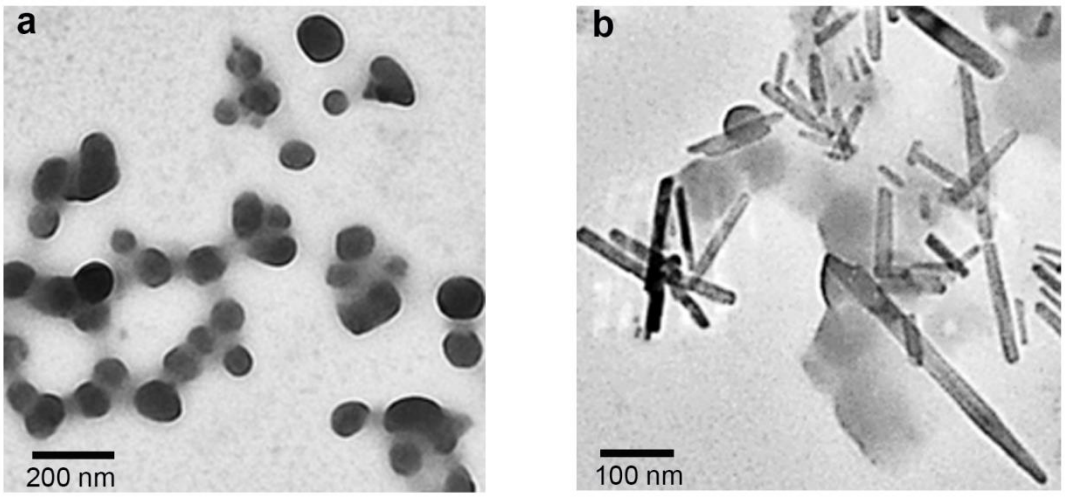

Figure 4.7 TEM micrographs of (a) PBBI-2 and (b) PBBI-170.

4.4.3 Optical properties of 2DSP-PBBI

We investigated the optical properties of the exfoliated 2DSP-PBBI using UV-Vis absorption spectroscopy. The absorption spectrum of 2DSP-PBBI exhibits a broad band with a maximum at 381 nm and minor peaks at 274 nm and at 461 nm, clearly different from the absorption bands of compound **1** and **3** (Figure 4.17). Each PBBI chain possesses bidentate pendant NO ligands, capable of forming complexation with Co(II), Cu(II), and Zn(II) ions (Figure 4.8a).[267-269] To confirm the complexation of NO–Co(II), titration of exfoliated 2DSP-PBBI in DMF was performed with cobalt(II) chloride ($CoCl_2$). Upon serial addition of a 5.2 mM $CoCl_2$ aliquot to the polymer solution, the absorbance at 381 nm progressively decreases, indicative of the metal–ligand complexation (Figure 4.8b). The titration spectra also show a successively increasing absorption band at 609 and 674 nm with the addition of Co(II). The inset of Figure 4.8b shows

the saturation point of NO–Co(II) complexation, based on which a 1.2:1 binding stoichiometry of Co(II) to the NO ligand was estimated. The $CoCl_2$ solution in DMF showed absorption bands at 609 and 674 nm, typical of pseudotetrahedral complexes of Co(II),[270] and the wavelength of these bands did not change during the titration of 2DSP-PBBI. This result indicates that ligand exchange between the NO and Cl^-/DMF occurred while maintaining the pseudotetrahedral geometry in the $CoCl_2$ solution (Figure 4.8c).[271] After titration of 2DSP-PBBI with Co(II), the polymer sample was analyzed by SEM imaging, showing that the planar sheet-like shape remained intact.

To test the realization of conjugated 2DSP-PBBI as a semiconducting material, the energy band gap was estimated from emission/excitation spectroscopy (Figure 4.18a).[272] From the excitation (at 382 nm) and emission (at 512 nm) spectra, an energy band gap of 1.08 eV was calculated, indicating that exfoliated 2DSP-PBBI is semiconducting. Having designed a semiconducting sensing material, we performed drop-casting of an exfoliated 2DSP-PBBI sample on a chip, but no significant conductance was observed in FET–IV curves (Figure 4.18b).

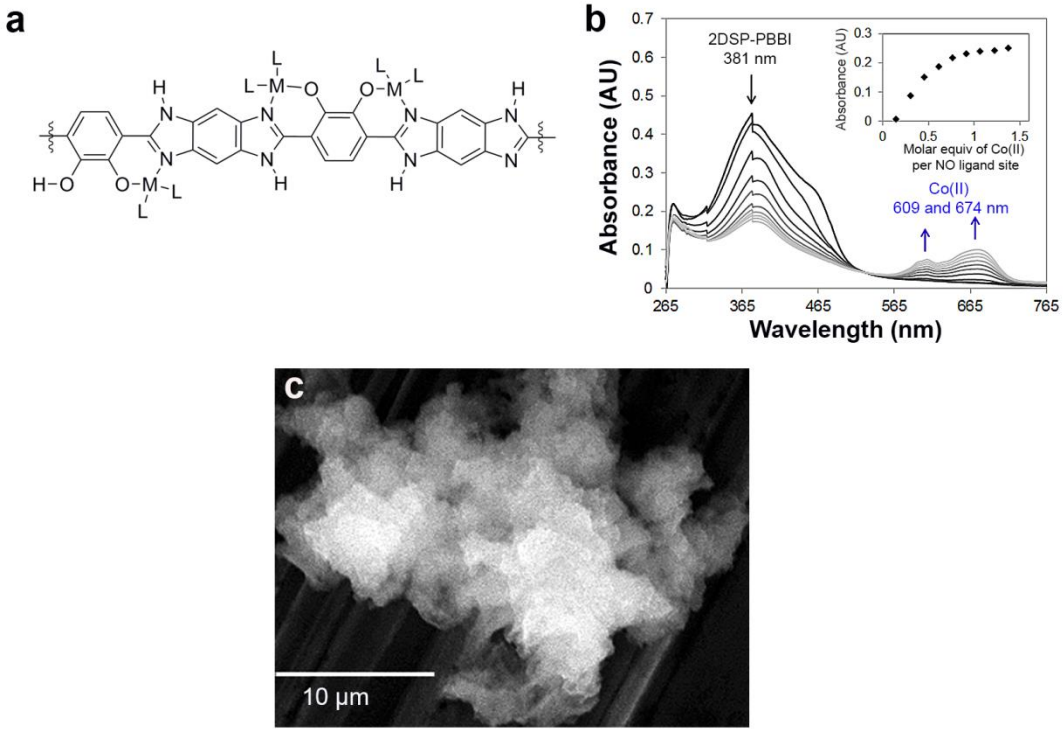

Figure 4.8 Titration of 2DSP-PBBI with Co(II). (a) Complexation between Co(II) ions and the bidentate ligands (NO) on the PBBI backbone (b) UV-Vis absorption spectra of an exfoliated 2DSP-PBBI solution in DMF upon addition of a 5.2 mM of $CoCl_2$ prepared in DMF. The arrows indicate the direction of absorbance change with increasing concentration of Co(II). Inset: Absorbance at 381 nm. Instrumental artifacts at 319 and 378 nm. (c) A sample of exfoliated 2DSP-PBBI solution titrated with $CoCl_2$ was deposited on a copper foil and dried at room temperature for SEM analysis.

4.4.4 Cu(II)-PBBI complexation and Fenton-like catalyst

A titration experiment with $CuSO_4$ confirmed the formation of Cu(II)/2DSP-PBBI complex with 2DSP-PBBI. Based on the titration result, a Fenton-like catalyst was prepared with the Cu(II)/2DSP-PBBI and the 2D metallosupramolecular polymer was employed as a surface catalyst for oxidation of highly ordered pyrolytic graphite (HOPG). Generally Fe(II)/Fe(III) has

shown better catalytic activity for Fenton or Fenton-like reactions, but titration of 2DSP-PBBI with Fe(II) or Fe(III) did not show a binding pattern between the polymer and either of iron ions.

As shown in eq.(1), the Fenton-like system activated from Cu(II) with H_2O_2 has also been demonstrated as effective as Fe(II)/Fe(III)-based systems.[127] Although reaction (1) is slower than (2), Cu(I) can generate a strong oxidant hydroxyl radical in (2); Cu(II) also directly oxidizes good reducing organic substrates, especially aromatic compounds (3).

$$Cu(II) + H_2O_2 \rightarrow Cu(I) + HO_2\bullet + H^+ \quad (1)$$

$$Cu(I) + H_2O_2 \rightarrow Cu(II) + HO\bullet + HO^- \quad (2)$$

$$Cu(II) + Ar–H \rightarrow Cu(I) + H^+ + Ar\bullet \quad (3)$$

Based on the oxidation condition optimized in a previous study using the Cu(II)/Cu(I) catalytic system,[127,129] the oxidative degradation of HOPG was studied. As the Cu(II)/Cu(I) catalyst is active in a broader pH range (4.0–7.0) compared to Fe(III)/Fe(II) (pH 2–3.5),[127] the oxidation of HOPG was performed at pH 5.0. After the Cu(II)/2DSP-PBBI catalyst was washed sequentially with base–acid and DMF/acetone, the defect density of the HOPG sample was analyzed with Raman spectroscopy. Figure 4.9a shows that the I_D/I_G ratio increases in a H_2O_2 dose-dependent manner. Also, the UV-activated photo-Fenton-like system was more effective than the sample heated at 65 °C with the same amount of H_2O_2 addition. TEM (Figure 4.9b) and AFM micrographs (Figure 4.9c–e) of the oxidized HOPG surfaces show defects in contrast to the pristine sample.

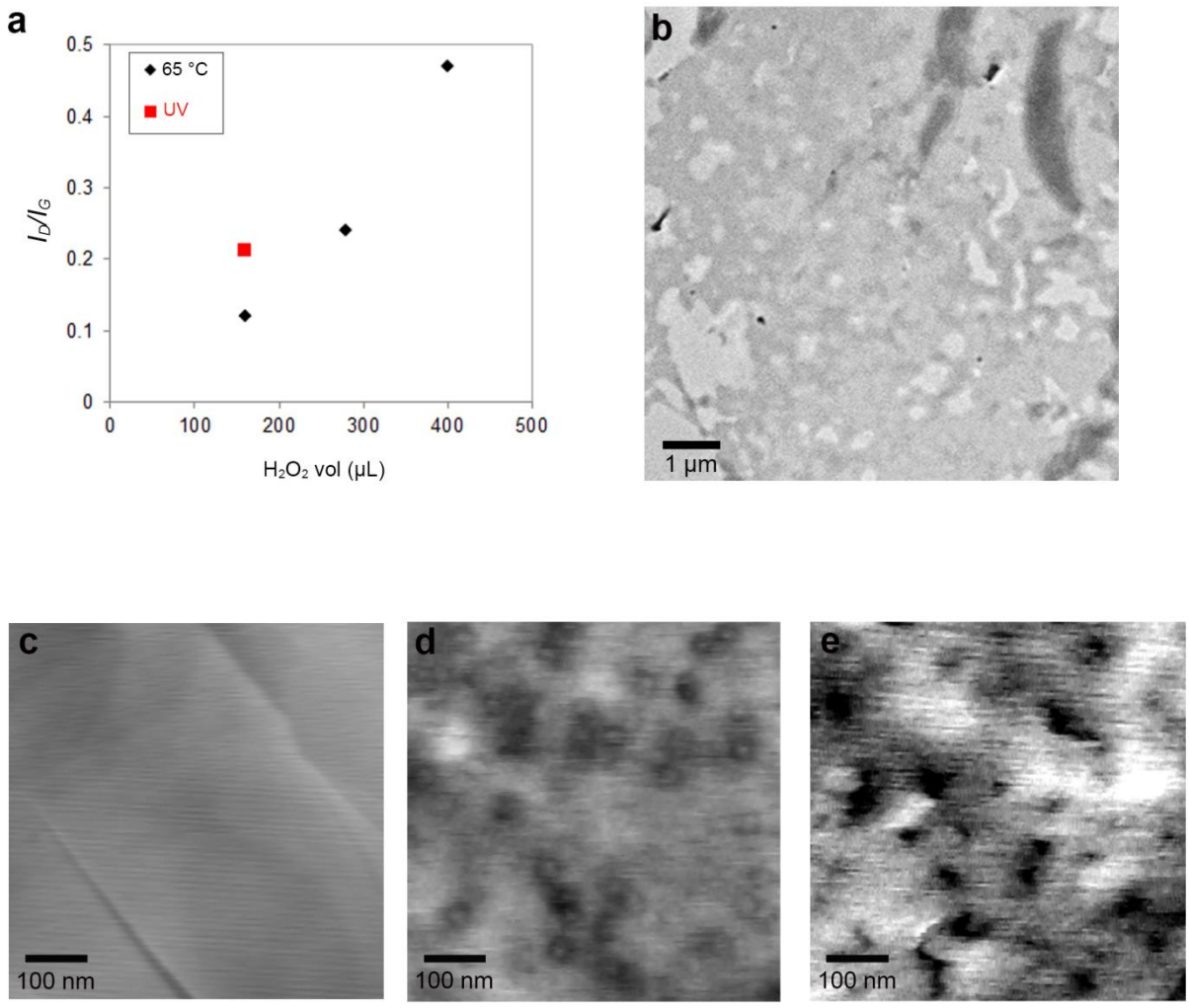

Figure 4.9 Fenton-like catalytic system of Cu(II)/Cu(I) and the oxidative degradation of HOPG using the Cu(II)/2DSP-PBBI catalyst. (a) D/G ratios by Raman spectroscopy. (b) TEM image of oxidized HOPG (total 160 µL addition of H_2O_2) under UV light. (c)–(e) AFM height micrographs of (c) pristine HOPG, (d) oxidized HOPG (total 160 µL addition of H_2O_2) at 65 °C, and (e) oxidized HOPG (total 160 µL addition of H_2O_2) under UV light.

4.5 CONCLUSION

We were able to develop a strategy for the one-step synthesis of 2DSP-PBBI by precipitation polymerization. The slow crystallite growth and precipitation under controlled conditions allowed formation of well-defined 2DSP-PBBI, and the lateral dimension of <10 μm was achieved by the nonisothermally controlled reaction temperature. PBBI building blocks were laterally grown into large self-assembled planar 2DSP sheets primarily by interchain hydrogen bonding. Also, π–π stacking facilitated formation of an orderly stacked architecture from individual 2DSP sheets. Liquid-exfoliation of the as-synthesized SP-PBBI polymer provided planar sheets of 2DSP-PBBI up to submicrometer lateral widths and nanometer heights. In addition, the complexation with Cu(II) was confirmed by the Cu(II)/2DSP-PBBI catalyst for the Fenton-like oxidation of HOPG. Despite some concerns regarding the susceptibility to mechanical forces, we anticipate that simple dropcast of exfoliated 2DSP-PBBI will provide convenient means for building various 2D heterostructures enabling cost-effective, scalable production.

4.6 SUPPORTING INFORMATION

4.6.1 General and instrumentation

Graphene oxide was purchased from Graphene Supermarket. All other chemicals were obtained from Sigma Aldrich and used without further purification. All reaction solvents were anhydrous reagent graded. Silica gel for column chromatography was obtained from Selecto Scientific. Thin layer chromatography was performed on Merck TLC plates pre-coated with silica gel 60 F254. Visualization of the developed plates was performed by fluorescence quenching or by ninhydrin and phosphomolybdic acid (PMA) stain.

Emission and excitation spectra were recorded on a Horiba Jobin Yvon Nanolog fluorescence spectrophotometer equipped with a 450 W Xe lamp and double excitation/emission monochromators. Scanning Electron Microscopy (SEM) and SEM-EDS was performed with JEOL JSM-6510LV/LGS and an EDS detector equipped with Oxford X-Max large area SDD detector with INCA microanalysis system, INCAEnergy. Thermogravimetric analysis (TGA) was conducted on a TGA Q500 thermal analysis system. ^{1}H NMR spectra were recorded on a Bruker (400 MHz) and were internally referenced to residual protio solvent signals (TMS) at δ 0.00 ppm (1H). ^{13}C CP MAS spectra were recorded on a Bruker Avance spectrometer (500 MHz). Data were reported as chemical shift (δ ppm) and multiplicity (s = singlet, d = doublet, t = triplet, q = quartet, qn = quintet, m = multiplet, br = broad), integration, and coupling constant (J) in Hz. Mass spectra were acquired on Q-Exactive, Thermo Scientific.

4.6.2 Synthesis

Synthesis of monomer 2,3-dihydroxybenzene-1,4-dicarbaldehyde (1). Compound **1** was prepared by the two-step synthesis based on literature procedures.[273] To improve the purity, the crude product was vigorously stirred in 15% sodium thiosulfate solution with addition of dichloromethane for 6 h. The organic layer was dried over Mg_2SO_4 and filtered, and then the solvent was dried in vacuo. Purification through silica gel flash chromatography (dichloromethane : methanol : acetic acid = 98:1:1) and further recrystallization from 100% hexanes afforded 83% yield of **1** as a yellow solid. mp 100–101 °C. ^{1}H NMR (400 MHz, $CDCl_3$, δ) 7.28 (s, 2H), 10.03 (s, 2H), 10.91 (s, 2H). ^{13}C NMR (125 MHz, $CDCl_3$, δ) 196.3, 150.9, 123.2, 122.2. IR (KBr, ATR) 3371, 3051, 2866, 1654, 1562, 721 cm^{-1}. HRMS (Multimode-ESI/APCI) calc'd for $C_8H_6O_4$ $[MH]^+$ = 167.08335; found 167.08245.

Preparation of monomer 3,6-diimino-1,4-cyclohexadiene-1,4-diamine (3). 1,2,4,5-Benzenetetramine tetrahydrochloride (1.0 g, 3.5 mmol) and Cs_2CO_3 (4.0 g, 12.3 mmol) suspended in MeOH (150 mL) was stirred at room temperature under air for 2 h.[274] The precipitated solid was washed with cold ethanol and then boiling methanol. The crude product was purified by soxhlet extraction using ethyl acetate as an extraction solvent for 2 d. Compound **3** was obtained as a dark brown solid (recovery: 63%). ^{1}H NMR (400 MHz, DMSO-d_6, δ) 9.35 (s, 1H), 5.77 (s, 2H), 5.42 (s, 1H). ^{13}C NMR (125 MHz, DMSO-d_6, δ) 158.9, 148.4, 97.5. IR (KBr, ATR) 3444, 3417, 3286, 3244, 1631, 1446, 1346, 1280, 875 cm^{-1}. HRMS (Multimode-ESI/APCI) calc'd for $C_6H_8N_4$ $[MH]^+$=137.0822; found 137.0812.

Synthesis of SP-PBBI-LC. To a solution of compound **1** (6.0 mg, 0.04 mmol) and 1,2,3,4-tetrafluorobenzene (5.4 mg, 0.04 mmol) in *N*,*N*-dimethylformamide (1 mL) was added compound **3** (3.3 mg, 0.02 mmol) in a pyrex tube (OD: 1 mm, H: 18 cm) and degassed by two

freeze–pump–thaw cycles. The reaction mixture was stored under the nonisothermal condition as described in the synthesis of SP-PBBI. The tube was flame-sealed using a propane torch after two freeze–pump–thaw cycles. Then the reaction was left undisturbed in a convection oven at 95–145 °C for 6 d. ^{13}C CP/MAS solid-state NMR (15 kHz, δ) 198.6, 175.6, 164.7, 150.0, 147.0, 138.4, 130.1, 119.1, 116.5, 98.8. IR (KBr, ATR). 3325–3118 (br), 2931, 1641, 1558, 1531, 1390, 1300, 1249, 1219, 1153, 1060, 833 cm^{-1}.

Synthesis of PBBI-170. A solution of **1** (12.0 mg, 0.072 mmol) and **3** (6.65 mg, 0.05 mmol) in a mixture of dimethylsulfoxide (2 mL) and mesitylene (0.2 mL) was prepared in a 25 mL round bottom flask fitted with a Dean–Stark apparatus and a reflux condenser under N_2. The solution was heated as described in the synthesis of PBBI except for 170 °C as the final temperature. The crude product was washed with dichloromethane and methanol, followed by drying in vacuo for 72 h over 100 °C heat. PBBI-170 was obtained as a black solid (78 %). ^{13}C CP/MAS NMR (10 kHz, δ) 175.9, 150.6, 129.1, 97.8. IR (KBr, ATR) 3560–3360 (br), 2920, 2854, 1693, 1600, 1535, 1435, 1249, 1195, 1161, 1118, 1041, 948 cm^{-1}.

Synthesis of a small molecule model compound (4). Salicylaldehyde (0.12 g, 1.0 mmol) and 3,6-diimino-1,4-cyclohexadiene-1,4-diamine **3** (34 mg, 0.25 mmol) were suspended in *N*,*N*-dimethylformamide (12 mL). Using the same nonisothermal temperature control described in the SP-PBBI synthesis, the reaction mixture was heated over 3 d. The crude product was triturated with hot acetone to give light dull yellow precipitates of compound **4** (65 mg, 0.19 mmol, 77% yield). ^{1}H NMR (400 MHz, DMSO-d_6, δ) 13.28 (d, 2H), 13.17 (d, 2H), 8.10 (br, 2H), 8.03 (br, 1H), 7.87 (s,1H), 7.67 (s,1H), 7.41 (t, 2H), 7.04–7.08 (dd, 4H). ^{13}C NMR (125 MHz, DMSO-d_6, δ) 158.6, 132.2, 126.6, 119.6, 117.7, 113.2. HRMS (Multimode-ESI/APCI) calc'd for $C_{20}H_{15}O_2N_4$ $[MH]^+$=343.1190; found 343.1170.

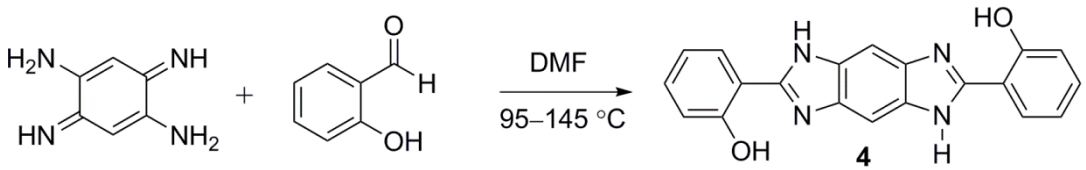

Figure 4.10 Synthetic scheme of model compound **4**.

4.6.3 FTIR spectra

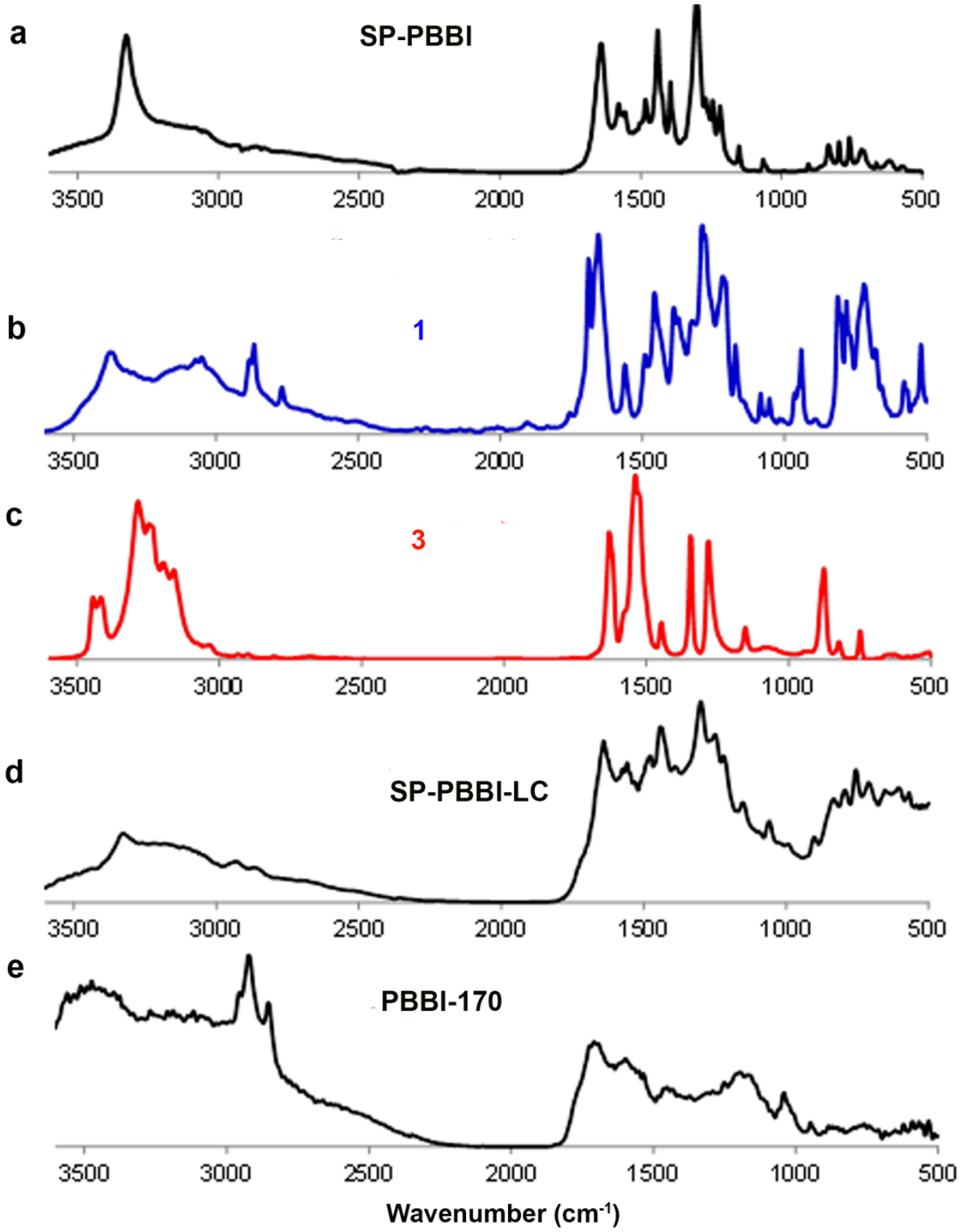

Figure 4.11 FTIR spectra of (a) SP-PBBI, (b) and (c) monomers (compound **1** and **3**), (d) a less crystalline SP-PBBI-LC sample, and (e) PBBI-170.

4.6.4 NMR Spectra

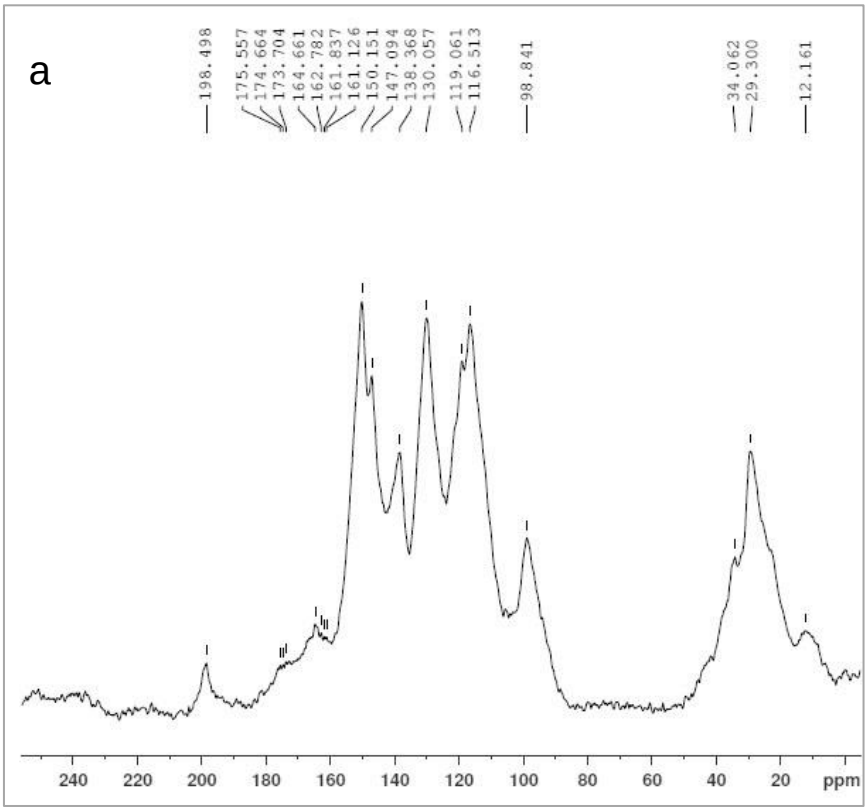

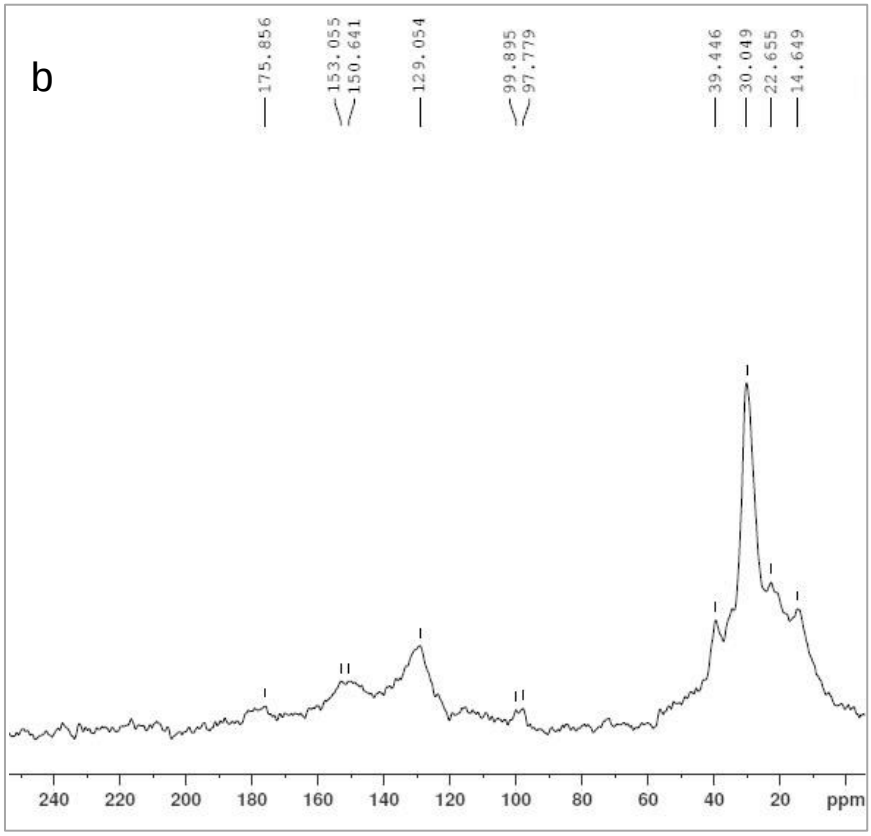

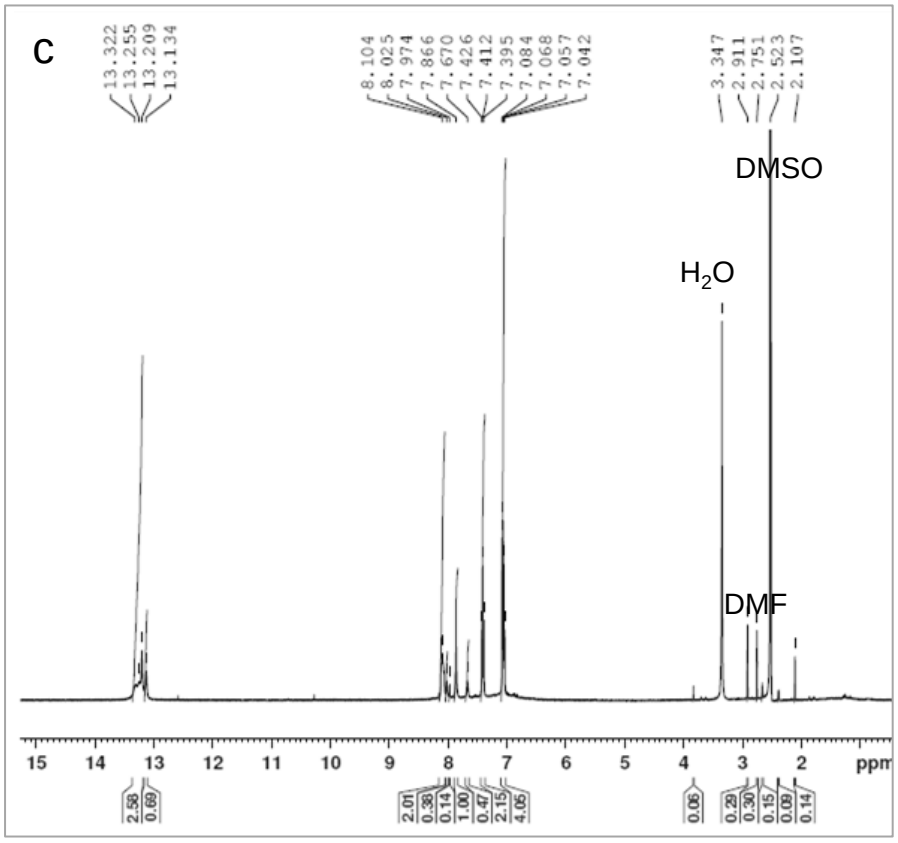
c
13.322
13.255
13.209
13.134
8.104
8.025
7.974
7.866
7.670
7.426
7.412
7.395
7.084
7.068
7.057
7.042
3.347
2.911
2.751
2.523
2.107
DMSO
H2O
DMF
15 14 13 12 11 10 9 8 7 6 5 4 3 2 ppm
2.56 0.69 2.01 0.38 0.14 1.00 0.47 2.15 4.05 0.06 0.29 0.30 0.15 0.09 0.14

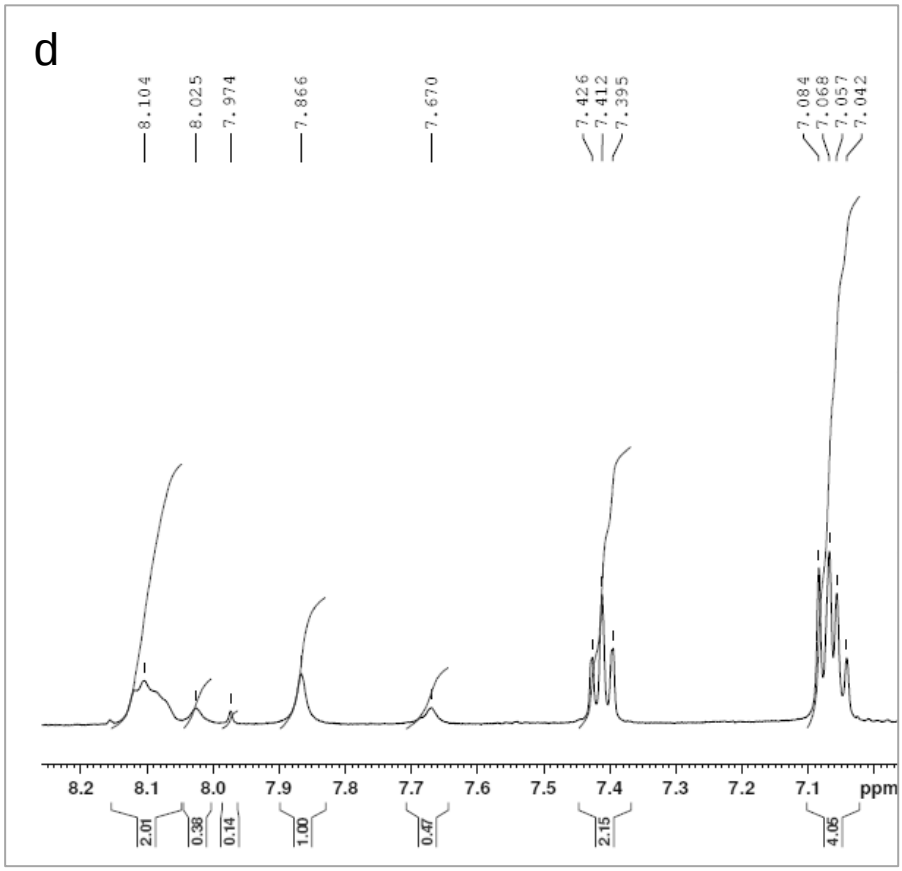
d
8.104
8.025
7.974
7.866
7.670
7.426
7.412
7.395
7.084
7.068
7.057
7.042
8.2 8.1 8.0 7.9 7.8 7.7 7.6 7.5 7.4 7.3 7.2 7.1 ppm
2.01 0.38 0.14 1.00 0.47 2.15 4.05

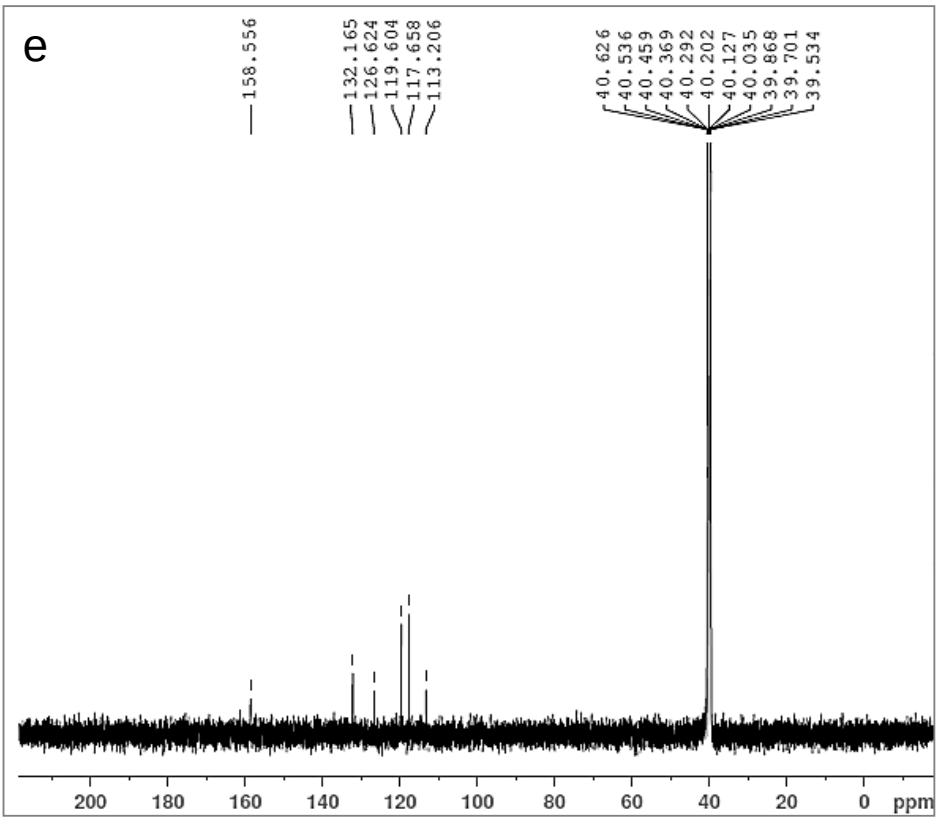

Figure 4.12 ^{13}C CP MAS solid state NMR spectra of (a) less crystalline SP-PBBI-LC and (b) PBBI-170. (c) and (d) ^{1}H NMR spectra of model compound **4**. (e) ^{13}C NMR spectrum of model compound **4**.

4.6.5 PXRD

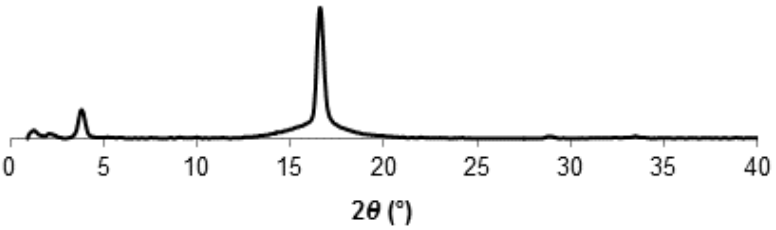

Figure 4.13 PXRD of PBBI-170. 2θ (°) found: 3.80, 16.68, 28.92, 33.46. d spacing (Å) calc'd: 23.22, 5.31, 3.09, 2.68.

4.6.6 TGA analysis

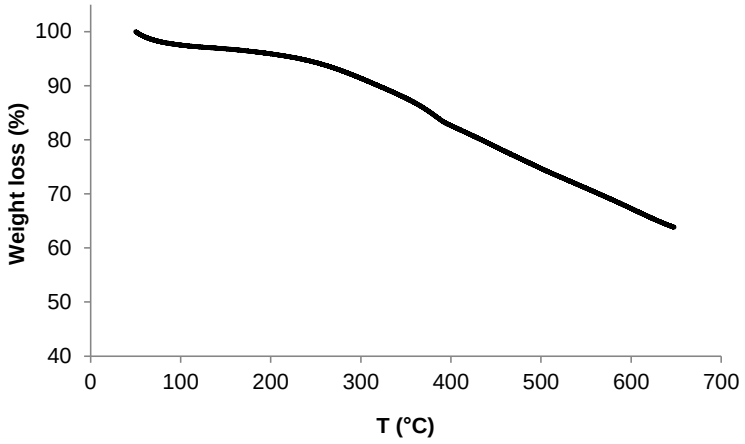

Figure 4.14 TGA trace of SP-PBBI. The data was acquired up up to 650 °C with a 5 °C/min ramp.

4.6.7 TEM micrographs of SP-PBBI and 2DSP-PBBI

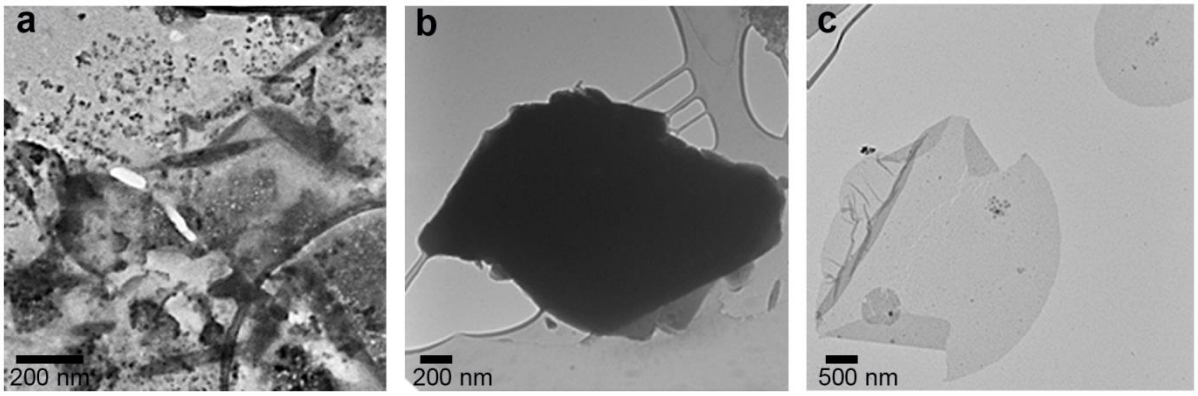

Figure 4.15 (a) 10 min-manual grinding in methanol, (b) 9 d-exfoliation, and (c) 2 d-exfoliation of a SP-PBBI sample in DMF.

4.6.8 AFM micrographs and height profiles

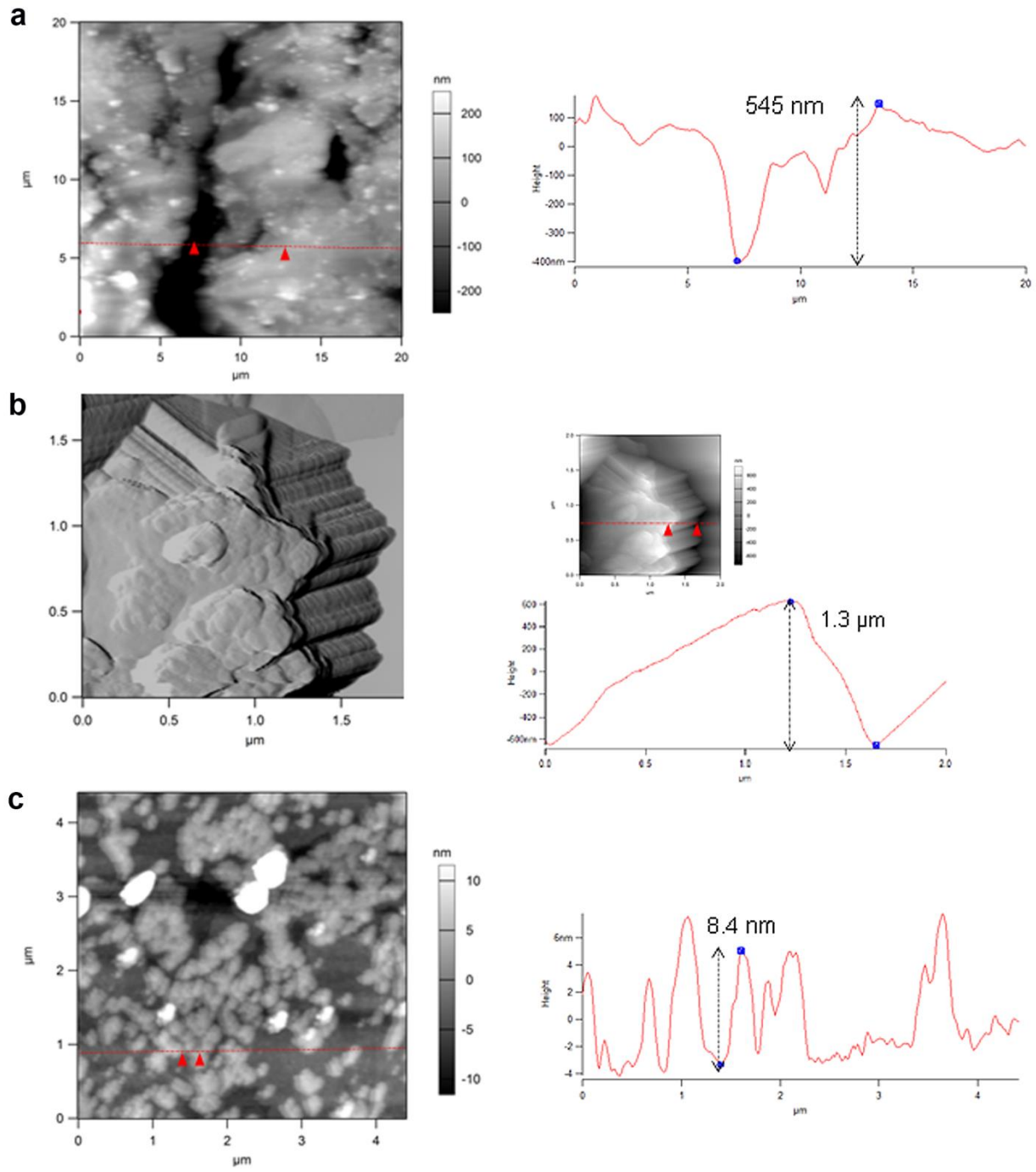

Figure 4.16 AFM microographs of 2DSP-PBBI. (a) Top-down surface and (b) stacked profile of bulk SP-PBBI samples. (c) Exfoliated 2DSP-PBBI samples on mica and their height profiles.

4.6.9 UV-Vis spectra for 2DSP-PBBI and monomers (compound 1 and 3)

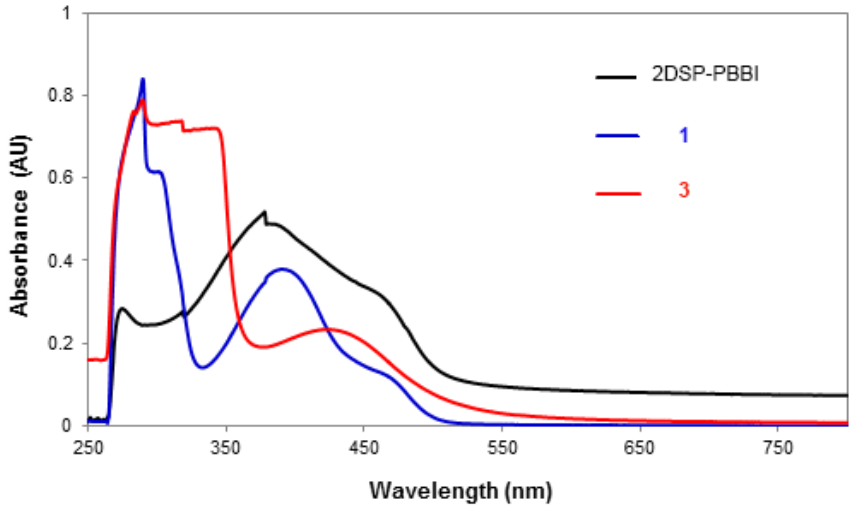

Figure 4.17 UV-Vis absorption spectra of 2DSP-PBBI and the monomers in DMF.

4.6.10 Energy band gap of 2DSP-PBBI and conductance

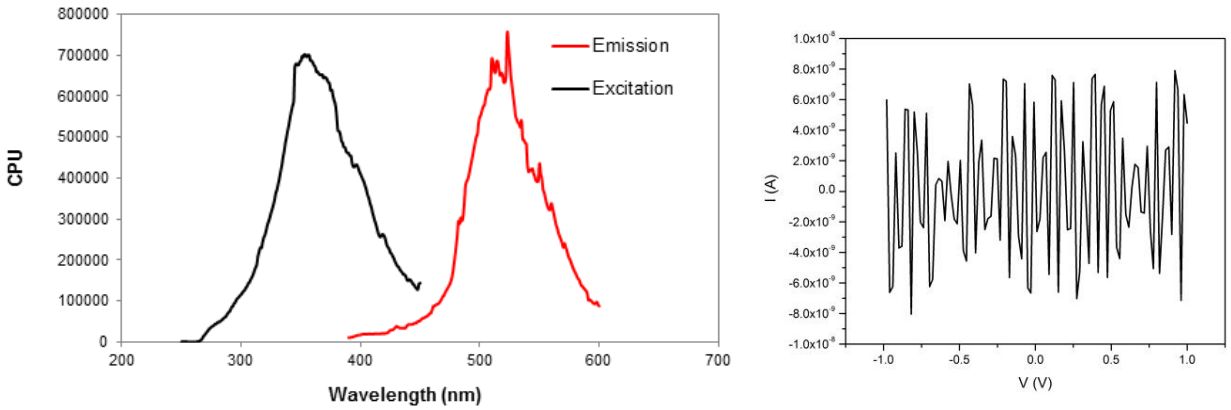

Figure 4.18 (a) Emission (582 nm) and excitation (382 nm) spectra of 2 d-exfoliated 2DSP-PBBI. Conductance measurement of 2DSP-PBBI. (b) Conductance measurement of 2DSP-PBBI.

5.0 COVALENT ORGANIC FRAMEWORKS AS SURFACE CATALYSTS FOR FABRICATING PATTERNED GRAPHENE

5.1 CHAPTER PREFACE

A communication entitled *Fabrication of Holey Graphene: Catalytic Oxidation by a Metalloporphyrin–Based Covalent Organic Framework Immobilized on Highly Ordered Pyrolytic Graphite* was prepared based on this project described in Chapter 5 and submitted to *Chem. Commun*.

5.2 INTRODUCTION

General properties of covalent organic frameworks (COFs) and some aspects of solution-phase synthetic strategies were described in Chapter 4 within the context of 2DP synthesis. Chapter 5 focuses on metallated COFs as macromolecular surface catalysts, and discusses an effective chemical approach to the preparation of nanopatterned graphene using catalytic oxidation. The surface morphology and chemical transformation of the patterned surface are analyzed with respect to fabrication processes such as deposition methods of COF films on graphite.

Our strategy for developing a new type of nanopatterning employs a bifunctional metallated COF which serves as a surface catalyst and a master template for creating holes on the graphite surface that is subsequently exfoliated into multilayers of patterned graphene. This novel concept of copy–print process eliminates the need of preparing graphene–template superlattices on a solid support, and ultimately allows for scalable production of patterned graphene. The metalloporphyrin units covalently connected in a large polymer matrix are immobilized on the graphite surface. The network of the metal–ligand catalyst maintains the catalytic center and reactive site for oxidation at the interface of catalyst–substrate. Once the catalytic oxidation is complete, the COF layer is chemically removed and the patterned graphite is exfoliated into a few layers of graphene.

Inspired by the studies of peroxidase-catalyzed oxidative biodegradation of carbon nanomaterials[90, 99, 110] and the use of synthetic Fe(III) porphyrin catalysts for oxidation of polycyclic aromatic hydrocarbons (PAHs),[275-276] we develop an catalytic oxidative method of patterning holes on the basal plane of graphite using a synthetic Fe(III) porphyrin COF as a catalyst–template. The catalytic oxidation is initiated with oxidant(s) (e.g., H_2O_2, NaOCl) and porous graphene is prepared on the highly ordered pyrolytic graphite (HOPG) surface.

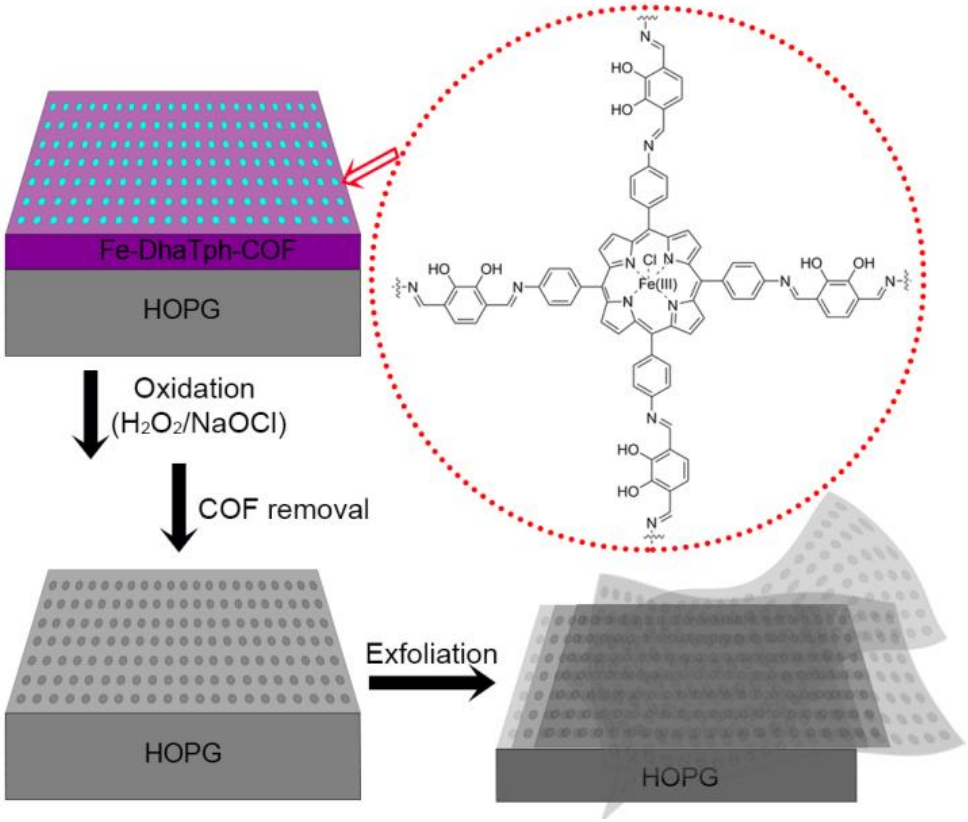

Figure 5.1 Illustration of fabricating porous graphene with Fe-DhaTph-COF catalyst deposited on HOPG and exfoliation of the patterned bulk graphite.

5.2.1 Metallated covalent organic frameworks

COFs can serve as excellent molecular platforms for high catalyst loadings and catalytic activities due to porosity and large surface-to-volume ratios.[277-278] Good thermal stability and resistance against swelling in solvents are advantageous for developing sustainable catalysts which can be easily separated from products and recycled.[268] A vast range of chemical modifications can be realized by employing different building blocks and linkers (or monomers), allowing for convenient tuning of electronic and redox properties.[278]

Catalytic functionalities are directly incorporated into the macromolecular framework, either in the main framework or in sidechains, providing dense catalytically reactive sites for chemical conversions.[277] Laterally, catalytic centers are homogeneously distributed; vertically, pore networks create molecular channels that facilitate mass transfer.[277] The easy accessibility to catalytically reactive sites on the substrate through porous networks can raise the effective concentration of reactants near the interface of catalyst–substrate and accelerate chemical reactions.[268] Studies demonstrated that the catalytic activity of a highly ordered, conjugated metalloporphyrin COF was higher than that of a linear polymer or a metal coordinated small porphyrin unit.[280] Metallated COFs can be prepared using two different methods (Figure 5.2): (1) co-ordination of metal ions with COF ligands, and (2) physical adsorption of metal NPs with different sizes onto COF layers.[281] Thus, NPs can be less stable and less recyclable over multiple catalytic cycles of reactions. In contrast, metal-COF complexation allows the metal ion catalytic center to be securely anchored.

In nanopatterning of porous graphene, metal-coordinated COFs provide unique advantages: (1) the regular arrangement of the repeating catalytic centers enables precise localization of chemical reactions, (2) hole periodicity (the center-to-center distance between two neighboring holes) can be conveniently controlled by reticular synthesis with different spacers or linkers, (3) COFs can be directly grown on solid substrates such as graphite and metals, simplifying the cumbersome pre-patterning step for template deposition, and (4) COF ligands can prevent aggregation of metal ions resulting from metal leaching and Fe(III) dimerization initiated by hydrolysis in aqueous environments and thus generate relatively uniform hole sizes in contrast to metal or metal oxide NPs.

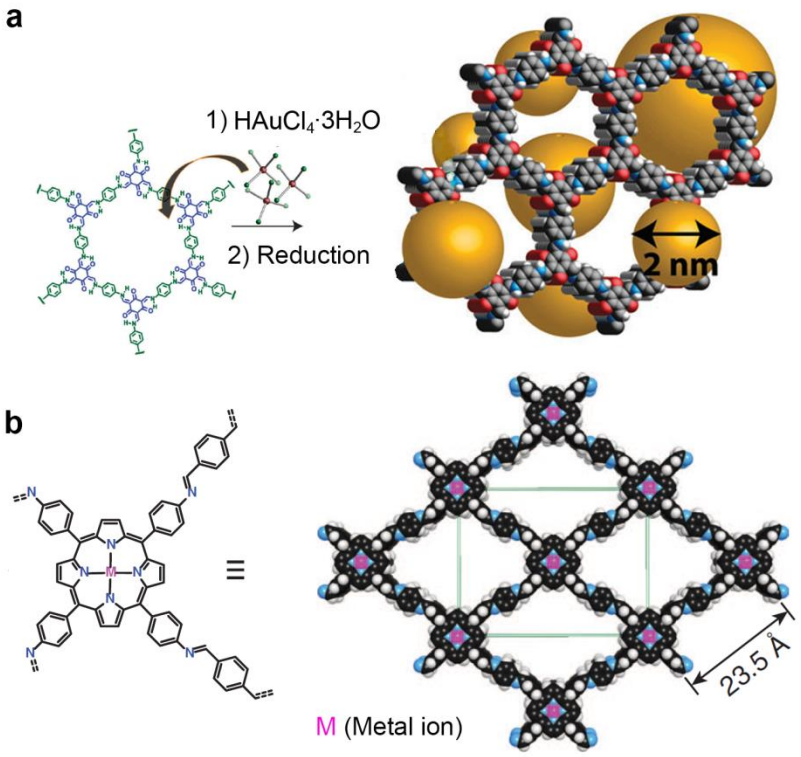

Figure 5.2 Metallated COF catalysts. (a) AuNPs are randomly adsorbed to the COF network.[281] (b) Metal ions are incorporated into the porphyrin COF building unit by forming metal–ligand complexes and regularly positioned.[278]

5.2.2 On-surface synthesis of covalent organic frameworks

The preparation of uniform COF thin films on solid substrates is important to achieve good catalytic performance. The deposited COF catalyst should homogenously coat solid substrates in both lateral and vertical directions, so that well-aligned catalytic functional moieties can efficiently promote reactions on selective sites. To this end, different bottom-up synthetic

strategies are required as most COF powders synthesized under solvothermal conditions are obtained as bulk materials.[282] To precisely control the position of catalytic functional moieties, direct synthesis (or growth) of COF films on the solid surface may improve film orientation.[282-283] Such thin composite architectures have been constructed by drop-cast of monomers on the solid support,[279] followed by polymerization under desired conditions.[284] The temperature range of on-surface COF synthesis varies significantly with the polymerization method.[84] Occasionally, an additional high-temperature annealing step is performed to remove water formed during polymerization, particularly polycondensation, and to increase the crystalline domain size.[282] For graphene/graphite substrates, aromatic species are good molecular surface assembly units. Cooperative π–π stacking can enhance the adhesion strength of COFs bearing multiple aromatic rings onto graphene, as corroborated by the superior stability of a tripod pyrene anchor to that of a single pyrene molecule on graphene.[285] To assemble organic precursors for the formation of well-defined surface architectures, high diffusion energy barriers should be overcome.[286] Finding the thermal activation energy for on-surface reactions is crucial because thermally activated decomposition and desorption of precursors are competing with the polymerization process.[286]

Examples of direct COF synthesis include scanning tunneling microscopy (STM) tip-induced polymerization, solid vaporization under ultrahigh vacuum (UHV) conditions,[284,287-288] electropolymerization, and solvothermal polymerization.[288] Although thin films prepared by solid vaporization have successfully shown the monolayer coverage of well-ordered COF structures on metal surfaces with the lateral growth of 10–40 nm, the process requires highly controlled environments and is impractical in regards to scalable fabrication. Dichtel and coworkers demonstrated multilayers of a boronate-based COF (COF-5) polymerized on graphene

using a solvothermal approach (Figure 5.3).[84] The film thickness range of 75–195 nm deposited on graphene with different solid supports (Cu, SiO_2, and SiC) and a lateral grain size of 46 nm were observed.[84] The most significant discovery of this study is that COF films can form in a gas tight glass vessel at 90 °C under atmospheric conditions within 0.5–8 h.[84] The same research group reported an oriented thin film of an anthraquinone-based COF directly grown on Au electrodes for the fabrication of a supercapacitance. The COF synthesis proceeded by slow introduction of a monomer into the reaction mixture already deposited on the Au surface at 90 °C.[283]

Generally, the bottom-up approach simplifies processing time but is challenging to optimize reaction conditions, and the surface quality of substrates can greatly affect film growth. Post-synthesis involves separate steps of exfoliation and deposition (e.g., dip and spin coating, drop-casting), and is more applicable to the scalable production of polymer films on graphene. However, the uniform alignment of COFs can be disrupted during the deposition process, which could lose desired material performance.

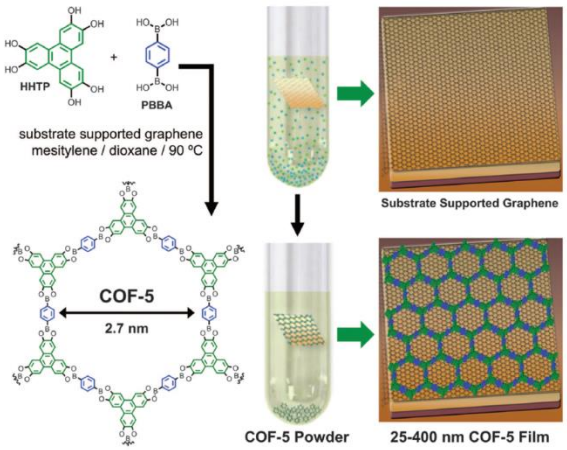

Figure 5.3 COF-5 grown on graphene. Solvothermal condensation of HHTP and PBBA in the presence of a substrate-supported single layer graphene surface provides COF-5 as both a film on graphene and a powder.[84]

5.2.3 Fabrication of porous graphene

Porous graphene comprises single- or few-layer graphene, an important substrate for nanoelectronics.[289] The fabrication of porous graphene (i.e., holey graphene,[117,290-291] graphene nanomesh,[292-294] graphene foam[295-296]) began mainly for modification of the intrinsic zero energy bandgap of semimetallic graphene.[32,292] Recently, porous graphene-based gas separation membranes have been developed, which exhibit high separation capacity and good mechanical properties.[297-299] A high-density array of nanoscale holes in large graphene sheets imparts semiconducting characteristics that are lacking in pristine graphene.[32,293] The energy band gap can be tuned by controlling the neck width between pores, the size and shape of pores, and the pore lattice symmetry.[291,293] Edges of periodic or quasi-periodic holes facilitate faster electron transport and higher electrocatalytic activity.[293] With high field transport efficiency and on–off ratios, porous graphene has shown great promise for high-performance FET devices and bio/chemical sensing.[293]

A variety of fabrication methods have been reported, including chemical (e.g., KOH,[300] HNO_3 oxidation,[301] and catalytic oxidation[117,126,302]) and physical etching (e.g., photo-, electron beam, oxygen plasma, and ion irradiation).[289,294] Top-down nanolithography, such as block copolymer lithography,[292] self-assembled monolayers of colloidal nano- and microspheres,[32] and photocatalytic patterning,[302] provides patterned graphene with high resolution.[289] Most lithography processes involve graphene mounted on a solid support before patterning, so that isolation of free standing patterned graphene is unnecessary (Figure 5.4a).[293] Lithographic patterning affords the pore size range from meso (2–50 nm) to microscale (<2 nm),[293] but have issues of high cost and low throughput.[303] A few approaches including metal NPs as hard templates under high temperatures (>500 °C) or using aggressive chemicals such as HF were

reported, but these conditions are not ideal for industrial applications (Figure 5.4b).[303] Non-lithographic methods using catalysts or reagents in solution are environmentally benign and may be more applicable in industry, but isolation and transfer of free standing graphene sheets without creating wrinkles is extremely difficult.[126,301] In addition, the generation of regular holey structures on selective sites is almost impossible given the current advancement of the technique.[290,301] Future directions for pattering graphene/graphite should aim at developing simple synthetic routes that are environmentally benign and industrially applicable.

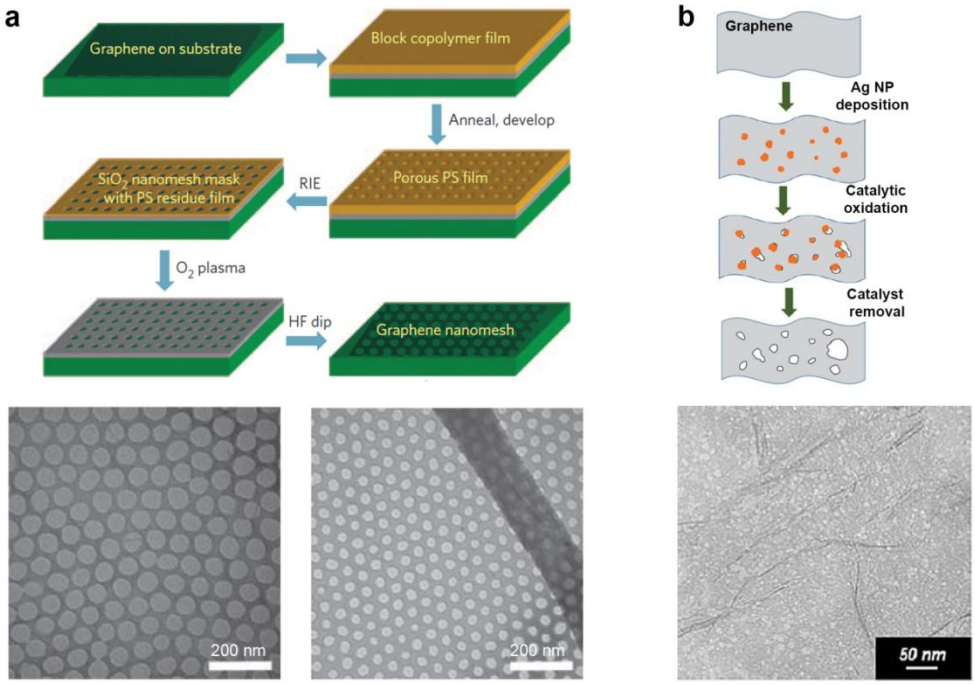

Figure 5.4 Patterned porous graphene. (a) Block copolymer lithography. Pristine graphene is covered by a thin layer of evaporated SiO_x (protecting layer) and a spin-coated block copolymer poly(styrene block-methyl methacrylate). After annealing, the porous polystyrene (PS) matrix is formed as a template. Fluoride-based reactive ion etching (RIE) reveals the SiO_x hard mask. Etching graphene by O_2 plasma and HF dip cleaning provides graphene nanomesh. TEM images below show a periodicity of 39 nm and a neck width of 7.1 nm (left) and a periodicity of 27 nm and a neck width of 9.3 nm (right) prepared by the different MWs (77 kDa and 48 kDa, respectively) of block copolymer.[292] (b) Uneven sizes of holes on graphene by catalytic air oxidation with AgNPs.[125]

5.3 EXPERIMENTAL

5.3.1 Synthesis and characterization of Fe-DpaTph-COF

Iron(III)-tetrakis(4-aminophenyl)porphyrin chloride (Fe-TAP-Cl) was prepared with iron(II) chloride tetrahydrate ($FeCl_2 \cdot 4H_2O$) and 5,10,15,20-tetrakis(4-aminophenyl)porphyrin.[304] The isolated **2** (8 mg, 0.01 mmol) and 2,3-dihydroxybenzene-1,4-dicarbaldehyde (3.4 mg, 0.02 mmol) were transferred to a glass tube (OD: 1 mm, H: 18 cm) dispersed in dimethylacetamide (DMA) (1.5 mL) and 1,2-dichlorobenzene (0.1 mL). After the starting compounds were completely dissolved, 6.0 M acetic acid (0.2 mL) was added to the reaction mixture and sonicated for 1 min, which precipitated out some of the starting compounds. The reaction tube was degassed by three freeze-pump-thaw cycles at 77 K (liquid N_2) and brought to room temperature for flame seal. Then the tube was stored in a convection oven at 120 °C for 6 d. The product was collected after two wash cycles using CH_2Cl_2 (100 mL) and MeOH (100 mL) over a PTFE membrane Millipore filter (0.2 μm) and dry over high vacuum for 24 h (yield, 76%). FTIR (KBr, ATR) $\bar{\upsilon}_{max}$, 3666–2826, 1646, 1617, 1512, 1414, 1347, 1289, 1184, 1068, 1002, 813, 715, 574. PXRD, 2θ (°) found: 3.70, 7.08–7.76 (br), 25.8, 44.64. d spacing (Å) calc'd: 23.9, 12.5–11.4 (br), 3.45, 2.03 (br, weak).

To grow the metallated COF (Fe(III)-DhaTph-COF), about 5–8 pieces of mechanically cleaved HOPG (0.5 mm × 0.5 mm) flakes were placed with the reaction mixture in a flame sealed test tube. After 6 d of condensation under the solvothermal condition, Fe-DhaTph-COF-deposited HOPG flakes were collected. A black powder of Fe-DhaTph-COF was collected from the same reaction batch for further characterization. The Fe-DhaTph-COF catalyst was also prepared by complexation of Fe(III) with DhaTph-COF in a separate post-polymerization step.[304]

DhaTph-COF (2.5 mg) was allowed to stir in NMP (7.0 mL) under N_2 at 160 °C for 24 h. Then $FeCl_2 \cdot 4H_2O$ (32 mg, 0.16 mmol) was added to the DhaTph-COF solution and stirred for 24 h for complexation. After the reaction mixture was cooled to room temperature, the crude product was washed with H_2O and MeOH over a milipore filter (pore size: 0.2 μm). A black solid powder was collected and dried *in vacuo*. A solution of Fe-DhaTph-COF (1.2 mg) was prepared in DMF 1.0 mL). After stirring for 2 h at 80 °C, the metallated COF solution was deposited on HOPG flakes by either dip-coating or drop-casting and was allowed to dry over a hot plate at 50 °C.

5.3.2 Fabrication of porous graphene

Deposition of Fe-DhaTph-COF. The solution of Fe-DhaTph-COF in post-polymerization process was prepared in DMF (1 mg/1 mL). Mechanically cleaved HOPG flakes were sequentially rinsed with DI H_2O, ethanol, and hexanes and then dried in a petri dish on a hot plate for 24 h at 50 °C. About 100 μL of the solution was drop-cast on a HOPG flakes on a glass slide and dried at 100 °C. The dip-coating method was performed on clean HOPG flakes that were completely immersed in the COF solution with tweezers and were stored for about 12 h. Then the flakes were dried over a hot plate in the same fashion.

Addition of oxidants. A dried Fe-DhaTph-COF on HOPG flake was placed in a 1-dram vial containing 0.2 mL of acetonitrile or a mixture of acetonitrile: pH 5.0 buffer (1:1, v/v). A 20 μL of H_2O_2 solution 30% (w/w) was added, followed by gentle shaking for 30 sec, and the capped vial was placed in a sand bath at 65 °C. The same amount H_2O_2 solution was replenished at every 6 h (20 μL per addition). When NaOCl was employed as a co-oxidant, 20 μL of a

NaOCl solution (available chlorine 10–15 %) was added after 2 h of the H_2O_2 addition and kept at the same temperature. When the oxidative patterning was completed, the oxidant-treated COF on HOPG was removed by the wash cycle of NaOH (5 M solution), HCl (7M solution), NaOH (1 M solution), DI water, and acetone. The sample was stored in each different solution of the acid and the base over 12 h with occasional stirring. The rinsed HOPG was dried at 50 °C and the smooth side of HOPG flake was used for characterization.

Exfoliation of patterned HOPG flakes with phosphoric acid (H_3PO_4). An oxidized HOPG flake was transferred to a 1-dram vial and 2 mL of DMF was added to the vial. After bath sonication for 10–30 min, the HOPG suspended DMF solution was collected with a disposable pipette and transferred to a new 1-dram vial. After DMF was dried off at 120 °C, concentrated phosphoric acid (0.5 mL) was transferred to the vial containing the small exfoliated HOPG particles. The mixture of HOPG and phosphoric acid was ground with a glass rod and heated in air at 125 °C for about 12 h. Fresh DMF (2 mL) was added to the acid treated HOPG and bath sonicated for about 30 min, followed by stirring in total 6 mL of DMF at room temperature.

5.4 RESULTS AND DISCUSSION

5.4.1 Characterization of Fe-DhaTph-COF

On-surface synthesis of DhaTph-COF on HOPG was attempted in a gas-tight vessel under atmospheric conditions at 90 °C using the same solvent condition and monomer stoichiometry reported in the previous study.[306] However, there was no sign of COF formation after 4 d based on the crude mixture collected from the bottom of the reaction vessel. Instead, a flame-sealed pyrex tube was used, in which HOPG flakes were immersed in the reaction mixture before the flame seal. The COF reaction proceeded *in vacuo* at 120 °C, and a DhaTph-COF powder and COF-deposited HOPG flakes were collected after 6 d. Under the same condition, the metallated porphyrin COF (Fe-DhaTph-COF) was prepared with an amine functionalized metalloporphyrin (Fe-TPA-Cl) monomer. The blue shift in the Soret bands of porphyrin (from 426 to 418 nm) shown in the UV–Vis spectra confirms the Fe(III) complexation with the porphyrin monomer (Figure 5.9). FTIR spectra of both DhaTph-COF and Fe-DhaTph-COF show the presence of an imine group at 1617 cm^{-1} (Figure 5.11b–d). The Fe-DhaTph-COFs samples were synthesized by different methods: (1) Polymerization with Fe-TPA-Cl, and (2) Polymerization of DhaTph-COF, followed by Fe(III)-complexation with DhaTph-COF. Both the spectra of Fe-TPA-Cl show less defined, broad imine peaks and a very distinct O–H stretching at 3666–2826 cm^{-1} in contrast to DhaTph-COF. The different procedures for synthesizing Fe-DhaTph-COF are further described in Ch.5.6.2.

The surface characteristics of Fe-DhaTph-COF and DhaTph-COF deposited on HOPG were very different. The dark purple layer of DhaTph-COF on HOPG exhibited a much smoother surface than dark brown Fe-DhaTph-COF. AFM micrographs confirm the different

surface textures of DhaTph-COF and Fe-DhaTph-COF (Figure 5.5). The directly grown and drop-cast Fe-DhaTph-COF layers exhibit different domain sizes. The direct growth method typically did not yield perfect surface coverage over the area of 0.25 mm^2 and some areas were not evenly coated. Post-synthetic deposition methods, either drop-casting or dip-coating, provided relatively thin, smooth films but large aggregates were visible under AFM (Figure 5.5c). Regardless of the synthetic method, the Fe-DhaTph-COF samples had rough, grainy surfaces compared to nonmetallated DhaTph-COF. These different surface morphologies may arise from conformational changes of the planar porphyrin ring upon metal complexation.

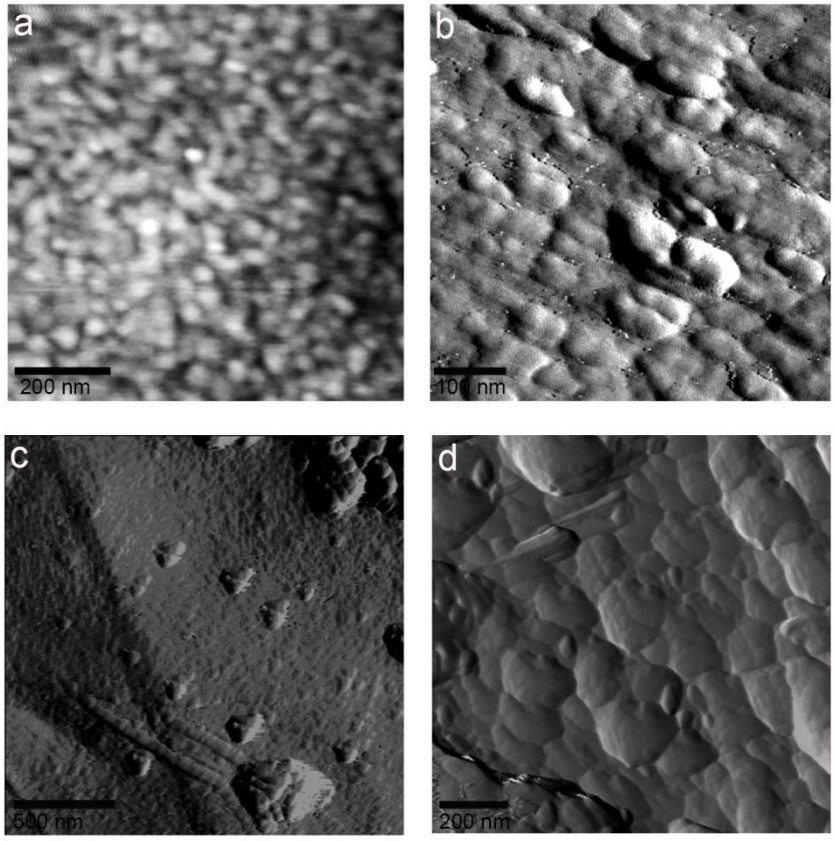

Figure 5.5 AFM micrographs of COF and metallated COFs. (a) DhaTph-COF grown on HOPG, (b) Fe-DhaTph-COF (drop-cast), (c) Fe-DhaTph-COF (drop-cast), (d) Fe-DhaTph-COF (direct growth). All samples were prepared on HOPG substrates.

5.4.2 Oxidative conditions for patterning graphite

As demonstrated in the MPO-catalyzed oxidation where an oxidant such as H_2O_2 converts Fe(III) into a reactive intermediate species Fe(IV=O•) and produces hydroxyl radical,[90, 110] we hypothesize that synthetic Fe(III)-porphyrin catalysts would oxidize graphite in a similar fashion. The oxidative condition was adjusted based on the Fe(III)-catalyzed oxidation of benzene and polycyclic aromatic hydrocarbons (PAHs).[275-276] The use of co-oxidants H_2O_2/NaOCl with a synthetic porphyrin catalyst is unprecedented although the noncatalytic oxidation of organic substrates has been reported.[307-308] Nonetheless, we sought to examine if the role of hypochlorite ($^-$OCl) formed in situ in the MPO-catalytic cycle would be also applicable to the COF-catalytic system. The catalytic cycle of Fe(III) was activated by addition of H_2O_2 at every 4 h. The co-oxidant system was tested by addition of NaOCl 2 h after the H_2O_2-activation. Upon addition of NaOCl, it immediately reacted with extra H_2O_2 remaining in the solution, resulting in vigorous formation of oxygen gas that can initiate singlet oxygen-mediated oxidation.[307-308]

After the metallated COF was removed from the HOPG surface, the morphology of HOPG was analyzed by TEM and AFM. The pristine HOPG sheets exfoliated with H_3PO_4[309] do not exhibit significant defects (Figure 5.6a, d, and g). In contrast, the HOPG samples treated with oxidants (H_2O_2/NaOCl) at 65 °C clearly show dense holes on the surface. Catalytic oxidation on the Fe-DhaTph-COF deposited graphite resulted in the formation of continuous hole arrays of 4–50 nm in diameter under TEM (Figure 5.6c), consistent with holes of 8–40 nm found in the AFM image (Figure 5.6f). This patterned surface suggests that the Fe(III) ions coordinated to the COF were anchored to the graphite surface and facilitated oxidative degradation. Based on the pore size of DhaTph-COF (ca. 2.3 nm) reported in the previous study,[306] the hypothetical hole periodicity can be roughly estimated by measuring the distance

between Fe-DhaTph-COF catalytic centers. The average hole periodicity of 8.3 nm and the average neck width (the smallest edge-to-edge distance between two neighboring holes) of 2.0 nm measured on TEM images were larger than the periodicity of Fe(III) catalytic center (i.e., the distance between porphyrin rings). The elongated shapes suggest that defect formation laterally propagated over the nearby graphitic surface.

When a pH 5.0 acetate buffer solution was mixed with acetonitrile (1:1, v/v) to examine the pH effect on HOCl formation over $^{-}$OCl, samples exhibited large, random holes (Figure 5.12a–c and e). The hole nanoarrays were also created by H_2O_2-activated oxidation (Figure 5.12d and f), but a larger amount of oxidant was required to generate a significant holey structure than the co-oxidant system. The co-oxidant system of H_2O_2/NaOCl is efficient for a short-term treatment probably because hypochlorite can induce reactive singlet oxygen-mediated oxidation by insertion of peroxy groups (O–O) on the graphitic carbons without a catalyst. Once sp^2 carbons are substituted with oxygen-containing groups, bond cleavage of C–C can undergo readily.[307] As hypochlorite can serve solely as an effective oxidant under noncatalytic conditions, we conducted a control reaction with only hypochlorite ($^{-}$OCl). However, no repeating holey structure was observed, suggesting that the Fe-DhaTph-COF catalytic systems were critical to generating site-selectivity for patterning. To verify our initial hypothesis of Fe-DhaTph-COF's bifunctional role of catalyst–template, we investigated the catalytic activity of iron(III)-tetrakis(4-aminophenyl)porphyrin chloride (Fe-TAP-Cl) that may be self-assembled into nanoaggregates with sufficient surface coverage on HOPG (Figure 5.13).[310-313] The excellent catalytic performance of small porphyrin units noncovalently bound to graphene was reported although Fe(III) porphyrin centers were randomly positioned on the graphene surface.[134] Nevertheless, the interactions and morphology of metal–ligand complexes were relatively

difficult to control in small-molecule catalyst systems.[279] TEM (Figure 5.6b) and AFM (Figure 5.6e) images show that Fe-TAP-Cl-catalyzed oxidation generated sparse holes, very different from the patterned surface with the metallated COF. This uneven distribution may suggest poor adhesion between HOPG and Fe-TAP-Cl aggregates (Figure 5.13), revealing the dynamic nature of association/dissociation when they are in contact with solvents. It is inconclusive whether some large holes observed under AFM resulted from those catalyst aggregates.

To successfully realize the copy–print concept in the fabrication of multiple holey graphene sheets, defect formation needs to propagate vertically and create regular nanochannel arrays through several graphitic layers. AFM height analysis in Figure 5.14 reveals that the vertical channel propagated from the top surface is about 1–3 nm (up to ~12 layers of graphene). However, the oxidation process appears to have also laterally expanded the defect area on the same plane of graphene to some extent, unavoidably generating some large holes. The lateral propagation is more pronounced near the metal catalytic center than the inner graphite. In addition, the irregular shapes might have resulted from the disintegrating COF catalyst under the oxidative condition. Thus the morphologies of Fe-DhaTph-COF deposited on HOPG before and after oxidation were analyzed with AFM. As shown in Figure 5.15, much of the COF catalyst remained intact under the oxidative condition. However, it is unclear if the degradation products or intermediate species of graphite that were produced during oxidation reacted with the inner COF layer, thereby disrupting the metal catalytic center.

The number of patterned graphene layers was also estimated from exfoliated samples (Figure 5.6g–i). The exfoliation of the pristine HOPG sample with phosphoric acid was not greatly effective. After an extensive amount of time of sonication (6 h) and stirring (2 d) in DMF at room temperature, the pristine HOPG sample afforded graphene sheets of 2–4 nm

(Figure 5.6g). Oxidized samples were easily exfoliated by sonication in 10–30 min, depending on the extent of oxidation applied to a sample, and stirring for about 1 d at room temperature. Despite the long hours of stirring, a few 2- or 3-layer (<1 nm in height) patterned graphene were observed with AFM analysis (Figure 5.6h). Mostly, the height of exfoliated patterned samples was 1–3 nm (Figure 5.6i). It appears that sonication was more effective in the exfoliation of oxidized HOPG than stirring. Longer sonication times (>total 1 h) were attempted, but reduced the size of graphene sheets, which may not be ideal for achieving high surface-volume-ratios. Exfoliation should be optimized further and other chemicals besides phosphoric acid should be explored to isolate single-layer graphene.

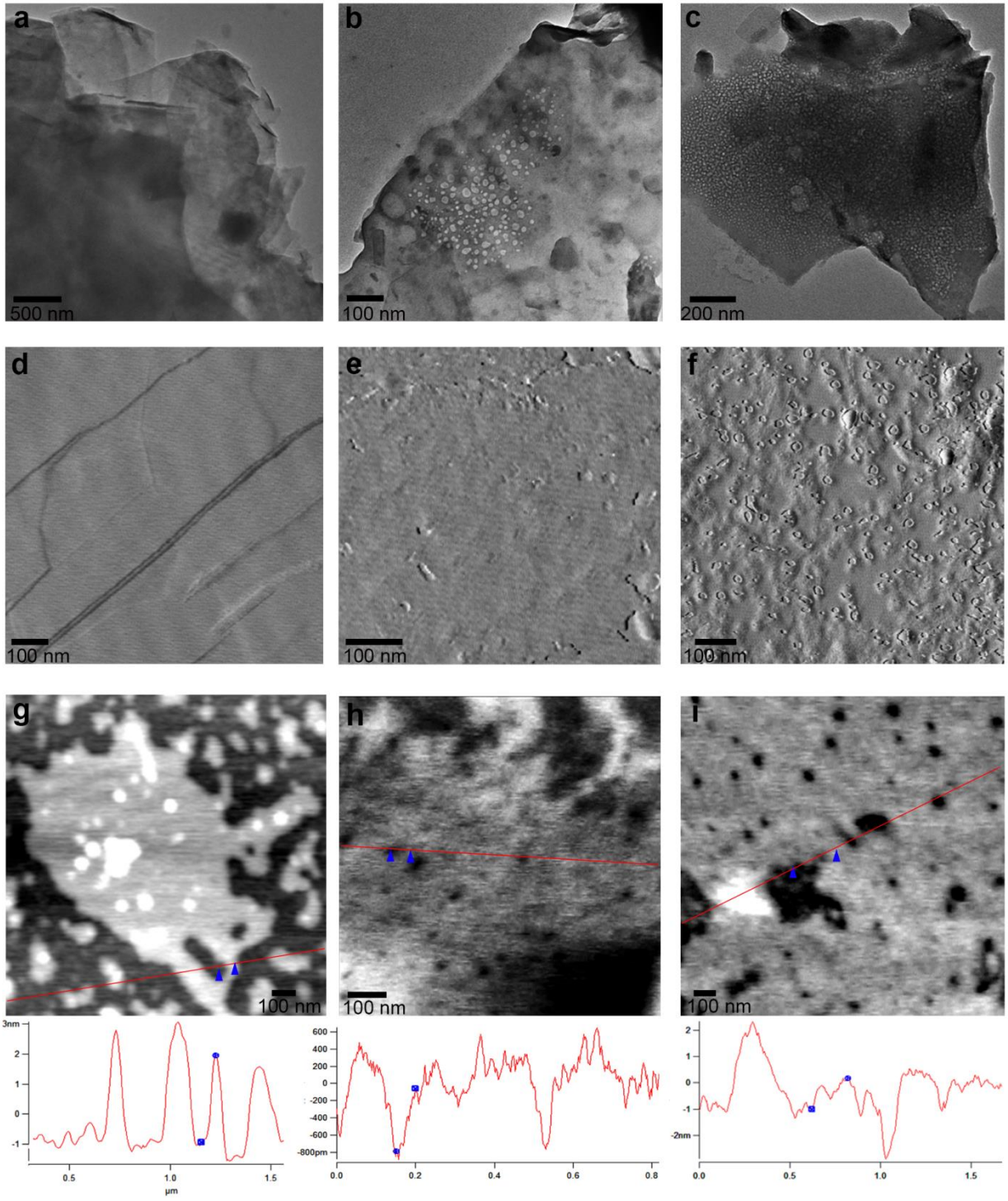

Figure 5.6 Micrographs of TEM (a)–(c) and noncontact mode AFM amplitude (d)–(f) and height (g)–(i). (a) and (d) Pristine HOPG. (b) and (e) Oxidized HOPG with Fe-TPA-Cl and H_2O_2/NaOCl. (c) and (f) Patterned HOPG with Fe-DhaTph-COF and H_2O_2/NaOCl. (g) Exfoliated pristine HOPG (Height: 2.9 nm). (h) and (i) Exfoliated ox-HOPG samples with Fe-TPA-Cl and H_2O_2/NaOCl. (h) Height: 0.73 nm. (i) Height1: 1.2 nm.

5.4.3 Characterization of patterned graphite with FTIR and Raman spectroscopy

Changes in the functional group of HOPG before and after oxidation were analyzed using FTIR. The spectra of patterned HOPG and freshly cleaved pristine HOPG samples are almost identical (Figure 5.7a). Generally, IR absorption spectra for HOPG and graphite samples are featureless, but the overall band profile of pristine HOPG appears close to those of graphene and graphene oxide.[314-315] The patterned HOPG shows a new peak at 1705 cm^{-1} can be attributed to C=O stretching modes due to oxidation.[316]

Raman spectroscopy was utilized to quantify the number of newly formed sp^3 defects relative to pristine sp^2 graphitic carbons and characterize the defect type. Figure 5.7b shows the average I_D/I_G of 0.31 for H_2O_2/NaOCl-treated samples whereas only a residual peak (1331 cm^{-1}) is shown in the pristine HOPG spectrum. The peak width (fwhm) of D′ band at 1607–1635 cm^{-1}, indicative of the formation of vacancy-like defects, appears far more pronounced than those of other samples. The spectrum of the small porphyrin unit (Fe-TAP-Cl)-catalyzed oxidation shows a clear indication of sp^3 defect formation despite the low average I_D/I_G of 0.15 and the barely noticeable D′ peak. The TEM image in Figure 5.6b shows that the self-assembled metalloporphyrin (Fe-TAP-Cl) aggregates can catalyze oxidation on the HOPG surface and generate vacancy-like defects. However, the uneven distribution of holes could result in a very subtle D′ band. This inconsistency may be due to the skewing of data from sampling spots randomly selected for Raman analysis. Table 5.1 lists the I_D/I_G values of the samples catalyzed by Fe-DhaTph-COF. To investigate the difference in catalytic activity between direct growth and drop-casting of Fe-DhaTph-COF, the average I_D/I_G values are compared. The direct growth method has slightly higher I_D/I_G values (higher degrees of oxidation) than drop-casting for both

H_2O_2 and H_2O_2/NaOCl systems. Based on Raman spectroscopic data, both deposition methods were effective in oxidatively patterning graphite.

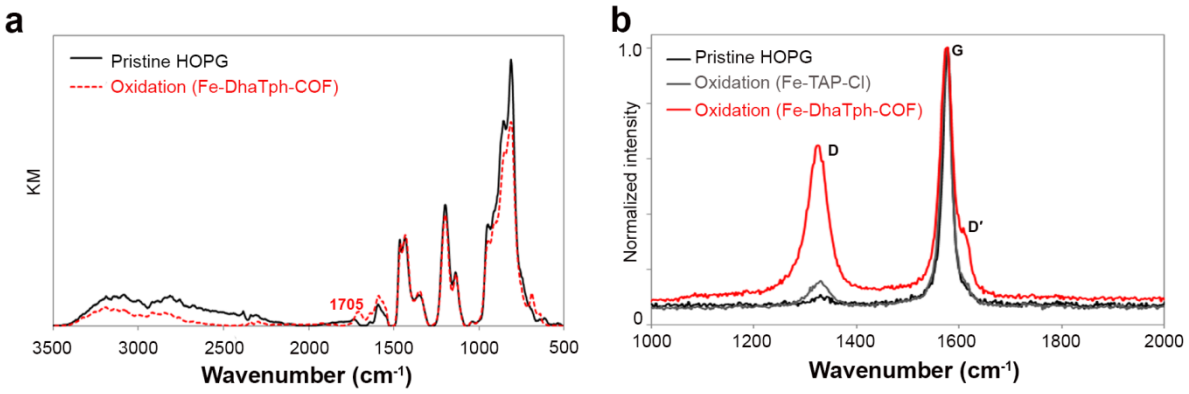

Figure 5.7 (a) ATR-FTIR spectra of HOPG samples before and after oxidation. (b) Raman spectrum of the patterned HOPG sample (Fe-DhaTph-COF in the presence of H_2O_2/NaOCl, total addition 80 μL/80 μL) shows distinct D and D′ bands. The metalloprophyrin (Fe-TAP-Cl)-catalyzed sample shows only sp^3-defects at D peak. Each of the spectra was normalized to the G peak for ease of comparison.

Table 5.1 Raman I_D/I_G values of oxidatively patterned HOPG with Fe-DhaTph-COF

Deposition method	Oxidant (total addition, μL)	I_D/I_G
Drop-casting	H_2O_2 (160)	0.23
Drop-casting	H_2O_2/NaOCl (80/80)	0.31
Direct growth	H_2O_2 (160)	0.26
Direct growth	H_2O_2/NaOCl (80/80)	0.38

5.5 CONCLUSION

We demonstrated a new chemical patterning method of utilizing an Fe(III) prophyrin COF as a surface catalyst and a template on HOPG. Few-layer patterned graphene sheets exhibited holey structures after treatment with H_2O_2 or H_2O_2/NaOCl. AFM imaging analysis showed that the oxidation process propagated vertically (oxidative perforation 12 layers of graphene), forming multiple layers of patterned graphene. The size and shape of holes varied with the oxidative condition and the proximity to the catalytic site. Metallated COFs can be an effective, robust catalyst for creating holes on graphitic carbon network under mild catalytically oxidative conditions that can be potentially translated into industrial processes. The copy-print concept of oxidative patterning–exfoliation will allow for facile processing and scalable production of patterned holey graphene. Future studies should focus on tuning the oxidative condition to achieve precise, uniform hole morphology. In addition, exfoliation methods should be improved to produce single-layer graphene.

5.6 SUPPORTING INFORMATION

5.6.1 Materials and instrumentation

Highly ordered pyrolytic graphite (HOPG SPI-1 Grade: #439HP-AB) was purchased from SPI Supplies (Westchester, PA). 5,10,15,20-tetrakis(4-aminophenyl)porphyrin was obtained from TCI America. Hydrogen peroxide (30% in solution) was purchased from EMD Chemical. All other chemicals were obtained from Sigma Aldrich and used without further purification. All reaction solvents were anhydrous reagent graded. Silica gel for column chromatography was purchased from Selecto Scientific. Thin layer chromatography was performed on Merck TLC plates pre-coated with silica gel 60 F254. Visualization of the developed plates was performed by fluorescence quenching or by phosphomolybdic acid (PMA) stain.

Fourier Transform spectroscopy (FTIR) was performed using an IR-Prestige spectrophotometer (Shimadzu Scientific) outfitted with an EasiDiff accessory (Pike Technologies). Solid samples were ground with KBr to prepare a homogenous mixture. Spectra were collected for 32 scans at 2 cm^{-1} resolution. Powder x-ray diffraction (PXRD) was recorded on a Bruker X8 Prospector Ultra equipped with a Bruker Smart Apex CCD diffractometer and a Copper micro-focus X-ray source employing Cu Kα radiation at 40 kV, 40 mA. A ground sample was loaded in a capillary tube (D: 1 mm) for analysis. The size and the morphology were analyzed with Transmission Electron Microscopy (FEI-Morgani, 80 keV). All TEM samples were prepared by drop-casting 3.5 µL of a sample onto a lacey carbon films/400 mesh copper grid and dried under ambient conditions over 24 h. An Asylum MFP-3D Atomic Force Microscope (AFM) was utilized with high resolution probes (Hi'Res-C14/Cr-Au) purchased from MikroMasch. Patterned HOPG samples were directly mounted on a metal disc using

double-sided scotch tape. UV-Vis-NIR spectra were acquired using a Lambda 900 spectrophotometer (PerkinElmer). ^{1}H NMR spectra were recorded on a Bruker (400 MHz) and were internally referenced to residual protio solvent signals (TMS) at δ 0.00 ppm (^{1}H). Data were reported as chemical shift (δ ppm) and multiplicity (s = singlet, d = doublet, t = triplet, q = quartet, qn = quintet, m = multiplet, br = broad), integration, and coupling constant (J) in Hz. Mass spectra were acquired on Q-Exactive, Thermo Scientific.

5.6.2 Synthesis

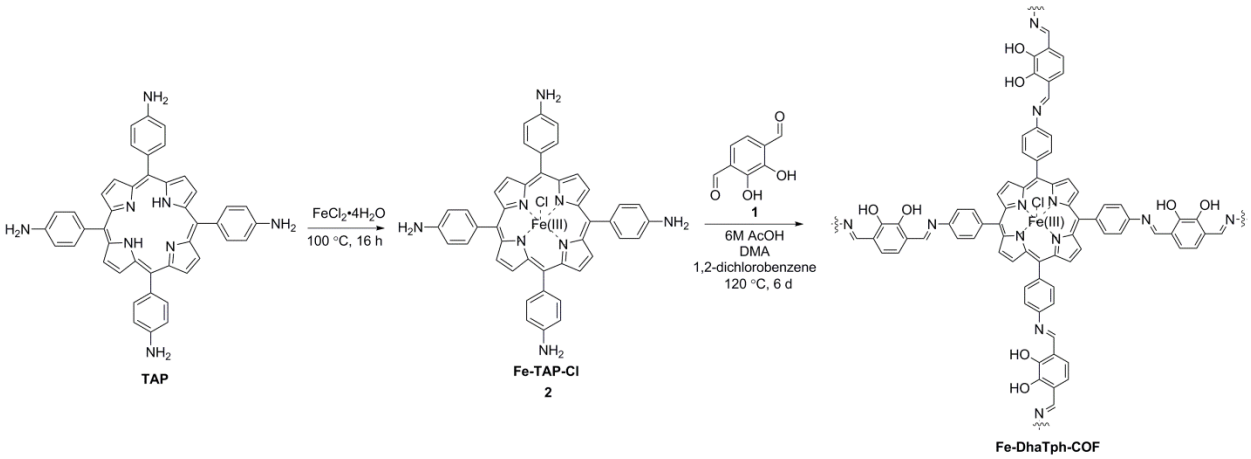

Figure 5.8 Scheme of the synthesis of **2** and Fe-DhaTph-COF.

Synthesis of iron(III)-tetrakis(4-aminophenyl)porphyrin chloride (Fe-TAP-Cl) (Compound 2). 5,10,15,20-tetrakis(4-aminophenyl)porphyrin (45 mg, 0.067 mmol) was suspended in $CHCl_3$ (2 mL) and then a $FeCl_2$•$4H_2O$ (35 mg, 0.18 mmol) dissolved in 2 mL of *N*,*N*-dimethyl formamide was added to the porphyrin solution. The reaction was heated under N_2 at 100 °C for 16 h. After the reaction solvent mixture was completely dried *in vacuo*, the crude product loaded

on a deactivated Al_2O_3 column was purified sequentially using 100% acetone and a mixture of ethyl acetate : acetonitrile : methanol (3:1:1, v/v/v) gave a dark green powder of Fe-TAP-Cl (yield, 64%). HRMS (Multimode-ESI/APCI) calc'd for $C_{44}H_{32}N_8ClFe$ $[MH]^+$=763.17824; found 763.17590. FTIR (KBr, ATR) $\bar{\upsilon}_{max}$, 3426, 3365, 3222, 3028, 2957, 2924, 2854, 1668, 1610, 1515, 1339, 1290, 1202, 1000, 875, 804 cm^{-1}. UV-Vis (CH_3CN) λ_{max}, 244, 315, 419, 576, 623 nm.

Synthesis of 2,3-dihydroxybenzene-1,4-dicarbaldehyde (Compound 1). 1 was prepared by the two-step synthesis based on the procedures previously reported.1 To improve the purity, the crude product was vigorously stirred in 15% sodium thiosulfate solution with addition of dichloromethane for 6 h. The organic layer was dried over Mg_2SO_4 and filtered, and then the solvent was dried in vacuo. Purification through silica gel flash chromatography (dichloromethane : methanol : acetic acid = 98:1:1) and further recrystallization from 100% hexanes afforded 83% yield as a yellow solid. mp 100–101 °C. ^1H NMR (400 MHz, $CDCl_3$, δ) 7.28 (s, 2H), 10.03 (s, 2H), 10.91 (s, 2H). ^{13}C NMR (125 MHz, $CDCl_3$, δ) 196.3, 150.9, 123.2, 122.2. IR (KBr, ATR) 3371, 3128, 3051, 2866, 2769, 1689, 1654, 1562, 721 cm^{-1}. HRMS (Multimode-ESI/APCI) calc'd for $C_8H_6O_4$ $[MH]^+$ = 167.08335; found 167.08245.

Synthesis of Fe-DhaTph-COF. The isolated **2** (8 mg, 0.01 mmol) and 2,3-dihydroxybenzene-1,4-dicarbaldehyde (3.4 mg, 0.02 mmol) were transferred to a glass tube (OD: 1 mm, H: 18 cm) dispersed in dimethylacetamide(DMA) (1.5 mL) and 1,2-dichlorobenzene (0.1 mL). After the starting compounds were completely dissolved, 6.0 M acetic acid (0.2 mL) was added to the reaction mixture and sonicated for 1 min, which precipitated out some of the starting compounds. The reaction tube was degassed by three freeze-pump-thaw cycles at 77 K (liquid N_2) and brought to room temperature for flame seal.

Then the tube was stored in a convection oven at 120 °C for 6 d. The product was collected after two wash cycles using CH_2Cl_2 (100 mL) and MeOH (100 mL) over a PTFE membrane Millipore filter (0.2 μm) and dry over high vacuum for 24 h (yield, 76%). FTIR (KBr, ATR) $\bar{\upsilon}_{max}$, 3666–2826, 1646, 1617, 1512, 1414, 1347, 1289, 1184, 1068, 1002, 813, 715, 574. PXRD, 2θ (°) found: 3.70, 7.08–7.76 (br), 25.8, 44.64. d spacing (Å) calc'd: 23.9, 12.5–11.4 (br), 3.45, 2.03 (br, weak).

5.6.3 Characterization of Fe-DhaTph-COF

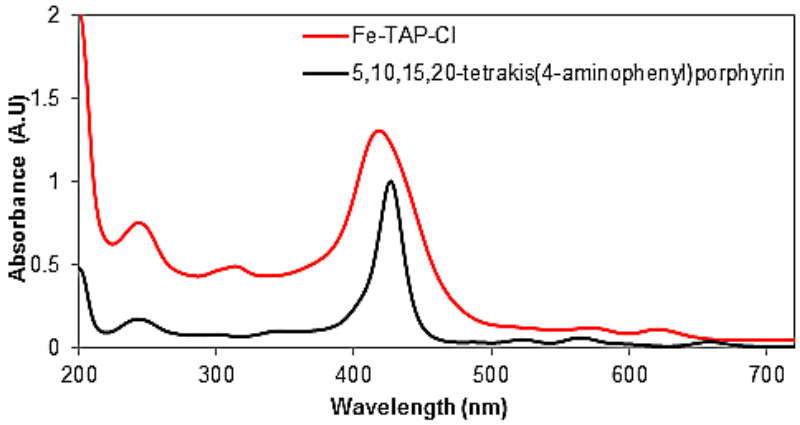

Figure 5.9 UV-Vis spectra of iron-metallated-porphyrin (Fe-TAP-Cl) and porphyrin monomer (5,10,15,20-tetrakis(4-aminophenyl)porphyrin) in acetonitrile. After the iron complexation, the Soret band of the monomer has blue-shifted by 8.5 nm and the entire Q-bands in 500–700 nm has significantly changed.

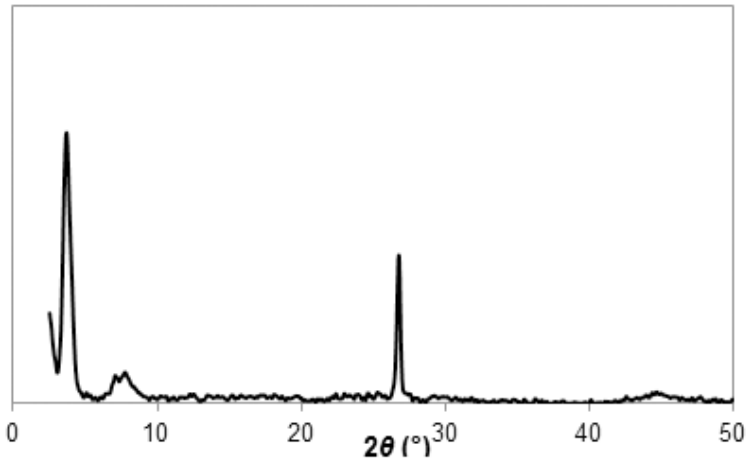

Figure 5.10 PXRD spectrum of Fe-DhaTph-COF. The 2θ (°) values of 3.7 and 7.08–7.76 are almost identical to the reported data.[305] The peak at 2θ =25.8 and 44.6 were not previously observed in DhaTph-COF spectrum.

5.6.4 FTIR spectra

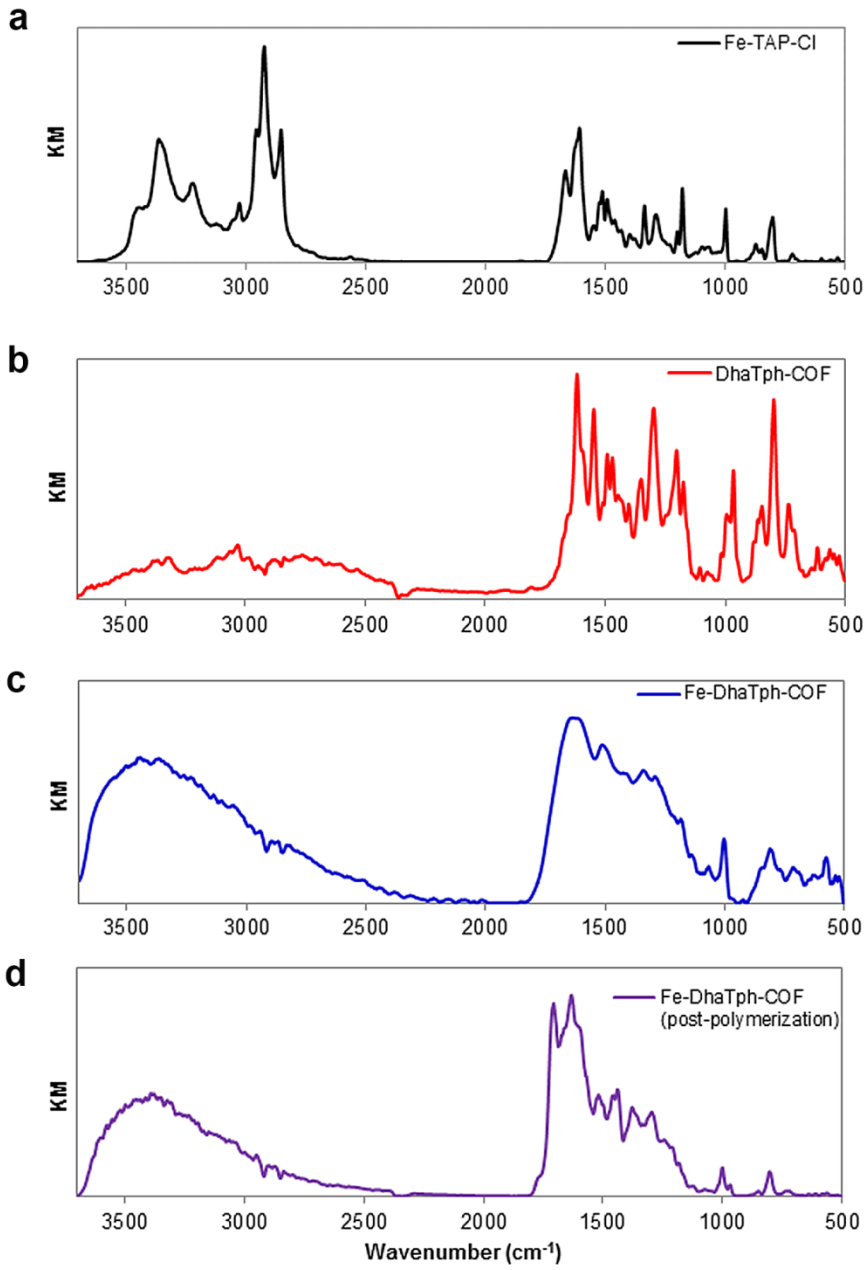

Figure 5.11 FTIR spectra of (a) Fe-TAP-Cl, (b) DhaTph-COF, (c) Fe-DhaTph-COF: The powder sample was collected from the reaction batch where the COF was grown on HOPG. (d) Fe-DhaTph-COF powder: Fe(III) was coordinated with DhaTph-COF after polymerization.

5.6.5 AFM and TEM micrographs of patterned HOPG after oxidation

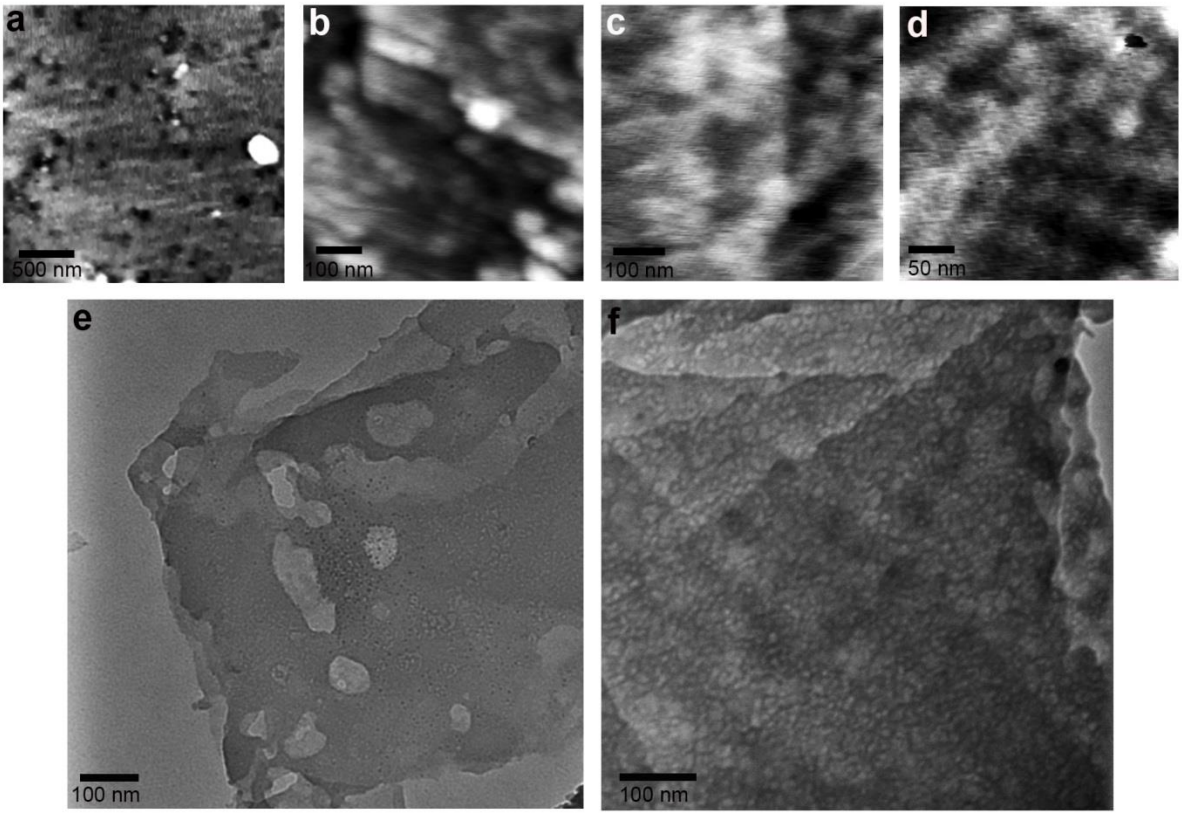

Figure 5.12 (a)–(d) AFM height images. (e) and (f) TEM images. COF deposition: (a) and (e) Fe-DhaTph-COF drop-cast, (b)–(d) Fe-DhaTph-COF grown on HOPG. Oxidant addition: (d) and (f) H_2O_2-initiated oxidation (total addition: 16 × 20 μL). (a)–(c) & (e) H_2O_2/NaOCl (4 × 20 μL/4 × 20 μL) at pH 5.0.

5.6.6 AFM Height analysis before oxidative patterning

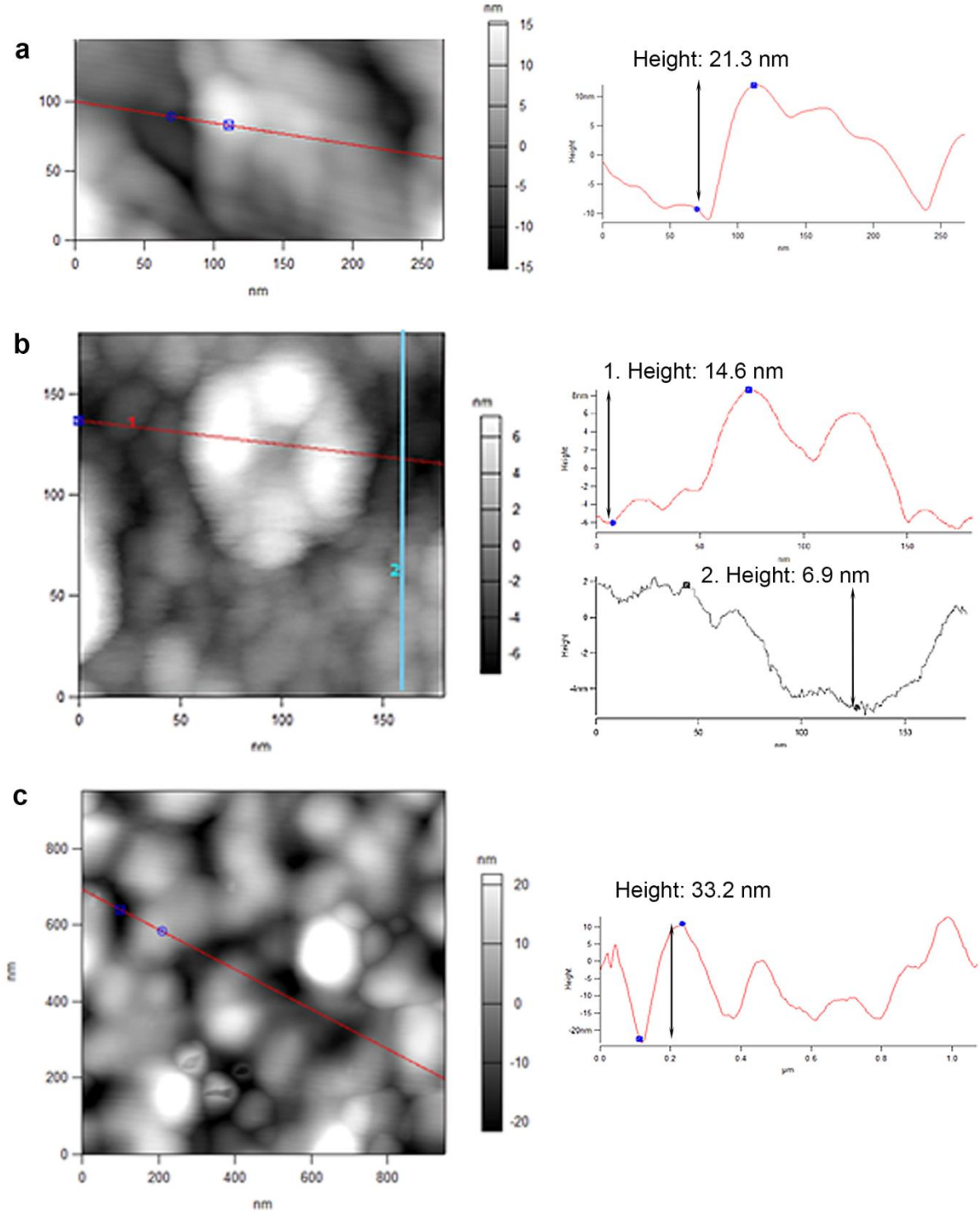

Figure 5.13 (a) and (b) Fe-DhaTph-COF grown on HOPG before oxidation. (c) Fe-TAP-Cl drop-cast on HOPG before oxidation.

5.6.7 AFM Height analysis after oxidative patterning

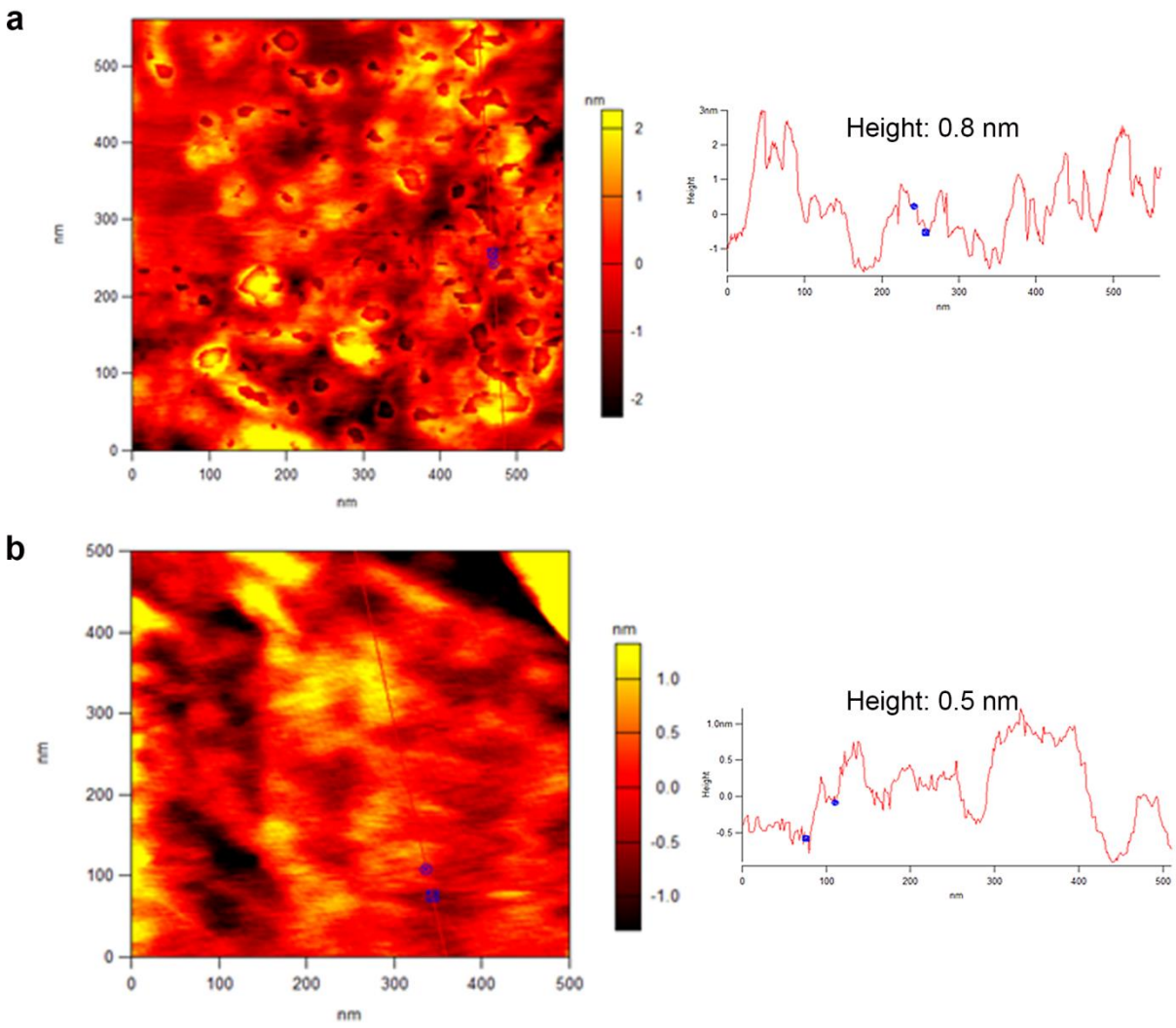

Figure 5.14 AFM height analysis of patterned HOPG. (a) Drop-cast and (b) Direct growth of Fe-DhaTph-COF on HOPG. The samples were patterned with (a) 4 × 20 µL/4 × 20 µL and (b) 4 × 20 µL/4 × 20 µL of H_2O_2/NaOCl.

5.6.8 AFM micrographs of remaining Fe-DhaTph-COF deposited on HOPG before and after removal of the metallated COF layer

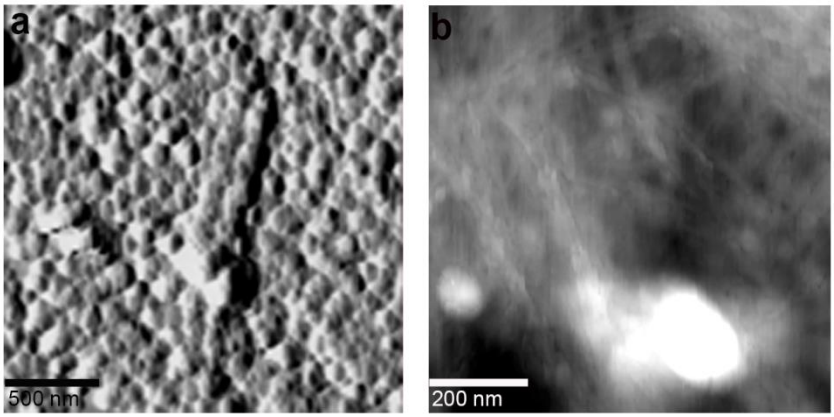

Figure 5.15 After oxidative treatment with H_2O_2/NaOCl. (a) The remaining metallated COF layer is still intact (AFM amplitude image). (b) After removal of the metallated COF with NaOH (5 M) and HCl (7 M) solutions. Generally, wash with HCl leaves large aggregates on the surface (AFM height image).

BIBLIOGRAPHY

1. Jariwala, D.; Sangwan, V. K.; Lauhon, L. J.; Marks, T. J.; Hersam, M. C. Carbon Nanomaterials for Electronics, Optoelectronics, Photovoltaics, and Sensing. *Chem. Soc. Rev.* **2013,** *42* (7), 2824–2860.
2. Hirsch, A. The Era of Carbon Allotropes. *Nat. Mater.* **2010,** *9* (11), 868–871.
3. Prasek, J.; Drbohlavova, J.; Chomoucka, J.; Hubalek, J.; Jasek, O.; Adam, V.; Kizek, R. Methods for Carbon Nanotubes Synthesis-Review. *J. Mater. Chem.* **2011,** *21* (40), 15872–15884.
4. Wu, J. S.; Pisula, W.; Müllen, K. Graphenes As Potential Material for Electronics. *Chem. Rev.* **2007,** *107* (3), 718–747.
5. Hu, M.; Zhao, Z. S.; Tian, F.; Oganov, A. R.; Wang, Q. Q.; Xiong, M.; Fan, C. Z.; Wen, B.; He, J. L.; Yu, D. L.; Wang, H. T.; Xu, B.; Tian, Y. J. Compressed Carbon Nanotubes: A Family of New Multifunctional Carbon Allotropes. *Sci. Rep.* **2013,** *3*.
6. Georgakilas, V.; Perman, J. A.; Tucek, J.; Zboril, R. Broad Family of Carbon Nanoallotropes: Classification, Chemistry, and Applications of Fullerenes, Carbon Dots, Nanotubes, Graphene, Nanodiamonds, and Combined Superstructures. *Chem. Rev.* **2015,** *115* (11), 4744–4822.
7. Ajayan, P. M. Nanotubes from Carbon. *Chem. Rev.* **1999,** *99* (7), 1787–1799.
8. Niyogi, S.; Hamon, M. A.; Hu, H.; Zhao, B.; Bhowmik, P.; Sen, R.; Itkis, M. E.; Haddon, R. C. Chemistry of Single-Walled Carbon Nanotubes. *Accounts. Chem. Res.* **2002,** *35* (12), 1105–1113.
9. Bandow, S.; Asaka, S.; Saito, Y.; Rao, A. M.; Grigorian, L.; Richter, E.; Eklund, P. C. Effect of the Growth Temperature on the Diameter Distribution and Chirality of Single-Wall Carbon Nanotubes. *Phys. Rev. Lett.* **1998,** *80* (17), 3779–3782.
10. Hersam, M. C. Progress towards Monodisperse Single-Walled Carbon Nanotubes. *Nat. Nanotechnol.* **2008,** *3* (7), 387–394.
11. Zhang, Q.; Huang, J. Q.; Qian, W. Z.; Zhang, Y. Y.; Wei, F. The Road for Nanomaterials Industry: A Review of Carbon Nanotube Production, Post-Treatment, and Bulk Applications for Composites and Energy Storage. *Small* **2013,** *9* (8), 1237–1265.
12. Tasis, D.; Tagmatarchis, N.; Bianco, A.; Prato, M. Chemistry of Carbon Nanotubes. *Chem. Rev.* **2006,** *106* (3), 1105–1136.
13. Karousis, N.; Tagmatarchis, N.; Tasis, D. Current Progress on the Chemical Modification of Carbon Nanotubes. *Chem. Rev.* **2010,** *110* (9), 5366–5397.
14. Collins, W. R.; Lewandowski, W.; Schmois, E.; Walish, J.; Swager, T. M. Claisen Rearrangement of Graphite Oxide: A Route to Covalently Functionalized Graphenes. *Angew. Chem. Int. Edit.* **2011,** *50* (38), 8848–8852.

15. Ghosh, S.; Bachilo, S. M.; Weisman, R. B. Advanced Sorting of Single-Walled Carbon Nanotubes by Nonlinear Density-Gradient Ultracentrifugation. *Nat. Nanotechnol.* **2010,** *5* (6), 443–450.
16. Weisman, R. B.; Bachilo, S. M. Dependence of Optical Transition Energies on Structure for Single-Walled Carbon Nanotubes in Aqueous Suspension: An Empirical Kataura Plot. *Nano Lett.* **2003,** *3* (9), 1235–1238.
17. Dresselhaus, M. S.; Dresselhaus, G.; Saito, R. Physics of Carbon Nanotubes. *Carbon* **1995,** *33* (7), 883–891.
18. Jeong, H. K.; Lee, Y. P.; Lahaye, R. J. W. E.; Park, M. H.; An, K. H.; Kim, I. J.; Yang, C. W.; Park, C. Y.; Ruoff, R. S.; Lee, Y. H. Evidence of Graphitic AB Stacking Order of Graphite Oxides. *J. Am. Chem. Soc.* **2008,** *130* (4), 1362–1366.
19. Liao, L.; Peng, H. L.; Liu, Z. F. Chemistry Makes Graphene Beyond Graphene. *J. Am. Chem. Soc.* **2014,** *136* (35), 12194–12200.
20. Ferrari, A. C.; Bonaccorso, F.; Fal'ko, V.; Novoselov, K. S.; Roche, S.; Boggild, P.; Borini, S.; Koppens, F. H. L.; Palermo, V.; Pugno, N.; Garrido, J. A.; Sordan, R.; Bianco, A.; Ballerini, L.; Prato, M.; Lidorikis, E.; Kivioja, J.; Marinelli, C.; Ryhanen, T.; Morpurgo, A.; Coleman, J. N.; Nicolosi, V.; Colombo, L.; Fert, A.; Garcia-Hernandez, M.; Bachtold, A.; Schneider, G. F.; Guinea, F.; Dekker, C.; Barbone, M.; Sun, Z. P.; Galiotis, C.; Grigorenko, A. N.; Konstantatos, G.; Kis, A.; Katsnelson, M.; Vandersypen, L.; Loiseau, A.; Morandi, V.; Neumaier, D.; Treossi, E.; Pellegrini, V.; Polini, M.; Tredicucci, A.; Williams, G. M.; Hong, B. H.; Ahn, J. H.; Kim, J. M.; Zirath, H.; van Wees, B. J.; van der Zant, H.; Occhipinti, L.; Di Matteo, A.; Kinloch, I. A.; Seyller, T.; Quesnel, E.; Feng, X. L.; Teo, K.; Rupesinghe, N.; Hakonen, P.; Neil, S. R. T.; Tannock, Q.; Lofwander, T.; Kinaret, J. Science and Technology Roadmap for Graphene, Related Two-Dimensional Crystals, and Hybrid Systems. *Nanoscale* **2015,** *7* (11), 4598–4810.
21. Allen, M. J.; Tung, V. C.; Kaner, R. B. Honeycomb Carbon: A Review of Graphene. *Chem. Rev.* **2010,** *110* (1), 132–145.
22. Huang, X.; Yin, Z. Y.; Wu, S. X.; Qi, X. Y.; He, Q. Y.; Zhang, Q. C.; Yan, Q. Y.; Boey, F.; Zhang, H. Graphene-Based Materials: Synthesis, Characterization, Properties, and Applications. *Small* **2011,** *7* (14), 1876–1902.
23. Stankovich, S.; Dikin, D. A.; Piner, R. D.; Kohlhaas, K. A.; Kleinhammes, A.; Jia, Y.; Wu, Y.; Nguyen, S. T.; Ruoff, R. S. Synthesis of Graphene-Based Nanosheets via Chemical Reduction of Exfoliated Graphite Oxide. *Carbon* **2007,** *45* (7), 1558–1565.
24. Kosynkin, D. V.; Higginbotham, A. L.; Sinitskii, A.; Lomeda, J. R.; Dimiev, A.; Price, B. K.; Tour, J. M. Longitudinal Unzipping of Carbon Nanotubes to Form Graphene Nanoribbons. *Nature* **2009,** *458* (7240), 872–876.
25. Yi, M.; Shen, Z. G. A Review on Mechanical Exfoliation for the Scalable Production of Graphene. *J. Mater. Chem. A* **2015,** *3* (22), 11700–11715.
26. Ciesielski, A.; Samori, P. Graphene via Sonication Assisted Liquid-Phase Exfoliation. *Chem. Soc. Rev.* **2014,** *43* (1), 381–398.
27. Xia, Z. Y.; Pezzini, S.; Treossi, E.; Giambastiani, G.; Corticelli, F.; Morandi, V.; Zanelli, A.; Bellani, V.; Palermo, V. The Exfoliation of Graphene in Liquids by Electrochemical, Chemical, and Sonication-Assisted Techniques: A Nanoscale Study. *Adv. Funct. Mater.* **2013,** *23* (37), 4684–4693.

28. Suk, J. W.; Kitt, A.; Magnuson, C. W.; Hao, Y. F.; Ahmed, S.; An, J. H.; Swan, A. K.; Goldberg, B. B.; Ruoff, R. S. Transfer of CVD-Grown Monolayer Graphene onto Arbitrary Substrates. *Acs Nano* **2011,** *5* (9), 6916–6924.
29. Kim, K. S.; Zhao, Y.; Jang, H.; Lee, S. Y.; Kim, J. M.; Kim, K. S.; Ahn, J. H.; Kim, P.; Choi, J. Y.; Hong, B. H. Large-Scale Pattern Growth of Graphene Films for Stretchable Transparent Electrodes. *Nature* **2009,** *457* (7230), 706–710.
30. Shin, H. J.; Choi, W. M.; Yoon, S. M.; Han, G. H.; Woo, Y. S.; Kim, E. S.; Chae, S. J.; Li, X. S.; Benayad, A.; Loc, D. D.; Gunes, F.; Lee, Y. H.; Choi, J. Y. Transfer-Free Growth of Few-Layer Graphene by Self-Assembled Monolayers. *Adv. Mater.* **2011,** *23* (38), 4392–4397.
31. Zhang, Y.; Zhang, L. Y.; Zhou, C. W. Review of Chemical Vapor Deposition of Graphene and Related Applications. *Accounts. Chem. Res.* **2013,** *46* (10), 2329–2339.
32. Sinitskii, A.; Tour, J. M. Patterning Graphene through the Self-Assembled Templates: Toward Periodic Two-Dimensional Graphene Nanostructures with Semiconductor Properties. *J. Am. Chem. Soc.* **2010,** *132* (42), 14730–14732.
33. Belin, T.; Epron, F. Characterization Methods of Carbon Nanotubes: A Review. *Mat. Sci. Eng. B: Solid* **2005,** *119* (2), 105–118.
34. Wepasnick, K. A.; Smith, B. A.; Bitter, J. L.; Fairbrother, D. H. Chemical and Structural Characterization of Carbon Nanotube Surfaces. *Anal. Bioanal .Chem.* **2010,** *396* (3), 1003–1014.
35. Naumov, A. V.; Ghosh, S.; Tsyboulski, D. A.; Bachilo, S. M.; Weisman, R. B. Analyzing Absorption Backgrounds in Single-Walled Carbon Nanotube Spectra. *Acs Nano* **2011,** *5* (3), 1639–1648.
36. Ferrari, A. C.; Basko, D. M. Raman Spectroscopy As a Versatile Tool for Studying the Properties of Graphene. *Nat. Nanotechnol.* **2013,** *8* (4), 235–246.
37. Eckmann, A.; Felten, A.; Mishchenko, A.; Britnell, L.; Krupke, R.; Novoselov, K. S.; Casiraghi, C. Probing the Nature of Defects in Graphene by Raman Spectroscopy. *Nano Lett.* **2012,** *12* (8), 3925–3930.
38. Malard, L. M.; Pimenta, M. A.; Dresselhaus, G.; Dresselhaus, M. S. Raman Spectroscopy in Graphene. *Phys. Rep.* **2009,** *473* (5–6), 51–87.
39. Coleman, K. S.; Chakraborty, A. K.; Bailey, S. R.; Sloan, J.; Alexander, M. Iodination of Single-walled Carbon Nanotubes. *Chem. Mater.* **2007,** *19* (5), 1076–1081.
40. Moniruzzaman, M.; Winey, K. I. Polymer Nanocomposites Containing Carbon Nanotubes. *Macromolecules* **2006,** *39* (16), 5194–5205.
41. Spitalsky, Z.; Tasis, D.; Papagelis, K.; Galiotis, C. Carbon Nanotube-Polymer Composites: Chemistry, Processing, Mechanical and Electrical Properties. *Prog. Polym. Sci.* **2010,** *35* (3), 357–401.
42. Emrick, T.; Pentzer, E. Nanoscale Assembly into Extended and Continuous Structures and Hybrid Materials. *Npg Asia Materials* **2013,** *5*, e43.
43. Georgakilas, V.; Tiwari, J. N.; Kemp, K. C.; Perrnan, J. A.; Bourlinos, A. B.; Kim, K. S.; Zboril, R. Noncovalent Functionalization of Graphene and Graphene Oxide for Energy Materials, Biosensing, Catalytic, and Biomedical Applications. *Chem. Rev.* **2016,** *116* (9), 5464–5519.
44. Byrne, M. T.; Gun'ko, Y. K. Recent Advances in Research on Carbon Nanotube-Polymer Composites. *Adv. Mater.* **2010,** *22* (15), 1672–1688.
45. Peng, X. H.; Wong, S. S. Functional Covalent Chemistry of Carbon Nanotube Surfaces. *Adv. Mater.* **2009,** *21* (6), 625–642.

46. Huang, X.; Qi, X. Y.; Boey, F.; Zhang, H. Graphene-Based Composites. *Chem. Soc. Rev.* **2012,** *41* (2), 666–686.
47. Feng, J. T.; Sui, J. H.; Cai, W.; Gao, Z. Y. Microstructure and Mechanical Properties of Carboxylated Carbon Nanotubes/Poly(L-lactic acid) Composite. *J. Compos. Mater.* **2008,** *42* (16), 1587–1595.
48. Hirsch, A. Functionalization of Single-Walled Carbon Nanotubes. *Angew. Chem. Int. Edit.* **2002,** *41* (11), 1853–1859.
49. Singh, P.; Campidelli, S.; Giordani, S.; Bonifazi, D.; Bianco, A.; Prato, M. Organic Functionalisation and Characterisation of Single-Walled Carbon Nanotubes. *Chem. Soc. Rev.* **2009,** *38* (8), 2214–2230.
50. Georgakilas, V.; Otyepka, M.; Bourlinos, A. B.; Chandra, V.; Kim, N.; Kemp, K. C.; Hobza, P.; Zboril, R.; Kim, K. S. Functionalization of Graphene: Covalent and Non-Covalent Approaches, Derivatives and Applications. *Chem. Rev.* **2012,** *112* (11), 6156–6214.
51. Banerjee, S.; Hemraj-Benny, T.; Wong, S. S. Covalent Surface Chemistry of Single-Walled Carbon Nanotubes. *Adv. Mater.* **2005,** *17* (1), 17–29.
52. Zhang, M. F.; Li, Y.; Su, Z. Q.; Wei, G. Recent Advances in the Synthesis and Applications of Graphene-Polymer Nanocomposites. *Polym. Chem.* **2015,** *6* (34), 6107–6124.
53. Tang, Q.; Zhou, Z.; Chen, Z. F. Graphene-Related Nanomaterials: Tuning Properties by Functionalization. *Nanoscale* **2013,** *5* (11), 4541–4583.
54. Su, Q.; Pang, S. P.; Alijani, V.; Li, C.; Feng, X. L.; Müllen, K. Composites of Graphene with Large Aromatic Molecules. *Adv. Mater.* **2009,** *21* (31), 3191–3195.
55. Zhang, X. F.; Shao, X. N. π–π Binding Ability of Different Carbon Nano-Materials with Aromatic Phthalocyanine Molecules: Comparison between Graphene, Graphene Oxide and Carbon Nanotubes. *J. Photoch. Photobio. A* **2014,** *278*, 69–74.
56. Gerstel, P.; Klumpp, S.; Hennrich, F.; Poschlad, A.; Meded, V.; Blasco, E.; Wenzel, W.; Kappes, M. M.; Barner-Kowollik, C. Highly Selective Dispersion of Single-Walled Carbon Nanotubes via Polymer Wrapping: A Combinatorial Study via Modular Conjugation. *Acs Macro. Lett.* **2014,** *3* (1), 10–15.
57. Kim, H.; Abdala, A. A.; Macosko, C. W. Graphene/Polymer Nanocomposites. *Macromolecules* **2010,** *43* (16), 6515–6530.
58. Pfeffermann, M.; Dong, R. H.; Graf, R.; Zajaczkowski, W.; Gorelik, T.; Pisula, W.; Narita, A.; Mullen, K.; Feng, X. L. Free-Standing Mono Layer Two-Dimensional Supramolecular Organic Framework with Good Internal Order. *J. Am. Chem. Soc.* **2015,** *137* (45), 14525–14532.
59. Park, S.; Vosguerichian, M.; Bao, Z. A. A Review of Fabrication and Applications of Carbon Nanotube Film-Based Flexible Electronics. *Nanoscale* **2013,** *5* (5), 1727–1752.
60. Hong, G. S.; Diao, S. O.; Antaris, A. L.; Dai, H. J., Carbon Nanomaterials for Biological Imaging and Nanomedicinal Therapy. *Chem. Rev.* **2015,** *115* (19), 10816–10906.
61. Shi, X. H.; von dem Bussche, A.; Hurt, R. H.; Kane, A. B.; Gao, H. J. Cell Entry of One-Dimensional Nanomaterials Occurs by Tip Recognition and Rotation. *Nat. Nanotechnol.* **2011,** *6* (11), 714–719.
62. De Volder, M. F. L.; Tawfick, S. H.; Baughman, R. H.; Hart, A. J. Carbon Nanotubes: Present and Future Commercial Applications. *Science* **2013,** *339* (6119), 535–539.
63. Yamada, T.; Hayamizu, Y.; Yamamoto, Y.; Yomogida, Y.; Izadi-Najafabadi, A.; Futaba, D. N.; Hata, K. A Stretchable Carbon Nanotube Strain Sensor for Human-Motion Detection. *Nat. Nanotechnol.* **2011,** *6* (5), 296–301.

64. Goenka, S.; Sant, V.; Sant, S. Graphene-Based Nanomaterials for Drug Delivery and Tissue Engineering. *J. Control. Release* **2014,** *173*, 75–88.
65. Lu, F. S.; Gu, L. R.; Meziani, M. J.; Wang, X.; Luo, P. G.; Veca, L. M.; Cao, L.; Sun, Y. P. Advances in Bioapplications of Carbon Nanotubes. *Adv. Mater.* **2009,** *21* (2), 139–152.
66. Dong, L.; Joseph, K. L.; Witkowski, C. M.; Craig, M. M. Cytotoxicity of Single-Walled Carbon Nanotubes Suspended in Various Surfactants. *Nanotechnology* **2008,** *19* (25), 255702.
67. Prencipe, G.; Tabakman, S. M.; Welsher, K.; Liu, Z.; Goodwin, A. P.; Zhang, L.; Henry, J.; Dai, H. J. PEG Branched Polymer for Functionalization of Nanomaterials with Ultralong Blood Circulation. *J. Am. Chem. Soc.* **2009,** *131* (13), 4783–4787.
68. Jokerst, J. V.; Lobovkina, T.; Zare, R. N.; Gambhir, S. S. Nanoparticle PEGylation for Imaging and Therapy. *Nanomedicine* **2011,** *6* (4), 715–728.
69. Fabbro, C.; Ali-Boucetta, H.; Da Ros, T.; Kostarelos, K.; Bianco, A.; Prato, M. Targeting Carbon Nanotubes against Cancer. *Chem. Commun.* **2012,** *48* (33), 3911–3926.
70. Liang, F.; Chen, B. A Review on Biomedical Applications of Single-Walled Carbon Nanotubes. *Curr. Med. Chem.* **2010,** *17* (1), 10–24.
71. Meng, L. J.; Zhang, X. K.; Lu, Q. H.; Fei, Z. F.; Dyson, P. J. Single Walled Carbon Nanotubes As Drug Delivery Vehicles: Targeting Doxorubicin to Tumors. *Biomaterials* **2012,** *33* (6), 1689–1698.
72. Heister, E.; Lamprecht, C.; Neves, V.; Tilmaciu, C.; Datas, L.; Flahaut, E.; Soula, B.; Hinterdorfer, P.; Coley, H. M.; Silva, S. R. P.; McFadden, J. Higher Dispersion Efficacy of Functionalized Carbon Nanotubes in Chemical and Biological Environments. *Acs Nano* **2010,** *4* (5), 2615–2626.
73. Heister, E.; Neves, V.; Lamprecht, C.; Silva, S. R. P.; Coley, H. M.; McFadden, J. Drug Loading, Dispersion Stability, and Therapeutic Efficacy in Targeted Drug Delivery with Carbon Nanotubes. *Carbon* **2012,** *50* (2), 622–632.
74. Meyers, S. R.; Grinstaff, M. W. Biocompatible and Bioactive Surface Modifications for Prolonged *In Vivo* Efficacy. *Chem. Rev.* **2012,** *112* (3), 1615–1632.
75. Xu, X. L.; Chen, X. S.; Ma, P. A.; Wang, X. R.; Jing, X. B. The Release Behavior of Doxorubicin Hydrochloride from Medicated Fibers Prepared by Emulsion-Electrospinning. *Eur. J. Pharm. Biopharm.* **2008,** *70* (1), 165–170.
76. Feng, L. Z.; Zhang, S. A.; Liu, Z. A. Graphene Based Gene Transfection. *Nanoscale* **2011,** *3* (3), 1252–1257.
77. Qiu, L. Y.; Bae, Y. H. Polymer Architecture and Drug Delivery. *Pharm. Res.* **2006,** *23* (1), 1–30.
78. Mao, H. Y.; Laurent, S.; Chen, W.; Akhavan, O.; Imani, M.; Ashkarran, A. A.; Mahmoudi, M. Graphene: Promises, Facts, Opportunities, and Challenges in Nanomedicine. *Chem. Rev.* **2013,** *113* (5), 3407–3424.
79. Kandambeth, S.; Venkatesh, V.; Shinde, D. B.; Kumari, S.; Halder, A.; Verma, S.; Banerjee, R. Self-Templated Chemically Stable Hollow Spherical Covalent Organic Framework. *Nat. Commun.* **2015,** *6*.
80. Zhang, L.; Li, C.; Liu, A. R.; Shi, G. Q. Electrosynthesis of Graphene Oxide/Polypyrene Composite Films and Their Applications for Sensing Organic Vapors. *J. Mater. Chem.* **2012,** *22* (17), 8438–8443.
81. Joo, S.; Brown, R. B. Chemical Sensors with Integrated Electronics. *Chem. Rev.* **2008,** *108* (2), 638–651.

82. Rajesh; Ahuja, T.; Kumar, D. Recent Progress in the Development of Nano-Structured Conducting Polymers/Nanocomposites for Sensor Applications. *Sensor Actuat. B: Chemical* **2009,** *136* (1), 275–286.
83. Yu, X.; Zhang, W.; Zhang, P.; Su, Z. Fabrication Technologies and Sensing Applications of Graphene-Based Composite Films: Advances and Challenges. *Biosens. Bioelectron.* **2016**. doi: 10.1016/j.bios.2016.01.081.
84. Colson, J. W.; Woll, A. R.; Mukherjee, A.; Levendorf, M. P.; Spitler, E. L.; Shields, V. B.; Spencer, M. G.; Park, J.; Dichtel, W. R. Oriented 2D Covalent Organic Framework Thin Films on Single-Layer Graphene. *Science* **2011,** *332* (6026), 228–231.
85. Lu, X. F.; Zhang, W. J.; Wang, C.; Wen, T. C.; Wei, Y. One-Dimensional Conducting Polymer Nanocomposites: Synthesis, Properties and Applications. *Prog. Polym. Sci.* **2011,** *36* (5), 671–712.
86. Hatchett, D. W.; Josowicz, M. Composites of Intrinsically Conducting Polymers As Sensing Nanomaterials. *Chem. Rev.* **2008,** *108* (2), 746–769.
87. Li, J.; Lu, Y. J.; Ye, Q.; Cinke, M.; Han, J.; Meyyappan, M. Carbon Nanotube Sensors for Gas and Organic Vapor Detection. *Nano Lett.* **2003,** *3* (7), 929–933.
88. Pengfei, Q. F.; Vermesh, O.; Grecu, M.; Javey, A.; Wang, O.; Dai, H. J.; Peng, S.; Cho, K. J. Toward Large Arrays of Multiplex Functionalized Carbon Nanotube Sensors for Highly Sensitive and Selective Molecular Detection. *Nano Lett.* **2003,** *3* (3), 347–351.
89. Ding, M. N.; Tang, Y. F.; Gou, P. P.; Reber, M. J.; Star, A. Chemical Sensing with Polyaniline Coated Single-Walled Carbon Nanotubes. *Adv. Mater.* **2011,** *23* (4), 536–540.
90. Kotchey, G. P.; Hasan, S. A.; Kapralov, A. A.; Ha, S. H.; Kim, K.; Shvedova, A. A.; Kagan, V. E.; Star, A. A Natural Vanishing Act: The Enzyme-Catalyzed Degradation of Carbon Nanomaterials. *Accounts. Chem. Res.* **2012,** *45* (10), 1770–1781.
91. Zhou, X. J.; Zhang, Y.; Wang, C.; Wu, X. C.; Yang, Y. Q.; Zheng, B.; Wu, H. X.; Guo, S. W.; Zhang, J. Y. Photo-Fenton Reaction of Graphene Oxide: A New Strategy to Prepare Graphene Quantum Dots for DNA Cleavage. *Acs Nano* **2012,** *6* (8), 6592–6599.
92. Nyska, A.; Kohen, R. Oxidation of Biological Systems: Oxidative Stress Phenomena, Antioxidants, Redox Reactions, and Methods for Their Quantification. *Toxicol. Pathol.* **2002,** *30* (6), 620–650.
93. Bianco, A.; Kostarelos, K.; Prato, M. Making Carbon Nanotubes Biocompatible and Biodegradable. *Chem. Commun.* **2011,** *47* (37), 10182–10188.
94. Kostarelos, K.; Bianco, A.; Prato, M. Promises, Facts and Challenges for Carbon Nanotubes in Imaging and Therapeutics. *Nat. Nanotechnol.* **2009,** *4* (10), 627–633.
95. Bhattacharya, K.; Sacchetti, C.; El-Sayed, R.; Fornara, A.; Kotchey, G. P.; Gaugler, J. A.; Star, A.; Bottini, M.; Fadeel, B. Enzymatic 'Stripping' and Degradation of PEGylated Carbon Nanotubes. *Nanoscale* **2014,** *6* (24), 14686–14690.
96. Bai, H.; Jiang, W. T.; Kotchey, G. P.; Saidi, W. A.; Bythell, B. J.; Jarvis, J. M.; Marshall, A. G.; Robinson, R. A. S.; Star, A. Insight into the Mechanism of Graphene Oxide Degradation via the Photo-Fenton Reaction. *J. Phys. Chem. C* **2014,** *118* (19), 10519–10529.
97. Auwarter, W.; Ecija, D.; Klappenberger, F.; Barth, J. V. Porphyrins at Interfaces. *Nat. Chem.* **2015,** *7* (2), 105–120.
98. Qu, R.; Shen, L. L.; Chai, Z. H.; Jing, C.; Zhang, Y. F.; An, Y. L.; Shi, L. Q. Hemin-Block Copolymer Micelle as an Artificial Peroxidase and Its Applications in Chromogenic Detection and Biocatalysis. *Acs Appl. Mater. Inter.* **2014,** *6* (21), 19207–19216.

99. Vlasova, I. I.; Kapralov, A. A.; Michael, Z. P.; Burkert, S. C.; Shurin, M. R.; Star, A.; Shvedova, A. A.; Kagan, V. E. Enzymatic Oxidative Biodegradation of Nanoparticles: Mechanisms, Significance and Applications. *Toxicol. Appl. Pharm* **2016,** *299*, 58–69.
100. Henderson, J.; Heinecke, J. Myeloperoxidase: Enzymology. *In Peroxidases and Catalases*; Dunford, H. B. Ed. Wiley: Hoboken, NJ, **2010**; 257–269.
101. Klebanoff, S. J. Myeloperoxidase: Friend and Foe. *J. Leukocyte. Biol.* **2005,** *77* (5), 598–625.
102. Szatrowski, T. P.; Nathan, C. F. Production of Large Amounts of Hydrogen-Peroxide by Human Tumor-Cells. *Cancer Res.* **1991,** *51* (3), 794–798.
103. Hampton, M. B.; Kettle, A. J.; Winterbourn, C. C. Inside the Neutrophil Phagosome: Oxidants, Myeloperoxidase, and Bacterial Killing. *Blood* **1998,** *92* (9), 3007–3017.
104. Radi, R., Peroxynitrite, a Stealthy Biological Oxidant. *J. Biol. Chem.* **2013,** *288* (37), 26464–26472.
105. Alvarez, M. N.; Peluffo, G.; Piacenza, L.; Radi, R. Intraphagosomal Peroxynitrite As A Macrophage-Derived Cytotoxin against Internalized Trypanosoma Cruzi Consequences for Oxidative Killing and Role of Microbial Peroxidredoxins in Infectivity. *J. Biol. Chem.* **2011,** *286* (8), 6627–6640.
106. Beckman, J. S.; Koppenol, W. H. Nitric Oxide, Superoxide, and Peroxynitrite: The Good, the Bad, and the Ugly. *Am. J. Physiol.* **1996,** *271* (5), C1424–C1437.
107. Kagan, V. E.; Kapralov, A. A.; St Croix, C. M.; Watkins, S. C.; Kisin, E. R.; Kotchey, G. P.; Balasubramanian, K.; Vlasova, I. I.; Yu, J.; Kim, K.; Seo, W.; MallampaIli, R. K.; Star, A.; Shvedova, A. A. Lung Macrophages "Digest" Carbon Nanotubes Using a Superoxide/Peroxynitrite Oxidative Pathway. *Acs Nano* **2014,** *8* (6), 5610–5621.
108. Nalwaya, N.; Deen, W. M. Peroxynitrite Exposure of Cells Cocultured with Macrophages. *Ann. Biomed. Eng.* **2004,** *32* (5), 664–676.
109. Pacher, P.; Beckman, J. S.; Liaudet, L. Nitric Oxide and Peroxynitrite in Health and Disease. *Physiol. Rev.* **2007,** *87* (1), 315–424.
110. Kagan, V. E.; Konduru, N. V.; Feng, W. H.; Allen, B. L.; Conroy, J.; Volkov, Y.; Vlasova, I. I.; Belikova, N. A.; Yanamala, N.; Kapralov, A.; Tyurina, Y. Y.; Shi, J. W.; Kisin, E. R.; Murray, A. R.; Franks, J.; Stolz, D.; Gou, P. P.; Klein-Seetharaman, J.; Fadeel, B.; Star, A.; Shvedova, A. A. Carbon Nanotubes Degraded by Neutrophil Myeloperoxidase Induce Less Pulmonary Inflammation. *Nat. Nanotechnol.* **2010,** *5* (5), 354–359.
111. Andon, F. T.; Kapralov, A. A.; Yanamala, N.; Feng, W. H.; Baygan, A.; Chambers, B. J.; Hultenby, K.; Ye, F.; Toprak, M. S.; Brandner, B. D.; Fornara, A.; Klein-Seetharaman, J.; Kotchey, G. P.; Star, A.; Shvedova, A. A.; Fadeel, B.; Kagan, V. E. Biodegradation of Single-Walled Carbon Nanotubes by Eosinophil Peroxidase. *Small* **2013,** *9* (16), 2721–2729.
112. Bhattacharya, K.; El-Sayed, R.; Andon, F. T.; Mukherjee, S. P.; Gregory, J.; Li, H.; Zhao, Y. C.; Seo, W. J.; Fornara, A.; Brandner, B.; Toprak, M. S.; Leifer, K.; Star, A.; Fadeel, B. Lactoperoxidase-Mediated Degradation of Single-Walled Carbon Nanotubes in the Presence of Pulmonary Surfactant. *Carbon* **2015,** *95*, 506–517.
113. Allen, B. L.; Kichambare, P. D.; Gou, P.; Vlasova, I. I.; Kapralov, A. A.; Konduru, N.; Kagan, V. E.; Star, A. Biodegradation of Single-Walled Carbon Nanotubes through Enzymatic Catalysis. *Nano Lett.* **2008,** *8* (11), 3899–3903.
114. Allen, B. L.; Kotchey, G. P.; Chen, Y. N.; Yanamala, N. V. K.; Klein-Seetharaman, J.; Kagan, V. E.; Star, A. Mechanistic Investigations of Horseradish Peroxidase-Catalyzed

Degradation of Single-Walled Carbon Nanotubes. *J. Am. Chem. Soc.* **2009,** *131* (47), 17194–17205.
115. Zhao, Y.; Allen, B. L.; Star, A. Enzymatic Degradation of Multiwalled Carbon Nanotubes. *J. Phys. Chem. A* **2011,** *115* (34), 9536–9544.
116. Kurapati, R.; Russier, J.; Squillaci, M. A.; Treossi, E.; Menard-Moyon, C.; Del Rio-Castillo, A. E.; Vazquez, E.; Samori, P.; Palermo, V.; Bianco, A. Dispersibility-Dependent Biodegradation of Graphene Oxide by Myeloperoxidase. *Small* **2015,** *11* (32), 3985–3994.
117. Kotchey, G. P.; Allen, B. L.; Vedala, H.; Yanamala, N.; Kapralov, A. A.; Tyurina, Y. Y.; Klein-Seetharaman, J.; Kagan, V. E.; Star, A. The Enzymatic Oxidation of Graphene Oxide. *Acs Nano* **2011,** *5* (3), 2098–2108.
118. Kotchey, G. P.; Gaugler, J. A.; Kapralov, A. A.; Kagan, V. E.; Star, A. Effect of Antioxidants on Enzyme-Catalysed Biodegradation of Carbon Nanotubes. *J. Mater. Chem. B* **2013,** *1* (3), 302–309.
119. Vlasova, I. I.; Vakhrusheva, T. V.; Sokolov, A. V.; Kostevich, V. A.; Ragimov, A. A. Peroxidase-Induced Degradation of Single-Walled Carbon Nanotubes: Hypochlorite Is a Major Oxidant Capable of *In Vivo* Degradation of Carbon Nanotubes. *J. Physics: Conf. Ser*. **2011**, *291* (1), 012056.
120. Konduru, N. V.; Tyurina, Y. Y.; Feng, W. H.; Basova, L. V.; Belikova, N. A.; Bayir, H.; Clark, K.; Rubin, M.; Stolz, D.; Vallhov, H.; Scheynius, A.; Witasp, E.; Fadeel, B.; Kichambare, P. D.; Star, A.; Kisin, E. R.; Murray, A. R.; Shvedova, A. A.; Kagan, V. E. Phosphatidylserine Targets Single-Walled Carbon Nanotubes to Professional Phagocytes *In Vitro* and *In Vivo*. *Plos One* **2009,** *4* (2).
121. Vlasova, I. I.; Vakhrusheva, T. V.; Sokolov, A. V.; Kostevich, V. A.; Gusev, A. A.; Gusev, S. A.; Melnikova, V. I.; Lobach, A. S. PEGylated Single-Walled Carbon Nanotubes Activate Neutrophils to Increase Production of Hypochlorous Acid, the Oxidant Capable of Degrading Nanotubes. *Toxicol. Appl. Pharm.* **2012,** *264* (1), 131–142.
122. Kotchey, G. P.; Zhao, Y.; Kagan, V. E.; Star, A. Peroxidase-Mediated Biodegradation of Carbon Nanotubes *In Vitro* and *In Vivo*. *Adv. Drug Deliver. Rev.* **2013,** *65* (15), 1921–1932.
123. Zhang, J.; Zou, H. L.; Qing, Q.; Yang, Y. L.; Li, Q. W.; Liu, Z. F.; Guo, X. Y.; Du, Z. L., Effect of Chemical Oxidation on the Structure of Single-Walled Carbon Nanotubes. *J. Phys. Chem. B* **2003,** *107* (16), 3712–3718.
124. Que, L.; Tolman, W. B. Biologically Inspired Oxidation Catalysis. *Nature* **2008,** *455* (7211), 333–340.
125. Lin, Y.; Watson, K. A.; Kim, J. W.; Baggett, D. W.; Working, D. C.; Connell, J. W. Bulk Preparation of Holey Graphene via Controlled Catalytic Oxidation. *Nanoscale* **2013,** *5* (17), 7814–7824.
126. Radich, J. G.; Kamat, P. V. Making Graphene Holey. Gold-Nanoparticle-Mediated Hydroxyl Radical Attack on Reduced Graphene Oxide. *ACS Nano* **2013,** *7* (6), 5546–5557.
127. Nichela, D. A.; Berkovic, A. M.; Costante, M. R.; Juliarena, M. P.; Einschlag, F. S. G. Nitrobenzene Degradation in Fenton-Like Systems Using Cu(II) as Catalyst. Comparison between Cu(II)- and Fe(III)-Based Systems. *Chem. Eng. J.* **2013,** *228*, 1148–1157.
128. Brillas, E. S., I.; Oturan, M. A. Electro-Fenton Process and Related Electrochemical Technologies Based on Fenton's Reaction Chemistry. *Chem. Rev.* **2009,** *109*, 6570–6631.
129. Gabriel, J.; Baldrian, P.; Verma, P.; Cajthaml, T.; Merhautova, V.; Eichlerova, I.; Stoytchev, I.; Trnka, T.; Stopka, P.; Nerud, F. Degradation of BTEX and PAHs by Co(II) and

Cu(II)-Based Radical-Generating Systems. *Appl. Catal. B: Environmental* **2004,** *51* (3), 159-164.
130. Beletskaya, I.; Tyurin, V. S.; Tsivadze, A. Y.; Guilard, R.; Stern, C. Supramolecular Chemistry of Metalloporphyrins. *Chem. Rev.* **2009,** *109* (5), 1659–1713.
131. Meunier, B. Metalloporphyrins as Versatile Catalysts for Oxidation Reactions and Oxidative DNA Cleavage. *Chem. Rev.* **1992,** *92* (6), 1411–1456.
132. Zakzeski, J.; Bruijnincx, P. C. A.; Jongerius, A. L.; Weckhuysen, B. M. The Catalytic Valorization of Lignin for the Production of Renewable Chemicals. *Chem. Rev.* **2010,** *110* (6), 3552–3599.
133. Artaud, I.; Benaziza, K.; Mansuy, D. Iron Porphyrin-Catalyzed Oxidation of 1,2-Dimethoxyarenes: A Discussion of the Different Reactions Involved and the Competition between the Formation of Methoxyquinones or Muconic Dimethyl Esters. *J. Org. Chem.* **1993,** *58* (12), 3373–3380.
134. Xue, T.; Jiang, S.; Qu, Y. Q.; Su, Q.; Cheng, R.; Dubin, S.; Chiu, C. Y.; Kaner, R.; Huang, Y.; Duan, X. F. Graphene-Supported Hemin as a Highly Active Biomimetic Oxidation Catalyst. *Angew. Chem. Int. Edit.* **2012,** *51* (16), 3822–3825.
135. Fan, C. L.; Li, W.; Li, X.; Zhao, S. J.; Zhang, L.; Mo, Y. J.; Cheng, R. M. Efficient Photo-Assisted Fenton Oxidation Treatment of Multi-Walled Carbon Nanotubes. *Chinese Sci. Bull.* **2007,** *52* (15), 2054–2062.
136. Li, W. B., Y.; Zhang, Y.; Sun, M.; Cheng, R.; Xu, X.; Chen, Y.;; Mo, Y. J. Effect of Hydroxyl Radical on the Structure of Multi-Walled Carbon Nanotubes. *Synth. Met.* **2005,** *155*, 509–515.
137. Liu, Z.; Fan, A. C.; Rakhra, K.; Sherlock, S.; Goodwin, A.; Chen, X. Y.; Yang, Q. W.; Felsher, D. W.; Dai, H. J. Supramolecular Stacking of Doxorubicin on Carbon Nanotubes for *In Vivo* Cancer Therapy. *Angew. Chem. Int. Edit.* **2009,** *48* (41), 7668–7672.
138. Wipf, P.; Xiao, J. B.; Jiang, J. F.; Belikova, N. A.; Tyurin, V. A.; Fink, M. P.; Kagan, V. E. Mitochondrial Targeting of Selective Electron Scavengers: Synthesis and Biological Analysis of Hemigramicidin-TEMPO Conjugates. *J. Am. Chem. Soc.* **2005,** *127* (36), 12460–12461.
139. Xun, Z. Y.; Rivera-Sanchez, S.; Ayala-Pena, S.; Lim, J.; Budworth, H.; Skoda, E. M.; Robbins, P. D.; Niedernhofer, L. J.; Wipf, P.; McMurray, C. T. Targeting of XJB-5-131 to Mitochondria Suppresses Oxidative DNA Damage and Motor Decline in a Mouse Model of Huntington's Disease. *Cell Rep.* **2012,** *2* (5), 1137–1142.
140. Atkinson, J.; Kapralov, A. A.; Yanamala, N.; Tyurina, Y. Y.; Amoscato, A. A.; Pearce, L.; Peterson, J.; Huang, Z. T.; Jiang, J. F.; Samhan-Arias, A. K.; Maeda, A.; Feng, W. H.; Wasserloos, K.; Belikova, N. A.; Tyurin, V. A.; Wang, H.; Fletcher, J.; Wang, Y. S.; Vlasova, I. I.; Klein-Seetharaman, J.; Stoyanovsky, D. A.; Bayir, H.; Pitt, B. R.; Epperly, M. W.; Greenberger, J. S.; Kagan, V. E. A Mitochondria-Targeted Inhibitor of Cytochrome C Peroxidase Mitigates Radiation-Induced Death. *Nat. Commun.* **2011,** *2*.
141. Singh, R.; Lillard, J. W. Nanoparticle-Based Targeted Drug Delivery. *Exp. Mol. Pathol.* **2009,** *86* (3), 215–223.
142. Lawrence, M. J.; Rees, G. D. Microemulsion-Based Media as Novel Drug Delivery Systems. *Adv. Drug Deliver. Rev.* **2012,** *64*, 175–193.
143. Zrazhevskiy, P.; Sena, M.; Gao, X. H. Designing Multifunctional Quantum Dots for Bioimaging, Detection, and Drug delivery. *Chem. Soc. Rev.* **2010,** *39* (11), 4326–4354.
144. Kumari, A.; Yadav, S. K.; Yadav, S. C. Biodegradable Polymeric Nanoparticles Based Drug Delivery Systems. *Colloid Surface B* **2010,** *75* (1), 1–18.

145. Doane, T. L.; Burda, C. The Unique Role of Nanoparticles in Nanomedicine: Imaging, Drug Delivery and Therapy. *Chem. Soc. Rev.* **2012,** *41* (7), 2885–2911.
146. Geng, Y.; Dalhaimer, P.; Cai, S. S.; Tsai, R.; Tewari, M.; Minko, T.; Discher, D. E. Shape Effects of Filaments versus Spherical Particles in Flow and Drug Delivery. *Nat. Nanotechnol.* **2007,** *2* (4), 249–255.
147. Xu, Z. P.; Zeng, Q. H.; Lu, G. Q.; Yu, A. B. Inorganic Nanoparticles as Carriers for Efficient Cellular Delivery. *Chem. Eng. Sci.* **2006,** *61* (3), 1027–1040.
148. Chiang, I. W.; Brinson, B. E.; Huang, A. Y.; Willis, P. A.; Bronikowski, M. J.; Margrave, J. L.; Smalley, R. E.; Hauge, R. H. Purification and Characterization of Single-Wall Carbon Nanotubes (SWNTs) Obtained from the Gas-Phase Decomposition of CO (HiPco process). *J. Phys. Chem. B* **2001,** *105* (35), 8297–8301.
149. Kam, N. W. S.; Dai, H. J. Carbon Nanotubes as Intracellular Protein Transporters: Generality and Biological Functionality. *J. Am. Chem. Soc.* **2005,** *127* (16), 6021–6026.
150. Ali-Boucetta, H.; Nunes, A.; Sainz, R.; Herrero, M. A.; Tian, B. W.; Prato, M.; Bianco, A.; Kostarelos, K. Asbestos-Like Pathogenicity of Long Carbon Nanotubes Alleviated by Chemical Functionalization. *Angew. Chem. Int. Edit.* **2013,** *52* (8), 2274–2278.
151. Hong, G. S.; Lee, J. C.; Robinson, J. T.; Raaz, U.; Xie, L. M.; Huang, N. F.; Cooke, J. P.; Dai, H. J. Multifunctional *In Vivo* Vascular Imaging Using Near-Infrared II Fluorescence. *Nat. Med.* **2012,** *18* (12), 1841–1846.
152. Nel, A. E.; Madler, L.; Velegol, D.; Xia, T.; Hoek, E. M. V.; Somasundaran, P.; Klaessig, F.; Castranova, V.; Thompson, M. Understanding Biophysicochemical Interactions at the Nano-Bio Interface. *Nat. Mater.* **2009,** *8* (7), 543–557.
153. Danhier, F.; Feron, O.; Preat, V. To exploit the Tumor Microenvironment: Passive and Active Tumor Targeting of Nanocarriers for Anti-Cancer Drug Delivery. *J. Control. Release* **2010,** *148* (2), 135–146.
154. Liu, Z.; Sun, X. M.; Nakayama-Ratchford, N.; Dai, H. J. Supramolecular Chemistry on Water-Soluble Carbon Nanotubes for Drug Loading and Delivery. *Acs Nano* **2007,** *1* (1), 50–56.
155. Liu, Z.; Chen, K.; Davis, C.; Sherlock, S.; Cao, Q. Z.; Chen, X. Y.; Dai, H. J. Drug Delivery with Carbon Nanotubes for *In Vivo* Cancer Treatment. *Cancer Res.* **2008,** *68* (16), 6652–6660.
156. Wu, W.; Li, R. T.; Bian, X. C.; Zhu, Z. S.; Ding, D.; Li, X. L.; Jia, Z. J.; Jiang, X. Q.; Hu, Y. Q. Covalently Combining Carbon Nanotubes with Anticancer Agent: Preparation and Antitumor Activity. *ACS Nano* **2009,** *3* (9), 2740–2750.
157. Heister, E.; Neves, V.; Tilmaciu, C.; Lipert, K.; Beltran, V. S.; Coley, H. M.; Silva, S. R. P.; McFadden, J. Triple Functionalisation of Single-Walled Carbon Nanotubes with Doxorubicin, a Monoclonal Antibody, and a Fluorescent Marker for Targeted Cancer Therapy. *Carbon* **2009,** *47* (9), 2152–2160.
158. Schottler, S.; Becker, G.; Winzen, S.; Steinbach, T.; Mohr, K.; Landfester, K.; Mailander, V.; Wurm, F. R. Protein Adsorption Is Required for Stealth Effect of Poly(ethylene glycol)- and Poly(phosphoester)-Coated Nanocarriers. *Nat. Nanotechnol.* **2016,** *11* (4), 372–377.
159. Zeineldin, R.; Al-Haik, M.; Hudson, L. G. Role of Polyethylene Glycol Integrity in Specific Receptor Targeting of Carbon Nanotubes to Cancer Cells. *Nano Lett.* **2009,** *9* (2), 751–757.
160. Sacchetti, C.; Motamedchaboki, K.; Magrini, A.; Palmieri, G.; Mattei, M.; Bernardini, S.; Rosato, N.; Bottini, N.; Bottini, M. Surface Polyethylene Glycol Conformation Influences the

Protein Corona of Polyethylene Glycol-Modified Single-Walled Carbon Nanotubes: Potential Implications on Biological Performance. *ACS Nano* **2013,** *7* (3), 1974–1989.
161. Welsher, K.; Liu, Z.; Daranciang, D.; Dai, H. Selective Probing and Imaging of Cells with Single Walled Carbon Nanotubes As Near-Infrared Fluorescent Molecules. *Nano Lett.* **2008,** *8* (2), 586–590.
162. Liu, Z.; Cai, W. B.; He, L. N.; Nakayama, N.; Chen, K.; Sun, X. M.; Chen, X. Y.; Dai, H. J. *In Vivo* Biodistribution and Highly Efficient Tumour Targeting of Carbon Nanotubes in Mice. *Nat. Nanotechnol.* **2007,** *2* (1), 47–52.
163. Liu, Z.; Winters, M.; Holodniy, M.; Dai, H. J. siRNA Delivery into Human T Cells and Primary Cells with Carbon-Nanotube Transporters. *Angew. Chem. Int. Edit.* **2007,** *46* (12), 2023–2027.
164. Giorgio, M.; Trinei, M.; Migliaccio, E.; Pelicci, P. G. Hydrogen Peroxide: A Metabolic By-Product or A Common Mediator of Ageing Signals. *Nat. Rev. Mol. Cell Bio.* **2007,** *8* (9), 722–728.
165. Star, A. K., A. A.; Amoscato, A.; Tyurin, V. A.; Seo, W.; Epperly, M. W.; Greenberger, J. S.; Tyurina, Y. Y.; Kagan, V. E. Development of a Mitochondria-Targeted Nano-Complex of Imidazole-Substituted Oleic Aacid as a Radiomitigator. 2nd Annual Meeting for Society of Toxicology; The Toxicologist: Suppl. 1, Vol. 132, Abstract No. 2010, p. 428, San Antonio, TX, March 10–14, **2013**.
166. Dessolin, J.; Schuler, M.; Quinart, A.; De Giorgi, F.; Ghosez, L.; Ichas, F. Selective Targeting of Synthetic Antioxidants to Mitochondria: Towards a Mitochondrial Medicine for Neurodegenerative Diseases. *Eur. J. Pharmacol.* **2002,** *447* (2–3), 155–161.
167. Hoye, A. T.; Davoren, J. E.; Wipf, P.; Fink, M. P.; Kagan, V. E. Targeting Mitochondria. *Accounts. Chem. Res.* **2008,** *41* (1), 87–97.
168. Kagan, V. E.; Wipf, P.; Stoyanovsky, D.; Greenberger, J. S.; Borisenko, G.; Belikova, N. A.; Yanamala, N.; Arias, A. K. S.; Tungekar, M. A.; Jiang, J. F.; Tyurina, Y. Y.; Ji, J.; Klein-Seetharaman, J.; Pitt, B. R.; Shvedova, A. A.; Bayir, H. Mitochondrial Targeting of Electron Scavenging Antioxidants: Regulation of Selective Oxidation vs Random Chain Reactions. *Adv. Drug Deliver. Rev.* **2009,** *61* (14), 1375–1385.
169. Soule, B. P.; Hyodo, F.; Matsumoto, K.; Simone, N. L.; Cook, J. A.; Krishna, M. C.; Mitchell, J. B. The Chemistry and Biology of Nitroxide Compounds. *Free Radical Bio. Med.* **2007,** *42* (11), 1632–1650.
170. Tyurin, V. A. Z., H.; Kapralov, A. A.; Seo, W.; Huang, Z.; Jiang, J.; Skoda, E.; Star, S.; Stoyanovsky, D.; Wipf, P.; Epperly, M. W.; Greenberger, J. S.; Kagan, V. E. XJB Complexes with PEGylated Carbon Nanotubes as Mitigators of Irradiation Injury. *Unpublished Report*. **2013**.
171. Kalbac, M.; Hsieh, Y. P.; Farhat, H.; Kavan, L.; Hofmann, M.; Kong, J.; Dresselhaus, M. S. Defects in Individual Semiconducting Single Wall Carbon Nanotubes: Raman Spectroscopic and *In Situ* Raman Spectroelectrochemical Study. *Nano Lett.* **2010,** *10* (11), 4619–4626.
172. Dong, C. B.; Campell, A. S.; Eldawud, R.; Perhinschi, G.; Rojanasakul, Y.; Dinu, C. Z. Effects of Acid Treatment on Structure, Properties and Biocompatibility of Carbon Nanotubes. *Appl. Surf. Sci.* **2013,** *264*, 261–268.
173. Seo, W. J.; Kapralov, A. A.; Shurin, G. V.; Shurin, M. R.; Kagan, V. E.; Star, A. Payload Drug vs. Nanocarrier Biodegradation by Myeloperoxidase- and Peroxynitrite-Mediated Oxidations: Pharmacokinetic Implications. *Nanoscale* **2015,** *7* (19), 8689–8694.

174. Andersen, A. J. W., P. P.; Moghimi, S. M. Perspectives on Carbon Nanotube-Mediated Adverse Immune Effects. *Adv. Drug Deliv. Rev.* **2012,** *64*, 1700–1705.
175. Devadasu, V. R.; Bhardwaj, V.; Kumar, M. N. V. R. Can Controversial Nanotechnology Promise Drug Delivery? *Chem. Rev.* **2013,** *113* (3), 1686–1735.
176. Owens, D. E.; Peppas, N. A. Opsonization, Biodistribution, and Pharmacokinetics of Polymeric Nanoparticles. *Int. J. Pharmaceut.* **2006,** *307* (1), 93–102.
177. Shi, J. J.; Votruba, A. R.; Farokhzad, O. C.; Langer, R. Nanotechnology in Drug Delivery and Tissue Engineering: From Discovery to Applications. *Nano Lett.* **2010,** *10* (9), 3223–3230.
178. Chaudhuri, R. G.; Paria, S. Core/Shell Nanoparticles: Classes, Properties, Synthesis Mechanisms, Characterization, and Applications. *Chem. Rev.* **2012,** *112* (4), 2373–2433.
179. Mahmoudi, M.; Hofmann, H.; Rothen-Rutishauser, B.; Petri-Fink, A. Assessing the *In Vitro* and *In Vivo* Toxicity of Superparamagnetic Iron Oxide Nanoparticles. *Chem. Rev.* **2012,** *112* (4), 2323–2338.
180. Farokhzad, O. C.; Cheng, J. J.; Teply, B. A.; Sherifi, I.; Jon, S.; Kantoff, P. W.; Richie, J. P.; Langer, R. Targeted Nanoparticle-Aptamer Bioconjugates for Cancer Chemotherapy *In Vivo*. *Proc. Nat.l Acad. Sci. USA* **2006,** *103* (16), 6315–6320.
181. Allen, T. M. C., P. R. Drug Delivery Systems: Entering the Mainstream. *Science* **2004,** *303*, 1818–1822.
182. Ruenraroengsak, P.; Cook, J. M.; Florence, A. T. Nanosystem Drug Targeting: Facing up to Complex Realities. *J. Control. Release* **2010,** *141* (3), 265–276.
183. Zahr, A. S.; Davis, C. A.; Pishko, M. V. Macrophage Uptake of Core-Shell Nanoparticles Surface Modified with Poly(ethylene glycol). *Langmuir* **2006,** *22* (19), 8178–8185.
184. Merkel, T. J.; DeSimone, J. M. Dodging Drug-Resistant Cancer with Diamonds. *Sci. Transl. Med.* **2011,** *3* (73), 73ps8.
185. Sim, R. B.; Wallis, R. Surface Properties: Immune attack on nanoparticles. *Nat. Nanotechnol.* **2011,** *6* (2), 80–81.
186. Coussens, L. M. W., Z. Inflammation and Cancer. *Nature* **2002,** *420*, 860–867.
187. Henderson, J.; Heinecke, J. Myeloperoxidase: Enzymology. In *Peroxidases and Catalases*; Dunford, H. B. Ed. Wiley: Hoboken, NJ, **2010**; 257–269.
188. Rodriguez, P. L.; Harada, T.; Christian, D. A.; Pantano, D. A.; Tsai, R. K.; Discher, D. E. Minimal "Self" Peptides That Inhibit Phagocytic Clearance and Enhance Delivery of Nanoparticles. *Science* **2013,** *339* (6122), 971–975.
189. Hamad, I.; Al-Hanbali, O.; Hunter, A. C.; Rutt, K. J.; Andresen, T. L.; Moghimi, S. M. Distinct Polymer Architecture Mediates Switching of Complement Activation Pathways at the Nanosphere-Serum Interface: Implications for Stealth Nanoparticle Engineering. *Acs Nano* **2010,** *4* (11), 6629–6638.
190. Pelaz, B.; del Pino, P.; Maffre, P.; Hartmann, R.; Gallego, M.; Rivera-Fernandez, S.; de la Fuente, J. M.; Nienhaus, G. U.; Parak, W. J. Surface Functionalization of Nanoparticles with Polyethylene Glycol: Effects on Protein Adsorption and Cellular Uptake. *Acs Nano* **2015,** *9* (7), 6996–7008.
191. Minotti, G. M., P.; Salvatorelli, E.; Cairo, G.; Gianni, L. Anthracyclines: Molecular Advances and Pharmacologic Developments in Antitumor Activity and Cardiotoxicity. *Pharmacol. Rev.* **2004,** *56* (2), 185–229.
192. Reszka, K. J.; Wagner, B. A.; Teesch, L. M.; Britigan, B. E.; Spitz, D. R.; Burns, C. P. Inactivation of Anthracyclines by Cellular Peroxidase. *Cancer Res.* **2005,** *65* (14), 6346–6353.

193. Wagner, B. A.; Teesch, L. M.; Buettner, G. R.; Britigan, B. E.; Burns, C. P.; Reszka, K. J. Inactivation of Anthracyclines by Serum Heme Proteins. *Chem. Res. Toxicol.* **2007,** *20* (6), 920–926.
194. Pointon, A. V.; Walker, T. M.; Phillips, K. M.; Luo, J. L.; Riley, J.; Zhang, S. D.; Parry, J. D.; Lyon, J. J.; Marczylo, E. L.; Gant, T. W. Doxorubicin *In Vivo* Rapidly Alters Expression and Translation of Myocardial Electron Transport Chain Genes, Leads to ATP Loss and Caspase 3 Activation. *Plos One* **2010,** *5* (9).
195. Beijnen, J. H.; Wiese, G.; Underberg, W. J. M. Aspects of the Chemical-Stability of Doxorubicin and 7 Other Anthracyclines in Acidic Solution. *Pharm. Weekblad.* **1985,** *7* (3), 109–116.
196. Hofheinz, R. D.; Gnad-Vogt, S. U.; Beyer, U.; Hochhaus, A. Liposomal Encapsulated Anti-Cancer Drugs. *Anti-Cancer Drug* **2005,** *16* (7), 691–707.
197. Liu, Z.; Davis, C.; Cai, W. B.; He, L.; Chen, X. Y.; Dai, H. J. Circulation and Long-Term Fate of Functionalized, Biocompatible Single-Walled Carbon Nanotubes in Mice Probed by Raman Spectroscopy. *Proc. Natl. Acad. Sci. USA* **2008,** *105* (5), 1410–1415.
198. Welsher, K.; Liu, Z.; Sherlock, S. P.; Robinson, J. T.; Chen, Z.; Daranciang, D.; Dai, H. J. A Route to Brightly Fluorescent Carbon Nanotubes for Near-Infrared Imaging in Mice. *Nat. Nanotechnol.* **2009,** *4* (11), 773–780.
199. Floris, R.; Kim, Y.; Babcock, G. T.; Wever, R. Optical Spectrum of Myeloperoxidase: Origin of the Red Shift. *Eur. J. Biochem*. **1994**, *222* (2), 677–685.
200. Flavin, K.; Kopf, I.; Del Canto, E.; Navio, C.; Bittencourt, C.; Giordani, S. Controlled Carboxylic Acid Introduction: A Route to Highly Purified Oxidised Single-Walled Carbon Nanotubes. *J. Mater. Chem.* **2011,** *21* (44), 17881–17887.
201. Huang, H.; Yuan, Q.; Shah, J. S.; Misra, R. D. K. A New Family of Folate-Decorated and Carbon Nanotube-Mediated Drug Delivery System: Synthesis and Drug Delivery Response. *Adv. Drug Deliver. Rev.* **2011,** *63* (14-15), 1332–1339.
202. Hurst, J. Myeloperoxidase: Active Site Structure and Catalytic Mechanisms. In *Peroxidase in Chemistry and Biology* vol.1; Everse, J.; Everse, K. E.; Grisham, M. B. Eds. CRC press; Boca Raton, Fl. **2000**; 37–62.
203. Powis, G. Free-Radical Formation by Antitumor Quinones. *Free Radical Bio. Med.* **1989,** *6* (1), 63–101.
204. Beijnen, J. H.; Vanderhouwen, O. A. G. J.; Underberg, W. J. M. Aspects of the Degradation Kinetics of Doxorubicin in Aqueous-Solution. *Int. J. Pharmaceut.* **1986,** *32* (2–3), 123–131.
205. Stevens, R. V.; Chapman, K. T.; Weller, H. N. Convenient and Inexpensive Procedure for Oxidation of Secondary Alcohols to Ketones. *J. Org. Chem.* **1980,** *45* (10), 2030–2032.
206. Dunford, H. B.; Marquez-Curtis, L. A. Myeloperoxidase: Kinetic Evidence for Formation of Enzyme-Bound Chlorinating Intermediate. In *Methods in Enzymology*. Vol. 354; Purich. D. L. Ed. Elsevier Science: San Diego, CA, **2002**; 338–350.
207. Reszka, K. J.; McCormick, M. L.; Britigan, B. E. Peroxidase- and Nitrite-Dependent Metabolism of the Anthracycline Anticancer Agents Daunorubicin and Doxorubicin. *Biochemistry* **2001,** *40* (50), 15349–15361.
208. Maniezdevos, D. M.; Baurain, R.; Lesne, M.; Trouet, A. Degradation of Doxorubicin and Daunorubicin in Human and Rabbit Biological-Fluids. *J. Pharmaceut. Biomed.* **1986,** *4* (3), 353–365.

209. Doroshow, J. H.; Davies, K. J. A. Redox Cycling of Anthracyclines by Cardiac Mitochondria. 2. Formation of Superoxide Anion, Hydrogen-Peroxide, and Hydroxyl Radical. *J. Biol. Chem.* **1986,** *261* (7), 3068–3074.
210. Taatjes, D. J.; Gaudiano, G.; Resing, K.; Koch, T. H. Alkylation of DNA by the Anthracycline, Antitumor Drugs Adriamycin and Daunomycin. *J. Med. Chem.* **1996,** *39* (21), 4135–4138.
211. Zhao, Y.; Burkert, S. C.; Tang, Y. F.; Sorescu, D. C.; Kapralov, A. A.; Shurin, G. V.; Shurin, M. R.; Kagan, V. E.; Star, A. Nano-Gold Corking and Enzymatic Uncorking of Carbon Nanotube Cups. *J. Am. Chem. Soc.* **2015,** *137* (2), 675–684.
212. Solito, S.; Pinton, L.; Damuzzo, V.; Mandruzzato, S. Highlights on Molecular Mechanisms of MDSC-Mediated Immune Suppression: Paving the Way for New Working Hypotheses. *Immunol. Invest.* **2012,** *41* (6–7), 722–737.
213. Sweeny, J. G.; Estrada-Valdes, M. C.; Iacobucci, G. A.; Sato, H.; Sakamura, S. Photoprotection of the Red Pigments of Monascus Anka in Aqueous Media by 1,4,6-trihydroxynaphthalene. *J. Agric. Food Chem.* **1981**, *29* (6), 1189–1193.
214. Zhou, T.; Xu, S.; Wen, Q.; Pang, Z.; Zhao, X. One-Step Construction of Two Different Kinds of Pores in a 2D Covalent Organic Framework. *J. Am. Chem. Soc.* **2014**, *136* (45), 15885–15888.
215. Chen, X.; Addicoat, M.; Jin, E. Q.; Zhai, L. P.; Xu, H.; Huang, N.; Guo, Z. Q.; Liu, L. L.; Irle, S.; Jiang, D. L. Locking Covalent Organic Frameworks with Hydrogen Bonds: General and Remarkable Effects on Crystalline Structure, Physical Properties, and Photochemical Activity. *J. Am. Chem. Soc.* **2015**, *137* (9), 3241–3247.
216. Gou, P. P.; Kraut, N. D.; Feigel, I. M.; Star, A. Rigid versus Flexible Ligands on Carbon Nanotubes for the Enhanced Sensitivity of Cobalt Ions. *Macromolecules* **2013,** *46* (4), 1376–1383.
217. Wang, C.; Dong, H.; Hu, W.; Liu, Y.; Zhu, D. Semiconducting π-Conjugated Systems in Field-Effect Transistors: A Material Odyssey of Organic Electronics. *Chem. Rev.* **2012**, *112* (4), 2208–2267.
218. Zhuang, X. D.; Mai, Y. Y.; Wu, D. Q.; Zhang, F.; Feng, X. L. Two-Dimensional Soft Nanomaterials: A Fascinating World of Materials. *Adv. Mater.* **2015,** *27* (3), 403–427.
219. Colson, J. W.; Dichtel, W. R. Rationally Synthesized Two-Dimensional Polymers. *Nat. Chem.* **2013,** *5* (6), 453–465.
220. Geim, A. K.; Grigorieva, I. V. Van der Waals Heterostructures. *Nature* **2013,** *499* (7459), 419–425.
221. Withers, F.; Del Pozo-Zamudio, O.; Mishchenko, A.; Rooney, A. P.; Gholinia, A.; Watanabe, K.; Taniguchi, T.; Haigh, S. J.; Geim, A. K.; Tartakovskii, A. I.; Novoselov, K. S., Light-Emitting Diodes by Band-Structure Engineering in van der Waals Heterostructures. *Nat. Mater.* **2015,** *14* (3), 301–306.
222. Dou, L. T.; Wong, A. B.; Yu, Y.; Lai, M. L.; Kornienko, N.; Eaton, S. W.; Fu, A.; Bischak, C. G.; Ma, J.; Ding, T. N.; Ginsberg, N. S.; Wang, L. W.; Alivisatos, A. P.; Yang, P. D. Atomically Thin Two-Dimensional Organic-Inorganic Hybrid Perovskites. *Science* **2015,** *349* (6255), 1518–1521.
223. Feng, J.; Zhang, H. J. Hybrid Materials Based on Lanthanide Organic Complexes: A Review. *Chem. Soc. Rev.* **2013,** *42* (1), 387–410.
224. Xu, M. S.; Liang, T.; Shi, M. M.; Chen, H. Z. Graphene-Like Two-Dimensional Materials. *Chem. Rev.* **2013,** *113* (5), 3766–3798.

225. Butler, S. Z.; Hollen, S. M.; Cao, L. Y.; Cui, Y.; Gupta, J. A.; Gutierrez, H. R.; Heinz, T. F.; Hong, S. S.; Huang, J. X.; Ismach, A. F.; Johnston-Halperin, E.; Kuno, M.; Plashnitsa, V. V.; Robinson, R. D.; Ruoff, R. S.; Salahuddin, S.; Shan, J.; Shi, L.; Spencer, M. G.; Terrones, M.; Windl, W.; Goldberger, J. E. Progress, Challenges, and Opportunities in Two-Dimensional Materials Beyond Graphene. *ACS Nano* **2013,** *7* (4), 2898–2926.
226. Fiori, G.; Bonaccorso, F.; Iannaccone, G.; Palacios, T.; Neumaier, D.; Seabaugh, A.; Banerjee, S. K.; Colombo, L. Electronics Based on Two-Dimensional Materials. *Nat. Nanotechnol.* **2014,** *9* (10), 768–779.
227. Payamyar, P. K., B. T.; Ottinger, H. C.; Schluter, A. D. Two-dimensional polymers: concepts and perspectives. *Chem. Commun.* **2016,** *52*, 18–34.
228. Levesque, I.; Neabo, J. R.; Rondeau-Gagne, S.; Vigier-Carriere, C.; Daigle, M.; Morin, J. F. Layered Graphitic Materials from a Molecular Precursor. *Chem. Sci.* **2014,** *5* (2), 831–836.
229. Calik, M.; Auras, F.; Salonen, L. M.; Bader, K.; Grill, I.; Handloser, M.; Medina, D. D.; Dogru, M.; Lobermann, F.; Trauner, D.; Hartschuh, A.; Bein, T. Extraction of Photogenerated Electrons and Holes from a Covalent Organic Framework Integrated Heterojunction. *J. Am. Chem. Soc.* **2014,** *136* (51), 17802–17807.
230. Pachfule, P.; Kandambeth, S.; Diaz Diaz, D.; Banerjee, R. Highly Stable Covalent Organic Framework-Au Nanoparticles Hybrids for Enhanced Activity for Nitrophenol Reduction. *Chem. Commun.* **2014,** *50* (24), 3169–3172.
231. Das, G.; Biswal, B. P.; Kandambeth, S.; Venkatesh, V.; Kaur, G.; Addicoat, M.; Heine, T.; Verma, S.; Banerjee, R. Chemical Sensing in Two Dimensional Porous Covalent Organic Nanosheets. *Chem. Sci.* **2015,** *6* (7), 3931–3939.
232. Zhang, J.; Zhu, Z. P.; Tang, Y. P.; Müllen, K.; Feng, X. L. Titania Nanosheet-Mediated Construction of a Two-Dimensional Titania/Cadmium Sulfide Heterostructure for High Hydrogen Evolution Activity. *Adv. Mater.* **2014,** *26* (5), 734–738.
233. Aida, T.; Meijer, E. W.; Stupp, S. I. Functional Supramolecular Polymers. *Science* **2012,** *335* (6070), 813–817.
234. Brunsveld, L.; Folmer, B. J.; Meijer, E. W.; Sijbesma, R. P. Supramolecular Polymers. *Chem. Rev.* **2001,** *101* (12), 4071–4098.
235. Yang, L.; Tan, X.; Wang, Z.; Zhang, X. Supramolecular Polymers: Historical Development, Preparation, Characterization, and Functions. *Chem. Rev.* **2015,** *115* (15), 7196–7239.
236. Whittell, G. R.; Hager, M. D.; Schubert, U. S.; Manners, I. Functional Soft Materials from Metallopolymers and Metallosupramolecular Polymers. *Nat. Mater.* **2011,** *10* (3), 176–188.
237. De Greef, T. F. A.; Smulders, M. M. J.; Wolffs, M.; Schenning, A. P. H. J.; Sijbesma, R. P.; Meijer, E. W. Supramolecular Polymerization. *Chem. Rev.* **2009,** *109* (11), 5687–5754.
238. Ding, S. Y.; Wang, W. Covalent Organic Frameworks (COFs): From Design to Applications. *Chem. Soc. Rev.* **2013,** *42* (2), 548–568.
239. Feng, X.; Ding, X. S.; Jiang, D. L. Covalent Organic Frameworks. *Chem. Soc. Rev.* **2012,** *41* (18), 6010–6022.
240. Berlanga, I.; Mas-Balleste, R.; Zamora, F. Tuning Delamination of Layered Covalent Organic Frameworks through Structural Design. *Chem. Commun.* **2012,** *48* (64), 7976–7978.
241. Cai, S. L.; Zhang, W. G.; Zuckermann, R. N.; Li, Z. T.; Zhao, X.; Liu, Y. The Organic Flatland—Recent Advances in Synthetic 2D Organic Layers. *Adv. Mater.* **2015,** *27* (38), 5762–5770.

242. Belowich, M. E.; Stoddart, J. F. Dynamic Imine Chemistry. *Chem. Soc. Rev.* **2012,** *41* (6), 2003–2024.
243. Ji, Q.; Lirag, R. C.; Miljanic, O. S. Kinetically Controlled Phenomena in Dynamic Combinatorial Libraries. *Chem. Soc. Rev.* **2014,** *43* (6), 1873–1884.
244. Cote, A. P.; Benin, A. I.; Ockwig, N. W.; O'Keeffe, M.; Matzger, A. J.; Yaghi, O. M. Porous, Crystalline, Covalent Organic Frameworks. *Science* **2005,** *310* (5751), 1166–1170.
245. Ogi, S.; Sugiyasu, K.; Manna, S.; Samitsu, S.; Takeuchi, M. Living Supramolecular Polymerization Realized through a Biomimetic Approach. *Nat. Chem.* **2014,** *6* (3), 188–195.
246. Afshari, M.; Sikkema, D. J.; Lee, K.; Bogle, M. High Performance Fibers Based on Rigid and Flexible Polymers. *Polym. Rev.* **2008,** *48* (2), 230–274.
247. Zhang, T.; Jin, J. H.; Yang, S. L.; Li, G. A.; Jiang, J. M. Preparation and Properties of Novel PIPD Fibers. *Chinese Sci. Bull.* **2010,** *55* (36), 4203–4207.
248. Lin, H.; Huang, Y. D.; Wang, F. Synthesis and Properties of Poly[p-(2,5-dihydroxy)-phenylenebenzobisoxazole] Fiber. *Int. J. Mol. Sci.* **2008,** *9* (11), 2159–2168.
249. Huang, J.; Li, G. R.; Wu, Z. G.; Song, Z. B.; Zhou, Y. Y.; Shuai, L.; Weng, X. C.; Zhou, X.; Yang, G. F. Bisbenzimidazole to Benzobisimidazole: From Binding B-form Duplex DNA to Recognizing Different Modes of Telomere G-quadruplex. *Chem. Commun.* **2009,** (8), 902–904.
250. Gong, J.; Kohama, S. I.; Kimura, K.; Yamazaki, S.; Kimura, K. Preparation of Brush-Like Crystals of Poly[2,6-(1,4-phenylene)-benzobisimidazole]. *Polymer* **2008,** *49* (18), 3928–3937.
251. Takahashi, Y. Crystal Structure of Poly(pyridobisimidazole), PIPD. *Macromolecules* **2003,** *36*, 8652–8655.
252. Hageman, J. C. L. d. W., G. A.; de Groota, R. A.; Klop, E. A. The Role of the Hydrogen Bonding Network for the Shear Modulus of PIPD. *Polymer* **2005,** *46*, 9144–9154.
253. Klop, E. A.; Lammers, M. XRD Study of the New Rigid-Rod Polymer Fibre PIPD. *Polymer* **1998,** *39* (24), 5987–5998.
254. Dang, T. D.; Tan, L. S. Dihydroxy Pendent Benzobisazole Rigid-Rod Ladder Polymers. In *Proceedings of the ACS Division of Polymeric Materials, Science and Engineering*. Vol. *62*, Boston, MA, **1990**; pp 86–90.
255. Sikkema, D. J. Design, Synthesis and Properties of a Novel Rigid Rod Polymer, PIPD or 'M5': High Modulus and Tenacity Fibres with Substantial Compressive Strength. *Polymer* **1998,** *39* (24), 5981–5986.
256. Woodcock, H. L., 3rd; Hodoscek, M.; Gilbert, A. T.; Gill, P. M.; Schaefer, H. F., 3rd; Brooks, B. R. Interfacing Q-Chem and CHARMM to Perform QM/MM Reaction Path Calculations. *J. Comput. Chem.* **2007,** *28* (9), 1485–1502.
257. Becke, A. D., Density-Functional Thermochemistry. 3. The Role of Exact Exchange. *J. Chem. Phys.* **1993,** *98* (7), 5648–5652.
258. Gallant, A. J.; MacLachlan, M. J. Ion-Induced Tubular Assembly of Conjugated Schiff-Base Macrocycles. *Angew. Chem. Int. Ed.* **2003,** *42* (43), 5307–5310.
259. Brunsveld, L.; Meijer, E. W.; Prince, R. B.; Moore, J. S. Self-Assembly of Folded *m*-Phenylene Ethynylene Oligomers into Helical Columns. *J. Am. Chem. Soc.* **2001,** *123* (33), 7978–7984.
260. Takasuka, M.; Matsui, Y. Experimental Observations and CNDO/2 Calculations for Hydroxy Stretching Frequency Shifts, Intensities, and Hydrogen Bond Energies of Intramolecular Hydrogen Bonds in *ortho*-Substituted Phenols. *J. Chem. Soc., Perkin Trans.* **1979,** *2*, 1743–1750.

261. Boydston, A. J.; Vu, P. D.; Dykhno, O. L.; Chang, V.; Wyatt, A. R.; Stockett, A. S.; Ritschdbrff, E. T.; Shear, J. B.; Bielawski, C. W. Modular Fluorescent Benzobis(imidazolium) Salts: Syntheses, Photophysical Analyses, and Applications. *J. Am. Chem. Soc.* **2008,** *130* (10), 3143–3156.
262. Rabbani, M. G.; El-Kaderi, H. M. Synthesis and Characterization of Porous Benzimidazole-Linked Polymers and Their Performance in Small Gas Storage and Selective Uptake. *Chem. Mater.* **2012,** *24* (8), 1511–1517.
263. Spitler, E. L.; Koo, B. T.; Novotney, J. L.; Colson, J. W.; Uribe-Romo, F. J.; Gutierrez, G. D.; Clancy, P.; Dichtel, W. R. A 2D Covalent Organic Framework with 4.7-nm Pores and Insight into Its Interlayer Stacking. *J. Am. Chem. Soc.* **2011,** *133* (48), 19416–19421.
264. Sobczyk, L.; Grabowski, S. J.; Krygowski, T. M. Interrelation between H-bond and π-Electron Delocalization. *Chem. Rev.* **2005,** *105* (10), 3513–3560.
265. Bunck, D. N.; Dichtel, W. R. Bulk Synthesis of Exfoliated Two-Dimensional Polymers Using Hydrazone-Linked Covalent Organic Frameworks. *J. Am. Chem. Soc.* **2013,** *135* (40), 14952–14955.
266. Li, G. L.; Mohwald, H.; Shchukin, D. G. Precipitation Polymerization for Fabrication of Complex Core-Shell Hybrid Particles and Hollow Structures. *Chem. Soc. Rev.* **2013,** *42* (8), 3628–3646.
267. Dani, R. K.; Bharty, M. K.; Kushawaha, S. K.; Prakash, O.; Singh, R. K.; Singh, N. K. Ni(II), Cu(II) and Zn(II) Complexes of (Z)-N′(1,3,4-thiadiazol-2-yl) acetimidate: Synthesis, Spectral, Solid State Electrical Conductivity, X-ray Diffraction and DFT Study. *Polyhedron* **2013**, *65* (28), 31–41.
268. Zhang, G. F.; Han, X. W.; Luan, Y. X.; Wang, Y.; Wen, X.; Ding, C. R. L-Proline: An Efficient N,O-bidentate Ligand for Copper-Catalyzed Aerobic Oxidation of Primary and Secondary Benzylic Alcohols at Room Temperature. *Chem. Commun*. **2013**, *49* (72), 7908–7910.
269. Srinivasan, K.; Govindarajan, S.; Harrison, W. T. A. Divalent metal complexes of formylhydrazine: Syntheses and Crystal Structures of $M(CH_4N_2O)_2(H_2O)_2{\cdot}2NO_3$ (M = Zn, Co). *Inorg. Chem. Commun*. **2009**, *12* (7), 619–621.
270. Grzybkowski, W.; Pilarczyk, M. Ionization Equilibria of Cobalt(II) Chloride in *N*, *N*-Dimethylformamide. *J. Chem. Soc. Faraday Trans. 1*. **1986**, *82* (6), 1703–1712.
271. Costişor, O.; Pantenburg, I.; Tudose, R.; Meyer, G. New Copper(II) and Cobalt(II) Complexes with the *N*,*N*-Bis(antipyryl-4-methyl)-piperazine (BAMP) Ligand: $Co_2(BAMP)Cl_4$ and $[Cu(BAMP)(H_2O)](ClO_4)_2$. *Z. Anorg. Allg. Chem.* **2004**, *630* (11), 1645–1649.
272. Hou, J. H.; Park, M. H.; Zhang, S. Q.; Yao, Y.; Chen, L. M.; Li, J. H.; Yang, Y. Bandgap and Molecular Energy Level Control of Conjugated Polymer Photovoltaic Materials Based on Benzo[1,2-b : 4,5-b']dithiophene. *Macromolecules* **2008,** *41* (16), 6012–6018.
273. Akine, S.; Taniguchi, T.; Nabeshima, T. Helical Metallohost-Guest Complexes via Site-Selective Transmetalation of Homotrinuclear Complexes. *J. Am. Chem. Soc.* **2006,** *128* (49), 15765–15774.
274. Audi, H.; Chen, Z. R.; Charaf-Eddin, A.; D'Aleo, A.; Canard, G.; Jacquemin, D.; Siri, O. Extendable Nickel Complex Tapes That Reach NIR Absorptions. *Chem. Commun.* **2014,** *50* (96), 15140–15143.
275. Monfared, H. H.; Amouei, Z. Hydrogen Peroxide Oxidation of Aromatic Hydrocarbons by Immobilized Iron(III). *J. Mol. Catal. A: Chemical* **2004,** *217* (1–2), 161–164.

276. Andas, J.; Adam, F.; Rahman, I. A.; Taufiq-Yap, Y. H. Optimization and Mechanistic Study of the Liquid-Phase Oxidation of Naphthalene over Biomass-Derived Iron Catalyst. *Chem. Eng. J.* **2014,** *252*, 382–392.
277. Zhang, Y. G.; Ying, J. Y. Main-Chain Organic Frameworks with Advanced Catalytic Functionalities. *ACS Catal.* **2015,** *5* (4), 2681–2691.
278. Lin, S.; Diercks, C. S.; Zhang, Y. B.; Kornienko, N.; Nichols, E. M.; Zhao, Y. B.; Paris, A. R.; Kim, D.; Yang, P.; Yaghi, O. M.; Chang, C. J. Covalent Organic Frameworks Comprising Cobalt Porphyrins for Catalytic CO_2 Reduction in Water. *Science* **2015,** *349* (6253), 1208–1213.
279. Zhang, Y. G.; Riduan, S. N. Functional Porous Organic Polymers for Heterogeneous Catalysis. *Chem. Soc. Rev.* **2012,** *41* (6), 2083–2094.
280. Wang, X. S.; Chrzanowski, M.; Yuan, D. Q.; Sweeting, B. S.; Ma, S. Q. Covalent Heme Framework as a Highly Active Heterogeneous Biomimetic Oxidation Catalyst. *Chem. Mater.* **2014,** *26* (4), 1639–1644.
281. Pachfule, P.; Kandambeth, S.; Diaz, D. D.; Banerjee, R. Highly Stable Covalent Organic Framework-Au Nanoparticles Hybrids for Enhanced Activity for Nitrophenol Reduction. *Chem. Commun.* **2014,** *50* (24), 3169–3172.
282. Dienstmaier, J. F.; Gigler, A. M.; Goetz, A. J.; Knochel, P.; Bein, T.; Lyapin, A.; Reichlmaier, S.; Heckl, W. M.; Lackinger, M. Synthesis of Well-Ordered COF Monolayers: Surface Growth of Nanocrystalline Precursors versus Direct On-Surface Polycondensation. *ACS Nano* **2011,** *5* (12), 9737–9745.
283. DeBlase, C. R.; Hernandez-Burgos, K.; Silberstein, K. E.; Rodriguez-Calero, G. G.; Bisbey, R. P.; Abruna, H. D.; Dichtel, W. R. Rapid and Efficient Redox Processes within 2D Covalent Organic Framework Thin Films. *ACS Nano* **2015,** *9* (3), 3178–3183.
284. Yang, B.; Bjork, J.; Lin, H. P.; Zhang, X. Q.; Zhang, H. M.; Li, Y. Y.; Fan, J.; Li, Q.; Chi, L. F. Synthesis of Surface Covalent Organic Frameworks via Dimerization and Cyclotrimerization of Acetyls. *J. Am. Chem. Soc.* **2015,** *137* (15), 4904–4907.
285. Rodriguez-Lopez, J.; Ritzert, N. L.; Mann, J. A.; Tan, C.; Dichtel, W. R.; Abruna, H. D. Quantification of the Surface Diffusion of Tripodal Binding Motifs on Graphene Using Scanning Electrochemical Microscopy. *J. Am. Chem. Soc.* **2012,** *134* (14), 6224–6236.
286. Larrea, C. R.; Baddeley, C. J. Fabrication of a High-Quality, Porous, Surface-Confined Covalent Organic Framework on a Reactive Metal Surface. *Chemphyschem.* **2016,** *17* (7), 971–975.
287. Xu, L. R.; Zhou, X.; Tian, W. Q.; Gao, T.; Zhang, Y. F.; Lei, S. B.; Liu, Z. F. Surface-Confined Single-Layer Covalent Organic Framework on Single-Layer Graphene Grown on Copper Foil. *Angew. Chem. Int. Edit.* **2014,** *53* (36), 9564–9568.
288. Zwaneveld, N. A. A.; Pawlak, R.; Abel, M.; Catalin, D.; Gigmes, D.; Bertin, D.; Porte, L. Organized Formation of 2D Extended Covalent Organic Frameworks at Surfaces. *J. Am. Chem. Soc.* **2008,** *130* (21), 6678–6679.
289. Feng, J.; Li, W. B.; Qian, X. F.; Qi, J. S.; Qi, L.; Li, J. Patterning of Graphene. *Nanoscale* **2012,** *4* (16), 4883–4899.
290. Han, X. G.; Funk, M. R.; Shen, F.; Chen, Y. C.; Li, Y. Y.; Campbell, C. J.; Dai, J. Q.; Yang, X. F.; Kim, J. W.; Liao, Y. L.; Connell, J. W.; Barone, V.; Chen, Z. F.; Lin, Y.; Hu, L. B. Scalable Holey Graphene Synthesis and Dense Electrode Fabrication toward High-Performance Ultracapacitors. *ACS Nano* **2014,** *8* (8), 8255–8265.

291. Lin, Y.; Han, X. G.; Campbell, C. J.; Kim, J. W.; Zhao, B.; Luo, W.; Dai, J. Q.; Hu, L. B.; Connell, J. W. Holey Graphene Nanomanufacturing: Structure, Composition, and Electrochemical Properties. *Adv. Funct. Mater.* **2015,** *25* (19), 2920–2927.
292. Bai, J. W.; Zhong, X.; Jiang, S.; Huang, Y.; Duan, X. F. Graphene Nanomesh. *Nat. Nanotechnol.* **2010,** *5* (3), 190–194.
293. Yang, J.; Ma, M. Z.; Li, L. Q.; Zhang, Y. F.; Huang, W.; Dong, X. C. Graphene Nanomesh: New Versatile Materials. *Nanoscale* **2014,** *6* (22), 13301–13313.
294. Jiang, L. L.; Fan, Z. J. Design of Advanced Porous Graphene Materials: From Graphene Nanomesh to 3D Architectures. *Nanoscale* **2014,** *6* (4), 1922–1945.
295. Xu, Y. X.; Sheng, K. X.; Li, C.; Shi, G. Q. Self-Assembled Graphene Hydrogel via a One-Step Hydrothermal Process. *ACS Nano* **2010,** *4* (7), 4324–4330.
296. Wu, Z. S.; Yang, S. B.; Sun, Y.; Parvez, K.; Feng, X. L.; Müllen, K. 3D Nitrogen-Doped Graphene Aerogel-Supported Fe_3O_4 Nanoparticles as Efficient Eletrocatalysts for the Oxygen Reduction Reaction. *J. Am. Chem. Soc.* **2012,** *134* (22), 9082–9085.
297. Jiang, D. E.; Cooper, V. R.; Dai, S. Porous Graphene as the Ultimate Membrane for Gas Separation. *Nano Lett.* **2009,** *9* (12), 4019–4024.
298. Li, D. B.; Hu, W.; Zhang, J. Q.; Shi, H.; Chen, Q.; Sun, T. Y.; Liang, L. J.; Wang, Q. Separation of Hydrogen Gas from Coal Gas by Graphene Nanopores. *J. Phys. Chem. C* **2015,** *119* (45), 25559–25565.
299. Du, H. L.; Li, J. Y.; Zhang, J.; Su, G.; Li, X. Y.; Zhao, Y. L. Separation of Hydrogen and Nitrogen Gases with Porous Graphene Membrane. *J. Phys. Chem. C* **2011,** *115* (47), 23261–23266.
300. Zhang, L. L.; Zhao, X.; Stoller, M. D.; Zhu, Y. W.; Ji, H. X.; Murali, S.; Wu, Y. P.; Perales, S.; Clevenger, B.; Ruoff, R. S. Highly Conductive and Porous Activated Reduced Graphene Oxide Films for High-Power Supercapacitors. *Nano Lett.* **2012,** *12* (4), 1806–1812.
301. Wang, X. L.; Jiao, L. Y.; Sheng, K. X.; Li, C.; Dai, L. M.; Shi, G. Q. Solution-Processable Graphene Nanomeshes with Controlled Pore Structures. *Sci. Rep.* **2013,** *3*.
302. Zhang, L. M.; Diao, S. O.; Nie, Y. F.; Yan, K.; Liu, N.; Dai, B. Y.; Xie, Q.; Reina, A.; Kong, J.; Liu, Z. F. Photocatalytic Patterning and Modification of Graphene. *J. Am. Chem. Soc.* **2011,** *133* (8), 2706–2713.
303. Jhajharia, S. K.; Selvaraj, K. Non-Templated Ambient Nanoperforation of Graphene: A Novel Scalable Process and Its Exploitation for Energy and Environmental Applications. *Nanoscale* **2015,** *7* (46), 19705–19713.
304. Fleischer, E. B.; Palmer, J. M.; Srivasta, T. S.; Chatterjee, A. Thermodynamic and Kinetic Properties of an Iron-Porphyrin System. *J. Am. Chem. Soc.* **1971,** *93* (13), 3162–3167.
305. Oveisi, A. R.; Zhang, K. N.; Khorramabadi-Zad, A.; Farha, O. K.; Hupp, J. T. Stable and Catalytically Active Iron Porphyrin-Based Porous Organic Polymer: Activity as Both a Redox and Lewis Acid Catalyst. *Sci. Rep.* **2015,** *5*.
306. Shinde, D. B.; Kandambeth, S.; Pachfule, P.; Kumar, R. R.; Banerjee, R. Bifunctional Covalent Organic Frameworks with Two Dimensional Organocatalytic Micropores. *Chem. Commun.* **2015,** *51* (2), 310–313.
307. Foote, C. S.; Wexler, S.; Ando, W.; Higgins, R. Chemistry of Singlet Oxygen. 4. Oxygenations with Hypochlorite-Hydrogen Peroxide. *J. Am. Chem. Soc.* **1968,** *90* (4), 975–981.
308. Held, A. M.; Halko, D. J.; Hurst, J. K. Mechanisms of Chlorine Oxidation of Hydrogen-Peroxide. *J. Am. Chem. Soc.* **1978,** *100* (18), 5732–5740.

309. Kovtyukhova, N. I.; Wang, Y. X.; Berkdemir, A.; Cruz-Silva, R.; Terrones, M.; Crespi, V. H.; Mallouk, T. E. Non-Oxidative Intercalation and Exfoliation of Graphite by Bronsted Acids. *Nat. Chem.* **2014,** *6* (11), 957–963.
310. Drain, C. M.; Varotto, A.; Radivojevic, I. Self-Organized Porphyrinic Materials. *Chem. Rev.* **2009,** *109* (5), 1630–1658.
311. Wang, Z. C.; Li, Z. Y.; Medforth, C. J.; Shelnutt, J. A. Self-assembly and Self-Metallization of Porphyrin Nanosheets. *J. Am. Chem. Soc.* **2007,** *129* (9), 2440–2441.
312. Rananaware, A.; Bhosale, R. S.; Ohkubo, K.; Patil, H.; Jones, L. A.; Jackson, S. L.; Fukuzumi, S.; Bhosale, S. V.; Bhosale, S. V. Tetraphenylethene-Based Star Shaped Porphyrins: Synthesis, Self-Assembly, and Optical and Photophysical Study. *J. Org. Chem.* **2015,** *80* (8), 3832–3840.
313. Hu, J. S.; Guo, Y. G.; Liang, H. P.; Wan, L. J.; Jiang, L. Three-Dimensional Self-Organization of Supramolecular Self-Assembled Porphyrin Hollow Hexagonal Nanoprisms. *J. Am. Chem. Soc.* **2005,** *127* (48), 17090–17095.
314. Naebe, M.; Wang, J.; Amini, A.; Khayyam, H.; Hameed, N.; Li, L. H.; Chen, Y.; Fox, B. Mechanical Property and Structure of Covalent Functionalised Graphene/Epoxy Nanocomposites. *Sci. Rep.* **2014,** *4*.
315. Tang, Z. H.; Zhang, L. Q.; Zeng, C. F.; Lin, T. F.; Guo, B. C. General Route to Graphene with Liquid-Like Behavior by Non-Covalent Modification. *Soft Matter* **2012,** *8* (35), 9214–9220.
316. Peng, E. W.; Choo, E. S. G.; Chandrasekharan, P.; Yang, C. T.; Ding, J.; Chuang, K. H.; Xue, J. M. Synthesis of Manganese Ferrite/Graphene Oxide Nanocomposites for Biomedical Applications. *Small* **2012,** *8* (23), 3620–3630.